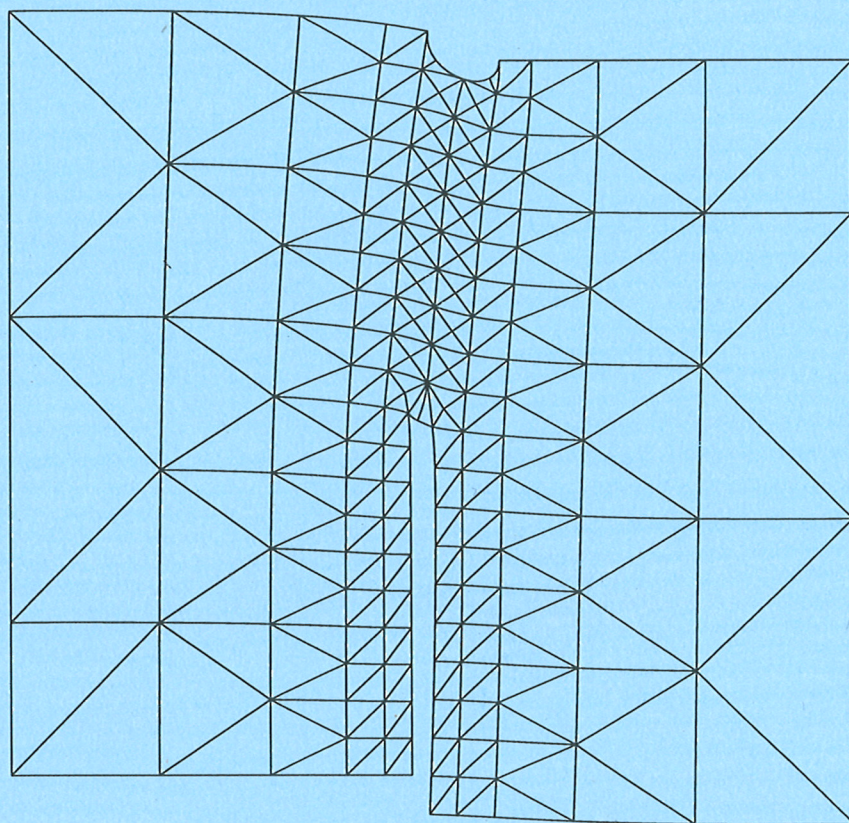Nordic Association for
Computational Mechanics

NINTH NORDIC SEMINAR ON COMPUTATIONAL MECHANICS

Technical University of Denmark
October 25-26, 1996

NINTH NORDIC SEMINAR ON COMPUTATIONAL MECHANICS

Technical University of Denmark
October 25-26, 1996

Edited by Lars Damkilde

Preface

The Nordic Association for Computational Mechanics (NoACM) was created in October 1988 with the purpose of promoting research and applications within the area of computational mechanics and to contribute to contacts and interchange of ideas between researchers and practitioners in this field. In 1991 the Baltic states joined NoACM.

The main activity of NoACM is the annual Seminar on Computational Mechanics. The format of the seminar is a small number of keynote lectures and a large number of short presentations. This preprint volume contains extended abstracts for both the invited lectures and the short presentations. The purpose is to allow the author to state the main ideas and give a few references for further study. Thus the contents of this volume should be considered as appetizers and not a substitute for the full text.

The organizing commitee gratefully acknowledge support from both the Department of Structural Engineering and Materials and the Technical University of Denmark. Personnally I should also like to express my thanks to Professor Steen Krenk, Lund Institute of Technology, for invaluable advice during the planning of the seminar.

Lyngby, October 1996

Lars Damkilde

Contents

Keynote lectures:

Short presentations:

Session 1a

Session 1b

ON ENGINEERING DESIGN OPTIMIZATION

Niels Olhoff

Institute of Mechanical Engineering

Aalborg University, DK-9220 Aalborg, Denmark

Abstract - A survey of problems of optimum engineering design is presented. The main emphasis is devoted to fundamental aspects and current methods and capabilities for topology and shape optimization, and a number of examples will be given.

The methods are selected from conditions of versatility and suitability for integration into an engineering design optimization system which realizes the design process as an iterative solution procedure of a multicriterion optimization problem based on the concept of integration of finite element analysis, design sensitivity analysis, and optimization by mathematical programming.

1. Introduction

Engineering activity has always involved endeavours towards optimization, and this particularly holds true for the field of engineering design. Earlier, engineering design was conceived as a kind of "art" that demanded great ingenuity and experience of the designer, and the development of the field was characterized by *gradual evolution* in terms of the continual improvement of *existing types* of engineering designs. The design process generally was a sequential "trial and error" process where the designer's skills and experience were the most important prerequisites for successful decisions for the "trial" phase.

In contrast, today's strong technological competition which requires reduction of design time and using of products with high quality and functionality with resulting high costs, together with the current emphasis on saving of energy and reuse of materials, consideration of environmental problems, etc., often involves the creation of new products for which prior engineering experience is totally lacking. The development of such products must naturally lend itself towards scientific methods.

Hence, during recent decades, engineering design has changed from "art" and "evolution" to scientifically based methods of rational design and optimization. This development has been strongly boosted by the advent of reliable general analysis methods such as finite element analysis, design sensitivity analysis, and methods of mathematical programming, together with the exponentially increasing speed and capacity of digital computers. Thus, methods of rational design and optimization are now finding widespread use in aeronautical, aerospace, mechanical, nuclear, civil, and off-shore engineering. In materials science, the techniques are now being used in research devoted to tailoring of materials with specific properties. The development has been supported by vigorous research in the fields of design sensitivity analysis and optimum design, see e.g., the proceedings [1-4] from recent conferences and the monograph [5].

In this lecture the engineering design process is conceived as an iterative solution procedure for a multicriteria optimization problem. The problem is defined, possibly redefined during the solution process, and finally solved, by the designer in an interactive dialogue with a suitable software system for design optimization. The process can be essentially considered as a rational search for the optimal spatial distribution of material within a prescribed admissible structural domain subject to multiple criteria and constraints. Accordingly, it is the

aim of this lecture to present basic concepts for problems of engineering design treate rationally as multicriterion problems, and to give a brief survey of selected enabling metho illustrated by examples. The topics of the lecture are outlined below. The methods select for presentation reflect those that constitute part of the backbone of the Optimum DESi SYstem ODESSY (see [6-9]), which is being developed at Aalborg University, and most the examples to be presented have been obtained using ODESSY. For reasons of brevity, tl CAD-integration and the interactive design capabilities [6,7] of the system will not be covere here.

The design optimization system is developed as part of a project within the Dani Technical Research Council's Programme of Research on Computer Aided Design. Th project is carried out in a fruitful collaboration between researchers from the Institute Mechanical Engineering of Aalborg University and the Department of Mathematics and tl Department of Solid Mechanics of the Technical University of Denmark. Many colleagues ar friends from abroad have also participated in the work, and their inspiring cooperation gratefully acknowledged.

2. Basic Concepts

The label engineering design optimization identifies the type of design problem where the s of structural parameters is subdivided into so-called "preassigned parameters" and "desig variables", and the problem consists in determining optimum values of the design variable such that they *maximize* or *minimize* a specific function termed the *objective* (or *criterion*, cost function), while satisfying a set of geometrical and/or behavioural requirements which ar specified prior to design, and are called *constraints*. A brief account of other basic concep will be given, and the types of different design variables, objective and constraint function which ODESSY can handle, will be discussed.

3. Mathematical Formulation for Multicriteria Optimization

The optimization system ODESSY is based on the concept of integration of modules of finit element analysis, design sensitivity analysis and mathematical programming. Since in practic problems of optimum engineering design it is necessary to take into account several structur performance and failure criteria in the problem formulation, a *multicriterion* approach has bee adopted. Moreover, in order to meet practical needs of versatility, the basic mathematic formulation for optimum design must possess sufficient flexibility such that the system ca handle both problems of minimizing cost subject to several constraints, and problems of multi criterion optimization for prescribed resource (and additional constraints). To achieve thes goals, the multicriterion problem is cast in scalar form by stating it as minimization of th maximum of a weighted set of the criteria. Such an interpretation of the multicriterio optimization problem can be formulated as a problem of minimizing a variable upper boun on the weighted criteria, and this *bound formulation* [10,11] implies the considerabl advantage that the multicriterion problem becomes differentiable.

4. Design Sensitivity Analysis

Structural shape optimization requires an efficient and reliable method of shape sensitivit analysis, and a commonly used technique is based on implicit differentiation of the finit element discretized equilibrium conditions for the structure with respect to the desig variables. The most general implementation of this technique, which is preferable from th viewpoint of computational cost and ease of implementation, implies application of numerica

differentiation of the finite element stiffness matrices [12,13], and is termed the *semi-analytical method of sensitivity analysis*. This method has been implemented as an integral part of a finite element system which is developed (and being continually extended) for structural analyses and integrated in ODESSY. This way semi-analytical sensitivity analyses can be carried out in a unified manner for a large number of different types of finite elements and types of structural behaviour [7,9].

It is well-known that the design sensitivity analysis of eigenvalues is complicated in the case of multiple eigenvalues as these are not differentiable functions of design variables in the usual Fréchet sense. However, based on a mathematical perturbation technique, a general framework [14] has been established for design sensitivity analysis and optimization of multiple eigenvalues of complex structures. This development is substantiated by a number of examples in [14,15].

Whereas the semi-analytical method of sensitivity analysis works very well for a large majority of problems, it has recently been shown by way of examples [16] that the method may yield erroneous shape design sensitivities for plates, shells, and long slender structures. However, a simple, easily implemented and computationally inexpensive numerical method of "exact" semi-analytical sensitivity analysis (exact except for round-off error) that completely eliminates the deficiencies is now available (see [17,18]), and has been successfully implemented in ODESSY.

5. Shape Optimization of Discrete Structures

While optimization of discrete 2D or 3D truss or frame structures with cross-sectional areas of bar or beam members as design variables is termed *sizing optimization*, and optimization with positions of a given number of joints as design variables is called *configuration optimization*, the combined problem of optimizing both sizing and configuration is labeled *shape optimization* of the discrete structure. Minimization of the structural weight is most often the design objective in such problems which usually encounter multiple loading conditions with constraints that include stresses, displacements, and elastic as well as plastic buckling of members in compression, see, e.g., [8,19].

6. Shape Optimization of Continuum Structures

In this type of problem, the goal is to determine the shape of the structural domain, i.e., the problem is defined on a domain that is unknown *a priori*. Like optimization problems in general, shape optimization is a highly non-linear problem where it is necessary to employ an iterative numerical solution scheme and to determine the optimum design through a sequence of redesign and reanalysis. This implies that the structural geometry must be repeatedly converted into a finite element model with the proper loads and boundary conditions, and that the variable structural design must be described (parameterized) in terms of a finite number of geometrical variables.

Particularly for problems of shape optimization of continuum structures, it is necessary to make a clear distinction between the *analysis model* as represented by the finite element model, and the parameterized geometric model of the variable structure which is termed the *design model* (cf. [20]). The design model is endowed with additional significance because it can be closely connected with a CAD model as described in [6].

The design model may consist of so-called *design elements* as presented in [7,20]. The boundaries of the design elements can be curves of almost any character, i.e., piecewise straight lines, arcs, b-splines of any degree of continuity, Bezier curves, Coons patches, etc. It is therefore very simple to generate relatively complicated geometries with a small number

of design elements. The shapes of the boundaries are controlled by a number of control point also often termed *master nodes*.

7. Topology Optimization

It is characteristic that the solution to a shape optimization problem (cf. Sections 5 and 6) wi always have the same topology as that of the initial design. Thus, the topology of mechanical structure or component to be optimized cannot be changed by using methods (shape optimization. As the choice of the best topology has considerable impact on the gai to be achieved by optimization, the development [21] of a method for topology optimizatic was a remarkable break-through in the field of optimum design. The reader is referred to ε exhaustive monograph [5] for recent developments and publications.

Contrary to shape problems, a problem of topology optimization is defined on a *fixe domain of space*, and the structure is considered as a spatial sub-domain with high density (material. The topology problem is basically one of discrete optimization, but this difficulty avoided by introducing relationships between stiffness components and density based o physical modelling of porous, periodic microstructures whose orientation and density ai described by continuous variables over the admissible design domain.

The topology optimization results in a prediction of the structural type and overall layou and gives a rough description of the shape of the outer as well as inner boundaries of th structure. This motivates the use of topology optimization as a *preprocessor* for subseque шi shape or sizing optimization [22]. Thus, depending on the amount of material available, th generated topology will basically either define the rough shape of a continuum structur possibly with macroscopic interior holes, or the skeleton of a truss- or beam-like structure wit slender members. This way, the optimal topology can be used as a basis for the abovemer tioned procedures for refined shape optimization.

8. Closure

This short paper reflects coordinated research activities towards the creation of an interactiv engineering design environment for rational design and optimization of mechanical product: systems and components. Current efforts are devoted to further extensions of the engineerin design facilities in terms of methods as well as design criteria and objectives, with a view c allowing for solution of as broad a spectrum of practical engineering design problems a possible. This to a large extent implies expansion of the system capabilities into other field of engineering, and will hopefully result in a truly multidisciplinary engineering design systen

References

1. *Olhoff, N.; Rozvany, G.I.N. (1995) (Eds.)*: Structural and Multidisciplinary Optimizatior Pergamon, Oxford, U.K.
2. *Gilmore, B.J.; Hoeltzel, D.A.; Azram, S.; Eschenauer, H.A. (1993) (Eds.)*: Advances in Desig Automation, Proc. 1993 ASME Design Technical Conferences - 19th Design Automatio Conference, Albuquerque, New Mexico, The American Society of Mechanical Engineers, Nev York.
3. *Herskovits, J. (1993) (Ed.)*: Proc. Structural Optimization '93 - The World Congress on Optimε Design of Structural Systems, Vol. 1 & 2. Federal University of Rio de Janeiro, Brazil.
4. *Pedersen, P. (1993) (Ed.)*: Optimal Design with Advanced Materials, Elsevier, The Netherland:
5. *Bendsøe, M.P. (1995)*: Optimization of Structural Topology, Shape, and Material, Springeı Verlag, Berlin.

6. Rasmussen, J.; Lund, E.; Olhoff, N. (1993): Integration of Parametric Modeling and Structural Analysis for Optimum Design. In: Proc. Advances in Design Automation, The American Society of Mechanical Engineers, (Eds. Gilmore et. al.), Albuquerque, New Mexico, USA, 1993.

7. Lund, E. (1994): Finite Element Based Design Sensitivity Analysis and Optimization, Ph.D. Thesis, Special Report No. 23, Institute of Mechanical Engineering, Aalborg University, Denmark, 240 pp.

8. Olhoff, N.; Lund, E.; Rasmussen, J. (1993): Concurrent Engineering Design Optimization in a CAD Environment. In: Concurrent Engineering: Tools and Technologies for Mechanical System Design (Ed. E.J. Haug), pp. 523-586, Springer-Verlag, Berlin (1993).

9. Olhoff, N.; Lund, E. (1995): Finite Element Based Engineering Design Sensitivity Analysis and Optimization. In: Advances in Structural Optimization (Ed. J. Herskovits), pp. 1-45, Kluwer Academic Publishers, The Netherlands.

10. Bendsøe, M.P.; Olhoff, N.; Taylor, J.E. (1983): A Variational Formulation for Multicriteria Structural Optimization. J. Struct. Mech., Vol. 11, pp. 523-544.

11. Olhoff, N. (1989): Multicriterion Structural Optimization Via Bound Formulation and Mathematical Programming. Structural Optimization, Vol. 1, pp. 11-17.

12. Zienkiewicz, O.C.; Campbell, J.S. (1973): Shape Optimization and Sequential Linear Programming. In: Optimum Structural Design, Theory and Applications (Eds. R.H. Gallagher, O.C. Zienkiewicz) pp. 109-126, Wiley and Sons, London.

13. Esping, B.J.D. (1984): Minimum Weight Design of Membrane Structures Using Eight Node Isoparametric Elements and Numerical Derivatives. Computers and Structures, Vol. 19, No. 4, pp. 591-604.

14. Seyranian, A.P.; Lund, E.; Olhoff, N. (1994): Multiple Eigenvalues in Structural Optimization Problems. Structural Optimization, Vol. 8, pp. 207-227.

15. Olhoff, N.; Krog, L.A.; Lund, E. (1995): Optimization of Multimodal Structural Eigenvalues. In: Proc. First World Congress of Structural and Multidisciplinary Optimization (Eds. N. Olhoff, G. Rozvany), pp. 701-708, Goslar, Germany, 28 May - 2 June, 1995. Pergamon, Oxford, U.K.

16. Barthelemy, B.; Haftka, R.T. (1988): Accuracy Analysis of the Semi-Analytical Method for Shape Sensitivity Analysis. AIAA Paper 88-2284, Proc. AIAA/ASME/ASCE/ASC 29th Structures, Structural Dynamics and Materials Conference, Part 1, pp. 562-581. Also Mechanics of Structures and Machines., Vol. 18, pp. 407-432 (1990).

17. Olhoff, N.; Rasmussen, J.; Lund, E. (1993): A Method of "Exact" Numerical Differentiation for Error Elimination in Finite Element Based Semi-Analytical Shape Sensitivity Analysis. Mechanics of Structures and Machines, Vol. 21, pp. 1-66.

18. Lund, E.; Olhoff, N. (1994): Shape Design Sensitivity Analysis of Eigenvalues Using "Exact" Numerical Differentiation of Finite Element Matrices. Structural Optimization, Vol. 8, pp. 52-59.

19. Pedersen, P. (1973): Optimal Joint Positions for Space Trusses. J. Struct Div., ASCE, Vol. 99, pp. 2459-2476.

20. Braibant, V.; Fleury, C. (1984): Shape Optimal Design Using B-splines. Computer Methods in Applied Mechanics and Engineering, Vol. 44, pp. 247-267.

21. Bendsøe, M.P.; Kikuchi, N. (1988): Generating Optimal Topologies in Structural Design Using a Homogenization Method. Computer Methods in Applied Mechanics and Engineering, Vol. 71, pp. 197-224.

22. Olhoff, N.; Bendsøe, M.P.; Rasmussen, J. (1991): On CAD-integrated Structural Topology and Design Optimization. Computer Methods in Applied Mechanics and Engineering, Vol. 89, pp. 259-279.

Parametric dependence in structural response

by

Anders Eriksson and Costin Pacoste

Department of Structural Engineering,
Structural Mechanics group,
Royal Institute of Technology,
Stockholm, 1996.

For all structures of some complexity, the behaviour under loading is dependent on the specific configuration and measures of the structural components. In particular, these parameters affect the relative importances of structural instabilities. The study of generalised path-following procedures, cf. [1,2,3], has had as one objective to find methods, with which these aspects can be clarified and quantified.

The primary target in using these these general paths has been the detailed description of structural instabilities. Although they can in many cases be seen as over-simplifications with respect to real behaviour, elastic instability analyses are useful tools for the understanding of the behaviour of many structures. On the other hand, formal instability analyses can be considered as overly sophisticated, but it is possible to show, that many instability aspects are missed by the common analysis models. It can also be shown that simplified analysis models sometimes give incorrect information concerning the stability or instability of critical situations. At least from a theoretical viewpoint, it is therefore interesting to study the complex instability phenomena that occur for particular instances of a structure, when the geometry is parameterised.

In order to accurately evaluate the instability behaviour of structures, three basic ingredients are needed: First, sufficiently accurate numerical elements are needed for the discretised structural model, as discussed in [4,5]. Second, suitable numerical methods are needed for treatment of the non-linear structural relations that arise from these discrete models, cf. [1,2,3]. Further, the analyses require methods for handling and describing the critical states. Some methods for this, related to e. g. catastrophe theoretical concepts, are discussed in [3,6].

From the application viewpoint, the generalised formulations allow studies of a structural equilibrium problem from unconventional directions. Rather than seeing the response as a function of a variable load, for a specified structure, the response is seen as a function also of the parameters defining the structure. By adding new dimensions to the model, the dependence of the results can be obtained, without complete re-calculation of alternative structural models. Although the stated problems will be slightly more complicated than the basic equilibrium problem, their

use can in many cases be time-saving in the total context of analysis. The study of structures in a multi-parametric setting also allows the treatment of the genericity of the behaviour, thus avoiding whole new paths to be evaluated in order to study variations in structural geometry or imperfections,

Also, a few other computational tools are considered in [3] for the description of the parameter dependence of structural response aspects. Using these different tools, it is possible to completely describe the phenomenological behaviour of the structure in different parametric regions.

These methods can be used for many practical purposes. Primarily, the sensitivity in instability situations can be described. In particular, for an obtained instability for a specific structural configuration, the sensitivity of this behaviour can be evaluated. Typical parameters in this case are geometric parameters, sectional parameters and imperfections in load or geometry; these aspects are discussed in [3]. In these cases, the variations of the used parameters are normally small, just aiming at describing the local variations in response.

The second application area is related to larger variations of the parameters of the structure. It is related to the different qualitative behaviours of structure in different parameter regions. In relation to instability problems, the question is dealing with whether certain instability phenomena can occur, and at what load. Results in this area can be obtained from generalised path-following, where turning points in the higher-dimensional space indicate the limits for a region where a certain phenomenon occurs. It is also possible to follow curves of parametric combinations, where a critical state exists or a certain stress level is reached at a specified external load. This problem, obviously closely related to structural optimisation, is shown by Fig. 1.

For the studied problem, the design variables have been chosen as the structural height H, and the sectional height h; the design load was chosen as $P_1 = -100$. The problem has been subjected to the constraints that the safety against the limit points should be ≥ 1.5, the safety against buckling ≥ 1.3, and that the maximum stress in the fundamental solution to the design load should be less than 10000. In the region of limited deflections, the maximum (compressive) stresses will be at either the ends or the quarter points of the beams. These two situations were considered individually in the present analysis. Altogether, four different paths were evaluated.

The results from the calculations are summarised in Fig. 1, where the combinations of the two parameters that fulfil the limiting criteria are shown, by paths shown as solid and dotted lines. Obviously these curves need interpretation to give any conclusions. The dotted parts of the σ related curves are thus excluded, as these solutions give higher tensile than compressive stresses in the studied sections; they correspond to structures that must be inverted before being able to carry the specified load. The top half of the bifurcation curve is also excluded as the points correspond to the load at the return of the bifurcation path being the specified value. The turning point on this curve obviously gives the parametric combination for which a degen-

8
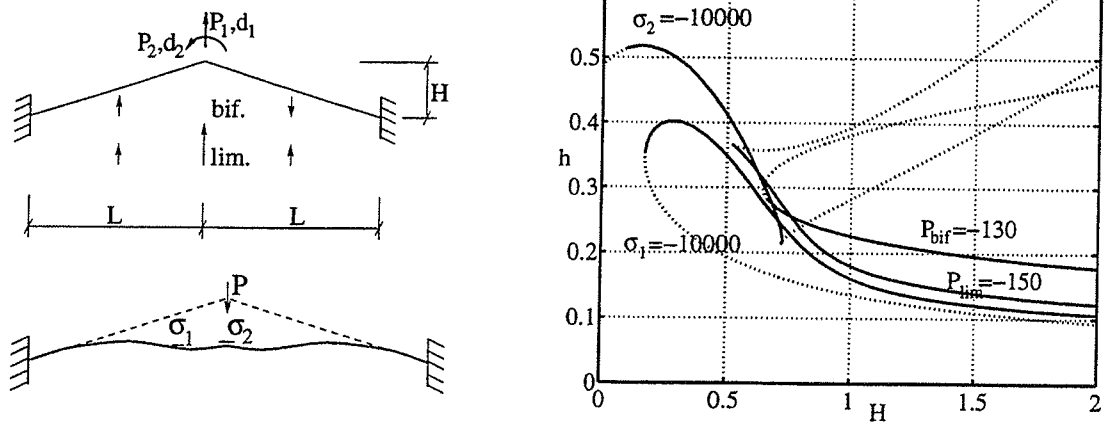
Figure 1: Evaluated parametric limits for different demands for clamped toggle frame.

erated bifurcation point is obtained at the studied load. The points on the top half of the limit load curve correspond to the 'minimum' load being the specified value. The turning point on this curve gives the parametric combination for which a third order limit point is obtained at the studied load.

From the remaining parts of the curves, as marked by solid lines in the figure, the feasibility region for the design is clearly shown.

Similar methods have also been used in a study of dome-shaped space grid structures. Emphasis was here put on the flexibility in the connections between the members. It is shown, that the instabilities are severely affected by these flexibilities, leading to a total disappearing of some of them for high enough joint stiffnesses. Further results from these analyses, together with some comments on the computational organisation of these complicated large-size analyses, will be given in the presentation.

From the theoretical viewpoint, the latter approach can give important phenomenological information. For instance, it has in [4] been shown that a simple toggle frame can give a butterfly catastrophe instability for a certain parametric combination. In the reference, this parametric combination was found manually, by evaluating the post-critical paths, for different structural heights. It has, however, in [3] been shown how this situation can be found from the generalised path-following procedure, by specifying an augmented fold line problem. Although the stated problem is of larger size than the fundamental problem, the obtained procedure is much more efficient then the manual method. The results and some comments on the computations will be given.

In a similar way, also other instances of complex instabilities can be found, e.g. swallowtail catastrophes, or hilltop-branching states. Although these only occur for specific instances, and thereby are of limited practical importance, these limiting situations are of major importance in the understanding of instability phenomena. Some aspects of this, and some examples of uncommon instabilities will be shown

9

in the presentation.

References

1. A. Eriksson, 'Fold lines for sensitivity analyses in structural instability', *Comp. Meth. Appl. Mech. Engng.*, **114**, 77–101 (1994).

2. A. Eriksson, 'Equilibrium subsets for multi-parametric structural analysis', Accepted for publication in *Comp. Meth. Appl. Mech. Eng.*, 1996.

3. A. Eriksson, 'Structural instability analyses based on generalised path-following', manuscript, 1996.

4. C. Pacoste, A. Eriksson, 'Element behaviour in post-critical plane frame analysis', *Comp. Meth. Appl. Mech. Eng.*, **125**, 319–343 (1995).

5. C. Pacoste, A. Eriksson, 'Beam elements in instability problems', Accepted for publication in *Comp. Meth. Appl. Mech. Eng.*, 1996.

6. C. Pacoste, 'On the application of catastrophe theory to stability analyses of elastic structures' (Dr. thesis), Dept. Struct. Engng., Royal Inst. Techn., 1993.

COMPUTER AIDED TAILORING OF COMPOSITES

A. PRAMILA

Department of Mechanical Engineering, University of Oulu, Linnanmaa,
SF-90570 Oulu, Finland

Abstract-A CAD-system for tailoring thermomechanical properties of composite structures is presented. The properties considered can be forced to a prescribed value, to a given range or the minimum or the maximum value of the property can be sought. The approach adopted is a macromechanical one, i.e. the properties of the plies are assumed to be given as is the case in normal design practise. Thus, the variables by which the designer can influence the properties are the ply orientations and ply thicknesses. The solution of this inverse problem, the search of ply orientation and thickness combinations leading to desired properties, is formulated as a constrained nonlinear minimization problem. Thus far, following thermomechanical properties have been considered for a typical point in an arbitrary laminated structure: in-plane and bending stiffnesses, coefficients of thermal expansion, strains, stresses, values of the failure criterion and curvatures due to mechanical and thermal loads. For plates and cylindrical shells the properties considered in addition to the abovementioned are displacements, buckling loads and eigenfrequencies

INTRODUCTION

"Composites are considered to be combinations of materials differing in composition or form on a macroscale. The constituents retain their identities in the composite, i.e. they do not dissolve or otherwise merge completely into each other although they act in concert". [1], [2].

There are many types of composites. Most used are polymers reinforced by thin fibres. The most common form is a laminate consisting of several unidirectional plies or layers. The plies used are anisotropic which gives the opportunity to vary the thermomechanical properties of the laminate or the laminated structure even after the dimensions and material (ply) have been chosen by varying the orientations and thicknesses of the different plies. The determination of the thermomechanical properties can be tedious, the range of calculations required extends from the use of explicit equations to solution of a nonlinear boundary-value problem. This together with large number of design variables makes the use of a trial-and-error method almost hopeless in the design of composite structures with specified properties.

The design, i.e. search of ply thickness and orientation combination leading to specified thermomechanical properties is called here the solution of an inverse problem to make clear the distinction to an analysis problem, where the design parameters are given and one derives the properties, and to the optimization, where the values of chosen properties are minimized or maximized. The term "inverse problem" has been used earlier, e.g. in vibration engineering, when structures having prescribed eigenfrequencies are searched for.

The optimization of composite structures has earlier concentrated almost exclusively on weight optimization, see, e.g. references [3] and [4]. In some cases extrema of some thermomechanical properties have also been sought for, see, e.g. [5] and [6].

Sigmund, [7] and [8], has numerically constructed materials with arbitrary prescribed positively semi-definite constitutive tensor. In his approach the cost function to be minimized is the weight, the prescribed constitutive parameters are taken into account as constraints and the design variables define the composition and topology of the material. This approach can, however, lead to materials which are very difficult to manufacture in practice.

This paper summarizes the work presented in references [9], [10], [11], [12]and [13]. In our approach the design variables are the ply orientations and/or ply thicknesses. This, of course, puts limits to the attainable properties. However, this approach produces laminates that can actually be manufactured. The programs developed are intended for and have already been applied in the practical design of composite structures.

FORMULATION OF THE INVERSE PROBLEM

The different thermomechanical properties and response parameters depend on ply properties, ply orientations, ply thicknesses and on the geometry, boundary conditions and loading of the structure, i.e.

$$F_i = F_i(\theta_j, t_j, \text{geom., bound., etc.}).$$
(1)

Usually the design task can be stated in the following way

$$F_i = \overline{F_i} \qquad i = 1, \ldots, m$$

$$F_i^L \le F_i \le F_i^U \quad i = m+1, \ldots, M$$
(2)

where an overbar indicates a prescribed value and superscripts U and L refer to upper and lower bounds, respectively.

The basic idea is simply to formulate the problem as a constrained minimization problem

(3)

$$\min \sum_{i=1}^{m} |F_i - \overline{F_i}|$$

subject to

$$F_i^L \le F_i \le F_i^U \quad i = m+1, \ldots, M$$
(4)

Search of maxima or minima can be carried out by replacing (3) by corresponding statement. The result of the constrained minimization is a set of orientations and thicknesses leading to the prescribed properties and response parameters. The result is by no means unique. The same response parameters and properties can be obtained by several combinations of design parameters. Of course, sometimes the specified values and bounds can be such that there is no solution at all.

CALCULATION OF PROPERTIES AND RESPONSE PARAMETERS

Classical lamination theory is used in the calculation of the properties and response parameters associated to a representative point of the laminate. The basic equations are the stress-strain relationships in ply co-ordinate system

$$\sigma = Q \, (\varepsilon - \alpha \, \Delta T),$$
(5)

in laminate co-ordinate system

$$\overline{\sigma} = \overline{Q}\,(\overline{\varepsilon} - \overline{\alpha}\,\Delta T) \tag{6}$$

and the kinematical assumption

$$\varepsilon(z) = \varepsilon^0 + z\,\kappa \tag{7}$$

where all the symbols have their standard meanings (see, e.g. [14]). From these the fundamental relationships

$$N = A\,\varepsilon^0 + B\,\kappa - N_T \tag{8}$$

and

$$M = B\,\varepsilon^0 + D\,\kappa - M_T \tag{9}$$

are derived. Here N and M are vectors containing the external forces and moments per unit width; A, B, D are the in-plane, coupling and bending stiffness matrices; ε^0 and κ are vectors containing the midplane strains and curvatures; N_T and M_T are vectors containing the apparent thermal forces and moments per unit width.

The cost function used and the constraints applied can contain any of the strains, stresses, curvatures, effective moduli and/or effective coefficients of thermal expansion which can be derived using the above equations.

As a failure criterion we apply the Tsai-Hill criterion, for which all the strength parameters are easily available.

In many applications laminates are used as shell or plate structures. The designer is interested in displacement, strain and stress fields of the structure under some transverse forces. Due to relatively high strength of advanced composites the structures tend to become quite slender. Thus, also buckling loads and eigenfrequencies must be possible to consider as design criteria.

One possibility to include these into the design system would have been to use the FEM. However, because the analysis part must be performed several times during the minimization, the computational effort would have been prohibitive. Therefore, approximate solution algorithms based on the application of the Ritz method together with continuous shape functions over the whole domain have been adopted. Beams, rectangular plates and cylindrical shells have this far been included into the program system.

For rectangular plates both Kirchhoff theory and First Order Shear Deformation Theory (FSDPT) have been applied. The trial functions used are either products of trigonometric functions or products of the eigenforms of beams. They are chosen in such a way that the essential boundary conditions will be satisfied. The accuracy of the solutions has been studied by doing comparisons with available analytical solutions in special cases and with FEM results for laminates of arbitrary

stacking sequence. For example, the differences between the eigenfrequency results are within a few percent when 100 trial functions are used. More details are given in reference [9].

Because the thickness to radius ratio can be relatively high in the applications (paper machine rolls) the shear deformable Sander's theory was chosen for the representation of the deformation kinematics of the cylindrical shell. Again, products of suitable trigonometric functions are used as shape functions. A special feature included into the program system is that the fibre orientation can vary as a function of the axial co-ordinate of the cylinder. This gives additional possibilities to improve the properties of the structure. When material properties of commercially available plies are applied to a composite cylinder of length 2.0m, radius 0.245m and thickness 10mm, the increase in the lowest eigenfrequency was at its maximum 45%, when linear orientation variation was employed, [12].

Paper machine rolls contain components like journals and steel heads. Therefore, component mode synthesis is applied in their vibration analysis. Heads and journals are taken into account as point masses.

MINIMIZATION ALGORITHMS EMPLOYED

The possible properties used in the cost function and in the constraints are complicated and highly nonlinear functions of the design variables. Therefore, nonlinear minimization methods which do not use gradients or which use numerically calculated gradients seemed to be the only suitable ones. The flexible tolerance method [15] and the sequential quadratic programming method [16] were chosen for the minimization.

The flexible tolerance method (FTM) is a Nelder-Mead-type search method, which improves the value of the cost function by using information provided by the feasible points as well as certain nonfeasible points called nearfeasible points. The nearfeasible limit is gradually made more and more restrictive as the search approaches the minimum, until only a feasible point is accepted at the minimum.

In sequential quadratic programming (SQP) each iteration consists of two stages: search direction is first determined as the solution of the quadratic programming subproblem and thereafter the step length to this direction is determined by using the augmented Lagrangian function.

According to the experience gained this far the FTM works quite well even if the initial guess of the design variables does not satisfy the constraints. However, it seems to be very slow compared with the SQP. For example, in maximizing the in-plane stiffness of a composite plate with a constraint on the first eigenfrequency of the flexural vibrations, the computational time required by FTM was 20 times the computational time needed by SQP.

On the other hand, SQP is more sensitive to the selection of initial starting point than FTM. An initial point, for which SQP cannot find the proper search direction, may give a good start when FTM is used. A promising idea seems to be to run first a few iterations by FTM and then continue by SQP.

COMPUTER PROGRAMS DEVELOPED

Two computer program systems have been developed based on the theory given in references [9], ..., [13]. The first one, LAMINV, is a general program for tailoring the properties of laminates (point properties) and properties of laminated plates and the second one, COMROL, is specifically developed for designing paper machine rolls made of composite materials.

The design variables used are the ply thicknesses and ply orientations. Thus, in a general case the number of design variables is twice the number of plies in the laminate. However, if the laminate is restricted to be of a special type, e.g. symmetric or symmetric and balanced, the number of design variables is reduced and, of course, also the computational effort. Design variables and properties used in cost function and constraints are scaled to same order of magnitude to avoid difficulties in the minimization.

Following properties can be included into the cost function or into the constraints in LAMINV

*in-plane elastic moduli E_x^0, E_y^0 and G_{xy}^0
*flexural moduli E_x^f, E_y^f and G_{xy}^f
*in-plane coefficients of thermal expansion
*coefficients of thermal warping and twisting
*buckling load of a rectangular laminated plate in uniaxial or biaxial compression
*three lowest eigenfrequencies of a laminated plate
*value of failure criterion
*ply strains due to mechanical or thermal loads
*curvatures and twist of the midplane
*maximum ply strains due to transverse loading in a laminated plate
*maximum displacement of a laminated plate
*total thickness of the laminate

The properties considered in COMROL are

*maximum deflection of the roll due to web tension and own weight
*critical speed of rotation
*coefficients of thermal expansion
*engineering constants of the shell laminate (in-plane and bending)
*value of the failure criterion
*buckling load of the shell
*total thickness of the laminate or mass of the laminate

The size of the eigenvalue problem depends on the number of terms used in the double trigonometric series. During the minimization process the eigenvalue problem is solved several times. Therefore, to save in computational time, the minimization is performed in two stages. First, the minimization is done with small number of terms, say 3x3 or 5x5, and the minimum obtained in this way is used as a starting point for minimization with larger number of points. Usually only a few iteration cycles are needed in this second stage.

EXAMPLES

As a first design example we consider the design of a symmetric eight ply Kevlar/epoxy laminate. The design specification is as follows:

*in-plane stiffness in x-direction 50 GPa
*CTE in x-direction 0.0 1/^{o}C (zero!)
*CTE in y-direction 12.0 10^{-6} 1/^{o}C(the same as in steel)
*value of Tsai-Hill criterion less than 0.8 in each ply due to in-plane loads 100 kN/m in both directions

The ply properties used are E_1=76.0 GPa, E_2=5.50 GPa, v_{12}=0.34, G_{12}=2.4 GPa, α_1=-4.0 10^{-6} 1/^{o}C, α_2=79.0 10^{-6} 1/^{o}C, X_t=1400 MPa, Y_t=12 MPa, X_c=235 MPa, Y_c=53 MPa and S=34 MPa. Thickness of each layer is chosen to be 0.5mm. Thus, as design variables we have four ply orientations.

As the starting points we use laminate stacking sequences

A: $[45^{o}/-45^{o}/45^{o}/-45^{o}]_s$
B: $[20^{o}/-40^{o}/60^{o}/-80^{o}]_s$
C: $[0^{o}/90^{o}/-60^{o}/40^{o}]_s$

The laminate stacking sequences obtained and corresponding properties are listed in table I.

Table I Results by SQP and by FTM

	Starting point A		Starting point B		Starting point C	
	SQP	FTM	SQP	FTM	SQP	FTM
Θ_1	-1.6	8.7	-25.2	-12.6	-24.4	-2.1
Θ_2	-24.3	-13.8	6.9	9.8	79.6	87.21
Θ_3	10.0	88.9	11.4	-12.4	3.7	-15.9
Θ_4	-86.1	-10.2	-84.1	-89.9	4.8	1.25
E_x^{o}/GPa	50.0	50.0	49.9	50.0	50.0	50.0
α_x/(10^{-6} 1/^{o}C)	0.01	0.01	-.8	0.06	-.01	0.01
α_y/(10^{-6} 1/^{o}C)	12.0	11.41	12.0	11.44	12.0	11.51
Max. of T-H crit	0.6	0.6	0.6	0.6	0.5	0.6
N of iter.	116	557	38	188	57	304
Comp. time/s	10.2	35.3	6.6	27.2	7.6	15.3

The results show, that both the methods can find a laminate stacking sequence having the prescribed properties. At first sight it seems that the specification can be fulfilled by many different orientation combinations. One should, however, keep in mind that in this design problem only in-plane properties were considered. Thus, the order of layers does not matter here.

Clearly FTM is more time consuming than SQP.

When also the ply thicknesses are taken into account the dimension of the design space increases from four to eight. The total thickness which, of course, should be as small as possible, is now added to the cost function. The starting points have same initial orientations as before and at point A all the ply thicknesses are 0.5mm, at point B the ply thicknesses are 0.2mm, 0.6mm, 0.6mm and 0.2mm and at point C all the ply thicknesses are 0.6mm.

Again both minimization algorithms find a laminate stacking sequence fulfilling the specification. By using SQP the total thickness varies from 2.62mm to 2.93mm. FTM results range from 3.19mm to 4.44mm. Computational time required by FTM is longer than needed by SQP.

The second example is concerning with the design of a tension measuring roll. The chosen dimensions of the roll are:

*total length 6400mm
*length of the cylindrical shell 5730mm
*inner diameter of the roll 603mm
*diameter of the journals 70mm
*mass of the steel head 60 kg
*mass of the rubber cover 60 kg
*web tension 0.14 kN/m
*contact angle 130^0

The further design requirements are:

*critical running speed 2800 m/min
*maximum deflection less than 0.745 mm
*circumferential CTE less than $10 \ 10^{-6} \ 1/^0C$

The roll will be manufactured by filament winding and thus the ply orientations are restricted into the range $5^0 ... 88^0$. The material used is carbon fibre reinforced epoxy and the ply properties are $E_1=139.0$ GPa, $E_2=6.509$ GPa, $v_{12}=0.29$, $G_{12}=G_{13}=2.41$ GPa, $G_{23}=1.44$ GPa, $\alpha_1=0.29 \ 10^{-6} \ 1/^0C$, $\alpha_2=58.6 \ 10\text{-}6 \ 1/^0C$ and density 1540 kg/m^3 .

The ply thickness is 0.3 mm and the number of layers is chosen to be 28. Moreover, to avoid thermal warping the laminate is required to be symmetric and balanced. Thus the number of design variables is seven.

Two different initial stacking sequences were used A: $[15/-15/30/-30/18/-18/10/-10/20/-20/45/-45/65/-65]_s$ and B:$[55/-55/15/-15/15/-15/15/-15/15\text{-}15/55/-55/55/-55]_s$. The results are given in table II.

Table II Resulting laminate stacking sequence for the tension measuring roll.

	Starting point	
	A	B
Θ_1	15.7	5.0
Θ_2	35.0	5.1
Θ_3	15.5	5.0
Θ_4	9.9	10.7
Θ_5	18.9	50.2
Θ_6	49.8	88.0
Θ_7	71.3	88.0
Max displ./mm	0.6271	0.5864
Crit. vel./(m/min)	2800.0	2800.0
$\alpha_{circ}/(10^{-6}\,1/^0C)$	9.87	5.44
Number of iterations	13+5	11+4

REFERENCES

1. Anon. (1988) *MIL-HDBK-17B: Volume I Polymer Matrix Composites*.

2. Anon. (1987) *Engineered Materials Handbook. Volume 1 Composites*. ASM International, Ohio.

3. Lin, C.-C. and Yu, A.-J. (1991) Optimum weight design of composite plates. *Computers&Structures* **38**, 581-587.

4. Fugunaga, H. and Vanderplaats, G.N. (1991) Minimum weight design of laminated composite panels under strength and displacement constraints. *JSME International Journal, Series I* **34** (2), 171-177.

5. Grenestedt, J.L. (1990) Composite plate optimization only requires one parameter. *Structural Optimization* **2**, 29-37.

6. Pramila, A. (1990) Extrema and zeros of coefficients of thermal expansion of a balanced symmetric laminate. *Journal of Composite Materials* **24**, 768-794.

7. Sigmund, O. (1993) Materials with prescribed constitutive parameters: an inverse homogenization problem. *DCAMM-report No. 470*, Technical University of Denmark

8. Sigmund, O. (1994) Tailoring materials with prescribed elastic properties. *DCAMM-report No. 480*, Technical University of Denmark.

9. Autio, M. (1992) Solving the design problem of composite structures. *Licentiate Thesis, University of Oulu.* (In Finnish)

10. Laitinen, M. (1995) A novel dimensioning system for composite paper machine rolls. *Licentiate Thesis*, University of Oulu.

11. Autio, M., Laitinen, M. and Pramila, A. (1993) Systematic creation of composite structures with prescribed thermomechanical properties. *Composites Engineering* 3, 249-259.

12. Laitinen, M. (1994) Ritz solution for a laminated composite cylinder with variable fibre orientation. In Blain, W.R. and de Wilde, W.P. (Eds.) *Computer Aided Design in Composite Material Technology IV*, Computational Mechanics Publications, Southampton, 31-38.

13. Autio, M. and Pramila, A. (1995) Inverse problems in thermoelasticity of composites. In Tabarrok, B. and Dost, S. (Eds.) *Proceedings of 15th Canadian Congress of Applied Mechanics*, University of Victoria, Victoria.

14. Jones, R. M. (1975) *Mechanics of composite Materials*. McGraw-Hill, New York.

15. Osyczka, A. (1984) *Multicriterion Optimization in Engineering with FORTRAN Programs*. John Wiley, New York.

16. Schittkowski, K. (1985) NLPQL: A FORTRAN subroutine for solving constrained nonlinear programming problems. *Annals of Operations Research* 5, 485-500.

Industrial Applications Of Computational Mechanics For Marine Structures

Peter Bjerager, Ph.D.
DET NORSKE VERITAS
Høvik, Norway

Introduction

A short introduction is given to the FEM-based structural analysis system SESAM from Det Norske Veritas, Norway. Some applications of SESAM for design and operation of ships and offshore platforms in order to ensure the life time safety and integrity of these marine structures is then summarised.

SESAM Structural Analysis System For Marine Structures

SESAM is a dedicated and comprehensive finite element based software system for structural and hydrodynamic design and analyses in the offshore and maritime industries. The system has integrated and special purpose facilities for structural modelling, hydrostatic and hydrodynamic load generation including first and second order wave diffraction analysis, linear and non-linear, static and dynamic FEM-based structural analysis, pile and soil analysis, results presentation and extended calculations for design such as fatigue analysis and checking of the structural capacities.

The system is efficient for marine structures compared to general purpose FEM systems due to integrated specialised capabilities such as
- modellers for structures such as stiffened plates and tubular members
- international rules for allowable geometry constructs
- loads from e.g., wave, wind, current, equipment and earthquake
- combined hydrodynamic and structural analysis
- codified checks on structural strength according to international standards
- ultimate strength, fatigue life and fracture mechanics analysis
- short and long term response estimation based on frequency as well as time domain calculations, and
- probabilistic inspection planning.

SESAM is offered worldwide by Det Norske Veritas. It is today recognised as a market leader for the marine industry and it is used by oil companies, engineering consultants, contractors, yards, research institutions and universities in more than 20 countries.

A distinct characteristic of SESAM is its role as a technology platform for the marine industry. Results from joint industry R&D projects are often implemented in SESAM to make these new developments available for practical engineering use in the industry. Furthermore, SESAM has integrated components from a number of products and technology partners including MIT, Sintef, Marintek, and Norwegian Geotechnical Institute.

PREPROCESSING		ENVIRONMENTAL ANALYSIS				POSTPROCESSING	
PREFEM general structures	PRE- FRAME frame structures	WADAM wave loads on general structures	WAJAC wave loads on frame structures	WAVE- SHIP wave loads on ships	LAUNCH launching of jackets	POSTRESP presentation of statistical response	PLATE- WORK plate design
		SESAM INTERFACE FILE				FRAME- WORK frame design	PROFAST probabilistic fatigue and inspection
PRETUBE tubular joints	PRESEL super- element assembly	SESTRA linear statics and dynamics	SPLICE structure- pile-soil interaction	ADVANCE non-linear statics and dynamics	USFOS progressive collapse	POSTFEM graphic presentation of results	VIEWER model and results visualisation
ASSOCIATED			MIMOSA mooring analysis			CUTRES presentation of sectional results	CONCODE concrete design
PROBAN probabilistic risk and sensitivity		STRUCTURAL ANALYSIS					
		BRIDGES TO CAD/CAE					

SESAM is available on MS Windows based Intel computers, as well as popular workstations from Digital, Hewlett Packard, IBM, Silicon Graphics and Sun Microsystem.

APPLICATIONS IN THE OFFSHORE INDUSTRY

SESAM is being used throughout the life time of offshore structures to help ensure a safe and cost-efficient design, construction and operation of these structures. The phases during the life of an offshore platform are

Design	Engineering	Construction	Transport & Mating	Operation & Maintenance	Abandonment
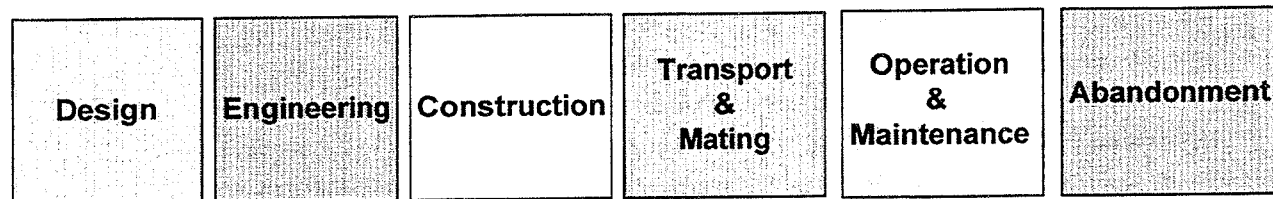
Besides a broad use during design, many operators of offshore installations (most often an oil company) have established re-analysis systems based on SESAM for use in modifications and integrity analyses in case of structural damages.

SESAM is used for many different types of offshore platforms, including jackets structures, semi-submersible structures, tension-leg platforms and concrete gravity structures. Examples of some of these structures are shown below.

The analyses can be very comprehensive with up to 2 million degrees of freedom for the larger models. These are executed on supercomputers or parallel configurations, typically networked workstations. When SESAM is used for regular design of e.g. jacket structures the analysis models are computationally less demanding and such analyses are typically executed on desktop computers including PCs.

Non-linear Collapse Analysis of Offshore Platforms

Today, non-linear collapse of jacket structures, topside decks and jack-up rigs are becoming increasingly common in the offshore industry. Accidental damage such as that caused by explosion, fire, dropped objects, extreme environmental events, or from ships collisions poses a threat to the safety and operation of offshore structures. By performing a non-linear analysis, the engineer can document the reserve strength of a structure, both before and after damage, and in this way help in the decision related to e.g. discontinued oil and gas production, evacuation of the platform and subsequent repair.
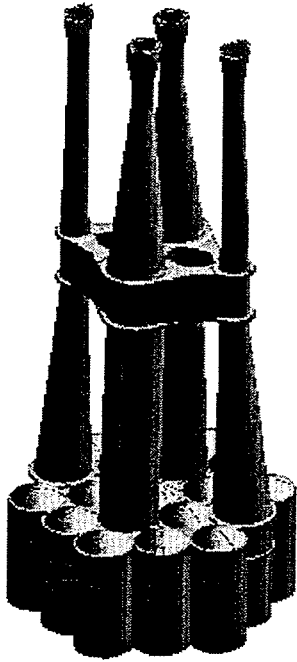
The Troll concrete gravity platform - the largest concrete structure in the world.
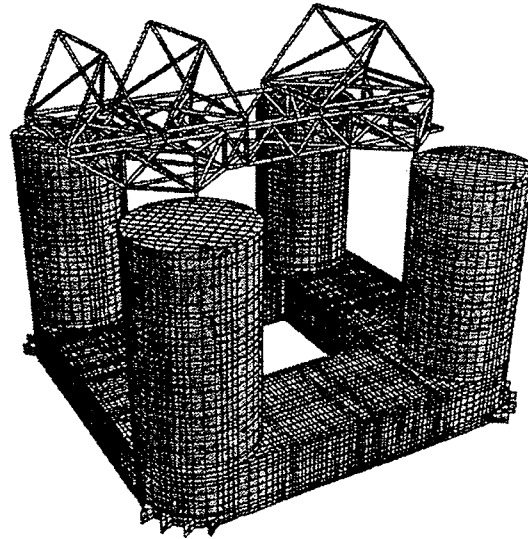
The Troll Olje floating offshore platform.
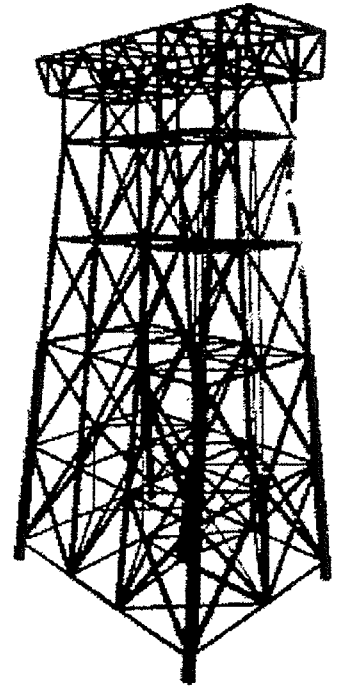
A jacket structures under non-linear collapse analysis.

Probabilistic Analysis for Inspection Planning

A fairly new and advanced type of structural analysis of offshore structures is probabilistic analysis for the purpose of repair and inspection planning with respect to fatigue damages. Such analyses are based on either an SN-approach or based on a crack growth model. The advantage of using a probabilistic approach is that information gained during inspections can be taken directly into account through so-called Bayesian updating.

Very substantial cost savings in inspection of offshore platforms have been achieved this way, notably in the Norwegian and British sectors of the North Sea.

Traditionally, the design of ships are based on experience-calibrated rules published by ship classification societies. As the first classification society, Det Norske Veritas introduced early on rules based on direct finite element calculations and calibrated to full scale measurements on ships in operation.

Today, the direct use of hydrodynamic and structural analysis in design and building of ships have become common. In particular, large ship yards use finite element analysis to improve design of details and to help ensure a safe and cost-efficient ship design.

Recently, the major ship classification societies have furthermore introduced class notations involving finite element calculations of parts of the ship. These class notations from Det Norske Veritas are Computational Ship Analysis I and II, where CSA I involves a structural analysis based on prescribed (rule-based) wave loadings, whereas CSA II involves a direct hydrodynamic simulation of the wave loadings.
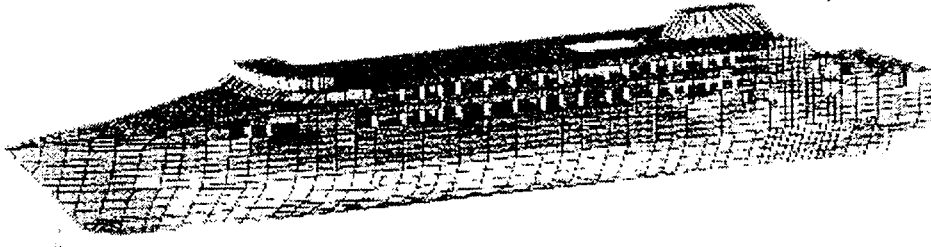
Direct finite-element based analysis of a passenger ship

NAUTICUS HULL for Ship Design

To facilitate the design of ships according to CSA I and II, Det Norske Veritas provides an integrated analysis system NAUTICUS HULL for classification rule checking, direct finite element based computations as well as other related analysis of a ship. The needed modules o the SESAM analysis system are integrated into NAUTICUS HULL.

Mooring Analysis of Ships

Based on vessel descriptions in terms of mass, force, coefficients for wind, current drag and wave drift excitation, motion transfer functions and damping coefficients, static and dynamic analyses of mooring systems for ships are performed within SESAM. In this way, frequency dependent transfer functions and wave drift coefficients as calculated in the hydrodynamic modules in SESAM can be directly applied.

DET NORSKE VERITAS

DET NORSKE VERITAS is an autonomous, independent foundation with the objective of safeguarding life, property and the environment. DNV is an international provider of classification, certification and advisory services. DNV has 4,000 employees and a network o 300 offices in 100 countries.

DET NORSKE VERITAS provides also commercial software products for the maritime and offshore industries worldwide. DNV SOFTWARE is the unit being responsible for development maintenance, support, sales, marketing and distribution of DNV's high technology software products. The products include the engineering analysis systems SESAM, NAUTICUS, PILOT and PROBAN and the client base consists of 300 companies in 30 countries. DNV SOFTWARE has 45 employees.

PRODUCT MODEL FOR STRUCTURAL ANALYSIS OF SKELETON

Markku Heinisuo, Dr. Tech.
Tampere University of Technology
Box 600
33101 Tampere, Finland
email:markku2@junior.ce.tut.fi

ABSTRACT

The paper deals with a product model which is used when transferring data from CAD to FEM of skeletal structures. The product data model is presented using EXPRESS-G (and EXPRESS) and the corresponding data is stored by using the standard ISO-10303-21 (STEP). The product model is used as a part of a knowledge based approach to the design of steel structures. The pilot programs are written to import the corresponding STEP-file from FST-model (product model including the geometry of the skeleton) and to export the input file into an analyzing program (ABAQUS). The present paper shows the main entities needed in the structural analysis. The model was originally developed for the design of steel structures, but it can be used for wooden, concrete and composite structures, too. Exact stiffness matrices (based on the solution of the governing differential eguations) are recommended to be used when ever they are available in order to keep the number of DOF as small as possible. The analysis types in the present model are the linear static and the buckling analysis.

INTRODUCTION

Many closed systems for the data transfer between different tasks e.g. the geometrical modelling and the analysis have been written for the structural design of wooden structures (Mikkola, 1985) and the design of steel structures (Heinisuo, et al, 1991). The solution for the data transfer problem in projects is searched nowadays in the open (i.e. hardware and software independent) environment and using neutral data files.

The product models are used to solve the data transfer problems. In this paper the product model for the structural analysis of skeletal structures is proposed. The model was originally developed for the structural analysis of steel structures, but it can be used for other structures, too. There exist at least two models for steel skeletons where the geometry model and the structural analysis have been combined (Haller, 1994, CIMsteel, 1995) and where the standard ISO-10303 have been used for the implementation. The use of parts ISO-10303-11 and ISO-10303-21 have proved to be efficient and widely accepted tools to present the product models. The analysis models given in the references (Haller, 1994, CIMsteel, 1995) are based on the use of beam elements. Moreover, the geometrical model and the analyzing model are combined to the same model in those references. The application independent proposition for the standard of the finite element analysis does exist (ISO-10303-104). This model is perhaps too large to apply in practical building projects, nowadays. The situation is changing all the time due to increasing power of computers. There exists general algorithms for the generation of the three dimensional analyzing models from the geometrical model (Boender et al, 1994), but also these algorithms lead to too heavy models in practice. However, some features are taken from the models of the literature to the present model.

tools for the creation of the analysis model from the geometry. This holds true especiall' for the joints of the skeleton. When modelling joints the very profound models ar needed (Romeijn et al, 1993) depending on the level of the knowledge wanted from th behavior of the joint and moreover, from the whole skeleton. Also, the bars betweel joints must be analyzed by using very profound beam elements in some cases (Heinisu et al, 1995). This situation holds especially for the open section thin walled purlins use widely in steel structures. The knowlegde based approach for the design of stee skeletons is proposed in (Heinisuo, Hyvärinen, 1996). One goal of the present study wa also, that the model should be as computer and software independent as possible. The use of the standard STEP (EXPRESS and EXPRESS-G for the product data model an ISO-10303-21 for the transfer file) was chosen to fulfill this demand. The analysis i based on the finite element method.

The following features were also decided to incorporate into the model because the were found, in the previous projects, to be essential in order to do practical design Unique reference to the geometrical model from the analysis model must exist. Ther may be needed different analysis models. At least linear and buckling analysis type must be available. The analysis model must include submodels with their own coordinate systems, 0D, 1D, 2D and 3D elements must be available with reference to the elemen type (not in details as in ISO-10303-104). Many kinds of beam elements must be available due to different needs in practice and due to interfaces between different leve local element models. Element constraints are needed for beam elements e.g. in the analysis of purlins. Moreover, the model must be as simple as possible but it should be possible to expand the model to the cases excluded so far from the model. The most urgent needs to expand the model are the loading schema and the results schema which are outside the scope of this paper. Also, the gap elements are badly neede when modelling joints. At the present stage the model is materially linear and the only non-linearity arises when running the buckling analysis. Static analysis is supported at the present stage.

PRODUCT DATA MODEL FOR THE STRUCTURAL ANALYSIS OF SKELETON

An EXPRESS-G diagram of the proposed product data model for the structural analysis of the skeleton is presented in Fig. 1. More details and the entities of the product data model are presented using EXPRESS in Ref. (Heinisuo, 1996). By tracing the entity PROPERTY it can be seen what kinds of element types are used in the model, so far.

CONCLUSIONS

As a conclusion, a part of the design process can now be done automatically by the computer without extra work of the structural designer and by using the neutral data files. The process starts from the geometrical model made by the CAD program (AutoCAD was used in tests) and the bar data is stored as a STEP-file (FST-model, Heinisuo, Hyvärinen, 1995, Hyvärinen, 1996). Simple joint models are used, so far. The STEP-file following the schema given in this paper is next generated from the geometrical model automatically and converted to the analysis program (ABAQUS was used in tests).
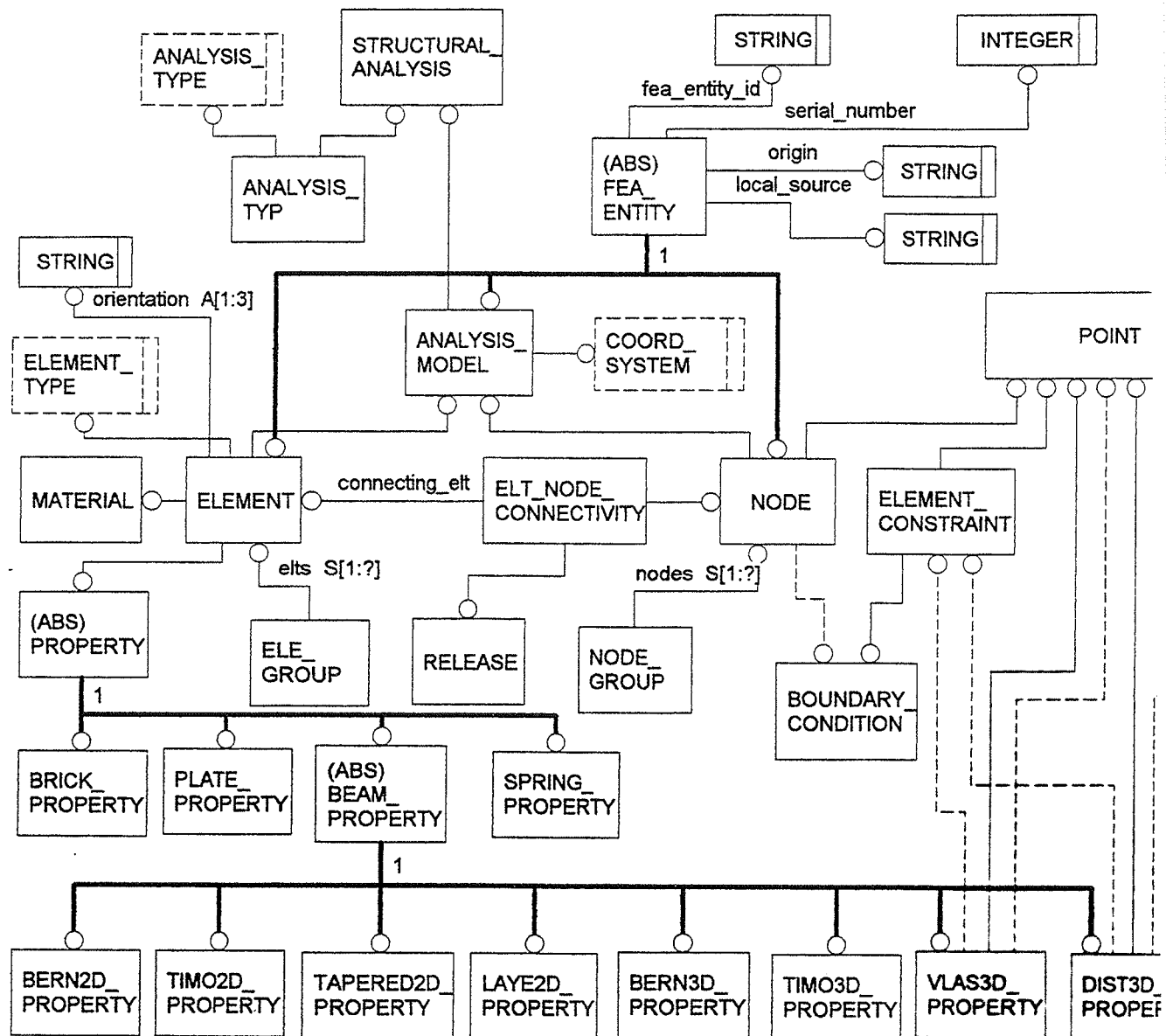
26

Figure 1. Product data model of structural analysis of skeleton

ACKNOWLEDGEMENTS

REFERENCES

Boender E., Bronsvoort W.F., Post F.H., Finite-element mesh generation from constructive-solid-geometry models, Computer-Aided Design, Volume 26, Number 5 May, 1994, pp. 379-392

CIMsteel Integration Standards (Release One), University of Leeds, Department of Civil Engineering, 23.6.1995

Haller H.-W., Ein Produktmodell für den Stahlbau, Dissertation, Bauingenieur- und Vermessungswesen der Universität Friedericiana zu Karlsruhe (TH), Karlsruhe, 1994

Heinisuo M., Möttönen A., Paloniemi T., Nevalainen P., Automatic design of steel frames in a CAD-system, Proceedings of the 4th Finnish Mechanics Days, Ed. Niemi E., Research Papers 17, Lappeenranta University of Technology, Lappeenranta 1991, pp. 197-204

Heinisuo M., Liukkonen V.-P., Tuomala M., New beam element including distortion, Proceedings Volume 1, Nordic Steel Construction Conference '95, Swedish Institute of Steel Construction, Malmö, Sweden, June 19-21,1995, pp. 65-72

Heinisuo M., Expert Systems for Design of Steel Structures, Part 5: Hierarchical models of steel skeleton analysis, Tampere University of Technology, Department of Civil Engineering, Structural Mechanics, Report 20, Tampere, 1996 (In preparation)

Heinisuo M., Hyvärinen J., Hierarchical aggregation form of steel skeleton, Product and Process Modelling in the Building Industry, Ed. R.J. Scherer, A.A. Balkema, Rotterdam, 1995, pp. 147-154

Heinisuo M., Hyvärinen J., Knowledge based approach to the design of structural steel joints, The Proceedings of Information Technology in Civil & Structural Engineering Design Conference 14th - 16th August 1996, Strathclyde, Glasgow, Scotland

Hyvärinen J., Expert systems for design of steel structures, Licenciate thesis, Tampere University of Technology, 1996 (In preparation)

ISO DIS 10303-11: Industrial Automation Systems - Product Data Representation and Exchange, Part 11: The EXPRESS language reference manual, 1992

ISO DIS 10303-21: Industrial Automation Systems - Product Data Representation and Exchange, Part 21: Clear text encoding of the exchange structure, 1993

ISO 10303-104 - FEA Reference Model, ISO TC184/SC4/WG3/P9, Document N 21, 3 January, 1991

Mikkola M., Computer Aided Design of Wood Trusses Using Nail Plates, Proceedings of CIVIL-COMP 85, Volume 1, CIVIL-COMP PRESS, Edinburgh, 1985, pp. 149-154

Romeijn A., Puthli R., Wardenier J., Guidelines on the numerical determination of stress concentration factors of tubular joints, Tubular Structures V, Eds. M.G. Coutie, G. Davies, E & FN SPON, London, 1993, pp. 625-639

Optimization of fiber-reinforced plastic circular plates

Jaan Lellep and Annely Mürk

Institute of Applied Mathematics,
Tartu University,
EE2400 Tartu, ESTONIA

The problems of optimization of rigid-plastic structural elements have been solved mostly under the condition that external loads acting on the element are quasi-static. Only little attention is paid to the optimization of plastic plates and shells subjected to dynamic loadings. Rigid-plastic reinforced beams have been studied in [3,5] and circular cylindrical shells of piece-wise constant thickness in [4,5]. Herein an attempt is made to determine the optimal parameters for a circular plate made of a fiber-reinforced composite material and subjected to an impulsive loading.

Let us consider a simply supported circular plate of piece wise constant thickness (Fig.1)

$$h = \begin{cases} h_0 \ , \ r \in (0, a), \\ h_1 \ , \ r \in (a, R) \end{cases} \tag{1}$$
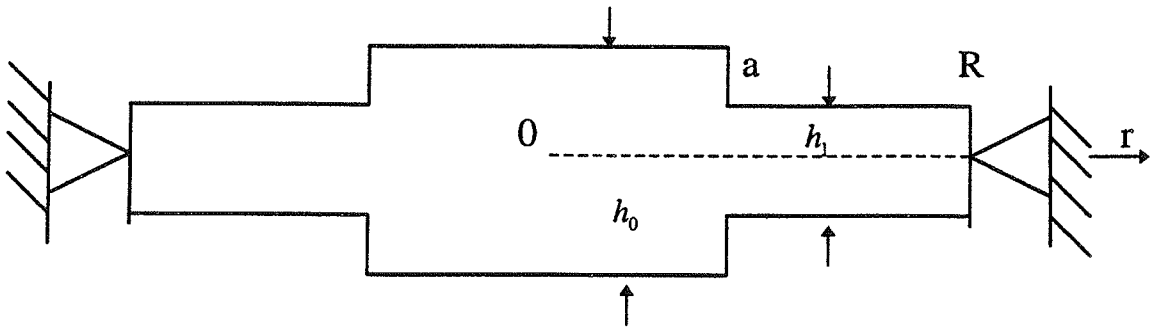
Fig.1. Circular plate of piece wise constant thickness.

Assume that the different thicknesses and radius a are preliminarily unfixed. We are looking for the design of the plate for which the maximal residual deflection has the minimal value for given total weight. The dual problem which consists in the minimization of the weight of the plate under given maximal residual deflection will be considered also.

The equilibrium equation of a plate element may be presented as

$$\frac{\partial}{\partial r}\left(\frac{\partial}{\partial r}(rM_1) - M_2\right)\mu\, r\, h\, \frac{\partial^2 W}{\partial t^2} \qquad (2)$$

where μ stands for the mass per unit area of the middle surface of the plate.
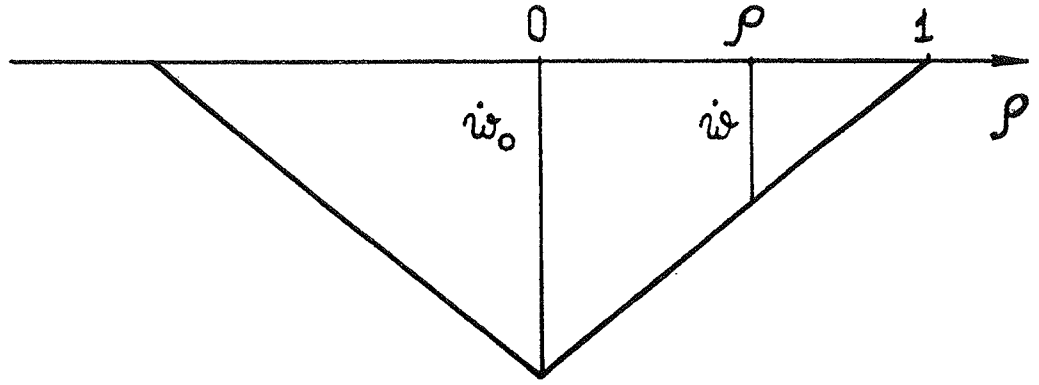
Fig.2. Velocity distribution.

The method of mode form solutions will be used in the present paper. Assume that the velocity distribution has the form of a triangle (Fig.2) where $\dot{W}_0 = \dot{W}_0(t)$ is an unknown function. According to the method of mode form solutions the initial kinetic energy

$$K_0 = \int\limits_0^R \mu\, \dot{W}^2(r,0)\, dr \qquad (3)$$

is considered as a given constant. The relation (3) serves for determination of the acceleration $\ddot{W}_0$ at the center of the plate whereas

$$\frac{\partial^2 W}{\partial t^2} = \ddot{W}_0\left(1 - \frac{r}{R}\right). \qquad (4)$$

30

The material of the plate is a fiber reinforced composite material. Lance and Robinson [1,2] suggested simple linear approximations of the yield surfaces for fiber reinforced circular plates and cylindrical shells. According to Lance and Robinson we consider the fiber reinforced composite as a quasi-homogeneous anisotropic material having different yield stresses in different directions.

For a radially reinforced sandwich plate the yield curve is formed by intersection of the lines

$$m_1 = \pm\beta\,\gamma^2 \quad , \quad m_2 = \pm\gamma^2 \quad , \quad m_2 - m_1 = \pm\beta\,\gamma^2 \tag{5}$$

Similarily, for a circumferentially reinforced circular plate the yield condition is formed by

$$m_1 = \pm\gamma^2 \quad , \quad m_2 = \pm\beta\,\gamma^2 \quad , \quad m_2 - m_1 = \pm\beta\,\gamma^2 \tag{6}$$

In (5) and (6)

$$m_{1,2} = \frac{M_{1,2}}{M_0} \quad , \quad \gamma = \frac{h}{h_0} \quad , \quad \beta = \frac{\sigma_1}{\sigma_0}, \tag{7}$$

M_0 being the yield moment for the matrix material. The quantities σ_1 and σ_0 stand for the yield stresses for the fibers and matrix, respectively. Note that if $\beta = 1$ the both yield conditions (5) and (6) coincide with the Tresca condition.

It appears that the plastic flow regime corresponds to the side of the yield hexagon where m_2 attains an extremal value. Substituting an appropriate value of m_2 from (5),(6) with (1) and (4) in (2) one can integrate the latter equation with respect to the coordinate r. When satisfying the conditions of continuity imposed on the generalized stresses at $r = a$ and the corresponding boundary conditions one can state that

$$\ddot{W}_0 = \ddot{W}_0(a, h_0, h_1) = const \tag{8}$$

It easily follows from the equations of motion that the parameters a, h_0, h_1 are coupled, e.g. one has

$$f(a, h_0, h_1) = 0 \tag{9}$$

and

$$a^2 h_0 + (R^2 - a^2)h_1 - V = 0 \tag{10}$$

According to the method of mode form solutions one obtains from (8) that the maximal residual deflection

$$W = \frac{[\dot{W}_0(0)]^2}{2\,\ddot{W}_0} \tag{11}$$

where the initial velocity $\dot{W}_0$ may be defined making use of (3).

The problem of non-linear programming (9),(10),(11) is solved by the use of the Lagrangian multipliers. The set of non-linear algebraic equations is solved numerically by the Newton's method. Calculations carried out show that the maximal residual deflection may be considerably decreased by the rational distribution of the material in the plate. For instance, in the case $\beta = 1$ and $V/V_* = 0.9$ the residual deflection may be diminished 6.3% using the plate of piece wise constant thickness.

References

1. R.H. Lance and D.N. Robinson, A maximum shear stress theory of plastic failure of fiber-reinforced material. J. Mech. Phys. Solids, 1971, **19**, No 2, 49-60.

2. R.H. Lance and D.N. Robinson, Limit analysis of ductile fiber-reinforced structures. Proc. ASCE. J. Eng. Mech. Div., 1972, **98**, No 1, 195-209.

3. J. Lellep and E. Sakkov, Optimum design of a reinforced beam under dynamic loading. Mech. Comp. Mater., 1993, **29**, No 6, 811-815.

4. J. Lellep and E. Sakkov, Optimization of cylindrical shells of fiber-reinforced composite materials. Mech. Comp. Mater., 1996, **32**, No 1, 65-71.

5. Ü. Lepik, Optimal Design of Inelastic Structures Under Dynamic Loading. Tallinn, Valgus, 1982.

CAD Integrated Shape Design Optimisation

by Anders S. Kristensen

Institute of Mechanical Engineering, Aalborg University, Pontoppidanstraede 101,

9220 Aalborg, Denmark

September 12, 1996

Abstract

The objective of this paper is to present CAD integrated shape optimisation of solid geometries. The objective has been to develop a computer-aided environment for interactive structural design, analysis, design sensitivity analysis, synthesis, and design shape optimisation. As a basis for this development the structural optimisation system ODESSY (Optimimum DESign SYstem) and the Solid Modelling system Pro/ENGINEER have been applied.

The introduction of design sensitivity analysis and optimum design concepts in the eighties and nineties, reviewed in for example Haug (1981), Schmitt (1982), Vanderplats (1982), and Olhoff and Taylor (1993), have provided computational techniques to evaluate structural effects of certain design changes quantatively. In addition to this has the ongoing development of more and more powerfull computers and enhanced computer graphics extended the geometric modelling techniques to include the concept of Solid Modelling. By this concept is it possible to create, process, communicate, and maintain a complete mathematical representation of the shape of a physical part by a computer and which moreover can be inspected visually in a computer graphics environment. The focus on CAD integrated design shape optimisation has increased in recent years as seen in papers by Braibant and Fleury (1984), Fleury (1987), Botkin (1991), Botkin (1992), Rasmussen (1990), Rasmussen (1991), and Zhang, Beckers, and Fleury (1995).

Interactive Shape Design Optimisation

In 1991 the development of an interactive 3D computer-aided environment for structural design, analysis, design sensitivity analysis, synthesis, and design optimisation was initiated. This system has been designated ODESSY (Optimum DESign SYstem). ODESSY is entirely developed and programmed[1] by people at the Institute of Mechanical Engineering (IME) at Aalborg University.

My colleague Oluf Krog has integrated ODESSY with the CAD system AutoCAD. However, the integration is limited to the problem definition, i.e. ODESSY features perform the design alterations during optimisation. This implies the presence of geometrical features in order to regenerate or recompute the geometry during optimisation. However, as the geometry becomes complicated the geometrical features become sophisticated and difficult to develop and implement in a general purpose optimisation system. This is solved by applying the Solid Modelling system Pro/ENGINEER which offers a ANSI C or C++ interfacing facility Pro/DEVELOP. By Pro/DEVELOP an interactive access to and control of the geometrical database and all geometrical features available in Pro/ENGINEER is possible. Pro/ENGINEER apply a parametrical representation as described by Mortenson (1985) and Faux and Pratt (1987). The parametric

---

[1] ODESSY is programmed in ANSI C and C++.

representation provides an explicit mathematical representation of relatively complex geometri both in 2D and 3D.
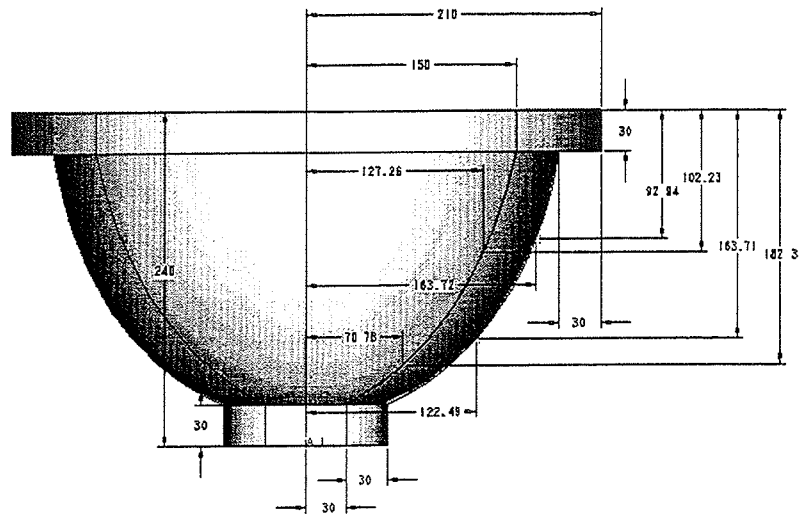
Figure 1: The parameterisation of a Solid Model in Pro/ENGINEER.

The advantage of applying the parametric representation is easy shape control of the geometr which is essential for performing design alterations of solid mechanical components. Within th graphical environment of Pro/ENGINEER a mechanical component or part is defined, i.e. geometrical model. Applying the Solid Modelling in general and Pro/ENGINEER in particula the definition of the shape of a mechanical component are accomplished by a few key dimensior which are independent variables. These parameters are used to compute a complete mathe matical representation in the form of parametric representations which are used in the surfac representation of the geometrical model.

The information needed to define the surfaces applied in a Pro/ENGINEER model are terme *basic geometrical data*, see figure 2. These data are collected in the geometrical database i Pro/ENGINEER and stored in a file as indicated by an arrow in figure 2.
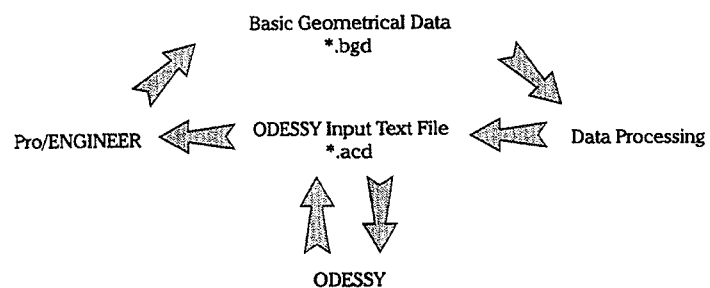
Figure 2: A schematic overview of the file transfer flow between Pro/ENGINEER and ODESSY The arrows indicate the direction of communication between Pro/ENGINEER and ODESSY.

The *basic geometrical data* are processed in order to accommodate the ODESSY data structur

34

and to establish a design and an analysis model for the problem, which are defined interactively in the Pro/ENGINEER design environment. Thus, the key dimensions in figure 1 can be chosen as design variables in the definition of a design model.

However, the implication of applying the Solid Model representation is related to the computation of mesh sensitivities as the intersection curves obtained from the boundary evaluations in the Solid Modelling system are not derived analytically for a spatial perturbation of a design variable. As a consequence of this it is necessary to determine mesh sensitivities by a finite difference approximation, that is

$$\frac{\partial \mathbf{x}(\mathbf{A})}{\partial A_i} \approx \frac{\Delta \mathbf{x}(A_1, \ldots, A_I)}{\Delta A_i} = \frac{\mathbf{x}(A_i + \Delta A_i) - \mathbf{x}(A_i)}{\Delta A_i} \tag{1}$$

Applying the finite difference scheme has an effect on the accuracy of the sensitivity analysis as both truncation and condition errors may occur. However, the accuracy problem can be resolved applying the improved method of semi-analytical shape design sensitivity analysis as devised by Olhoff and Rasmussen (1991), Olhoff, Rasmussen, and Lund (1992), and Lund (1994).

Examples

The interactive shape design optimisation approach will be illustrated through some simple examples. It will be shown that optimisation of generally applied mechanical solid components is accomplished by the outlined approach.

Conclusion

The succes of the optimisation process is affected by the quality of the mesh and therefore the accuracy of the mesh sensitivies. However, it is believed that having established this interactive shape design environment a basis for further improvements to the optimisation process is achieved.

Botkin, M. E. 1991: Shape design modelling using fully automatic three-dimensional mesh generation. *Finite Elements in Analysis and Design*, vol. 10, pp. 165–181.

Botkin, M. E. 1992: Three-dimensional shape optimization using fully automatic mesh generation. *AIAA Journal*, vol. 30, pp. 1932–1934.

Braibant, V.; Fleury, C. 1984: Shape optimal design using B-splines. *Computer Methods in Applied Mechanics and Engineering*, vol. 44, pp. 247–267.

Faux, I. D.; Pratt, M. J. 1987: Computational geometry for design and manufacture. John Wiley & Sons, ISBN 0-85312-114-1.

Fleury, C. 1987: Computer aided optimal design of elastic structures. *Computer Aided Optimal Design: Structural and Mechanical Systems*, pages pp. 831–900.

Haug, E. J. 1981: A review of distributed parameter structural optimization literature. *Optimization of Distributed Parameter Strucutres*, vol. 1, pp. 3–74.

Lund, E. 1994: Finite element based design sensitivity analysis and optimization. Ph.d. thesis, Aalborg University, Denmark.

Mortenson, M. E. 1985: Geometric modelling. John Wiley & Sons, ISBN 0-471-88279-8.

Olhoff, N.; Lund, E.; Rasmussen, J. 1992: Concurrent engineering design optimization in CAD enviroment. Special report no. 16, Institute of Mechanical Engineering, Aalborg Universi Denmark.

Olhoff, N.; Rasmussen, J. 1991: Study of inaccuracy in semi-analytical sensitivity analysis - model problem. *Structural Optimization*, vol. 3, pp. 203–213.

Olhoff, N.; Rasmussen, J.; Lund, E. 1992: Method of "exact" numerical differentiation for err elimination in finite element based semi-analytical shape sensitivity analyses. Special report r 10, Institute of Mechanical Engineering, Aalborg University, Denmark.

Olhoff, N.; Taylor, J. E. 1993: On structural optimization. *Journal of Applied Mechanics*, v 50, pp. 1139–1151.

Rasmussen, J. 1990: The structural optimization system CAOS. *Structural Optimization*, vol. pp. 109–115.

Rasmussen, J. 1991: Shape optimization and CAD. *International Journal for Systems Autom tion*, vol. 1, pp. 35–47.

Schmitt, L. A. 1982: Structural synthesis - Its genesis and development. *AIAA Journal*, vol. 2 pp. 992–1000.

Vanderplats, G. N. 1982: Structural optimization - Past, present and future. *AIAA Journal*, v 20, pp. 992–1000.

Zhang, W.; Beckers, P.; Fleury, C. 1995: A unified parametric design approach to structur shape optimization. *International Journal for Numerical Methods in Engineering*, vol. 38, p 2283–2292.

ADAPTIVE FINITE ELEMENT ANALYSIS FOR PROBLEMS WITH COMPLICATED GEOMETRY

X.D. Li and N.-E. Wiberg
Department of Structural Mechanics
Chalmers University of Technology
S–412 96 Göteborg, Sweden

SUMMARY

An adaptive finite element program for two-dimensional stress analysis based on using the Zienkiewicz-Zhu error estimator by SPR postprocessing and a quadrilateral mesh generator has been developed. This paper explains briefly the SPR and the approach used for mesh generation and reports numerical experiments of the adaptive analysis on some rather complicated geometries.

INTRODUCTION

Error estimation and adaptivity are a fundamental subject to all computational mechanics and, in particular, to the finite element method. For two-dimensional stress analysis, the Zienkiewicz-Zhu error estimator based on the superconvergent patch recovery (SPR) is the most practical *a posteriori* error estimator capable of estimating both local and global errors in the energy norm [1–3]. In our previously published papers on adaptive analysis using SPR, only simple problems e.g. a rectangular or an L–shape domain with one single material were considered. It is, therefore, very important to apply the SPR and the adaptive analysis to engineering problems in order to see that these new research results are truly applicable to structures with complicated geometry and multi-material properties. Recently, we have developed an automatic quadrilateral mesh generator which can deal with arbitrary two-dimensional domains and, based on that, an adaptive finite element program for two-dimensional stress problems using the SPR technique to calculate the error estimate. In the following, we shall explain briefly the SPR technique and the ideas used for mesh generation and report our numerical experiments on some problems with very complicated geometries.

THEORY

An *h*–remeshing adaptive finite element analysis consists of three main stages: (a) a mesh generator generating a new mesh according to the required element size distribution; (b) a finite element solver producing numerical solutions and (c) an error estimator evaluating the obtained solutions to check for stop or to predict nearly optimal new element size distribution for remeshing. Clearly, an efficient error estimator and a robust mesh generator are two key issues here.

We use the Zienkiewicz–Zhu error estimator which is based on the approximation that the error in stresses can be written as

$$e_\sigma = \sigma - \sigma^h \approx \bar{e} = \sigma^* - \sigma^h \tag{1}$$

in which σ are the exact stresses, σ^h are the stresses by finite element approximation and σ^* are 'recovered' values of σ^h obtained by some postprocessing process. When the energy norm is used, the global error estimator reads

$$\| \bar{e} \| = \left[\int_\Omega (\sigma^* - \sigma^h) D^{-1}(\sigma^* - \sigma^h) d\Omega \right]^{1/2} \tag{2}$$

In order to obtain σ^*, the SPR algorithm assumes that in a local patch (Figure 1 for 4-node bilinear elements) the values of σ are approximated by a simple polynomial expansion of one order (or more) higher than the expression of σ^h, which can be expressed as

$$\sigma_i^* = Pa_i \quad i = x, y, xy \tag{3}$$

where σ_i^* are the stress components, a_i are the unknown coefficients to be determined and P is a set of polynomial which for 4-node bilinear element is $P = [1, \ x, \ y, \ xy]$. By fitting σ_i^* in a least square sense to superconvergent values of σ_{ik}^s where k is the appropriate sampling point, we obtain the local patch equations as

$$Aa_i = B_i \quad P = P^T P, \ B_i = P^T \sigma_{ik}^s \tag{4}$$

▲ superconvergent point
○ nodal point
⊕ patch assembly point
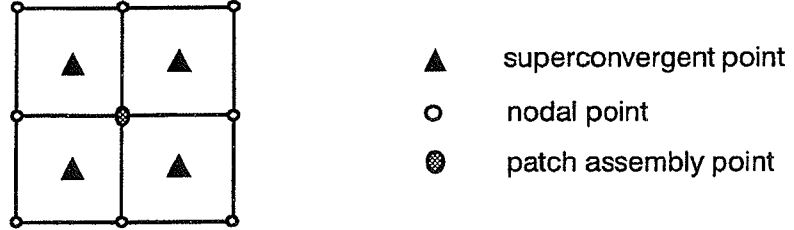
Figure 1. A typical local patch for 4-node quadrilateral elements

Quadrilateral mesh generation

A quadrilateral mesh generator for two-dimensional arbitrary domains has been developed. The approach is based on two steps: (1) generate a triangular mesh by the advancing front method presented by Peraie *et al* [4]; and (2) transform the triangular mesh to a pure quadrilateral mesh following the idea suggested by Rank *et al* [5].

In order to run the mesh generator, it is necessary to specify a background triangular mesh which covers the domain to be analyzed completely and contains the information of expected element size distribution. Nodes on the boundary of the region are created first and then an initial front is formed. Elements and interior nodes are generated simultaneously while the front is advanced and updated accordingly. When the front becomes empty, a triangular mesh will be at hand.

The strategy to transform a triangular mesh to a quadrilateral one is to split two neighbouring triangles into four quadrilateral elements as shown in Figure 2a. Before actually doing so, all possible combinations are stored in a list and sorted according to some criterion, for which we use the difference between largest and smallest interior angle. After the combinations, some triangle 'islands' will be left and need to be split into three quadrilaterals as shown in Figure 2b. Finally, the Laplacian smoothing and other postprocessing are performed to improve the quality of the mesh further.

(a)   (b)
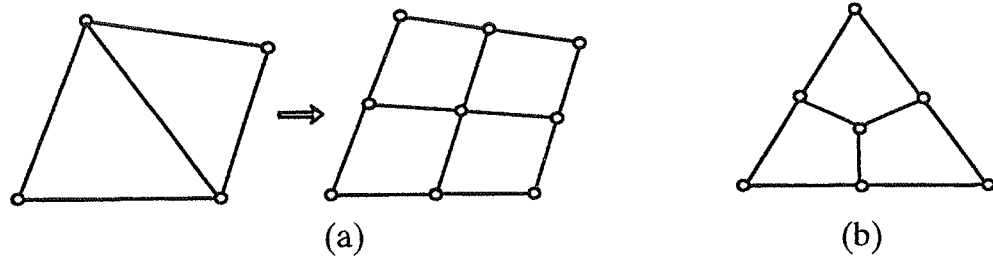
Figure 2. Creation of quadrilaterals by (a) splitting two neighbouring triangles into four and (b) splitting one triangle into three

NUMERICAL EXAMPLES

Two examples shown in Figures 3 and 4 are considered respectively here. The first one is a plane strain problem with a symmetric geometry. Starting with a fairly good mesh, only one step adaptive remeshing is needed to achieve an accuracy of 7.5%, as shown in Figure 5. The second one is a plane stress problem with a very complicated geometry. A tolerance of 12.5% is specified and three meshes adaptively generated are shown in Figure 6. We observe that, although very dense and refined meshes are used, the tolerance is still not met. This is due to the limitation of our machine and also the fact that linear elements are not accurate enough for such a problem.
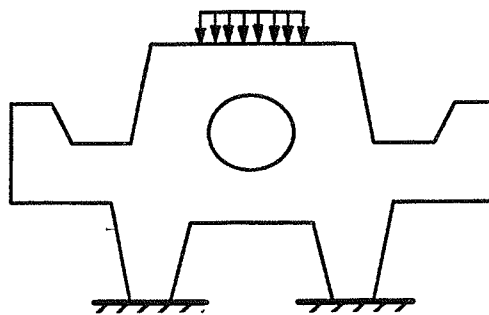
Figure 3 A plane strain problem
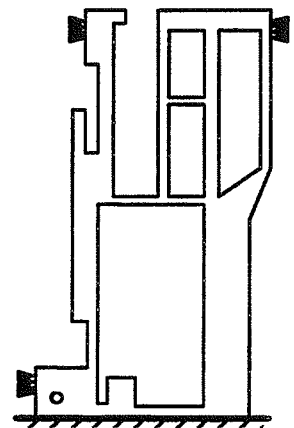
Figure 4 A plane stress problem
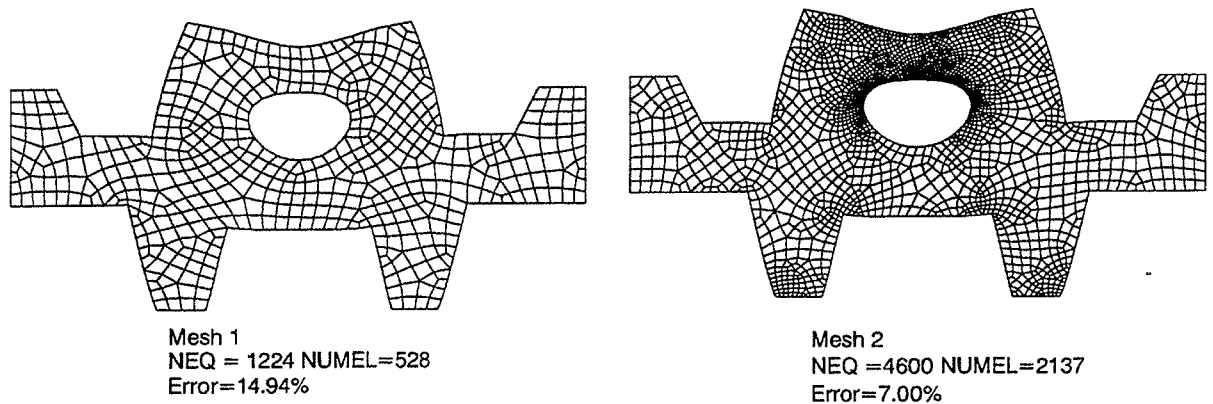
Figure 5 Meshes obtained for the plane strain problem in Figure 3.
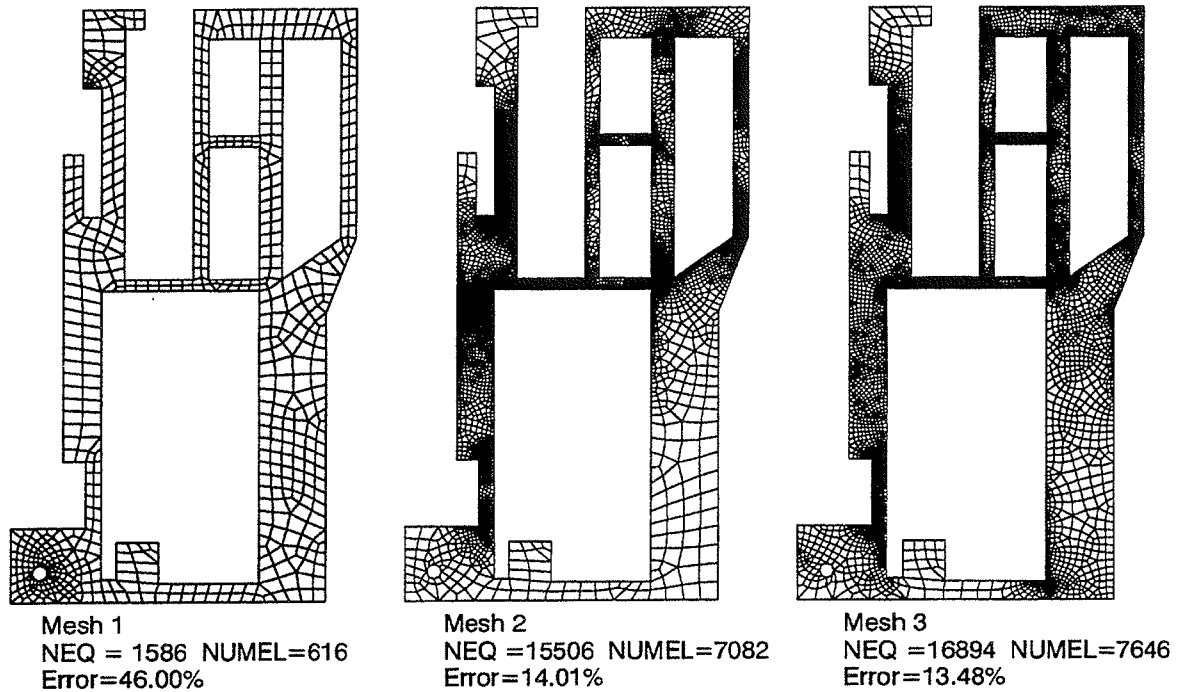
Figure 6 Meshes obtained for the plane stress problem in Figure 4.

REFERENCES

[1]   O.C. Zienkiewicz and J.Z. Zhu, 'A simple error estimator and adaptive procedure for practical engineering analysis', *Int. j. numer. methods eng.*, **24**, 333–357, (1987).

[2]   O.C. Zienkiewicz and J.Z. Zhu, 'The superconvergent patch recovery and *a posteriori* error estimates, Part 1: The recovery technique; Part 2: Error estimates and adaptivity', *Int. j. numer. methods eng.*, **33**, 1331– 1364, 1365–1382, (1992)

[3]   N.-E. Wiberg and F. Abdulwahab, 'Patch recovery based on superconvergent derivatives and equilibrium', *Int. j. numer. methods eng.*, **36**, 2703–2724, (1993).

[4]   J. Peraire, M. Vahdati, K. Morgan and O.C. Zienkiewicz, 'Adaptive remeshing for compressible flow computations', *J. Comp. Phys.*, **72**, 449–466, (1987).

[5]   E. Rank, M. Schweingruber and M. Sommer, 'Adaptive mesh generation and transformation of triangular to quadrilateral meshes', *Commun. numer. methods eng.*, **9**, 121–129, (1993).

Finite element analysis of the Erichsen cupping test with special reference to necking

Ramin Moshfegh and Larsgunnar Nilsson
Division of Solid Mechanics
Linköping Institute of Technology

Abstract

This paper presents a finite element analysis of the Erichsen Cupping Test in order to obtain the forming limit diagram. Special reference has been made to strain localization. The numerical analysis has been carried out both with non-adaptive and adaptive finite element methods. A method for the prediction of localized necking is developed. The numerical results are compared to experimental results for sheets of aluminium alloy, 2024-O.

Introduction

The forming of sheet metal components is a very common and important manufacturing process. In an effort to better understanding the sheet forming process, much research has been carried out using various technologies involving experimental and computational methods. Among these, the computational methods, especially finite element methods (FEM), have made significant progress during the last two decades. Sheet metal forming differs from most other metal forming processes in that different deformation modes can operate in different areas of the sheet, which makes it more difficult to control the process. The sheet is plastically deformed by bending and stretching. The process is predominantly tensile in nature and the amount of deformation that can be achieved in a single stage may be limited by the onset of tensile instabilities, i.e., necking and tearing. On the other hand the sheet is usually thin so that buckling or wrinkling may take

41

place in regions where at least one of the membrane stresses is compressive. Different testing methods are used to determine the suitability of the sheet metal for a forming process. One of the most common methods in stretch forming test is the so-called Erichsen cupping test. In this test rigidly held sheet strips are stretched by a punch to a cup until failure appears. The failure mode of sheet metals in a forming operation usually involves the formation of a localized neck, a locally thin region within which the strain field is concentrated, and a shear fracture in the necked region. The maximum strains that can be attained in the sheet material prior to the onset of localized necking are generally referred to as the forming limits strains. A plot of the major and minor limit strains in the principal strain space constitutes a forming limits diagram, FLD.

Finite element model for the analysis of the Erichsen test

The setup for the Erichsen cupping test consists of the punch, the blank holder, the die with draw-beads and the blank. Due to symmetry only one quarter of the system is modelled using FEM with the two symmetry planes xz- and yz-planes, respectively, see Figure 1. The numerical simulations have been carried out with the explicit finite element program LS-DYNA3D [1],[2], which includes both adaptive and non-adaptive program options. The FE discretization of the numerical model is shown in Figure 1. The blank is discretized using quadrilateral Hughes-Liu shell elements. By changing the blank width from 20 to 200 mm several deformation modes of the blank can be obtained. The punch, blank holder and die were modelled as rigid bodies and the blank as an elasto-plastic material with exponential hardening $\sigma_Y = C\epsilon_{eq}^n$. The friction was modelled using the Coulomb friction law. However, the friction coefficients are different between different contact surfaces as shown in Table 1. As an approximation all nodes outside the draw-beads area are assumed to be fixed, and the draw-beads are therefore not modelled.

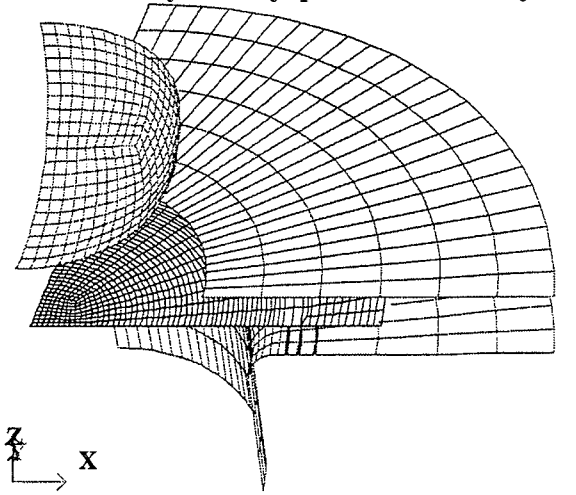Figure 1: Finite element model of the Erichsen cupping test setup

Contact surface		μ-value
Punch	Blank	0.05
Blank holder	Blank	0.61
Die	Blank	0.61

Table 1: The friction coefficients between different parts

The numerical results and comparison with experiments

To verify the numerical results against experiments, the aluminium alloy material 2024-O has been used as a reference material. Jöneby [4] measured the principal strains of the deformed blanks for the reference material from different suppliers, see Figure 2. As shown in this figure the measured principal strains are concentrated in different sides of the forming limit diagram with relatively large distributions of the strain values. The difference between the experimentally obtained FLD can be observed, in spite of the fact that the reference materials are the same in both of the experiments. The post-processor program LS-TAURUS [3]
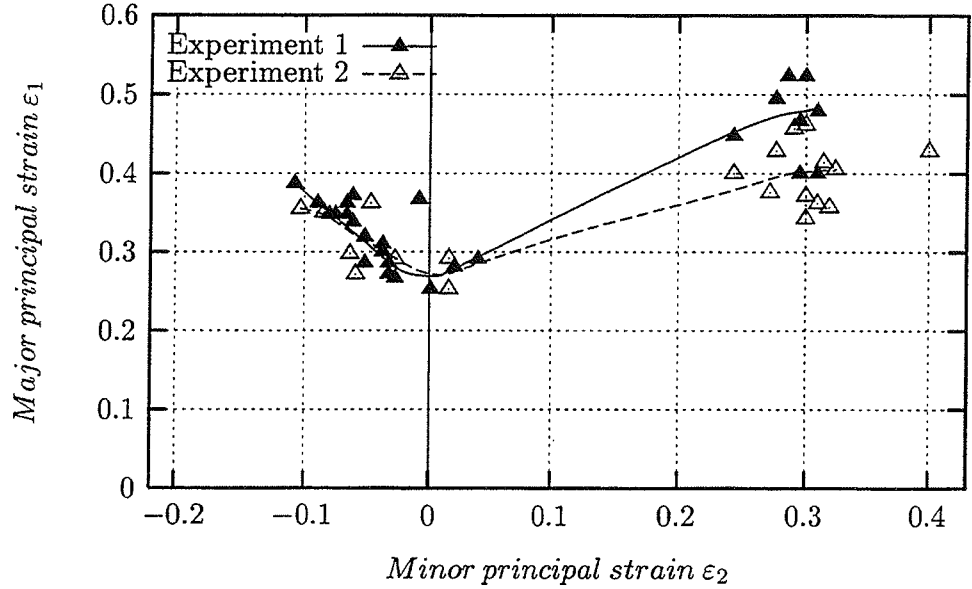
Figure 2: Comparison between the experimentally obtained forming limit diagrams (FLD)

has been used for evaluating the numerical results. This program has an option, "CGAT", which generate grid circles on the material surface. To evaluate the principal strains we choose those deformed circles which have 2 to 3 mm distance from the element with the minimum thickness. At the same time the strain values can be evaluated for those elements which are near to the selected circles around the necking zone (the element length is about 2 to 3 mm). Figure 3 compares the numerical results with the experimental measurements of the principal strain distribution in the FLD for a non-adaptive FE simulation. Figure 4 shows the comparison between the obtained FLD which was performed using the adaptive options in the LS-DYNA3D program and the experimental results.
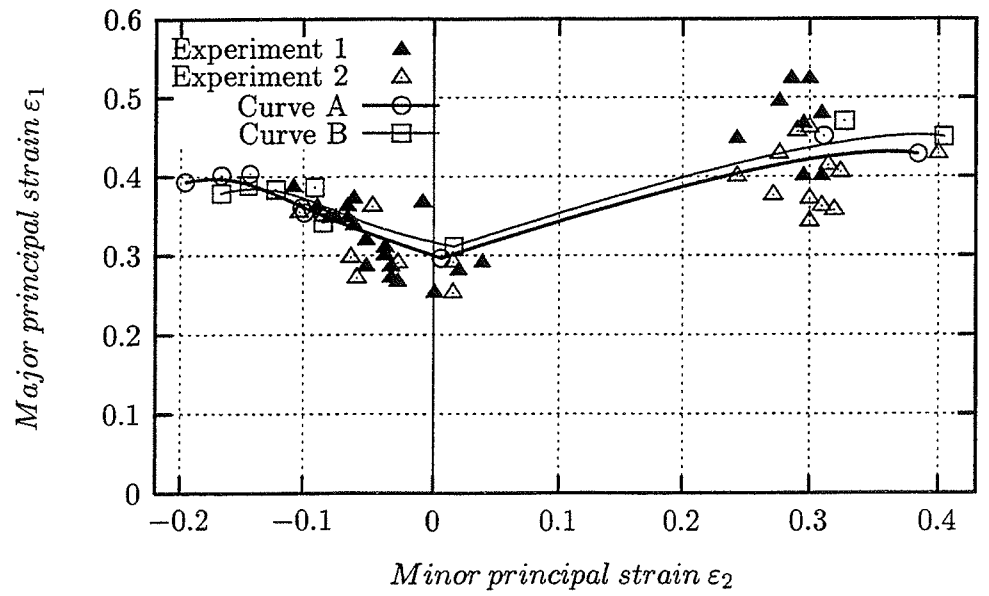
Figure 3: Comparison of experimental values of the principal strains with non-adaptive FE simulation results. (Curve A: The Circular Grid Analysis,"CGAT", and Curve B: The "selected" elements)
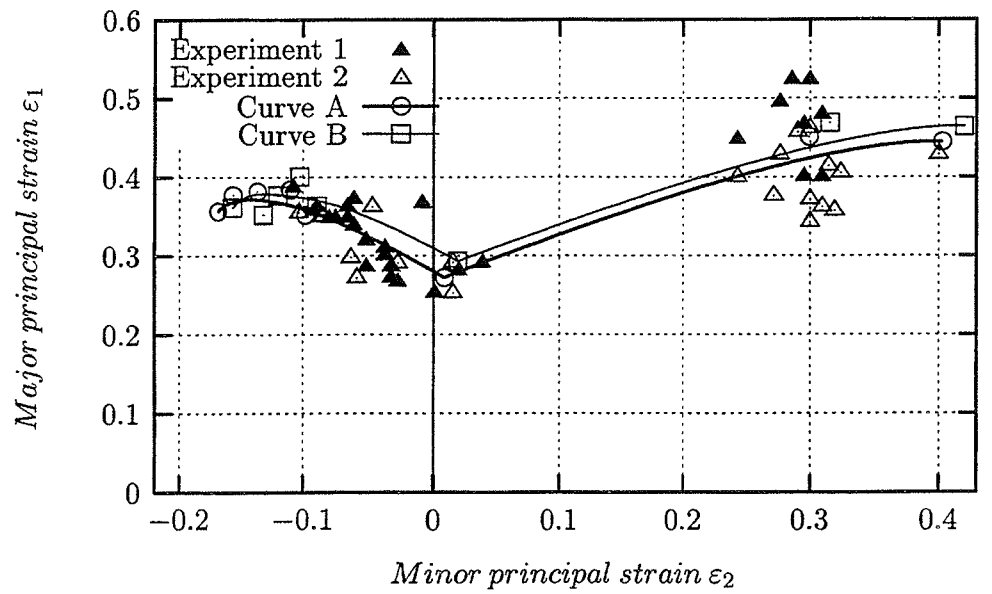
Figure 4: Comparison of experimental values of the principal strains with adaptive FE simulation results. (Curve A: The Circular Grid Analysis, "CGAT", and Curve B: The "selected" elements)

44

Conclusion

Both non-adaptive and adaptive FE simulations are shown to yield accurate results in the simulation of the Erichsen cupping test by the explicit FE method. The shape of the deformed blanks and the obtained values of the failure strains show good agreements with the experimental results.

Acknowledgements

References

[1] J. O. Hallquist. LS–DYNA3D Theoretical Manual. LSTC Report 1018, Livermore Software Technology Corporation, Livermore, 1991.

[2] J. O. Hallquist, D. W. Stillman, and T.-L. Lin. LS–DYNA3D, User's Manual, Version LS-DYNA3D 930. LSTC Report 1007 Rev.3, Livermore Software Technology Corporation, Livermore, 1994.

[3] J. O. Hallquist and D. J. Wynn. LS–TAURUS, An Interactive Post-Processor for the Analysis Codes LS–NIKE3D, LS–DYNA3D, and TOPAZ3D. LSTC Report 1001, Livermore Software Technology Corporation, Livermore, 1992.

[4] R. Jöneby. Forming limit diagram for several aluminium alloys. Technical report, Material and Process Technology, Saab Military Aircraft, Linköping, 1993.

Residual Stresses and Spring Back of Blade Forging Using Solid and Flow Approaches

Behzad Soltani , Kjell Mattiasson and Alf Samuelsson

Department of Structural Mechanics
Chalmers University of Technology
S — 412 96 Göteborg, Sweden

Introduction

The computation of residual stresses and spring back are of importance in blade forming as an example of closed die and precise forging. In finite element computations incorporating elastic effects in the constitutive equations, elastic recovery effects can be directly predicted. This type of analysis is called solid approach. On the other hand, in flow approach, a rigid— plastic (—visco-plastic) constitute equation is used and solved in Eulerian coordinates. In order to compute the elastic effects in this approach, one way is to solve the problem in unloading by a pure elastic analysis. It has been reported that this approach is accurate enough in open die forging [1] and sheet metal forming[2] in loading. And in unloading good results have been reported for the spring back.

We report here numerical analysis of blade forging solved by solid and flow approaches, for both loading and unloading. The final shape and volume of blade are very similar and regarding the calculated residual stresses the two approaches give results with small differences.

Possible reasons for the differences may be that the residual stresses are influenced by the stress distribution and elastic deformation at the ending step of loading, and the deformation history. The stress distribution is very similar for the two simulations at the closing of the dies so it has no influence on the residual stresses at the opening of the dies.

There is some elastic deformation in the billet and the dies obtained in the solid approach at the closing of the dies.

There is almost a closed cavity at the end of the loading and therefore the pressure on the workpiece material is very high which results in large elastic deformations and elastic volume change both in the dies and the workpiece. But these elastic effects are neglected in the flow approach computation and so the simulation of the remaining part of the process in unloading (opening of the dies) can be expected to have some errors.

To find out the influence of these elastic deformations on the residual stresses in closed die forging, another approach was used. The flow approach is used to solve the problem until some steps before closing the dies. At that time the two corners are still enough open to let the workpiece material escape from the applied pressure. And there are no considerable elastic deformations and elastic volume changes. From this time step, the simulation is switched to solid approach. This will introduce the correct elastic effects at the ending steps and therefore the simulation of unloading and the residual stresses can be more accurate. The primary solutions show only small changes

47

in the residual stresses. Therefore, the deformation history has the main effect on the resic stresses.

1. Blade Forging

Blade forming is one of the bulk forming processes in which two dies form an original bi of metal, normally of circular shape [3]. This problem, as other closed die forging proces involves contact surfaces with friction as well as geometrical and material nonlinearities.

The dies come down slowly during the process, therefore, this process is quasistatic and beca the problem is assumed to be in plane strain, the deformation of the cross section is considei In finite element discretization, the upper and lower dies and the billet are divided into 39 ,42 : 1200 elements, respectively. The total number of nodes are 1369.
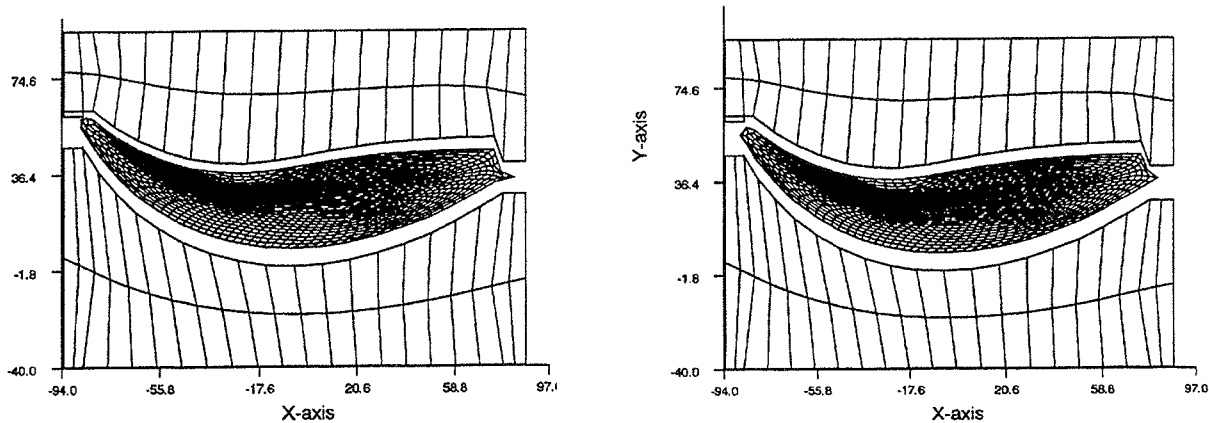
Figure 1. left (solid) right (flow)

The friction between the dies and the material is simulated using the Coulomb law and a fricti coefficient of 0.577. The load curve is a linearly—prescribed displacement of the top surface of t upper die which moves down about 44 mm during the process.

The characteristics used are E=210 GPa, ν=0.3, ϱ=8400 kg/m^3, K=658 MPa, n=0.19 : the billet and E=2100 GPa,ν=0.3, ϱ=8400 kg/m^3 for the dies.

2. Description of the code

The finite element code used was DEFORM (version 4.0)[1],Scientific Forming Technology Corp ration(1994)[4].

DEFORM is an implicit code in which the flow approach and solid approach are used for sta problems. It can handle finite deformation in two dimensions and is designed specially for t forming processes.
In flow approach, the Levy—Mises constitute equation is used and the velocity of nodes are t

1. This code was provided by the Production Engineering department, professor Ralph Crafoord.

48

variables. In the solid approach, the Updated Lagrangian formulation and the Green—Naghdi stress rate are used.

In the code, a four—noded isoparametric element with 2x2 Gaussian points and elastoplastic material was used.

The flow rule used for the billet is a power law plasticity with obvious notations :

$$\sigma_y = K(\bar{\varepsilon}^p)^n + y \tag{1}$$
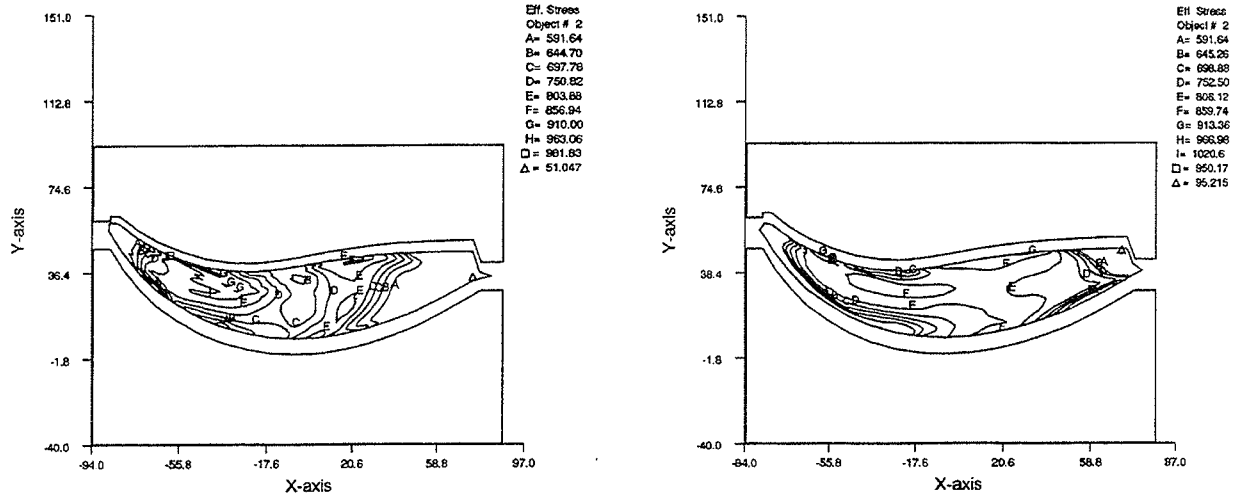
Figure 2. Effective residual stresses in solid (left) and flow (right) solutions

3. Computations and Comparisons

The problem was solved first by the solid approach. Both closing and opening of the dies was included in the simulation. In order to turn to the unloading situation, the dies either are removed or are moved to be separated from the billet. The volume of the billet increases in opening the dies because the elastically—compressed workpiece material is recovered. Volume change percentage in the billet at the end of the simulation is trivial (0.3%) as is expected. The dies are also deformed elastically resulting in a spring back. The remaining stresses after separation of the dies are the residual stresses.

Blade forging with the same characteristics was simulated again by the flow approach. The solving methods, step sizes, convergence criteria, contacting algorithms, etc. were the same as for the solid simulation. When switching to unloading, the linear elastic material was invoked for the billet and the dies were opened. At the end, the shape of blade was similar to the last result and the volume change percentage was also as before (0.3%). Figure 1 shows the deformed billet at the end of simulation in both approaches. The effective residual stresses were more than the former simulation. Moreover, there was no spring back for the billet in this solution. Figure 2 shows the effective residual stresses for the two solutions showing only small differences.

Another simulation was made by the flow approach. However, some steps before the dies were

49

closed, the code was switched to the solid approach. Final shape of blade was the same as be but the effective residual stresses are close to the flow solution.

4. Conclusion

Computation of the blade forging in the isothermal case was performed by three methods. In the solid approach the whole process was simulated using an elasto−plastic constitute e tion. In the flow approach combined with pure elastic approach in opening the dies, the effe residual stresses show small differences while the final shapes of blade are very similar.
In the third approach, the simulation starts with the flow approach and is followed by solid proach some steps before closing the dies. This new way seems to be more effective than the others in the loading part of simulation. The primary computations show that in unloading, final shape is the same as the two others and the effective residual stresses are more close to flow formulation. The likely reason is that the largest part of the simulation history are the s in these two solutions.

Bibliography

[1]   Kobayashi, S., oh, S.K., Altan, T., "Metal Forming and the F.E.M." Oxford University Press I New York,1989.

[2]   Onate,E., Agelet de Saracibar, C.," Alternatives for finite element analysis of sheet metal forn problems",in "Numerical Methods in Industrial Forming Processes", Chenot,Wood, Zienkiev (eds), 1992.

[3]   Soltani, B., Mattiasson, K., Samuelsson, A., "Implicit and explicit solutions of blade f ing using the finite element method" in Journal of Materials Processing Technology, ' 45, pp 69 (1994).

[4]   DEFORM, Design Environment for FORMing, Version 4.0, Users Manual. Scien Forming Technologies Corporation (1994).

On Anisotropic Yield Criteria for Aluminium Alloys

H Ilstad, O-G Lademo, O S Hopperstad, M Langseth and K A Malo

Department of Structural Engineering
The Norwegian University of Technology and Science
Richard Birkelandsvei 1a
N-7034 Trondheim, NORWAY

Introduction

In numerical analysis of plastic forming processes for aluminium extrusions it has been shown that an accurate modelling of the alloy's plastic properties is important for reliable predictions of the final geometry of the extrusion[1]. Experiments indicate that extruded aluminium profiles have significant plastic anisotropy in yield strength, plastic flow and ductility, and thus rather advanced plasticity models are needed to capture the physical response[2].

In this paper we focus on the accuracy and computational efficiency of some anisotropic plasticity models proposed in the open literature. The models are based on the incremental theory of plasticity, and the main ingredients in this class of models are a yield criterion, a flow rule and a strain hardening rule.

Three yield criteria proposed by Hill[3], Barlat[4] and Karafillis and Boyce[5] were investigated, using an associated flow rule and an isotropic strain hardening rule. These yield criteria are all valid for orthotropic and plastic incompressible materials. The plasticity models were implemented in the finite element code LS-DYNA3D[6] for shell elements.

Material tests

The elastoplastic material characteristics of the aluminium alloy AA 7108 T5 were identified by tensile testing[2]. Tensile specimens were taken from an extruded aluminium plate in directions $\alpha = 0°, 35°, 45°, 55°$ and $90°$ with the extrusion axis.

The tests were performed in a universal testing machine under quasi-static loading conditions at room temperature, measuring the load, the cross-head displacement, and the length and width strains.

Based on the test results the stress-plastic strain curves, $\sigma_\alpha = \sigma_\alpha(\varepsilon_\alpha^p)$, and the R-ratios, $R_\alpha = R_\alpha(\varepsilon_\alpha^p)$, in the five directions were calculated, where ε_α^p is plastic length strain. The R-ratio is the ratio of the width-to-thickness plastic strains and gives information on the plastic flow of the material. It was found that the R-ratios varied only slightly with increasing plastic length strains, and a mean R-ratio, $\overline{R}_\alpha$, was fitted to the experimental data for each direction.

The flow stress ratios, $r_\alpha = \sigma_\alpha/\sigma_0$, can be used to check the strain hardening characteristics of the alloy. For the actual alloy only small variations in the flow stress ratios were observed with increasing plastic length strains, which indicates that isotropic strain hardening is sufficient to model the tensile stress-strain behaviour. Hence, a mean flow stress ratio, $\overline{r}_\alpha$, was identified for each direction.

Identification

The three yield criteria can all be calibrated by means of flow stress ratios, $\overline{r}_\alpha$, and R-ratios, $\overline{R}_\alpha$, from tensile tests in the 0°, 45° and 90° directions. Unfortunately, no unique identification of the material constants is available for either of the yield criteria.

Several identifications are possible for the Hill criterion but only two are considered here. The first identification (ID1) gives an optimal calibration of the yield criterion and uses three flow stress ratios $\bar{r}_0$, $\bar{r}_{45}$ and $\bar{r}_{90}$ and one R-ratio $\bar{R}_0$. In the second (ID2) three R-ratios $\bar{R}_0$, $\bar{R}_{45}$ and $\bar{R}_{90}$ and one flow stress ratio $\bar{r}_0$ are used, and the identification is optimal with regards to plastic flow.

Barlat[4] describes two methods of identification for his yield criterion: the first (ID1) uses $\bar{r}_0$, $\bar{r}_{90}$, $\bar{R}_0$, $\bar{R}_{45}$ and $\bar{R}_{90}$, whereas the second (ID2) requires $\bar{r}_0$, $\bar{R}_0$, $\bar{R}_{45}$ and $\bar{R}_{90}$. Here the first identification gives a better prediction of the yield condition, whereas the second gives optimal results for the plastic flow.

For the Karafillis and Boyce criterion only one identification was established, using a method similar to that described in their paper[5]. In the calibration $\bar{r}_0$, $\bar{R}_0$, $\bar{R}_{45}$ and $\bar{R}_{90}$ are utilised.

The isotropic strain hardening rule was identified from the stress-plastic strain curve in the 0° direction: $\sigma_0 = \sigma_0(\varepsilon_0^p)$. The elastic properties of the alloy were assumed to be isotropic.

Numerical Study

Numerical studies of the tensile tests were carried out using LS-DYNA3D in order to assess the accuracy and the computational efficiency of the anisotropic plasticity models.

In the tensile tests it was observed that the location of necking was dependent on the direction α, and therefore a full model of the test specimen was used. The model consists of 1316 Belytschko-Lin-Tsay shell elements[6] with one-point quadrature. The finite element model is depicted in Figure 1. The load was applied through the pins in each end of the specimen which were given a prescribed velocity in opposite directions. The pins were modelled as rigid bodies tied to the specimen.

Explicit time stepping algorithms like the central difference method used in LS-DYNA3D, put strong limitations on the size of the time step. In order to reduce the number of time steps, the quasi-static simulations were performed using mass-scaling. It was assumed that 10 000 time steps were sufficient to solve the problem, and the density of the alloy was then scaled with a factor of $1.6 \cdot 10^7$.

Results

Figure 2 compares the experimental and predicted force-displacement curves in the five directions. The figure clearly illustrates the plastic anisotropy of the aluminium alloy – in strength and ductility. It is also seen that the aluminium alloy 7108 in temper T5 has very limited strain hardening.

The Hill criterion identified by three flow stress ratios and one R-ratio (ID1) gives correct force levels in four of the five directions and conservative estimates on the ductility of the alloy. However, the force level in the 35° direction is somewhat underestimated. The results also indicate that isotropic hardening is a reasonable assumption for the tensile behaviour of the alloy. The first identification of the Barlat criterion gives also acceptable results, but the predicted force levels in the 35°, 45° and 55° directions are lower than the experimental ones.

It is obvious that calibrations based mainly on the R-ratios may lead to very erroneous predictions of the force levels. This is the case for the second identification (ID2) of the Hill and Barlat criteria, and to some extent for the Karafillis and Boyce criterion.

The relative CPU time requirements for the Hill, Barlat and Karafillis and Boyce yield criteria were 1.0, 2.0 and 3.3, respectively.

References

1. Hopperstad O.S., Remseth S., and Leira B., 'Reliability-based analysis of a stretch-bending process for aluminium extrusions', submitted for publication, 1996.
2. Lademo O.-G., Hopperstad O.S, and Langseth M., 'An evaluation of yield criteria, flow rules and strain hardening rules for extruded aluminium alloys', submitted for publication, 1996.
3. Hill R., "The Mathematical Theory of Plasticity", (*Oxford: Clarendon Press*), 1950.
4. Barlat F. and Lian J., 'Plastic Behavior and Stretchability of Sheet Metals. Part I: A Yield Function for Orthotropic Sheets Under Plane Stress Conditions', *International Journal of Plasticity*, **5** (1989), 51-66.
5. Karafillis A. P., Boyce M. C., 'A General Anisotropic Yield Criterion Using Bounds and a Transformation Weighting Tensor', *J. Mech. Phys. Solids*, **41** (1993), 1859-1886.
6. Hallquist J.O., Stillman D.W. og Lin T.-L., 'LS-DYNA3D User's Manuals', Livermore Software Technology Corporation, Report 1007, Rev. 2, 1994.
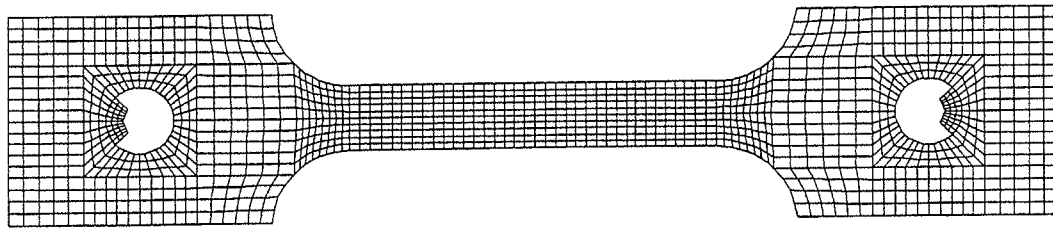
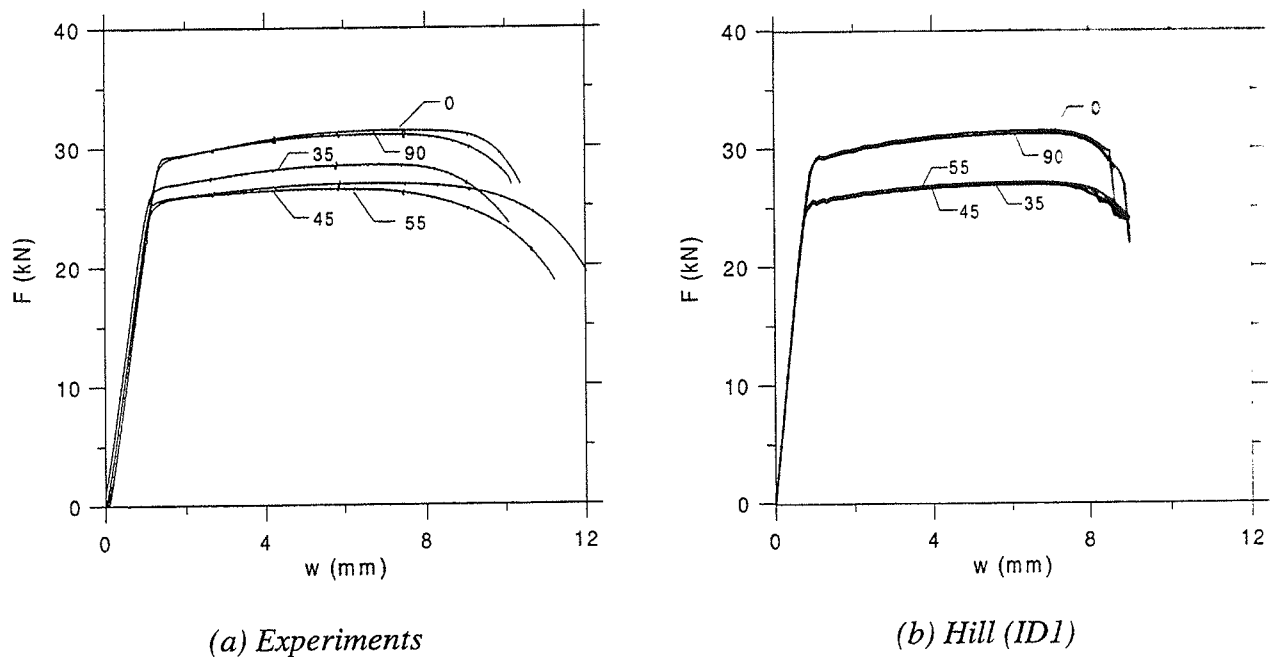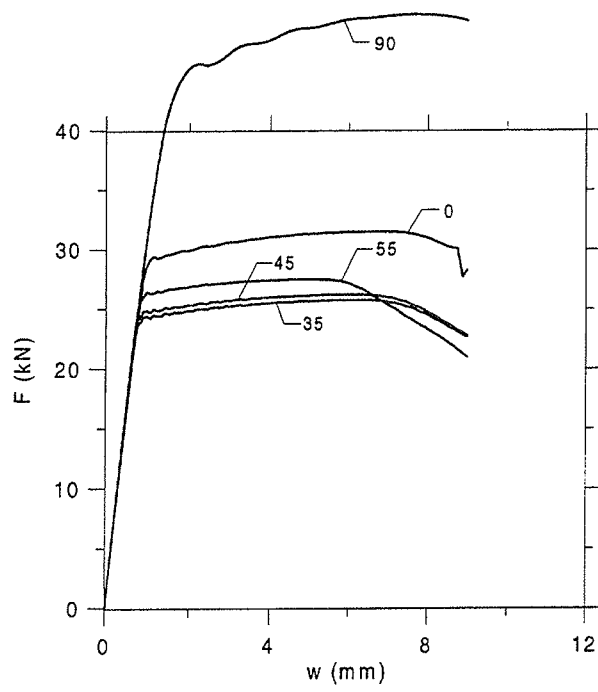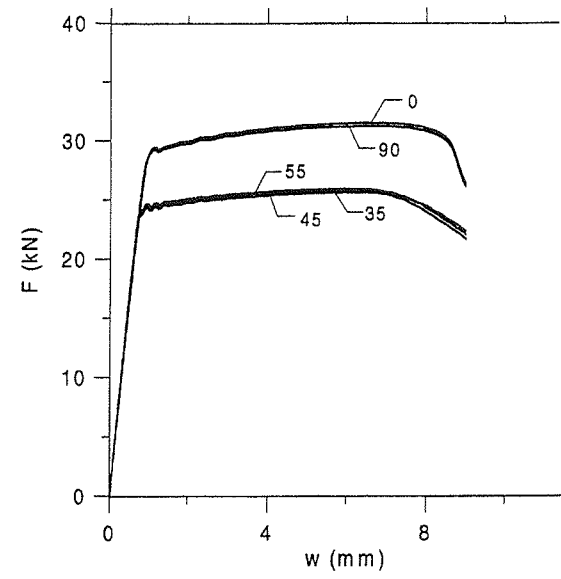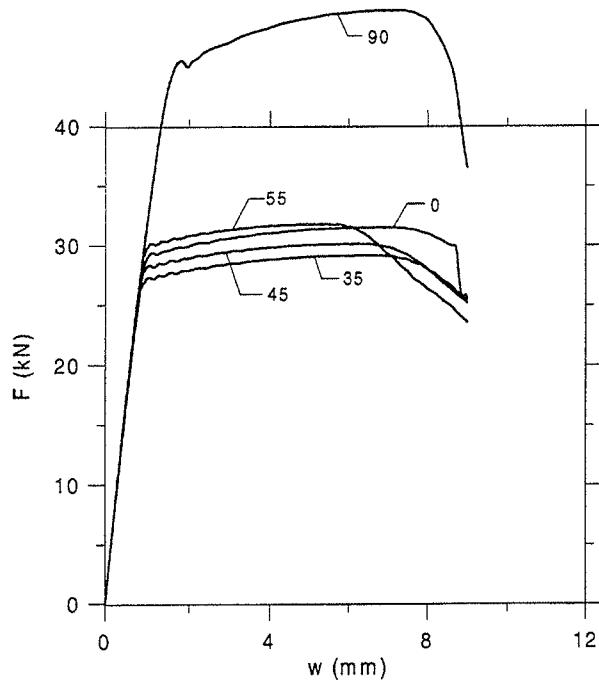Figure 1: Finite element model

(a) Experiments

(b) Hill (ID1)

Figure 2: Force-displacement curves from physical and simulated tensile tests on aluminium alloy AA7108 T5 in five directions 0°, 35°, 45°, 55° and 90° with the extrusion axis

(c) Hill (ID2)

(d) Barlat (ID1)

(e) Barlat (ID2)
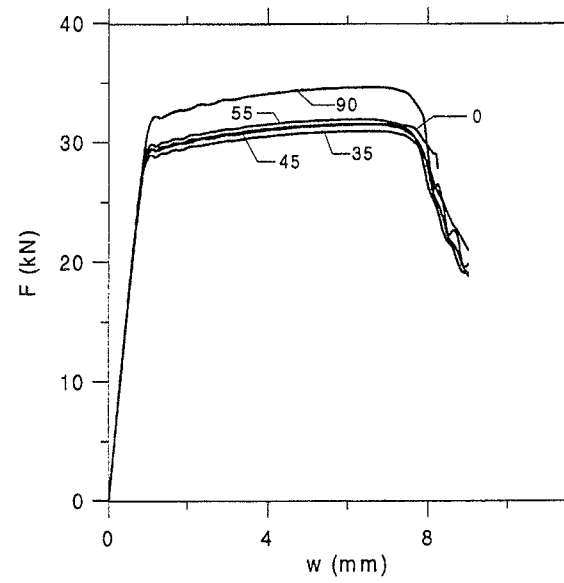
(f) Karafillis & Boyce

Figure 2: (cont.)

54

Viscoplasticity with Dynamic Yield Surface Coupled to Damage - Formulation and Integration

Magnus Johansson and Kenneth Runesson

Division of Solid Mechanics, Chalmers University of Technology,
S-412 96 Göteborg, Sweden

1 Introduction

A wealth of literature deals with the description and constitutive modeling of the rate-dependent macroscopic characteristics of metals and alloys, including creep, at elevated temperature. The simple creep law NORTON [1] has been used extensively in engineering practice to simulate stationary creep. More realistic models are obtained within the framework of viscoplasticity, by which a threshold value of stress must be exceeded before rate-dependent inelastic strain can develop, e.g. PERZYNA [3]. A major feature (advantage) of the classical viscoplastic theory is that the rate-independent elastic-plastic behavior will be activated at very small loading rate. The behavior close to rupture has been modeled by introducing damage, which approach goes back to KACHANOV [2]. Viscoplastic deformation may be coupled kinetically to damage, as described by LEMAITRE [4], and the theory can be based on the sound thermodynamic principle of non-negative dissipation of energy. As a result, the classical transient, stationary and rupture phases of creep are described conveniently, as shown in Fig. 1. For example, transient phase is modelled with aid of nonlinear saturation hardening of the quasistatic viscoplastic yield surface.

In the classical viscoplasticity formulations, the response becomes completely elastic without limit on the stress at infinite loading rate, which is not realistic. Therefore, we introduce a dynamic yield surface, that is approached asymptotically at infinite loading rate. This essential behavior is accomplished by a special choice of "overstress" function, which has the property that the apparent fluidity becomes infinite when the stress approaches (from inside) the dynamic yield surface. Although rather simple in concept, this feature is essential for the possibility to describe, in a quite realistic fashion, the influence of large strain-rate on the total stress-strain relation.

As to the choice of viscoplastic formulation, a generalization of the concept of DUVAUT & LIONS [5] is adopted in order to include the pertinent hardening or (thermal) softening characteristics.

2 Integration technique

The fully implicit Backward Euler rule is adopted for integrating the evolution equations (for the effective stress, the hardening stresses and the damage variable). Due to the presence of damage, it also appears that the quasistatic (elastic-plastic) solution is affected by the viscoplastic characteristics, which represents an additional "nonlinearity" as compared to the situation without damage, cf. SIMO & HUGHES [6]. In order to achieve quadratic convergence in the FE-algorithm at equilibrium iterations in each timestep, it is necessary to derive the proper Algorithmic Tangent Stiffness (ATS) tensor.
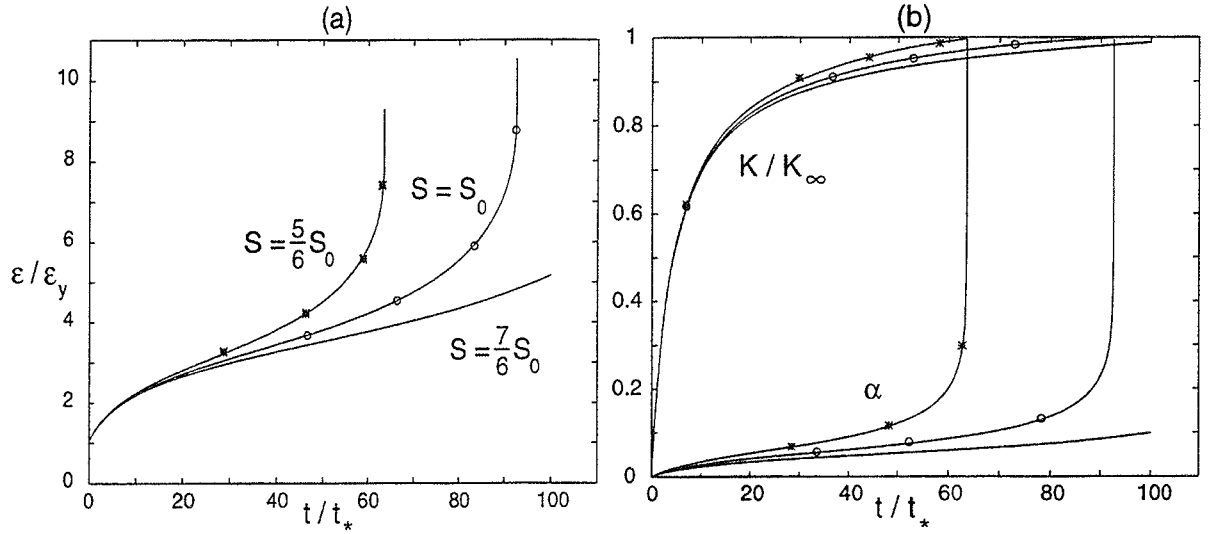
Fig. 1. Monotonic creep behavior in *biaxial* stress $(\sigma_1/\sigma_y = \sigma_2/\sigma_y = 1.5)$ for different values of the damage modulus. (a) Strain versus time, (b) Hardening stress and damage versus time.

References

[1] F.H. Norton. *The creep of steel at high temperatures*. McGraw-Hill, 1929.

[2] L.M. Kachanov. Time of the rupture process under creep conditions. *Izv. Akad.*, *S.S.S.R. Otd. Tech. Nauk*, 8:26–31, 1958.

[3] P. Perzyna. Fundamental problems in viscoplasticity. *Advances in Appl. Mech.*, 9:244–368, 1966.

[4] J. Lemaitre. *A Course on Damage Mechanics*. Springer-Verlag, 1992.

[5] G. Duvaut and J.L. Lions. *Les Inequations en Mecanique et en Physique*. Dunod, Paris, 1972.

[6] J.C. Simo and T.J.R Hughes. *Elastoplasticity and Viscoplasticity, Computational Aspects*. Springer, Berlin, 1988.

Acoustic analysis applied to aircrafts

Göran Sandberg, Mats Gustavsson

Division of Structural Mechanics, LTH, Lund University, Lund, SWEDEN

Abstract

A practical approach is outlined for decomposing a large fluid domain for acoustic calculations. The scheme is based on modal description of the separate subdomains. The suggested scheme results in a final symmetric problem of the type $Ax = b$ where x contains the modal coordinates. The approach is utilized on an aircraft cabin.

Theory

Consider a large acoustic domain, using fluid pressure, p, as the independent variable. By introducing an interior boundary with displacement as independent variable, the finite element model of the total domain achieves properties that can be used for domain decomposition. Fluid pressure, a force type variable, and displacement are conjugate variables in the virtual work sense. The information handling between the subdomains is sketched below.
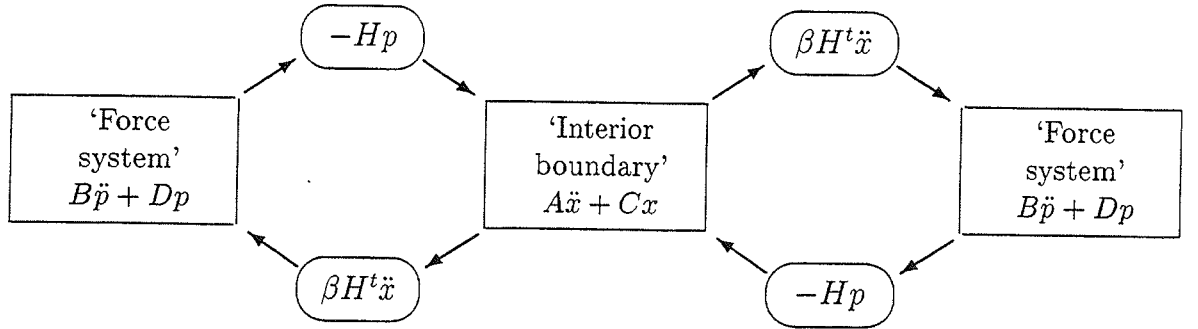
Figure 1: *Two pressure (force) type systems coupled by a displacement type system.*

The finite element matrix description of the total system reads

$$
\begin{pmatrix} M_{f1} & \rho c^2 H_1^T & 0 \\ 0 & M_{layer} & 0 \\ 0 & \rho c^2 H_2^T & M_{f2} \end{pmatrix} \begin{pmatrix} \ddot{p}_1 \\ \ddot{u}_{layer} \\ \ddot{p}_2 \end{pmatrix} + \begin{pmatrix} c^2 K_{f1} & 0 & 0 \\ -H_1 & 0 & -H_2 \\ 0 & 0 & c^2 K_{f2} \end{pmatrix} \begin{pmatrix} p_1 \\ u_{layer} \\ p_2 \end{pmatrix} = \begin{pmatrix} F_{f1} \\ 0 \\ F_{f2} \end{pmatrix} \tag{1}
$$

where, M_{f1}, M_{f2}, K_{f1}, K_{f2} are the fluid system matrices for the two separate domains, and M_{layer} is the mass matrix of the interior fluid boundary, using a displacement formulation. u_{layer} is the displacement of the boundary. The 'stiffness' of the boundary is neglected.

57

layer and n is the unit vector in the normal direction at the fluid layer. The symmet
property of the matrix blocks for each subdomain makes it possible to diagonalize ea
block independently. Let Φ_{layer} and Φ_{fr}, $r = 1,2$ be sets of eigenvectors so that

$$\begin{cases} \Phi_{layer}^T M_{layer} \Phi_{layer} = D_{layer}, \\ \Phi_{fr}^T M_{fr} \Phi_{fr} = I_{fr} \quad \text{and} \quad \Phi_{fr}^T K_{fr} \Phi_{fr} = D_{fr}, \quad r = 1,2, \end{cases}$$

where D_{layer} and D_{fr} are diagonal matrices. The modal form of Eq. (1) reads

$$\begin{pmatrix} I_{f1} & \rho c^2 \widetilde{H}_1^T & 0 \\ 0 & D_{layer} & 0 \\ 0 & \rho c^2 \widetilde{H}_2^T & I_{f2} \end{pmatrix} \begin{pmatrix} \ddot{\xi}_{f1} \\ \ddot{\xi}_{layer} \\ \ddot{\xi}_{f2} \end{pmatrix} + \begin{pmatrix} D_{f1} & 0 & 0 \\ -\widetilde{H}_1 & 0 & -\widetilde{H}_2 \\ 0 & 0 & D_{f2} \end{pmatrix} \begin{pmatrix} \xi_{f1} \\ \xi_{layer} \\ \xi_{f2} \end{pmatrix} = \begin{pmatrix} \Phi_{f1}^T F_{f1} \\ 0 \\ \Phi_{f2}^T F_{f2} \end{pmatrix} .$$

where $\xi_\square$ represents the modal coordinates in each subdomain, and $\widetilde{H}_r = \Phi_{layer}^T H_r \Phi_f$
$r = 1,2$. The inverse of the modal mass matrix is

$$\begin{pmatrix} I_{f1} & -\rho c^2 \widetilde{H}_1^T D_{layer}^{-1} & 0 \\ 0 & D_{layer}^{-1} & 0 \\ 0 & -\rho c^2 \widetilde{H}_2^T D_{layer}^{-1} & I_{f2} \end{pmatrix} .$$

Multiplying from the left by this inverse then yields

$$\begin{pmatrix} \ddot{\xi}_{f1} \\ \ddot{\xi}_{layer} \\ \ddot{\xi}_{f2} \end{pmatrix} + \begin{pmatrix} \boxed{D_{f1}+ \rho c^2 \widetilde{H}_1^T D_{layer}^{-1} \widetilde{H}_1} & 0 & \rho c^2 \widetilde{H}_1^T D_{layer}^{-1} \widetilde{H}_2 \\ -D_{layer}^{-1} \widetilde{H}_1 & 0 & -D_{layer}^{-1} \widetilde{H}_2 \\ \rho c^2 \widetilde{H}_2^T D_{layer}^{-1} \widetilde{H}_1 & 0 & \boxed{D_{f2}+ \rho c^2 \widetilde{H}_2^T D_{layer}^{-1} \widetilde{H}_2} \end{pmatrix} \begin{pmatrix} \xi_{f1} \\ \xi_{layer} \\ \xi_{f2} \end{pmatrix} = \begin{pmatrix} \Phi_{f1}^T F_{f1} \\ 0 \\ \Phi_{f2}^T F_{f2} \end{pmatrix} .$$

Apart from the zero eigenmodes the system matrix is equivalent to the following matri

$$\begin{pmatrix} D_{f1} + \rho c^2 \widetilde{H}_1^T D_{layer}^{-1} \widetilde{H}_1 & \rho c^2 \widetilde{H}_1^T D_{layer}^{-1} \widetilde{H}_2 \\ \rho c^2 \widetilde{H}_2^T D_{layer}^{-1} \widetilde{H}_1 & D_{f2} + \rho c^2 \widetilde{H}_2^T D_{layer}^{-1} \widetilde{H}_2 \end{pmatrix} .$$

This system is then used for eigenvalue analysis. Only a limited selection av mode
from the subdomains is used. The interior boundary is treated as 'virtual', meaning, th
stiffness is set to zero for simplicity and the mass contribution is given as small a valu
as possible.

A section of an aircraft cabin is studied. The total length of the cabin section is 8.4 meter and the diameter is 2.3 meter. The cabin is divided in two parts and the result, eigenvectors computed according to the suggested scheme, is compared to an eigenvalue analysis of the complete model.

- The complete model holds 7068 nodes.

- The individual parts are 4.9 m and 3.5 m and have 2976 and 4216 nodes respectively.

- 80 modes from each part are used to compute the first 20 modes of the complete cabin section.
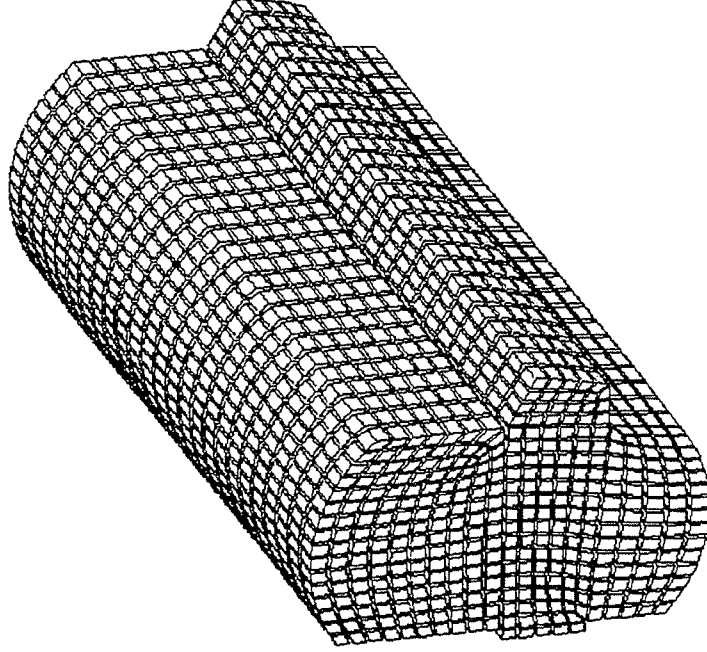
Figure 2: *Section of aircraft cabin used in this study.*

It is of interest to compare not only the eigenvalues, but the shape of the eigenvectors as well. As a simple measure of the shape correlation we use

$$\epsilon = \frac{v_{reduced} \cdot v_{complete}}{|v_{reduced}||v_{complete}|}$$

where $v_{reduced}$ is an eigenvector computed from the decomposed modes and $v_{complete}$ is an eigenvector computed from the original model. Hence, if they are identical we get $\epsilon = 1$. In Table 1 the first 20 modes are listed. They are compared and listed so that the 'shape correlation factor', as defined above, is as close to one as possible for each mode. Mode 13 and 14 in the complete model are in reversed order compared to the suggested scheme. The 'shape correlation factor' are listed in Table 2.

mode No	suggested scheme	complete model
1	0.0	0.0
2	25.49	20.37
3	43.20	40.73
4	61.82	61.06
5	81.65	81.65
6	85.55	81.34
7	85.65	84.09
8	92.41	91.04
9	101.3	101.6
10	102.7	101.5
11	109.2	109.2
12	112.1	111.0
13	117.3	116.3
14	119.9	114.6
15	125.3	124.5
16	125.7	121.7
17	129.4	129.4
18	139.0	135.2
19	143.2	141.7
20	147.7	147.8

Table 2: *Shape correlation factor.*
Result for the first 20 modes

1
0.9982
0.9627
0.9889
1
0.9632
0.9945
0.9556
0.9992
0.9879
1
0.9958
0.9576
0.9265
0.9886
0.9695
0.9985
0.9407
0.9951
0.9987

Topological fluid mechanics
of axisymmetric flows

Morten Brøns
Department of Mathematics
Technical University of Denmark
DK-2800 Lyngby
Denmark

When the dynamic equations for a fluid problem are solved a velocity field $v(x,t)$ is obtained. The streamlines are found as the trajectories of this field, i.e. by solving the ordinary differential equations

$$dx/dt = v(x,t). \tag{1}$$

These differential equations can be studied using qualitative methods from the theory of dynamical systems such as bifurcation theory and singularity theory. By this, a link from concepts from dynamical systems to concepts from fluid mechanics can be established. For instance, if a critical point of (1) is a center, the fluid mechanics interpretation is a vortex, while a saddle is a stagnation point.

Topological fluid mechanics in the sense of the present paper is the study and classification of flow patterns close to a critical point. Bakker [1] has given an extensive classification of such patterns in two-dimensional flows close to a plane wall, and the present author [2] has in the same vein classified flows near free and viscous interfaces.

Here we discuss the topology of steady viscous incompressible axisymmetric flows in the vicinity of the axis. Symmetry allows one to study the flow patterns in the meridional plane only, making the system (1) two-dimensional.

Following previous studies the vector field v is expanded in a Taylor series at a point on the axis. From the dynamic equations, the equation of continuity, and boundary conditions relations between the expansion coefficients are obtained, making it possible to eliminate some of them. The remaining coefficients are considered as bifurcation parameters.

When the expansion point is a critical point the Jacobian matrix $A = \partial v/\partial x$ is generically hyperbolic, and the critical point is a stagnation point. The simplest degeneration occurs when zero is an eigenvalue of A with multiplicity one.
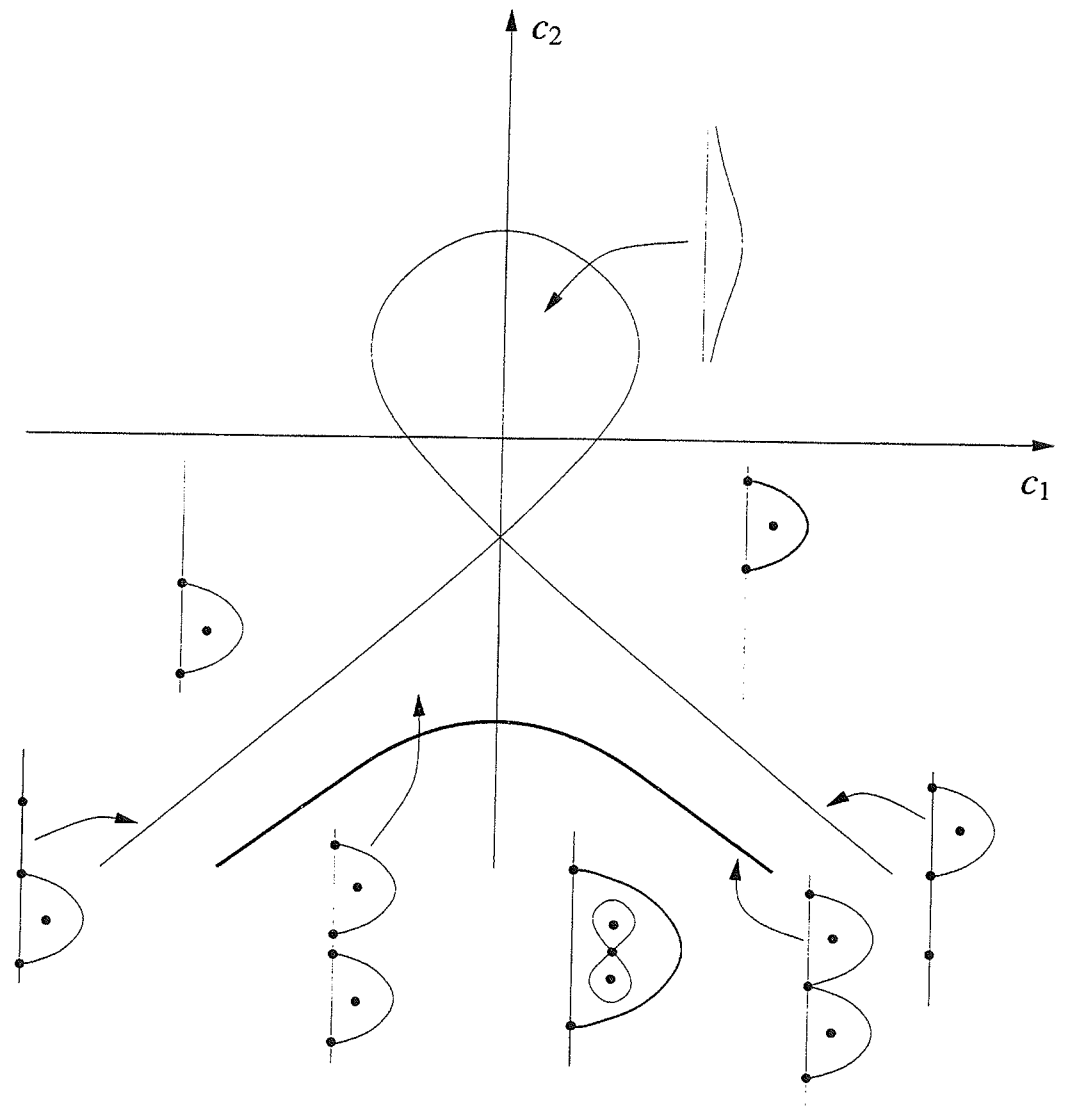
Figure 1: An example of an unfolding showing possible patterns of separation bubbles on the axis.

We consider this singularity as the organizing center for unfoldings depending on higher-order terms.

The equations are simplified using the theory of normal forms, that is, a series of near-identity coordinate transformations. To the authors knowledge this has not been used in topological fluid mechanics before. This results in a significant reduction of the number of terms involved, and with this we easily obtain the most common bifurcations of the flow patterns. We compare these with experimental results by Escudier [3] on the Vogel-Ronneberg flow (a cylindrical vessel filled with fluid where the lid is rotated uniformly to create a vortex motion.) We show that the topology changes observed when recirculating bubbles on the vortex axis are created and interact follow the topological classification and that the complete set of patterns found is contained in a codimension-3 unfolding of the singularity.

Hence, we propose topological fluid mechanics as a tool for understanding visualisations of flows, whether they are obtained experimentally or numerically. Furthermore, one may speculate if the basic topological structures we obtain can be used as elements in a numerical procedure, generalising well-known vortex methods.

References

[1] P. G. Bakker. *Bifurcations in Flow Patterns*. Klüver Academic Publishers, Dordrecht, 1991.

[2] M. Brøns. Topological fluid dynamics of interfacial flows. *Physics of Fluids*, 6(8):2730–2737, 1994.

[3] M. P. Escudier. Observations of the flow produced in a cylindrical container by a rotating endwall. *Experiments in Fluids*, 2:189–196, 1984.

Tracking non-spherical particles in combustion systems

Lasse Rosendahl and Thomas J. Condra

Institute of Energy Technology, Aalborg University,
Pontoppidanstraede 101, DK-9220 Aalborg, Denmark
e-mail: lar @iet.auc.dk and tc@iet.auc.dk

Abstract. For the purposes of tracking in combustion systems particles have hitherto been treated as being near-spherical. This paper presents a unified superellipsoid based formulation for spherical and non-spherical particles together with a treatment of the extra forces which arise when tracking elongated particles.
Keywords: Computational fluid dynamics, non-spherical particles, biomass, combustion

1 Introduction

The application of Computational Fluid Dynamics (CFD) to the analysis of the combustion of discrete fuel droplets or particles has been normally based on the solution of the continuous phase using a Navier-Stokes solver and then using a Lagrangian tracking method on the discrete phase. The tracking procedure is normally based on the assumption that the particles are perfect spheres, with perhaps a correction factor for non-sphericity (Kunii and Levenspiel, 1969). This assumption, in a pragmatic spirit, can be accepted, especially for droplets and in pulverised coal combustion applications. However where the particle is of a material such as waste or biomass then the sphericity assumption is clearly deficient.

This paper deals with a unified formulation for the analysis of the tracking behaviour of solid particles whose shapes stretche from the spherical to an elongated cylindrical shape. The paper considers the practical formulation of a unified geometrical particle description and deals with the extra forces which arise for elongated cylindrical particles.

The inspiration for this work is the development of a CFD based system to analyse the co-firing of coal and biomass particulate material (straw). The gas phase is calculated using the CFD commercial code CFX, and the combustion and particle tracking is carried out in a program Pcombust, where the particle tracking formulation has been incorporated. Pcombust calculates particle trajectories, phase coupling information as well as detailed information about the individual particles. For further details on Pcombust refer to Rosendahl (1996) and to http://www.iet.auc.dk.

2 Description of formulation

2.1 Particle shape

The main feature of the dispersed phase formulation is the shape description. A superelliptic shape function (Hein, 1964) is applied, which allows for a three-parameter description of a particle:

$$\frac{x'^{\,n}}{a} + \frac{y'^{\,n}}{b} = 1, \qquad n \geq 2.0, \quad \frac{b}{a} = \beta \geq 1.0 \tag{1}$$

By variation of n and the axis aspect ratio, β, a range of axi-symmetric particles from spheres via ellipsoids to cylinders can be generated, all using the same shape formulation.(see fig.1)

2.2 Particle forces

The primary force to be considered is the drag force, which dominates the motion of an individual particle. Independent of particle shape, the drag force (see fig. 2) is formulated as:

$$\mathbf{F}_D = \frac{1}{2} C_D \rho_g A_p |\mathbf{u}_g - \mathbf{u}_p|(\mathbf{u}_g - \mathbf{u}_p) \tag{2}$$
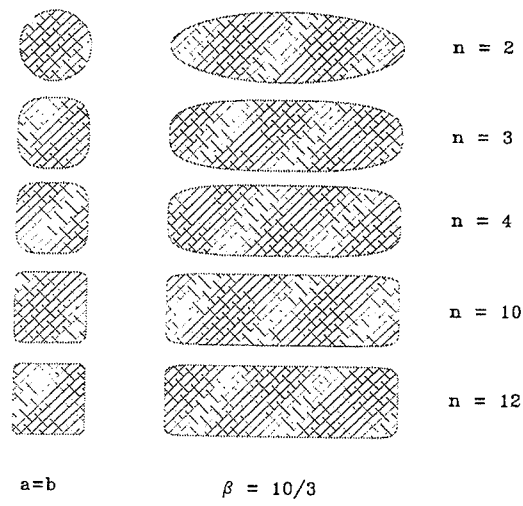
Fig. 1. Various shapes generated using different parameters in the superelliptic formulation

The main difficulty lies in the formulation of the drag coefficient which must be done so that variations in the two shape-determining parameters, n and β, are included in the drag coefficient, as well as the standard correlation arising from departure from Stokes conditions. The current formulation utilises a Stokes correlation due to A. Kaskas (Brauer,1971) as well as a number of numerical correlations due to shape variation, valid for particle Reynolds numbers less than 10^3:

$$C_D = C_{D,sphere} \left[\frac{Re_p}{(\beta - 1) + f_{1\beta}Re_p} \right]^{f_{2\beta}} f_n \tag{3}$$

with

$$f_n = 0.857 + 1.46 \times 10^{-3}(n - 2.0)$$
$$f_{1\beta} = 0.07 + 2.65 \times 10^{-3}(100.0 - \beta) \tag{4}$$
$$f_{2\beta} = 0.142 + 5.68 \times 0^{-4}(\beta - 5.0)$$

Lift forces include aerodynamic lift, arising from orientability, lift due to velocity gradients (Saffmann forces) in the flow, or particle rotation, which induces a velocity difference on opposing sides of the particle (Magnus forces). The current model includes aerodynamical
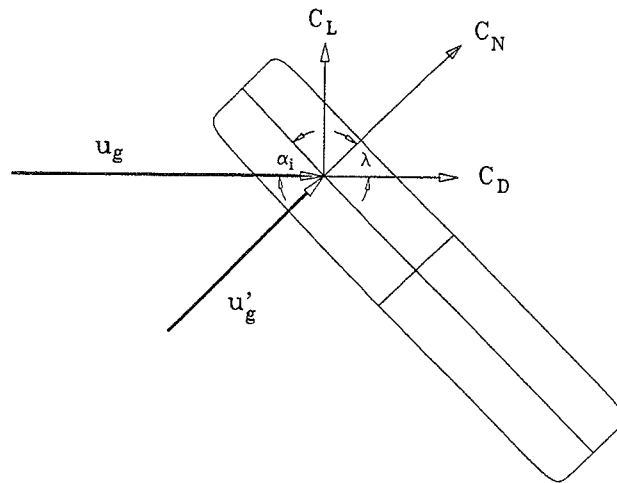
Fig. 2. The aerodynamic forces on a particle

66

lift forces only, as these are considered the dominant lift forces. The cross-flow principle (Horner, 1965) is used, essentially making the lift force a function of the drag coefficient, and subsequently the particle Reynolds number:

$$C_{L,aero} = C_D f_\beta \sin^2 \alpha_i \cos \alpha_i \tag{5}$$

Finally, through a dominant force consideration, gravity is included in the force balance as a conservative force.

2.3 Particle torques

Two contributions to the rotational motion of the particle are considered. The first is the inherent fluid vorticity, which will act on the particle as a torque due to the viscous forces at the particle surface. Based on Besnard and Harlow (1986), the viscous torque can be expressed as:

$$\mathbf{T}_{visc} = K_\omega \mu_g A_s \bar{d}_p \left(\frac{1}{2} \nabla \times \mathbf{u}_g - _p \right) \tag{6}$$

with K_ω of order unity. The second particle torque included in Pcombust is the pitching moment, arising from the aerodynamic forces. These forces act at the centre of pressure, thus giving rise to a torque about an axis perpendicular to the plane defined by the major particle axis and flow velocity vector. Maintaining the coefficient formulation and still utilizing the cross-flow principle, the pitching moment coefficient can be expressed as:

$$C_N = C_D \sin \alpha_i \cos \alpha_i \tag{7}$$

The location of the centre of pressure is a function of the incidence angle α_i and axes aspect ratio β:

$$x_{cp} = 0.5b \left(1 - \exp(1 - \beta)\right) \left(1 - \sin^3 \alpha_i\right) \tag{8}$$

2.4 Orientability

The orientability necessitates the determination of the incidence angle between the particle and the flow velocity vector. Using directional cosines, this relationship is:

$$\alpha_i = \sum_i \arccos(\cos \theta_{\mathbf{u}_g} \cos \theta_{y'}) \tag{9}$$

The projected area can thus be expressed as a function of the incidence angle:

$$A_p = \pi a^2 (\cos^2 \alpha_i + R_\beta \sin^2 \alpha_i) \tag{10}$$

with $R_\beta = \frac{A_{\alpha_i = 0}}{A_{\alpha_i = 0.5\pi}}$.

3 Concluding remarks

Although this work shows that it is possible to extend the existing methodology of particle tracking from spheres to superellipsoids, it is clear that much work need still be done. This is primarily true of the experimental data available to verify a code like Pcombust, where particularly more extensive drag measurements would be very valuable.

4 Nomenclature

4.1 Symbols

ρ: density $[kg/m^3]$

u: velocity in inertial frame of reference $[m/s]$

x: inertial coordinate system $[m]$

a, b: minor and major particle semi-axis, respectively $[m]$

$\bar{d}_p$: equivalent spherical diameter $[m]$

β: axes aspect ratio, b/a $[-]$

R_β: area ratio, $\frac{A_{\alpha_i=0}}{A_{\alpha_i=0.5\pi}}$, $[-]$

n: superelliptic exponent $[-]$

m: particle mass $[kg]$

I: moment of inertia in the inertial coordinate system $[]$

ω: inertial system angular velocity $[rad/s]$

F: force $[N]$

T, T: torque $[Nm]$

$f'(t)$: time derivative (velocity)

$f(t)$: position

C: non-dimensional coefficient

A: area $[m^2]$

Re: Reynolds number $[-]$

f: correlation $[-]$

α_i: angle of incidence $[rad]$

x_{cp}: distance from centre of gravity to pressure centre $[m]$

θ: direction angle $[rad]$

References

Besnard, D., Harlow, F. (1986): Nonspherical particles in two-phase flow. International Journal of Multiphase Flow 12(6), pp.891-912

Brauer, H. (1971): Grundlagen der Einphasen und Mehrphasenstromungen. Verlag Sauerlander Aarau, Switzerland. (in German)

Hein, P. (1964): The superellipse - a simple solution to an ordinary problem. Dansk Kunsthaandvaerk 37(4), pp97-112. (In Danish)

Horner, S. F. (1965): Fluid-dynamic drag - theoretical, experimental and statistical information. Published by the author

Kunii, D., Levenspiel, O. (1969): Fluidization Engineering Krieger Publishing Company, Florida, USA

Rosendahl L., Condra, T. (1996): A new basis for the formulation of the dispersed phase in gas-particle systems. 19th ICTAM Congress, Kyoto, Japan. August 1996

Nonlocal plasticity and continuum damage at shear band formation in soil slope

LENA STRÖMBERG

Dep. of Solid Mechanics and Materials Engineering
University of Lund, Box 118, S-221 00 Lund, Sweden

Material model

A decoupled nonlocal plasticity and damage model is proposed. Damage is represented by a scalar field that reduces the mean stress and is assumed to depend on a portion of the mean strain energy when this is positive, in accordance with Simo and Ju (1987). The plasticity model consists of a modified Drucker-Prager yield function with local hardening nonlocal softening as proposed by Strömberg and Ristinmaa (1996). From the assumption of nonlocal softening, a material length scale enters the constitutive equations.

The resulting equations are analysed for uniaxial compression, and the local version allows for the derivation of a stress-strain relation, cf. Figure 1.
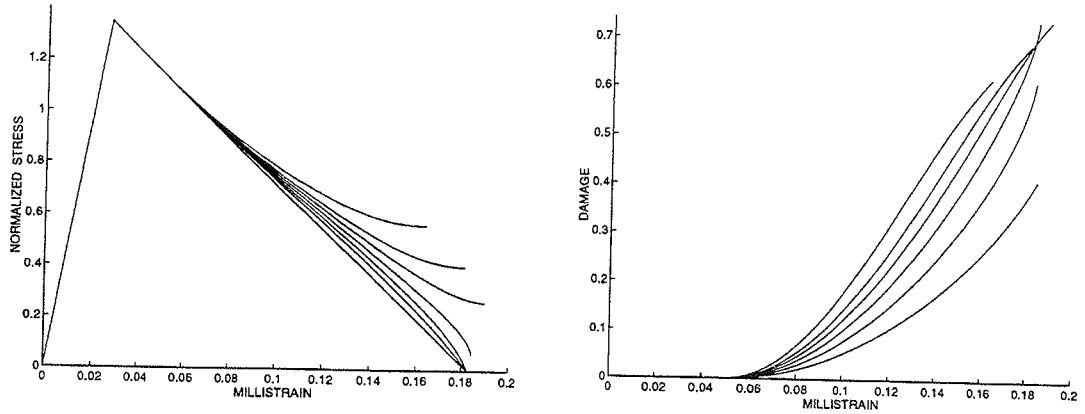
(a) Stress versus millistrain, for $c =$ 2, 1.5, 1.25, 1, 0.75, 0.5, 10^{-6} Pa^{-1} from top.

(b) Damage versus millistrain for $c =$ 2, 1.5, 1.25, 1, 0.75, 0.5, 10^{-6} Pa^{-1} from top.

Figure 1: Material parameters $h/G = -0.24$, $\nu = 0.25$ and different damage parameters c.

Finite element formulation

In order to simulate shear band formation in plane strain, a finite element model is implemented in the code CALFEM given as a toolbox in MATLAB(R). The solution strategy is split into a displacement estimate for equilibrium and the integration of constitutive equations. The consistency condition will result in a matrix equation for determination of the field of plastic multipliers. An iteration algorithm taken from Strömberg and Ristinmaa (1996) is used for finding the solution. When the displacement estimate and the plastic multiplier are given, the state of damage is determined.

Results

The model is applied to a slope loaded by gravity, also considered in Ortiz *et al.* (1984), Pamin and deBorst (1995). In the slope, damage and nonlocal plasticity interact to redistribute the displacement field to become localized in a shear band of a certain width, dependent of the material length scale, denoted by l, cf Figure 2, 3. The direction of the shear band depend on damage. In the shear band, damage is distributed, however more localized than the effective plastic strain. The shear band formation will cause instability in the global force-displacement relation and a parameter study shows the influence of damage and nonlocal plasticity.
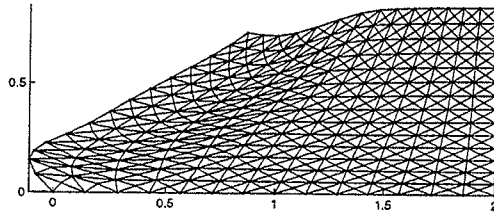
(a) Deformed mesh 14×14, $l = 0.17m$, magnification factor: 2000.
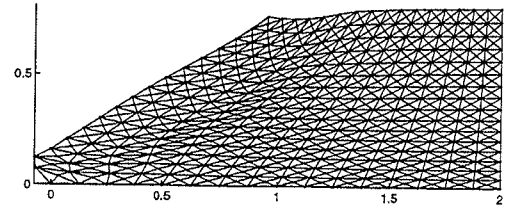
(b) Deformed mesh 16×16, $l = 0.083m$, magnification factor: 2500.

Figure 2: Material parameters $h/E = -0.08$ and $(c = 0.5 \ Pa^{-1}, \ s = 0)$.
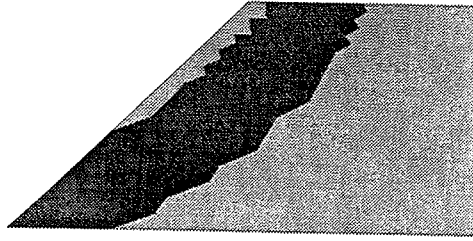
(a) $h/E = -0.08$, $l = 0.17m$,
$c = 0.5\ Pa^{-1}$, $s = 0$.
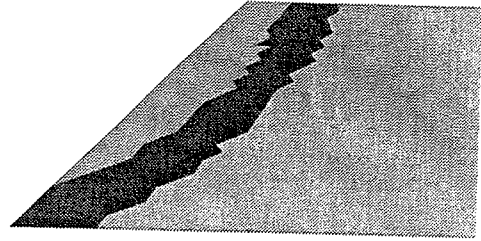
(b) $h/E = -0.08$, $l = 0.083m$,
$c = 0.5\ Pa^{-1}$, $s = 0$.
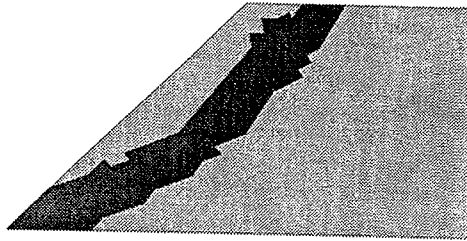
(c) $h/E = -0.08$, $l = 0.083m$,
$c = 1\ Pa^{-1}$, $s = 0$.

Figure 3: Plastic elements, variation of l and c.

References

CALFEM, Div. of Structural Mechanics and Div. of Solid Mechanics, LUND
http://hult.byggmek.lth.se/Calfem/calfem.html

Ortiz, M., Leroy, Y., and Needleman, A. (1987). A finite element method for localized failure analysis. *Comp. Meth. in App. Mech. and Engrg.* 61, pp 189-214.

Pamin J. and deBorst R, (1995) Numerical simulation of localization phenomena using gradient plasticity and finite elements, *HERON*, editor A.C.W.M. Vrouwenvelder, Stevinweg 1, P.O. Box 5048, 2600 GA Delft, The Netherlands, Vol 40, No 1

Simo J.C. and Ju J.W, (1987) Strain- and stress-based continuum damage models-I. formulation, *Int. J. Solids Structures*, Vol 23, No7.

Strömberg L and Ristinmaa M. (1996) FE-formulation of a nonlocal plasticity theory, *Comp. Meth. in App. Mech. and Engrg*, 136, pp. 127-144.

71

LOCALIZATION IN DRAINED AND UNDRAINED FRICTIONAL MATERIAL

J. LARSSON and R. LARSSON

Department of Structural Mechanics, Chalmers University of Technology, S-412 96 Göteborg

INTRODUCTION

A characteristic feature of most failures in geomaterials is the localization of deformations into narrow band zones. In this contribution a FE-method to capture localization at undrained conditions is discussed. The model is based on the concept of regularized displacement discontinuities which are embedded within the finite elements. The discontinuities are considered as strain enhancements according to the enhanced strain approach, Simo and Rifai [1]. Conditions for onset of localization as well the critical bifurcation directions are provided from bifurcation analysis of the constitutive equation, Runesson et al. [2]. The material is modeled on mixture theory for the solid and the fluid phase. The solid phase (soil skeleton) is assumed elastic-plastic based on a generalized Mohr-Coulomb criterion, cf. Larsson and Runesson [3]. Numerical results will be presented for a rectangular specimen of cohesive-frictional material. In particular, we are concerned with the issue of mesh objectivity and influence of the undrained condition.

ELEMENT EMBEDDED LOCALIZATION BAND IN UNDRAINED SOIL

In the spirit of the developments in Larsson et al. [4], let us briefly review the basic concepts of the embedded localization band as follows: Upon introducing a narrow band zone Ω_{be} (of width δ), the strain field within an element is expressed in terms of a compatible and an enhanced (incompatible) portion $\tilde{\varepsilon}$ defined as

$$\varepsilon = \varepsilon_c + \tilde{\varepsilon} \quad , \quad \varepsilon_c = (\nabla_x \otimes u)^{sym} \quad , \quad \tilde{\varepsilon} = \tilde{\varepsilon}_c + \frac{1}{\delta}f(n)(n \otimes [\![\tilde{u}]\!])^{sym} \tag{1}$$

Here, the irregular "block" function $f(n)$, shown in Figure 1, represents the consequent regularization of the strain due to a discontinuous displacement field constructed as $u = u_c + H(x)[\![u]\!]$, where H is the Heaviside function, cf. Larsson et al. [4]. Moreover, the matching pore pressure field is introduced in a similar fashion as the strain field, i.e.

$$p = p_c + \tilde{p} \quad , \quad \tilde{p} = \tilde{p}_c + f(n)[\![\tilde{p}]\!] \tag{2}$$

where $[\![\tilde{p}]\!]$ is the pore pressure discontinuity.

For each element, the continuous part of the pressure, the displacement and the corresponding compatible strain are interpolated by using the standard compatible shape functions ψ^I, which gives
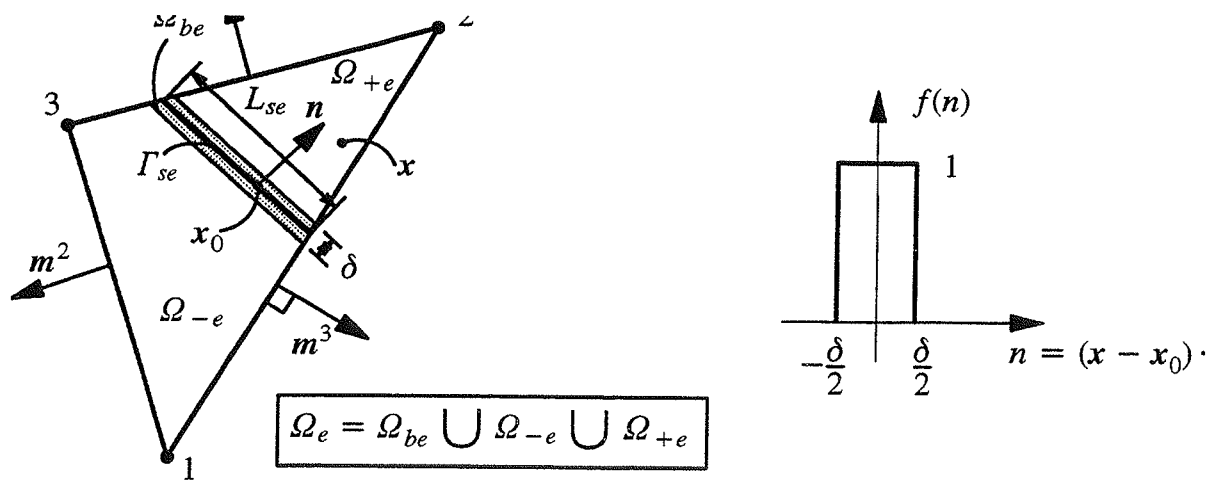
Figure 1. Enhanced CST-element with embedded localization band and the "block" function $f(n)$.

$$u = \sum_{I=1}^{NODEL} \psi^I(x)\, u_e^I \quad, \quad \varepsilon_{ce} = (\nabla_x \otimes u)^{sym} = \sum_{I=1}^{NODEL} (u_e^I \otimes m^I)^{sym} \quad, \quad p_{ce} = p_e$$

where $NODEL$ is the number of element nodes and m^I is the gradient of each shape funct ψ^I, i.e. we have $m^I = \nabla_x \psi^I$.

Let us next restrict to the case of piecewise linear approximation for the displacement, co sponding to the CST−element. Hence, the (independent) total stresses τ and the enhan strains $\tilde{\varepsilon}$ are chosen as piecewise constant functions (within each Ω_e) such that

$$\tau = \sum_{e=1}^{NEL} \chi_e \tau_e \quad, \quad \tilde{\varepsilon}_c = \sum_{e=1}^{NEL} \chi_e \tilde{\varepsilon}_{ce} \quad, \quad [\![\tilde{u}]\!] = \sum_{e=1}^{NEL} \chi_e [\![\tilde{u}]\!]_e$$

where χ_e is defined as

$$\chi_e = \begin{cases} 1 & iff\ x \in \Omega_e \\ 0 & otherwise \end{cases}$$

Due to momentum balance, we obtain the "orthogonality" conditions pertinent to the hanced assumed strain approach, Simo and Rifai [1], as follows

$$\int_{\Omega_e} \tau_e' : \tilde{\varepsilon}_e'\, d\Omega \equiv 0 \quad e = 1, ..., NEL$$

$$\int_{\Omega_e} \tilde{\varepsilon}_e' : (\sigma(\varepsilon_e) - p_e \delta) d\Omega = 0 \quad e = 1, ..., NEL$$

where n is the spatially constant unit normal vector of the localization band, as depicted in F ure 1. In (6)$_2$, σ is the solid (in geomechanics often referred to as effective) stress tensor t is obtained in terms of the strain via the constitutive relation.

74

$$\gamma_v = \sum_{e=1}^{NEL} \chi_e \gamma_{ve}, \quad \tilde{p}_c = \sum_{e=1}^{NEL} \chi_e \tilde{p}_{ce}, \quad [\![\tilde{p}]\!] = \sum_{e=1}^{NEL} \chi_e [\![\tilde{p}]\!]_e \tag{7}$$

where γ_v is the (independent) total volumetric strain. Due to mass conservation of the fluid phase, we then obtain the integrated (orthogonal) balance equations

$$\int_{\Omega_e} \gamma'_{ve}\, \tilde{p}'_e d\Omega \equiv 0 \quad e = 1,...,NEL$$

$$\int_{\Omega_e} \tilde{p}'_e \left(\Delta\varepsilon_{ev} + \frac{1}{K^f}\Delta p_e \right) d\Omega = 0 \quad e = 1,...,NEL \tag{8}$$

Here K^f is the bulk modulus of the fluid and ε_v is the volumetric strain of the solid phase.

We note that the orthogonality conditions $(6)_1$ and $(8)_1$ must hold for arbitrary constant τ'_e and γ'_{ve} in each element. In addition, if n is considered constant, the integration of these conditions can be carried out explicitly. Combining these with $(6)_2$ and $(8)_2$, while observing that σ takes the constant values $\sigma_\pm$ and σ_b in $\Omega_{\pm e}$ and in Ω_{be}, respectively, we obtain the continuity relationships

$$\left.\begin{array}{ll}
\dfrac{A_e}{l_e}\left(1 - \dfrac{\delta}{l_e} \right)\left[-n \cdot \sigma_{\pm e} + n \cdot \sigma_{be} - n[\![\tilde{p}]\!]_e \right] = 0 & e = 1,2...NEL \\[3mm]
\dfrac{A_e}{l_e}\left(1 - \dfrac{\delta}{l_e} \right)\left[\dfrac{1}{\delta}n \cdot \Delta[\![\tilde{u}]\!]_e + \dfrac{1}{K^f}\Delta[\![\tilde{p}]\!]_e \right] = 0 & e = 1,2...NEL
\end{array}\right\} \tag{9}$$

where $l_e = A_e/L_e$, $A_e = m(\Omega_e)$ and $L_e = m(\Gamma_e)$. In $(9)_1$ we may eliminate the pressure discontinuity to obtain the combined traction−mass continuity relation

$$r_e = \frac{A_e}{l_e}\left(1 - \frac{\delta}{l_e} \right)\left[-n \cdot \sigma_{\pm e} + n \cdot \sigma_{be} + \frac{1}{\delta}K^f(n \otimes n) \cdot \Delta[\![\tilde{u}]\!]_e - n^{\,n}[\![\tilde{p}]\!]_e \right] = 0 \tag{10}$$

Remark: By considering the rate form of (10) within the plasticity framework and the loading assumption that the whole element responds plastically, we obtain the bifurcation problem

$$\frac{1}{\delta}Q^{u,ep} \cdot [\![\dot{u}]\!] = 0, \quad Q^{u,ep} = n \cdot D^{ep} \cdot n + K^f(n \otimes n) \tag{11}$$

where D^{ep} is the CTS-tensor. This is precisely the proper localization condition for a mixed continuum with a compressible pore fluid. We thus conclude that localization is possible when the undrained acoustic tensor $Q^{u,ep}$ is singular. From (11) we may obtain the critical orientation $n = n^{cr}$ corresponding to the critical hardening modulus, cf. the analytical investigation in Runesson et al. [2] ∎

75

The finite element discretized problem is solved by evaluating the local traction contin problems $r_e = 0$, $e = 1,\ldots,NEL$ completely for each global iterate i. Hence, a displacem format is obtained at the global level, which may be stated as: For a given iterate i, comp an improved solution from $u_e^{(i+1)} = u_e^{(i)} + \xi_e$ where ξ_e is solved from

$$\mathop{\mathbf{A}}_{e=1}^{NEL} \left[\hat{K}_e \xi_e = -g_e^{(i)} \right]$$

(

where $\hat{K}_e$ is the part inverted element tangent stiffness matrix at $\Delta[\![\bar{u}]\!]_e$ and $[\![\bar{p}]\!]_e$.

SOLUTION OF THE LOCAL TRACTION CONTINUITY PROBLEM

As alluded to in the previous section, the traction continuity relation (10) is evaluated cc pletely in all elements for each global iteration. At first thought, this might be considered co as compared to partial inversion of the iterative improvements of the discontinuities for total system. However in the latter situation, a loading assumption must be applied to the ements, which can only be checked after convergence of the global iterations. This probler particularly delicate in the case of ductile failure, where onset of localization is reached ai a certain amount of plastic deformation. With the adopted procedure, we thus maintain c trol of the loading situation within each element throughout the analysis. For example, an element may localize at a certain load level, in the sense that elastic loading is obtained in Ω and plastic loading take place in Ω_{be}. At the next load level, the element may become diff corresponding to plastic loading in the whole element.

A problem closely connected to the local element problem is how to choose the vector n wh defines the orientation of the band. As mentioned above the band orientation is defined $n = n^{cr}$ at onset of localization, and it is thereafter held fixed. In general however, this dir tion is not unique. In the plane case there are two equally possible critical directions. In numerical treatment however, we must at some point choose one of these orientations. For t purpose, a procedure where we try to maximize the plastic dissipation is suggested. The inf ence of various choices of n of the global response and deformation mode is investigated i merically.

REFERENCES

[1]   J. C. Simo and M. S. Rifai. A class of mixed assumed strain methods and the method of incompati modes. *Int. J. Num. Meth. Eng.*, **29** pp. 1595–1638 (1990).

[2]   K. Runesson, D. Peric and S. Sture. Effect of pore fluid compressibility on localization in elastic-pla porous solids under undrained conditions. *Int. J. Solids Structures*, **33**, pp. 1501–1518 (1996).

[3]   R. Larsson and K. Runesson. Implicit integration and consistent linearization for yield criteria of Mohr-Coulomb type. *Mechanics of Cohesive-Frictional Materials*, **1**, pp. 1–17 (1996).

[4]   R. Larsson, K. Runesson and S. Sture. Embedded localization band in undrained soil based on regul ized strong discontinuity – theory and FE-analysis. *Int. J. Solids Structures*, **33**, pp. 3081–3101, (199

Robert Tano, Marek Klisinski

Division of Structural Mechanics
Luleå University of Technology, S-971 87 Luleå, Sweden
E-mail : Robert.Tano@ce.luth.se

Abstract

The inner softening band concept is based on simple assumptions which have proved to be able to capture various types of failure mechanisms that occur in concrete, rocks and soils. Most problems can successfully be modelled by using a crack function governed by the strength of the material and a linear softening law for the band tractions and displacements. The extra parameters that have to be defined are those that describe the softening function. However, by invoking the fracture energy some reasonable values are easily found. A large number of numerical results and comparisons with experiments show that the method can deal with the major part of failure types in brittle materials.

Introduction

The approach of using interelement displacement discontinuities based upon a relationship between increments of band tractions and displacements, the fictitious crack model (Hillerborg et al 1976), has been used by Dvorkin et al 1990, Klisinski et al 1991 and Lotfi & Sheng 1995. The inner softening band method (ISB), Klisinski et.al 1991, has successfully been implemented and tested versus experimental data for concrete structures. Such tests mainly deal with mode I fracture and are therefore simple to carry out in comparison with problems that include large stress rotations, e.g. in soil stability analysis. By introduction of the possibility for each element to contain several active cracks, stress locking situations are avoided and hence the ISB-method performs better.

Basic concepts

For a more detailed description of the method, see Klisinski et al 1995, Klisinski & Tano 1995. The total rate of nodal displacements is divided into a continuous part and one part that is due to band opening. Since the discontinuous contribution is dependent on the continuous deformation the following relation can be obtained for a single fixed crack

$$du = du^c + du^b = (I + G) \, du^c$$

or for multiple fixed cracks

$$du = (I + \sum G) \, du^c$$

where I is the unity matrix and G is a product of matrices containing shape functions, trans-

lations all lead to the following constitutive relation between rates of tractions and displacements in the band

$$dv = \frac{1}{A+B} m \Phi^T dt$$

where A is a non-zero scalar for kinematic softening, B is non-zero for isotropic softening, m is the local direction of the band opening and Φ contains derivatives of the fracture function with respect to the tractions. State changes such as cracking, unloading and reloading are limited to just one at each increment in order to avoid convergence difficulties. If many cracks indicate the change of state during an increment the size of the increment is reduced. Most cal culations have been performed under displacement control but arc-length control is sometimes necessary, e.g. for the snap-back behaviour in the four-point-shear beam test, Fig. 4.

Numerical results

Slope stability with concentrated load

Three different meshes were tested in this problem. For the finest mesh two active bands could develop which might lead to the somewhat weaker response. Displacement control, linear kinematic softening, the Mohr-Coulomb's fracture criterion and constant strain triangles (CST) were used.
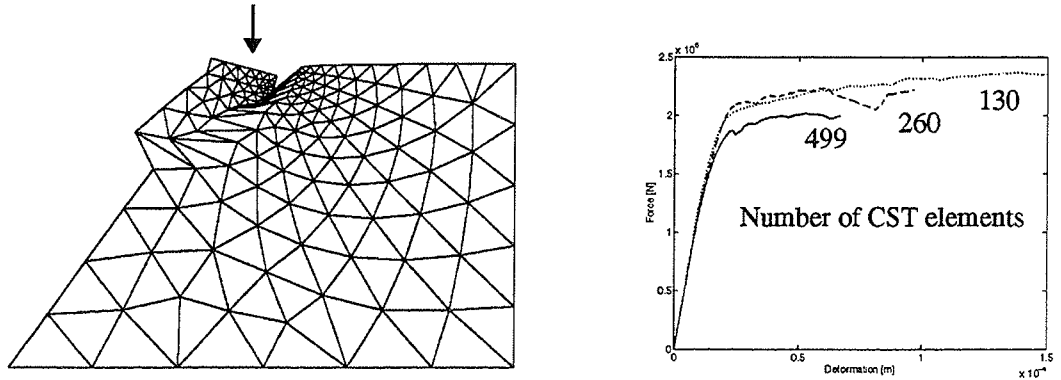
Figure 1. Displacement controlled slope stability analysis. The right figure shows responses for three different meshes.

Slope stability with density load

Two different types of loading paths were tested for the 100-m-high vertical slope. The first model has a free vertical slope while the density increases, Fig.2, and the second model has supports outside the slope until the material density is reached, Fig.3. After that the supports are gradually removed in order to model a true excavation.
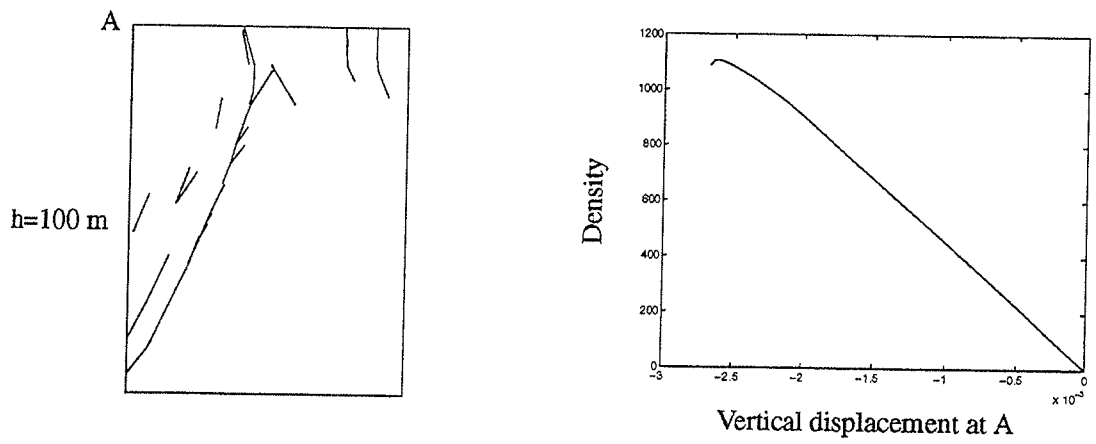
Figure 2. Crack pattern and density-displacement diagram for vertical slope stability.
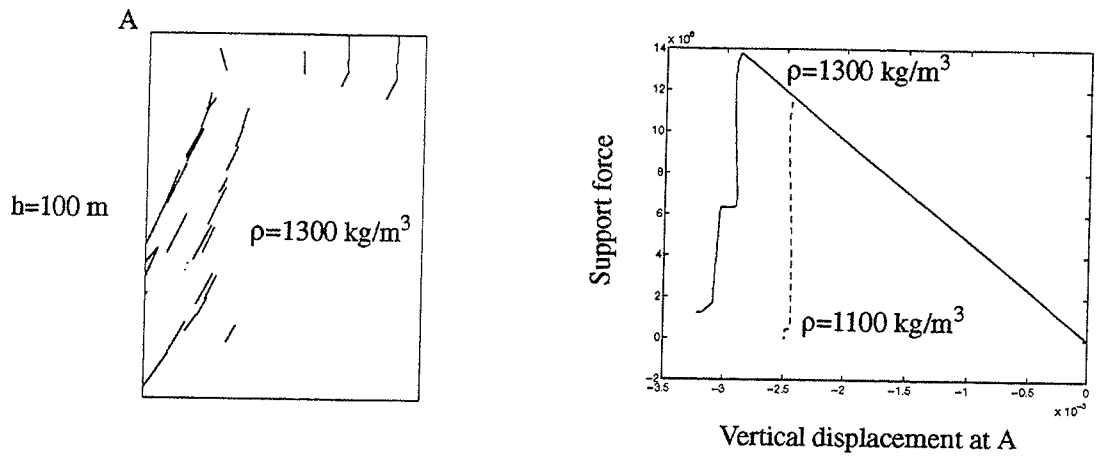
Figure 3. Crack pattern and total force from the gradually removed supports.

Four-point-shear beam

This test is interesting since it involves snap-back behaviour.
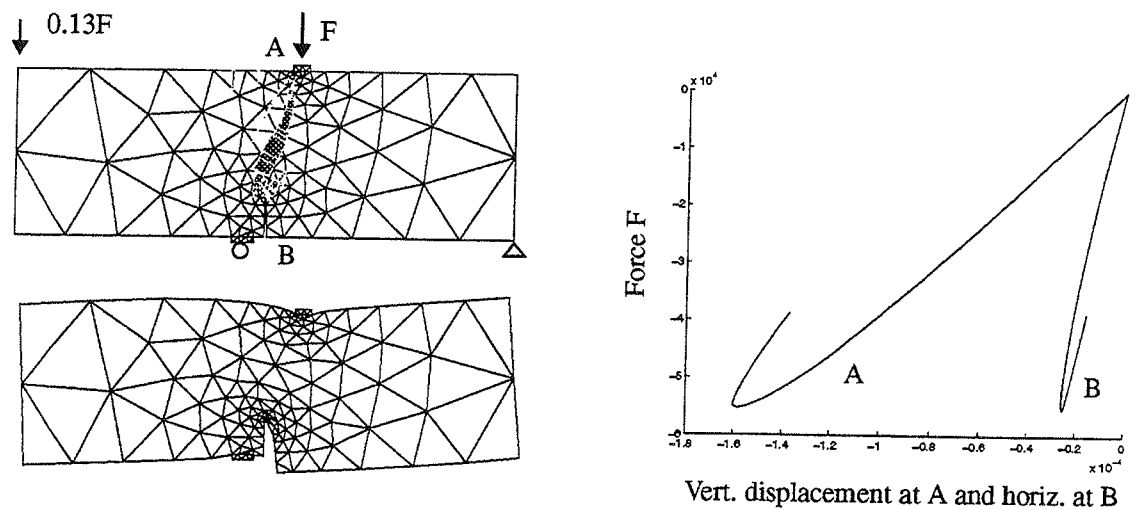
Figure 4. Crack pattern, deformations and load-displacement diagram for the four-point-shear beam test.

Anchor pull-out tests & mixed mode fracture, Olofsson & Ohlsson 1995. Cylinder splitting pressure tests, Noghabai 1995. There is also ongoing research on fiber reinforced beams.

References

Hillerborg, A., Modeer, M., Petersson, P-E. Analysis of crack formation and crack growth in concrete by means of fracture mechanics and finite elements. Cement and Concrete Research 6, 773-782, 1976.

Klisinski, M., Olofsson, T., Tano, R. Mixed mode cracking of concrete modelled by inner softening band. In: D.R.J. Owen, E. Oñate & E. Hinton, editors, Computational Plasticity, 1595-1606, Pineridge Press Ltd., Swansea, 1995.

Klisinski, M., Tano, R. Crack modelling with inner softening band. NSCM - 8th Nordic Seminar on Computational Mechanics. November 16-18, 1995, Göteborg, Sweden.

Noghabai, K. Splitting of concrete in the anchoring zone of deformed bars. Licentiate thesis, Luleå University of Technology, ISSN 0208-8242, Luleå, Sweden, 1995.

Ohlsson, U. Fracture mechanics analysis of concrete structures. Doctoral thesis, Luleå University of Technology, ISSN 0348-8373, Luleå, Sweden, 1995.

CONVEX APPROXIMATION METHODS FOR LARGE SCALE STRUCTURAL PROBLEMS

Pierre DUYSINX

*Department of Mathematics, Technical University of Denmark,
2800 Lyngby, Denmark*

October 2, 1996

Abstract

KEY WORDS: topology optimization; dual methods; convex approximations; CONLIN; generalised MMA; quasi-Newton method;

1 INTRODUCTION

As a result of several researches (e.g.[6, 9, 8, 12]), structural optimization problems with sizing or shape design variables can be solved efficiently by the mathematical programming approach and real-life applications can be handled. With the *homogenization method* proposed by Bendsøe and Kikuchi [2] and then further developed in several other works (see Bendsøe [1] for a review), structural optimization is now able to attack the topology design problem.

Despite the fact that the material distribution problem looks like a sizing optimization, topology problems have its own characteristics and difficulties. The discretization of the material density introduces generally between 1000 and 10000 design variables, number that was never reached before. Furthermore, solving topology problems requires often a very high number of iterations to get a stationary distribution. It is usual to spend more than 100 iterations to solve the topology problem.

Up to now, few solvers for huge optimization problems, other than simple optimality criteria, were available in topology. Thus, topology design was often restricted to formulations involving few design constraints. Generally, the topology design was formulated as a minimum problem of a stiffness criterion, like the compliance, with a bound over the volume.

This communication wants to report how we improve the solution procedure of optimization of topology huge size problem by extending the mathematical programming approach that was successful for other structural optimization problems. At first we use dual methods that are well adapted to solve the convex separable optimization problems even if the number of design variables is large. On another hand, we look at the problem of selecting the most appropriate approximations. The choice of an approximation is a compromise between

precision and conservativity, between accuracy and computation effort to generate the data. After having compared available first order approximations, we wanted to further reduce the number of stages necessary to arrive to the solution. To this end, we developed and validated a new approximation procedure based on second order approximations and quasi-Newton updates preserving the diagonal structure of the estimates.

2   A DUAL SOLVER

Solution of convex subproblems of sizing and shape problems can be performed efficiently by dual methods [5, 8]. This is more than ever true with the subproblems of topology design. The primal constrained problem with a large number of design variables is replaced by a quasi unconstrained maximisation of the dual function. The dimension of the dual space is limited to the number of active constraints, which is small. The advantage of the dual formulation is real if the relationships between primal and dual variables are rigorous and inexpensive to compute. This is the case if the objective function and the constraints are linearised by *separable* and *convex* approximations.

3   CONVEX APPROXIMATIONS

3.1   FIRST ORDER CONVEX APPROXIMATIONS

The simplest first order approximation is the first order Taylor expansion. This linear approximation is efficient for the volume constraint, but its lack of convexity makes it too few reliable for structural constraints. For structural responses, it is better to turn our choice towards convex approximations. From our experiences, CONLIN [9] approximation gives rise to good results in topology. For the compliances that are self-adjoint, all the derivatives are negative and CONLIN restores the reciprocal design variables expansion that is well known to reduce the non-linearity of the structural responses. But convexity properties of CONLIN are important when treating eigenfrequencies or constraints whose first derivatives have mixed signs. The main disadvantage of CONLIN is that the approximation introduces fixed curvatures, so that the approximation might be too much or too few convex. This might give rise to a slow or unstable convergence towards the optimum. To remedy to this problem, we select MMA [12] approximation that generalises and improves CONLIN by introducing two sets of asymptotes. The choice of the moving asymptotes provides the way to modify the curvature and to fit better to the characteristics of the problem.

Nevertheless, we can conclude that both CONLIN and MMA lead to satisfactory results for topology design and improve often greatly the performances of the solution. In a lot problems, we observed that a solution was often achieved in 30 to 50 iterations depending on the difficulty of the problem and the precision of the stopping criterion. One strong advantage of CONLIN and MMA arises from the very reliable dual solvers that are used to solve the associated convex subproblems. On another hand, one major drawback of first order approximations is that we can observe a deceleration of the progression towards the optimum once the algorithm arrives in the neighbourhood of the optimum.

To accelerate the convergence rate in the final stage, one needs better approximations based on curvature information [7].

3.2 SECOND ORDER CONVEX APPROXIMATIONS

Second order are high quality approximations that are indeed more precise and that lead to faster convergence rates. Nevertheless, second order sensitivity is very onerous to compute and to store so that the overall cost of the optimization can be similar to the one of first order approximations [10]. The problem becomes quickly cumbersome and impossible to manage when the size of the problem increases.

To be able to use second order approximation schemes with large scale optimization problems, we developed a new procedure to generate an estimation of the curvature information with a small computation cost [3, 4]. As separable approximations needs only diagonal second derivatives, the idea is to built an estimation of the curvature information with a quasi-Newton update able to preserve diagonal structure of the Hessian estimates. This update scheme is derived form the general theory of quasi-Newton update with sparse Hessian estimates made by Thapa [13]. The diagonal version of the BFGS update [3, 4] that we implemented is very un-expensive even for large scale problems since it introduces only vectors manipulations. In [3], it was observed that for a given topology problem, the time spent in the diagonal BFGS update is only 3 % of the time spent in the optimizer CONLIN [6, 8] and only 0.01 % of the time needed for sensitivity analysis with a commercial finite element package.

The theoretical algorithms was adapted to the characteristics of structural optimization problems to yield quickly convergent estimates of the Hessian. This adaption relies on the key role of the reciprocal design variables to reduce the non-linearity of the structural responses. The Hessian is updated in the space of reciprocal design variables and then converted into curvatures in terms of the direct variables to be used in the approximation. The initial guess of the Hessian is also very important. Starting in the reciprocal design space from a diagonal matrix of small terms restores the curvatures of CONLIN which is generally a good starting point.

This second order information is introduced into two well known second order approximations. The first one is a second order version of MMA proposed by Smaoui et al. [11]. The second approximation is the separable quadratic approximation suggested by Fleury [7]. Combining diagonal BFGS update with both these approximations gives very interesting results that results in important savings in terms of number of iterations and of computation time. This conclusion can be explained as follow. Firstly, the estimation of the curvature improves greatly the quality of the approximation with only the help of the accumulated first order information. Secondly, instead of ignoring the second order coupling terms, diagonal BFGS provides a way to take them into account by correction terms on the diagonal coming from the diagonal update. Due to our initial guess of the Hessian, one can observe, in the first iterations, a convergence history that is very similar to first order approximations. But after some iterations, the update procedure improves the estimation of the Hessian and one can see a real advantage in the convergence speed. Around an accumulation point satisfying the optimality conditions, we could observe a convergence speed superior to first order methods, sometimes closed from super-linear behaviour.

References

[1] M. Bendsøe. *Optimization of Structural Topology, Shape and Material.* Springer Verlag, Heidelberg, 1995.

[2] M. P. Bendsøe and N. Kikuchi. Generating optimal topologies in structural design using a homogenization method. *Computer Methods in Applied Mechanics and Engineering*, 71:197–224, 1988.

[3] P. Duysinx. *Optimisation Topologique : du Milieu Continu à la Structure Elastique.* PhD thesis, Institut de Mécanique, Université de Liège, Belgium, February 1996. (in French).

[4] P. Duysinx, W. Zhang, C. Fleury, V. Nguyen, and S. Haubruge. A new separable approximation scheme for topological; problems and optimization problems characterized by a large number of design variables. In G. Rozvany and N. Olhoff, editors, *First World Congress of Structural and Multidisciplinary Optimization*, pages 1–8, 1995.

[5] C. Fleury. Structural weight optimization by dual methods of convex programming. *International Journal of Numerical Methods in Engineering*, 14:1761–1783, 1979.

[6] C. Fleury. CONLIN: an efficient dual optimizer based on convex approximation concepts. *Structural Optimization*, 1:81–89, 1989.

[7] C. Fleury. Efficient approximation concepts using second order information. *International Journal for Numerical Methods in Engineering*, 28:2041–2058, 1989.

[8] C. Fleury. *Mathematical Programming Methods for Constrained Optimization: Dual Methods*, volume 150 of *Progress in Astronautics and Aeronautics*, chapter 7, pages 123–150. AIAA, 1993.

[9] C. Fleury and V. Braibant. Structural optimization: a new dual method using mixed variables. *International Journal for Numerical Methods in Engineering*, 23:409–428, 1986.

[10] H. Mlejnek, U. Jehle, and R. Schirrmacher. Second order approximations in structural genesis and shape finding. *International Journal of Numerical Methods in Engineering*, 34:853–872, 1992.

[11] H. Smaoui, C. Fleury, and L. Schmit. Advances in dual algorithms and convex approximations methods. In *AIAA/ASME/ASCE 29 Structures, Structural Dynamics and Material Conference*, pages 1339–1347, 1988.

[12] K. Svanberg. The method of moving asymptotes - a new method for structural optimization. *International Journal for Numerical Methods in Engineering*, 24:359–373, 1987.

[13] K. Thapa. *Optimization of Unconstrained Functions with Sparse Hessian Matrices.* PhD thesis, Stanford University, Department of Operations Research, 1981.

Reliability Analysis of a Midship Section

P. Friis Hansen

Department of Naval Architecture and Offshore Engineering,
Technical University of Denmark,   DK-2800 Lyngby.

1   Introduction

This extended abstract presents a reliability analysis of a midship section of a new double hull tanker design. The reliability analysis is performed with respect to ultimate bending failure of the midship section and addresses the effect of geometrical and material uncertainties as well as the ageing effect due to corrosion.

The yearly extreme value distribution of the combined still water and wave induced bending moment is calculated based on a simplified load combination procedure. Corrosion rates in different areas around the hull section are estimated based on available statistical data. Also the effect of coating durability is included in the analysis.

The ultimate load capacity of the midship section is calculated by use of an approximate beam-column method. The initial imperfections are for all panel elements modelled as independent identically distributed variables. One of the major complexities in the reliability analysis is to handle this large set of independent identically distributed variables as the optimisation performed under FORM/SORM may be jeopardised by their presence. A procedure based on order statistics is therefore applied to handle the set of identically distributed variables.

The vessel examined is a new double hull tanker with transverse-less system, Paik *et. al* [10]. Main particulars are: Length between perpendiculars is 234 m, breadth moulded 42.6 m, and depth moulded 19.2 m. The vessel has nine cargo oil tanks. The width of the double sides and the depth of the double bottom are both 2 m, which satisfies the OPA 90 and IMO requirements for oil pollution prevention. The analysed double hull tanker is assumed to be operating under 5 different loading conditions in a North-Atlantic routing.

Results from the analysis are presented in terms of the yearly failure probabilities over the lifetime of the vessel. Also the major uncertainties in the ultimate failure analysis of the midship section are identified. The reliability analysis was performed using the order statistical approach. The complete evaluation was very time consuming, and a model correction factor approach was used instead. The model correction factor method was found to be preferable in the reliability analysis of the midship section as this method predicted both reliability indices and importance factors with high accuracy at a fraction of time.

2 Extreme Vertical Bending Moment

The extreme value distribution of the wave-induced bending moment is established using technic given in [4] taking into account the manoeuvring philosophy. The extreme value distribution is each loading condition fitted to the Gamma distribution

$$F_{M_{wi}}(m_{wi}) = \frac{\gamma(\kappa, \lambda m_{wi})}{\Gamma(\kappa)}$$

where m_{wi} is the extreme wave induced moment in a voyage of duration τ. κ and λ are distribution parameters. It is assumed that each voyage of the ship last for one month. ' distribution function for the maximum sagging moment $m_{voy} = m_{sw} + m_{wi}$ within a voyage duration τ is given as the convolution of the densities of the still-water induced moment m_{sw} the wave-induced m_{wi},

$$F_{\max M_{voy}}(m_{voy}) = \int_0^\infty \frac{\lambda}{\Gamma(\kappa)}(\lambda x)^{\kappa-1}\exp(-\lambda x)\Phi\left(\frac{m_{voy} - x - \mu_{sw}}{\sigma_{sw}}\right)dx$$

in which $\Phi(\cdot)$ is the standard normal distribution function, μ_{sw} and σ_{sw} are the mean value the standard deviation of the still-water bending moment. $F_{M_{voy}}$ in Eq. 2 is defined for the sagg moment (maximum). A similar distribution is formulated for the minimal hogging (moment).

The yearly long term extreme value distribution for the maximum value (sagging) over voyages of the vessel is:

$$F_{\max(M)}(m) = \prod_{i=1}^{5}\{F_{\max M_{voy}}(m)\}_i^{NP_i}$$

In the probabilistic analysis, the extreme bending moment is multiplied with a model uncertai factor of mean value one and CoV=10% .

3 Corrosion

The single most important cause to failure of ship structures is possible due to corrosion. Fr survey reports of ships registered with Nippon Kaija Kyokai (reported in the period from 1976 1981) Akita [1, 2] observed that almost 80% of all failures in ships was due to corrosion. The ar where a double hull tanker may be particularly exposed to corrosion include the cargo tanks, 1 double-hull vertical wing spaces, and the double bottom. The cargo tanks will most likely o carry cargo oil throughout the ships service life, although designated cargo tanks may be used heavy weather ballast in emergency situations. The corrosion risk within these tanks is theref normally very low.

The applied probabilistic model for corrosion covers: the coating protection time (corros initiation period); the ageing effect; and the location dependent corrosion rates when coating longer offers successful protection. The corrosion wastage W as a function of time is modelled i

$$W(t) = Af(t)^B$$

in which A is the location dependent corrosion rate, $f(t)$ defines the corrosion time function, a B the ageing parameter. Basically, the corrosion time function $f(t)$ is the real time t minus t

corrosion initiation time t_0 but in the analysis modelled as a continuous differentiable function, see [7].

The corrosion initiation period t_0 is taken as log-normally distributed with a mean value of 5 years and a standard deviation of 3 years. This is in accordance with the DnV Guidelines for Corrosion [6]. The ageing parameter B is modelled as a common parameter for the entire hull with a mean value of 1.0 and a subjectively chosen COV of 10%. The corrosion rate A is taken to be log-normally distributed with mean value of twice the average mean rate given in [9] and a standard deviation equal to the reported average standard deviation.

4 Ultimate bending capacity of hull section

The factors determining the ultimate collapse capacity of the hull section are the material characteristics, the level of initial imperfections such as distortion and residual stresses, and the amount of corrosion.

The method used to calculate the bending strength of the hull section is described in Hansen [8]. The method divides the stress-strain curve of each beam into four regions: (1) a plastic tension region in which the material behaviour is assumed to be perfectly plastic, (2) a perfectly elastic tension region, (3) an elastic compression region, where the stress-strain curve is derived from a Bernoulli-Euler beam theory in connection with an effective width approach, and finally (4) a plastic compression unloading region, where the stress-strain curve is modelled by assuming that plastic hinges are formed.

Given the stress-strain relationship for all individual stiffened plate panels in the hull-section, the resulting bending moment M and the axial force N is calculated as a function of the vertical location of the neutral axis η and the curvature κ. The ultimate bending moment of the hull section is then obtained by solving the optimisation problem

$$\max \quad M(\eta, \kappa) \tag{5}$$
$$\text{s.t.} \quad N(\eta, \kappa) = 0 \tag{6}$$

in which η is the vertical location of the neutral axis, and κ the curvature.

The uncertainty modelling of the parameters describing the ultimate bending capacity is

Variable Name	Distribution
Yield stress	Log-Normal (314.0, Cov=7%)
Model uncertainty strength	Normal (1.0, Cov=7%)
Plate imperfections	Normal ($t/2$, Cov=20%)
Stiffener imperfections	Normal ($L/100$, Cov=20%)
η (in residual stress)	Normal (5.25, Cov = 12%)

5 Formulation of reliability analysis

The hull section consists of large plate structures which are stiffened by a relatively large number of longitudinal stiffeners. Traditionally, the load carrying capacity of the hull section is calculated by considering the capacity of the individual sub-elements built up of a stiffener and a part of the plating. The ultimate load capacity of these individual sub-elements are influenced by the level of initial imperfections such as distortion and residual stresses − at least as far as compression is

concerned. The presence of the correlated identical stiffeners jeopardises the optimisation perfor
under FORM/SORM, because the optimisation routine at a certain stage starts interchanging
location of the weakest stiffener, second weakest, third weakest, and so on. In this context *iden*
stiffeners means: (1) that the stiffeners have identical geometry, (2) that they have the same s
common material parameters, and (3) that they are subjected to the same strain. To overcome
problem the ultimate load capacity of the identical stiffeners have been be ordered as a functio
their initial imperfections using order statistics.

The conditional distribution function of the ultimate load capacity of the identical stiffen
conditioned on the common set of material parameters, must be provided to obtain the ord
set of the load capacity, and thereby the ordered set of initial imperfections. These conditic
distributions are mutually independent for the individual stiffeners.

The procedure formulated utilises the simplicity in standard reliability analysis of events in
evaluation of the reliability of a system consisting of correlated identical events will not be revie
here. The problem must, however be solved as a nested reliability problem. Reference is left to
for further description.

6 Model correction factor method

The procedure outlined in the previous section is very time consuming, and infeasible for n
practical purposes. The *model correction factor method* proposed in [3, 5] seems to be an attrac
alternative.

The idea behind the model correction factor method is to formulate a simplified structu
model – e.g. an ideal rigid-plastic yield hinge structural model – and then, in a probabilistic sei
perform a calibration of the simplified model to the complicated, but more realistic, model.
probabilistic calibration procedure assures that the simplified model is made "realistic" – at le
around the design point.

The model correction factor function $\nu(Z)$ assures that the relation

$$M_{real}(Z) = \nu(Z)M_{ideal}(Z)$$

holds everywhere. $M_{real}(Z)$ is the realistic moment and $M_{ideal}(Z)$ the simplified. It is evident t
the reliability analysis is unaffected of whether the left hand side or the right hand side of E
enters the analysis. $\nu(Z)$ is approximated by a zero or first order Taylor expansion with expans
point around the design point Z^* obtained using the ideal model. Within a few iterations
serie $\{Z^*\}$ of design points, obtained by consecutive reliability calculations using the ideal mo
in connection with the model correction factor, will converge.

The model correction factor approach was implemented within the reliability analysis progr
PROBAN [11], and Figure 2 shows a comparison of the reliability index calculated using the ex
model and the simplified fully plastic model multiplied with the model correction factor. The mo
correction factor $\nu(Z)$ was calculated based only on a zero order Taylor expansion. Only three
four iterations lead to the final design point. The stars represent the results of the realistic mo
and the solid line the result obtained from the model correction factor approach. It is seen t
the results from the two methods coincide perfectly.

Figure 3 shows a comparison of the corresponding importance factors obtained by the t
models. For simplicity the importance factors are lumped into variable groups of (1) a load
group, which covers uncertainty in wave loading and still water loading, and model uncertainty,
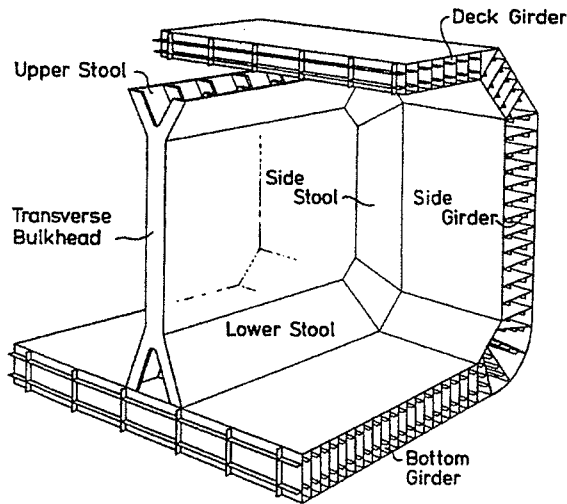
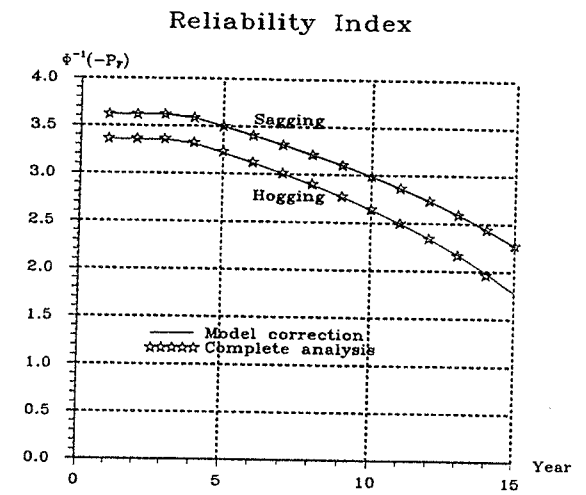Figure 1: *Structural outline of the examined vessel – from Paik et al. [10]*

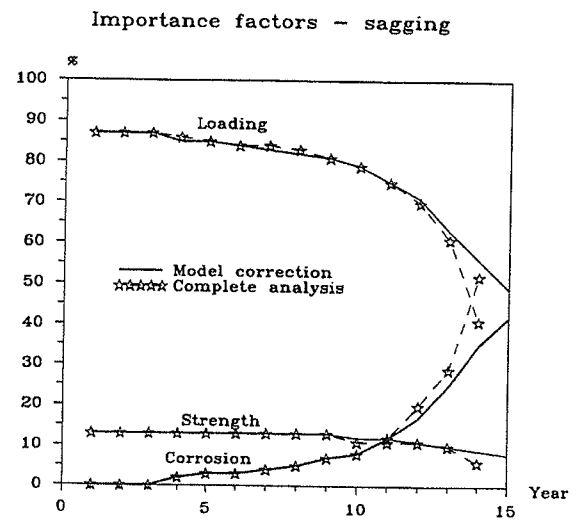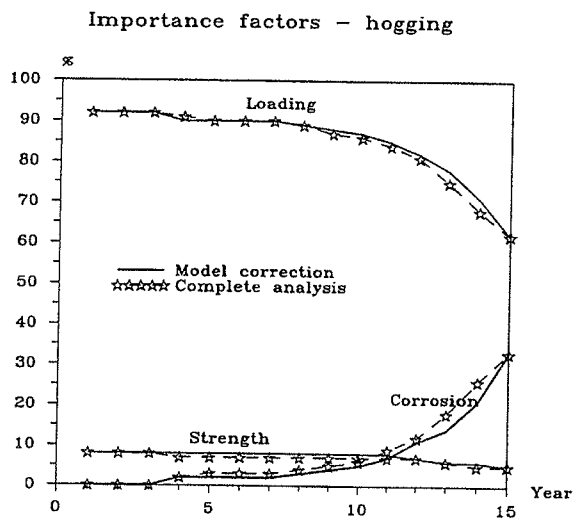Figure 2: *Variation of yearly reliability index with time*

Figure 3: *Variation of lumped importance factor with time*

a strength group of yield strength, imperfections, and model uncertainty of strength calculat and (3) a corrosion group, containing corrosion rates, ageing parameter, and corrosion initial time. It is seen that also the importance factors coincide satisfactory.

The CPU-time in obtaining the reliability index due to the realistic model was around se days compared to approximately one hour for the simplified model.

References

[1] Yoshio Akita. Reliability analysis of ship strength (first report). *Journal of SNAJ*, 155, J 1984.

[2] Yoshio Akita. Reliability analysis of ship strength (second report). *Journal of SNAJ*, 1 Dec. 1984.

[3] T. Arnbjerg-Nielsen. *Rigid-Ideal Plastic Model as a Reliability Analysis Tool for Ductile Str tures*. PhD thesis, Department of Structural Engineering, Technical University of Denma Lyngby, Denmark, 1991.

[4] E.H. Cramer and P. Friis Hansen. Stochastic modeling of the longterm wave induced respo of ship structures. *Marine Structures*, 7(6):537–566, 1994.

[5] O. Ditlevsen and T. Arnbjerg-Nielsen. Effectivity factor method in structural reliability. R. Rackwitch and P. Toft-Christensen, editors, *Reliability and Optimization of Structural S tems '91*. Lecture Notes in Engineering, Springer-Verlag, Berlin, November 1991.

[6] DSO-230. Guidelines for corrosion protection of ships. Technical report, Det Norske Verit Høvik, Oslo, 1992. Paper Series No: 92-P001.

[7] P. Friis Hansen. *Reliability Analysis of a Midship Section*. PhD thesis, Department of Oce Engineering, The Technical University of Denmark, Lyngby, January 1994.

[8] A. Melchior Hansen. Strength of structural systems. Technical report, Dept. of Ocean En neering, The Technical University of Denmark, 1993. SHIPREL – 2.4d – (5).

[9] R. Løseth, G. Sekkesætter, and S. Valsgård. Economics of high-tensile steel in ship hu *Marine Structures*, 7(1):31–50, 1994.

[10] J.K. Paik, D.H. Kim, H.S. Bong, M.S Kim, and S.K. Han. Deterministic and probabilis safety evaluation for a new double-hull tanker with transverseless system. In *SNAME Tra actions*, volume 100, pages 173–198, 1992.

[11] L. Tvedt. PROBAN-2 theory-manual. Technical report, Veritas Research, Høvik, Norw 1989.

Brittle Materials Using Weibull Statistics

by

Erik Lund
Institute of Mechanical Engineering, Aalborg University
Pontoppidanstraede 101, DK-9220 Aalborg East, DENMARK

1 Introduction

This paper is devoted to the problem of designing mechanical components made of brittle material such as ceramics by using Weibull statistics combined with finite element based shape optimization and mathematical programming. Such design optimization problems are rarely discussed but design with brittle materials calls for use of structural shape optimization as design with new materials very often cannot be based on design rules or engineering tradition. One of the few examples of using structural shape optimization in the design of ceramic components can be found in a very interesting paper by Koski & Silvennoinen (1990).

In the last decades there has been an increasing use of ceramic materials in mechanical enginering applications where good wear resistance properties, high hardness, sufficient high-temperature capability, high stiffness, and good corrosion resistance are needed. However, design with brittle materials is different from design with traditional ductile materials due to the brittle behaviour of ceramics.

The use of ceramic materials for load carrying components involves two basic features that must be taken into account in the design phase. First, even at high temperature, the material has very low strain tolerance and practically exhibits no yielding. Thus, the material behaviour is linearly elastic up to the fracture point where an unstable crack growth suddenly takes place. Second, there is frequently large scatter in the strength data so probabilistic methods must be used. A reliability evaluation based on a two-parameter Weibull distribution has been generally accepted in design of ceramics, see, e.g., McLean & Hartsock (1989). Weibull (1939) developed a probabilistic failure criterion based only on tensile stresses in the component. Compressive failure is not considered in this criterion because brittle materials usually fail from tensile stresses due to their very high compressive strength.

2 Analysis of Probability of Failure

The probability of failure is computed for a ceramic component from its stress field by using the weakest link theory based on the Weibull distribution, and for uniaxial stress, Weibull established the following function that describes the cumulative probability of failure P_f of a ceramic component

$$P_f = 1 - \exp\left[- \left(\frac{1}{m}!\right)^m \frac{1}{V_c} \int_V \left(\frac{\sigma}{\sigma_c}\right)^m dV \right] \tag{1}$$

teristic mean fracture stress associated with a characteristic reference volume V_c. V
total volume of the component and the term

$$\left(\frac{1}{m}!\right) = \Gamma\left(\frac{1}{m}+1\right) = \int_0^\infty t^{\frac{1}{m}}\exp\left[-t\right]\,dt$$

is the value of the gamma function Γ at $\frac{1}{m}+1$ which is easily evaluated.

In order to expand Eq. 1 to three-dimensional stress states, the concept of integr
the normal stress σ_n and the maximal shear stress τ around the portion of the unit r
sphere where the normal stress is positive is generally used, see, e.g., Evans (1978), Mc
& Hartsock (1989), Andreasen (1993a, 1993b), and Fig. 1.
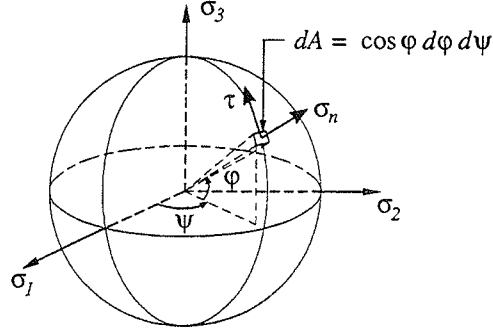
Figure 1: *Geometric variables describing location on the unit sphere.*

The normal stress and the maximal shear stress at a given location on the unit spher
given as

$$\sigma_n = \cos^2\phi\left(\sigma_1\cos^2\psi + \sigma_2\sin^2\psi\right) + \sigma_3\sin^2\phi$$

$$\tau = \sqrt{\cos^2\phi\left(\sigma_1^2\cos^2\psi + \sigma_2^2\sin^2\psi\right) + \sigma_3^2\sin^2\phi - \sigma_n^2}$$

An equivalent stress σ_e that is a function of σ_n and τ is introduced, i.e.

$$\sigma_e = \sigma_e\left(\sigma_n, \tau\right)$$

The combination of stresses causing failure is not uniquely determined due to a la
knowledge of the precise geometry of the actual flaws in the structure and a lack of
sensus regarding an appropriate crack extension criterion as stated by Andreasen (19
Therefore, different definitions of the equivalent stress can be chosen, depending or
wanted influence of shear stresses in the fracture criterion.

Thus, integrating this equivalent stress σ_e over the unit sphere with area A_{us}, the ge
equation for the probability of failure for a three-dimensional stress state is

$$P_f = 1 - \exp\left[-B\right]$$

where the exponent B, known as the risk of rupture, is given as

$$B = \left(\frac{1}{m}!\right)^m \frac{1}{V_c}\int_V\left[k\int_{A_{us}}\left(\frac{\sigma_e}{\sigma_c}\right)^m dA\right]dV$$

92

Facilities for computing the probability of failure of solid structural ceramic component discretized by the finite element method have been implemented in the general desig system ODESSY, see Lund (1995). This system has been developed at the Institut of Mechanical Engineering at Aalborg University, Denmark, and ODESSY has genera facilities for doing structural shape optimization, see Rasmussen, Lund & Olhoff (1993 and Lund (1994).

The direct differentiation approach has been used to derive expressions for design sensitiv ities of the probability of failure P_f, see Lund (1995), and it has thereby been possible t do shape optimization of structures with design criteria involving the probability of failure

3 Shape Optimization of Cutting Bit from a Circulai Saw Blade

An example of minimizing the probability of failure of a mechanical component made o: a brittle material is given in this section. The example deals with shape optimization of a cutting bit from a circular saw blade as illustrated in Fig. 2.

Circular Saw Blade (D = 150 mm)   Zoom on Cutting Bit
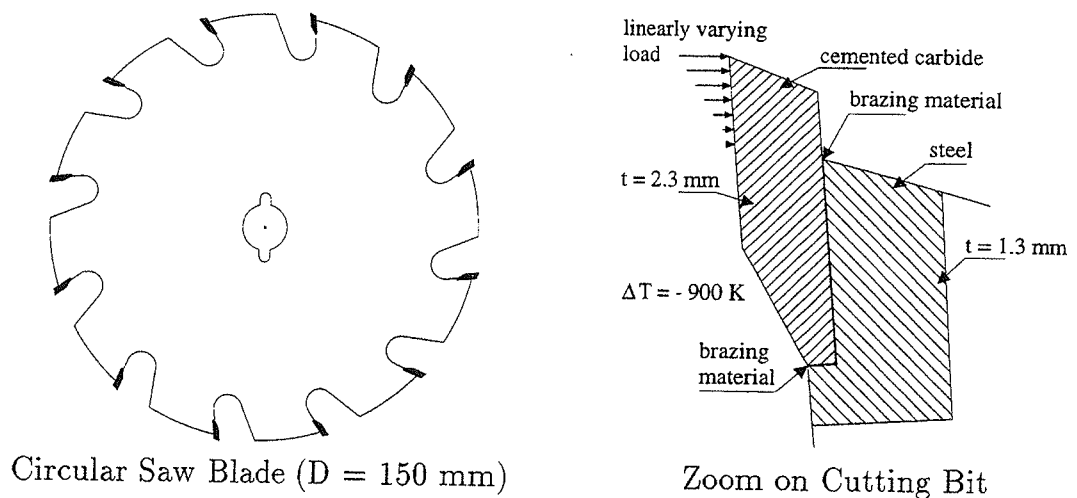
Figure 2: Cutting bit from a circular saw blade.

The saw blade is made of steel and the cutting bit of a cemented carbide. The cutting bit is brazed to the saw blade at a temperature of approximately 920°C and the structure is then cooled down. This process causes thermally induced stresses which are taken into account. Furthermore, a linearly varying load corresponding to a maximum loading situation is applied at the cutting bit. The cemented carbide has a characteristic mean fracture stress σ_c of 1300 MPa associated with a reference volume V_c of 13 mm^3 and Weibull modulus m of 11.

A 2D finite element model is used and the objective is to redesign the shape of the cutting bit such that the probability of failure in this maximum loading situation is minimized. The boundaries are described by quadratic B-splines having 19 shape design variables and a SLP algorithm is used as optimizer. The only constraints originate in allowable geometric

5000 quadratic 2D solid finite elements. The probability of failure of the initial des $P_f = 4.7\%$, i.e., 1 out of 21 bits fails but having performed the shape optimizatio probability of failure is reduced to $P_f = 0.0014\%$, i.e., 1 out of 7250 bits fails. The i and final design of the cutting bit can be seen in Fig. 3.

$$P_f = 4.7\%: \text{1 out of 21 fails} \qquad P_f = 0.0014\%: \text{1 out of 7250 fails}$$
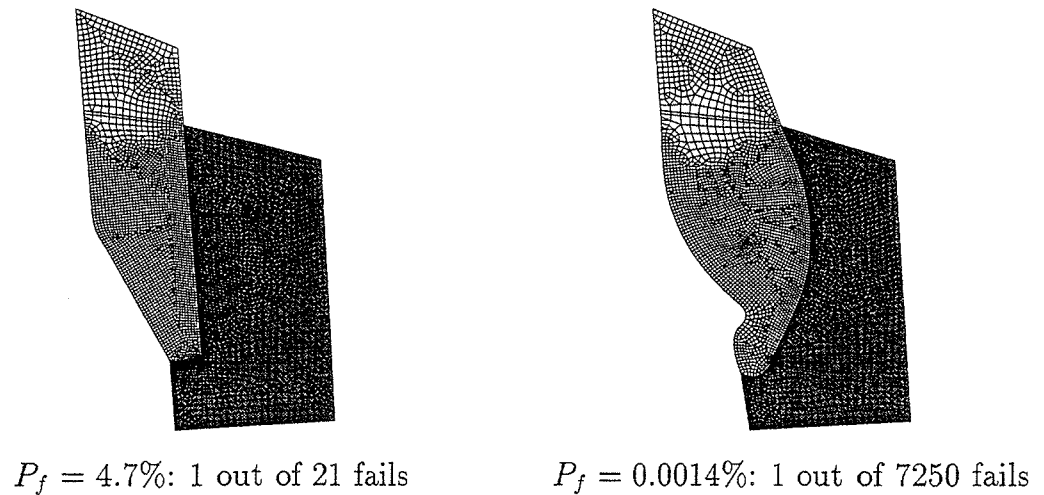
Figure 3: Initial and final design of cutting bit from a circular saw blade.

The example illustrates the effectiveness of designing mechanical components ma brittle materials by using Weibull probabilistic methods combined with finite ele based shape optimization and mathematical programming.

References

Andreasen, J.H. (1993a): Statistics of Brittle Failure in Multiaxial Stress States. *Journal American Ceramic Society*, Vol. 76, No. 11, pp. 2933-2935.

Andreasen, J.H. (1993b): Reliability Based Design of Ceramics. Report No. 57, *Institute of Mech Engineering, Aalborg University*, Denmark, 27 pp. (To appear in *Materials & Design*).

Evans, A.G. (1978): A General Approach to the Statistical Analysis of Multiaxial Fracture. *Jour the American Ceramic Society*, Vol. 61, No. 7-8, pp. 302-308.

Koski, J.; Silvennoinen; R. (1990): Multicriteria Design of Ceramic Components. In: *Multic Design Optimization* (Eds. H.A. Eschenauer, J. Koski & A. Osyczka), pp. 447-463, Springer-\ Berlin.

Lund, E. (1994): Finite Element Based Design Sensitivity Analysis and Optimization. Ph.D. I tation. Special Report No. 23, *Institute of Mechanical Engineering, Aalborg University*, Denmar. pp.

Lund, E. (1995): Shape Optimization of Ceramic Components Using Weibull Statistics. In: *Proc. World Congress of Structural and Multidisciplinary Optimization* (Eds. Niels Olhoff & G.I.N. Roz pp. 323-328, Pergamon Press, Oxford, UK.

McLean, A.F.; Hartsock, D.L. (1989): Design with Structural Ceramics. In: *Structural Mec.* (Ed. J.B. Wachtman), pp. 27-97, Academic Press, London.

Rasmussen, J.; Lund, E.; Olhoff, N. (1993): Parametric Modeling and Analysis for Optimum C In: *Proc. Structural Optimization '93 - The World Congress on Optimal Design of Structural S* (Ed. J. Herskovits), Vol. 2, pp. 407-414, Federal University of Rio de Janeiro, Brazil.

Weibull (1939): A Statistical Theory of the Strength of Materials. *Ingeniörs Vetenskabs Akade Handlinger*, Nr. 151, pp. 5-45.

Gradient-Regularized Plasticity Coupled to Damage - Formulation and Numerical Algorithm

Thomas Svedberg and Kenneth Runesson

Division of Solid Mechanics, Chalmers University of Technology, S-41296 Göteborg, Sweden

1 Introduction

A well-known characteristic of a local continuum theory is that the localization zone can be infinitely thin, i.e. a displacement discontinuity can develop. This means that diffuse localization phenomena, such as the development of a smooth neck in a tension-bar, can not be accurately described within classical continuum theory (at least not without suitable regularization in the post-localized range). That a displacement discontinuity is possible also leads to numerical difficulties when conventional FE-methods, which employ continuous displacement approximation, are used to capture localization phenomena. In particular, it appears that the calculated energy dissipation will tend to zero when the FE-mesh becomes infinitely refined, which is translated into the physically unrealistic result that the global postlocalized response becomes infinitely brittle. Since this is the characteristic result of refining the FE-mesh, it is known as "pathological" mesh-dependence.

As was already alluded to above, one possibility to ensure that the correct amount of energy is dissipated is to employ a "local regularization" strategy such that a non-standard interface is introduced along the localization zone. Such "dissipation-objective" regularization of the local theory has a long tradition in the modeling of semi-brittle material response, cf. WILLAM & AL. [10], BAZANT [1], and has relied heavily on the "fictitious crack" concept launched by HILLERBORG & AL. [4]. Recent contributions within FE-technology are those of LARSSON & AL. [6], SIMO & AL. [8], LARSSON & RUNESSON [5] and STEINMANN & AL. [9].

A rational approach to model postlocalized behavior, at least from a fundamental mechanics viewpoint, is to introduce "global" regularization of the governing equations by resorting to higher order continuum theory. In this paper, we present a thermodynamically consistent theory of gradient-regularized plasticity coupled to damage. The theoretical formulation is presented along

with its numerical treatment. Only those internal variables controlling hardening (in the local sense) are augmented with gradient terms. In particular, it is shown that this approach leads to the introduction of "dissipative stresses", cf. HALPHEN & SON [3], on the boundary of a given body. The CDI then imposes restrictions, in a rational fashion, on possible boundary conditions for the plastic multiplier. This is believed to be a novel feature, that contributes in establishing a self-consistent constitutive theory. At this point, we remark that, so far in the literature, only heuristic arguments have been used for choosing the (mostly homogeneous) boundary conditions.
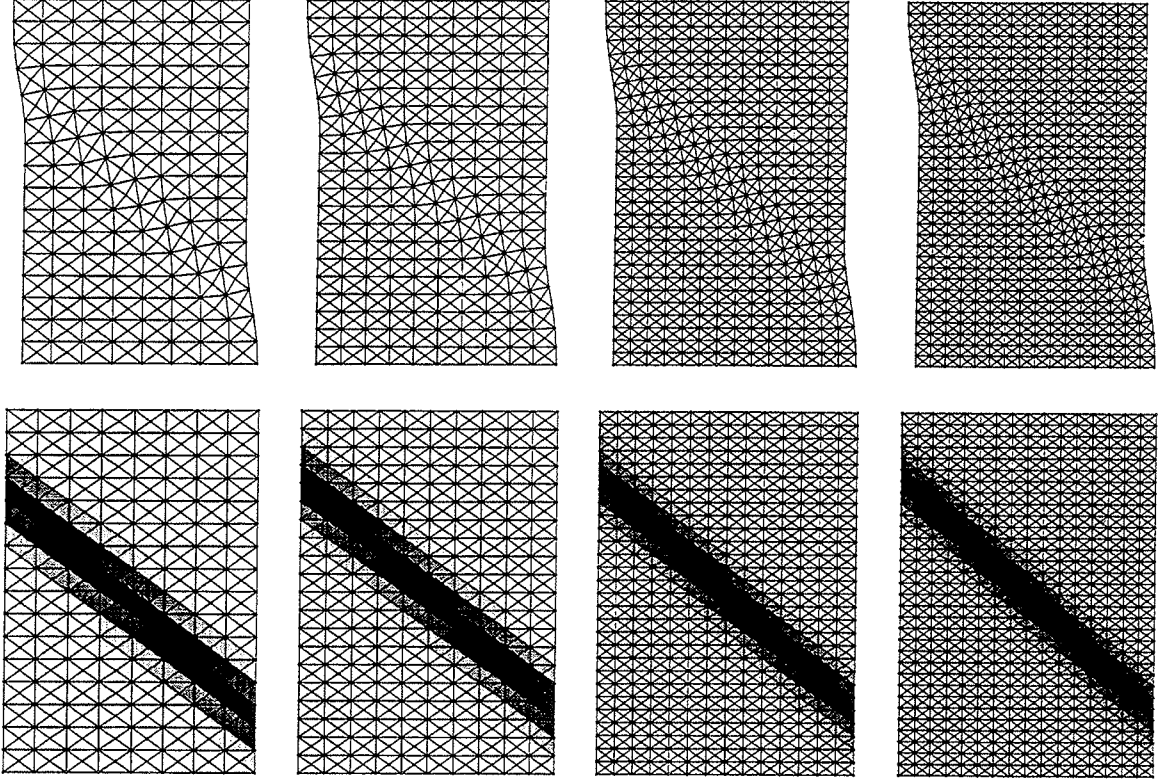
Fig. 1. Displacements (top row) and accumulated plastic strain (bottom row) for gradient theory.

2   Numerical algorithm

Previous attempts to establish reliable FE-algorithms for gradient (and non-local) formulations of plasticity are based on full coupling between the displacements and the plastic multiplier in the discrete problem, cf. PAMIN [7].

In this paper we rather employ a *staggered* solution technique for the quite conventional equilibrium problem and the non-classical boundary value problem in the plastic multiplier. An implicit integration strategy, viz. Backward Euler (or CPPM), is used to solve for the plastic multiplier within a fully

nonlinear equilibrium step. The corresponding FE-formulation is of a non-standard *mixed* type, cf. BREZZI & FORTAIN [2], which is believed to be an important novel feature of the present work.

References

[1] Z.P. Bažant. Mechanics of distributed cracking. *Appl. Mech. Rev.*, 39:675–705, 1986.

[2] F. Brezzi and M. Fortain. *Mixed and Hybrid Finite Element Methods.* Springer Verlag, New York, 1991.

[3] B. Halphen and N.Q. Son. Sur les matériaux standards généralisés. *J. Mécanique*, 14:39–63, 1975.

[4] A. Hillerborg, M. Modéer, and P.E. Petersson. Analysis of crack formation and crack growth in concrete by means of fracture mechanics and finite elements. *Cement and Concr. Res.*, 6:773–782, 1976.

[5] R. Larsson and K. Runesson. Element-embedded localization band based on regularized strong discontinuity. *ASCE, J. Engng. Mech.*, 122:402–411, 1996.

[6] R. Larsson, K. Runesson, and N.S. Ottosen. Discontinuous displacement approximation for capturing plastic localization. *Int. J. Num. Meth. Engng.*, 36(12):2087–2105, 1993.

[7] J. Pamin. *Gradient-dependent plasticity in numerical simulation of localization phenomena.* PhD thesis, Delft University of Technology, 1994.

[8] J.C. Simo, J. Oliver, and F. Armero. An analysis of strong discontinuities by strain-softening in rate-independent solids. *Comp. Mech.*, 12:277–296, 1993.

[9] P. Steinmann, R. Larsson, and K. Runesson. On the localization properties of multiplicative hypoelasto-plastic continua with strong discontinuities. *Int. J. Solids Structures*, 1995. Accepted for publication.

[10] K. Willam, N. Bicanic, and S. Sture. Constitutive and computational aspects of strain-softening and localization in solids. In K. Willam, editor, *ASME/WAM 1984 Symposium on Constitutive Equations, Macro and Computational Aspects*, pages 233–252. ASME, 1984.

Concrete modelling by damage mechanics

Mario Polanco-Loria
The Norwegian University of Science and Technology
Department of Structural Engineering
N-7034, Trondheim, Norway.
e-mail: mario.polanco@bygg.ntnu.no

Abstract

1 The scalar damage model

The damage theory of Kachanov [2], has been applied successfully by several authors [3], [4] to simulate the non-linear behaviour of concrete. This is done by introducing an internal damage variable d which monitors the degradation of the elastic properties of the material. This paper presents a scalar damage model capable to simulate a variety of plain and reinforced concrete problems. The model is very attractive for large scale computations because is developed in the strain space where an explicit algorithm is obtained.

Assuming the material behaviour to be elastic-damaging the constitutive equation reads:

$$\sigma_{ij} = (1 - d)\, C^o_{ijkl}\, \varepsilon_{kl} = (1 - d)\, \hat{\sigma}_{ij} \tag{1}$$

Thus, given a relationship $d = g(\varepsilon_{ij})$, the model is fully determined and assuming an increasing function $g(\varepsilon_{ij})$, positive dissipation is guaranteed.

The equivalent strain ε_{eq} adopted here represents a good compromise to simulate the non-linear dependency between hydrostatic and shear effects observed in the concrete and it is defined as [8]:

$$\varepsilon_{eq} = (1 - \theta(\hat{\sigma}_{ij})) \left\{ \frac{(M-1)\, I^\varepsilon_1}{2\, M\, (1-2\nu)} + \sqrt{\left(\frac{(M-1)\, I^\varepsilon_1}{2\, M\, (1-2\nu)} \right)^2 - \frac{3\, J^\varepsilon_2}{M\, (1+\nu)^2}} \right\} \tag{2}$$

A value of $M = 1.35$ is assumed in this work. The factor $(1 - \theta(\hat{\sigma}_{ij}))$ is introduced to improve the response of the model around the shear dominated zone. Thus, the damage criterion is postulated simply as: *Damage growth is possible if the loading function f vanishes*, e.g.

$$f = \varepsilon_{eq} - k(d) = 0 \tag{3}$$

Under a general state of stresses the total damage d is assumed to be a linear combination of the tensile damage d^+ and the compressive damage d^- as:

$$d = \alpha(\hat{\sigma}_{ij}) \ d^+ + (1 - \alpha(\hat{\sigma}_{ij})) \ d^- \tag{4}$$

where $\alpha(\hat{\sigma}_{ij})$ has the following definition:

$$\alpha = 1 - \exp(-\beta \ \gamma_t^{1.3}) \tag{5}$$

$$\gamma_t = \frac{\sum_{i=1}^3 \langle \hat{\sigma}_i \rangle_+}{\sum_{j=1}^3 |\hat{\sigma}_j|}$$

The β parameter is introduced to control the post-peak shear behaviour quite important to model the transition between plain and reinforced concrete.

Interested in normal strength type of concretes, the tensile damage law d^+ [4] and compressive damage law d^- [3] adopted have the following definitions:

$$d^+ = 1 - \frac{\varepsilon_o}{\varepsilon_{eq}} \ \exp\left[k \ \left(1 - \frac{\varepsilon_{eq}}{\varepsilon_o}\right)\right] \tag{6}$$

$$d^- = 1 - \frac{(1 - A^-) \ \varepsilon_o}{\varepsilon_{eq}} - A^- \ \exp(-B^-(\varepsilon_{eq} - \varepsilon_o)) \tag{7}$$

The parameters A^-, B^- are identified by fitting to data from the uniaxial compression test. However, these parameters can be related to the maximal compressive stress f_c' and its corresponding strain ε_{max}. The k parameter is found from the total specific dissipated energy g_f (the area under $\sigma - \varepsilon$ curve). This requirement necessities the introduction of the fracture energy G_f and the crack band width h. In order to reduce mesh dependency the crack band h is linked to the size of the element used and in particular for 2D problems $h = \sqrt{A_e}$. Thus this model requires basically 6 parameters: E, ν, f_t, G_f, f_c' and ε_{max} .

2 Numerical results

The following numerical examples shows the capability of the model to simulate some well known concrete tests. Because of space limitations we present only the global (F - δ curve) and some local (strain or damage distribution) results. A fully detailed description of the tests and input parameters used will be given during the presentation of this paper.

Splitting test [6]
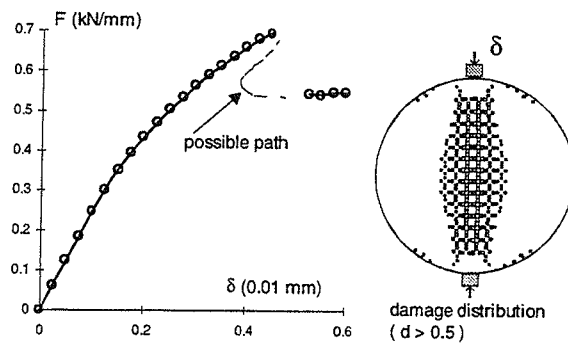
Numerical results of the splitting test

SEN beam [7]
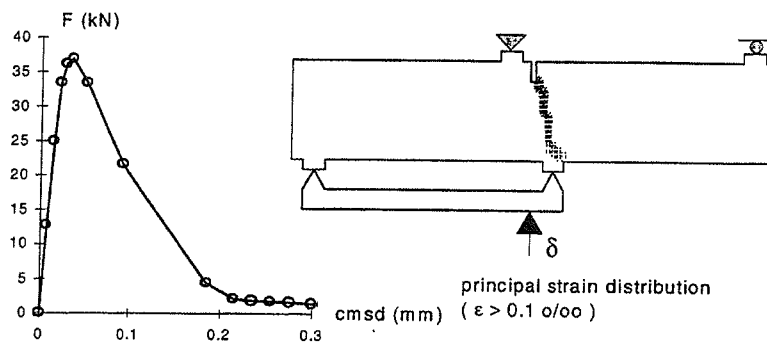
Numerical results of the SEN beam

Bresler & Scordelis beam [1]
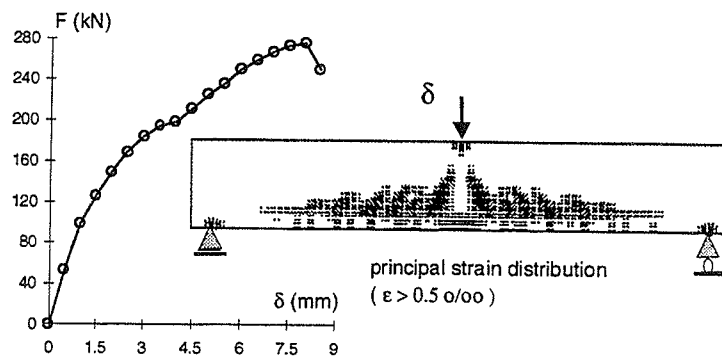
Numerical results of the B&S beam

A complete description of the previous model can be found in [5].

101

References

[1] Bresler B. and Scordelis A.C. (1964) " Shear strength of reinforced concrete beams - series II". SESM report no. 64-2, University of California, Berkeley, USA.

[2] Kachanov L.M. (1986) "Introduction to continuum damage mechanics". Martinus Nijhoff Publishers. The Hague.

[3] Mazars J. and Pijaudier-Cabot G. (1989) "Continuum damage theory: application to concrete". Journal of eng. mechanics, vol.115, no.2, ASCE, 55-64.

[4] Oliver J., Cervera M., Oller S. and Lubliner J. (1990) "Isotropic damage models and smeared crack analysis of concrete". Proc. 2nd. Int. Conf. on Comp. Aided Analysis and Design of Concrete Structures, Austria, 945-957.

[5] Polanco-Loria M. (1996) " Numerical modelling of plain and reinforced concrete by damage mechanics". Dissertation, The Norwegian University of Science and Technology, Trondheim, Norway. To appear.

[6] Saouridis C. (1989) "Identification et numerisation objectives des comportements adoucissants: une approche multiechelle de l'endomagement du beton". These de Doctorat, Universite de Paris 6, L.M.T., Cachan, France.

[7] Schlangen E. (1993) "Experimental and numerical analysis of fracture processes in concrete". Dissertation, Delft University of Technology, Delft, The Netherlands.

[8] Vree J.H. de, Brekelmans W.A. and van Gils M.A. "Comparison of non-local approaches in continuum damage mechanics". Accepted for publication in Computer & Structures.

Tensile Strength of Concrete at Early Age

Anders Boe Hauggaard[1] and Lars Damkilde[1]

Introduction

The purpose of the present work is to analyse the tensile strength development of early age concrete by numerical and experimental means. The one-dimensional tensile strength is needed when the development and distribution of stresses in the early age are considered. The stresses are used to predict the risk of harmful cracking which may affect the durability of the concrete structure, [1]. The early age is characterised by chemical reactions between cement particles and moisture giving the strength development, and the reactions are termed the hydration process.
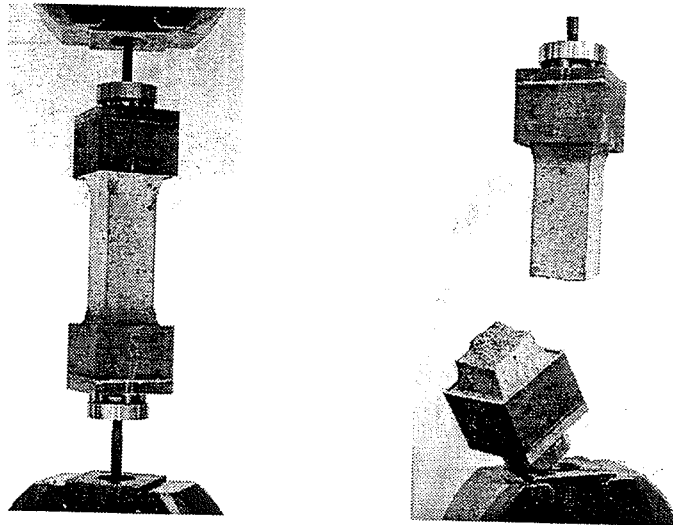
Figure 1: Dog-bone test specimen

Experimental Procedure

Dog-bone shaped test specimens have been developed to obtain the one-dimensional tensile strength of concrete from one day after start of hydration. Normally splitting tensile tests are used to obtain the tensile strength at these

[1]Department of Structural Engineering and Materials, Technical University of Denmark, DK-2800, Lyngby, Denmark.

early ages and this is because of difficulties in gluing loading plates to the wet surfaces of the concrete. The splitting test is an indirect method and the result depends on the Poisson ratio which is changing rapidly at early ages. The results obtained from the dog-bone tests have been compared with the splitting tensile strength. In Fig. 1 the dog-bone test specimen glued

Figure 2: Splitting test specimen

into the testing machine before and after testing is shown. The position of the fracture has been confirmed by finite element analysis. The dimensions, complying with the danish standard, are

- length: total: 480 mm and narrow section: 200 mm

- cross section: narrow section: 100 mm × 100 mm and large section: 140 mm × 140 mm

The specimens are glued into steel cups and the glue thickness is 5 mm on the sides and no glue on the bottom, which means that the load is transferred through shear from the loading plates to the specimen.

The splitting test specimen is shown in Fig. 2 and the test is a standard procedure. Based on assumptions of the stiffness properties the failure load is transformed to the splitting tensile strength. It is often assumed, see e.g. [2], that the one-dimensional tensile strength is equal to 60% of the splitting tensile strength. Surprisingly the experiments carried out indicated that this only was true for concrete older than about 2 weeks whereas at earlier stages the one-dimensional tensile strength seemed to be larger.

104

Numerical Analysis

At early age the Poisson ratio is 0.5 immediately after start of hydration where the cement particles are distributed in the moisture and the concrete behaves as a liquid. In the following hours, the setting time, the Poisson ratio decrease to a minimum followed by an increase until a final value of about 0.2. Finite element analysis of the dog-bone and the splitting experiments have been carried out to clarify if the development of the Poisson ratio may explain the observed relation between the one-dimensional strength and the splitting tensile strength. The program used is COSMOS and a simple crack criteria has been applied where failure takes place when the maximum principal stress reaches the tensile strength. A more refined analysis could include a crack model e.g. using the smeared-out concept, [3]. In Fig. 3 the finite element
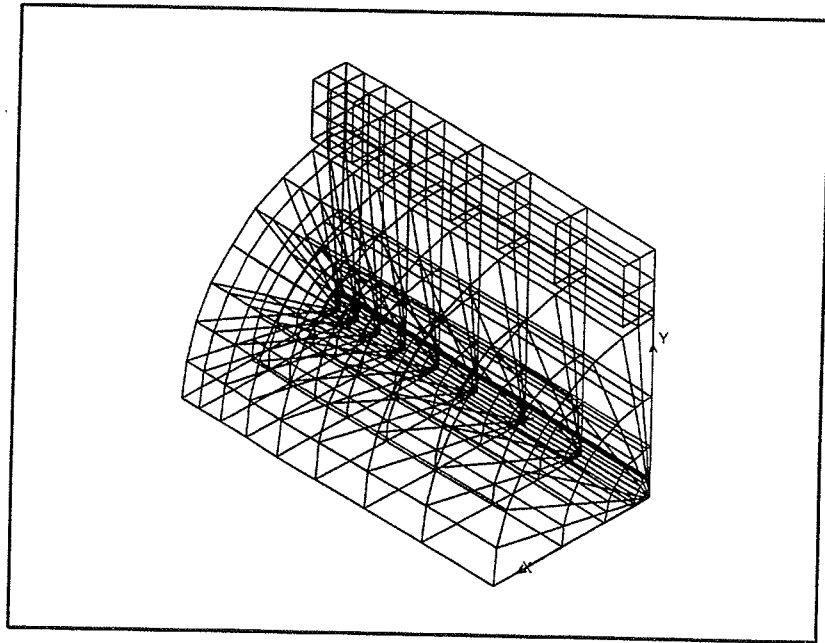
Figure 3: Mesh used in the analysis of the splitting test

mesh used in the splitting case is shown and $\frac{1}{8}$ of the structure is modelled due to symmetry. The loading is applied through steel plates and a wood insert which are also modelled in the analysis. In the case of the dog-bone analysis the glue and the steel cups have also been modelled. Fig. 4 shows the influence of the Poisson ratio on the value of the splitting tensile stress and the one-dimensional stress, respectively, giving a maximum principal stress of $p_1 = 1.0$ MPa. For the splitting test the influence from the Poisson
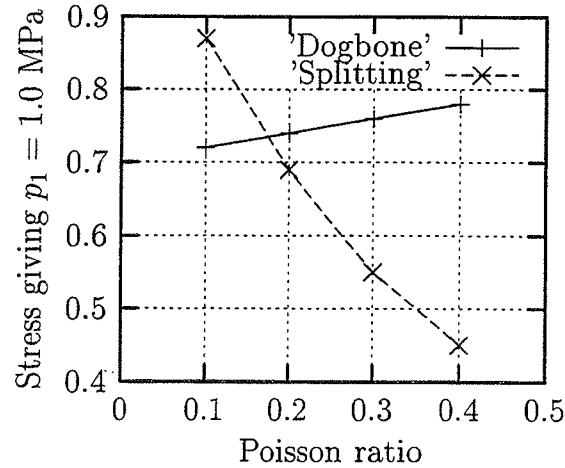
Figure 4: Failure stresses for dogbone and splitting test

ratio is seen to be larger and also a shift in behavior is observed. For large values of the Poisson ratio failure occurs for lower stresses in the splitting test whereas the opposite holds for small values of the Poisson ratio.

Conclusion

The development of the tensile strength at early age has been analysed. A test equipment has been developed for measuring the one-dimensional strength from one day after start of hydration and onwards, and the results are compared with the standard splitting tensile strength. The results indicate that the one-dimensional tensile strength is larger than the splitting tensile strength for ages less than 2 weeks whereas the opposite holds true for later ages. Numerical analysis studying the influence of the development of the Poisson ratio confirm the experimental results.

References

[1] Emborg, M., (1989). *Thermal stresses in concrete structures at early ages*, Doctoral Thesis, Div. of Struc. Eng., Luleå University of Technology.

[2] Herholdt, Aa.D., Justesen, Chr.F.P., Nepper-Christensen, P. and Nielsen, A., (1985). *The Concrete-Book*, (in danish), CtO, 2. udg.

[3] Dahlblom, O., and Ottosen, N.S., (1990). *Smeared Crack Analysis Using Generalized Fictitous Crack Model*, J. Eng. Mech., 116, 1, 55–76.

LOUDSPEAKER DIAPHRAGM

by
Søren T. Christensen and Niels Olhoff
Institute of Mechanical Engineering, Aalborg University,
Pontoppidanstraede 101,DK-9220 Aalborg East, Denmark,

1 Abstract

This abstract presents a novel method for optimizing the directivity of the sound emission from the diaphragm of an electro dynamic loudspeaker. The analysis of the loudspeaker is performed by using a finite element based modal analysis of the structural dynamic behaviour of the diaphragm and the boundary element method for the acoustic analysis. Through optimization of a dead mass distribution on the loudspeaker diaphragm, it has been possible to improve the directivity.

2 Introduction

Electro mechanical loudspeaker units have been used for decades, but unlike other components of the loudspeaker, the design of the diaphragm has essentially remained unchanged from the classical conical shape.

An ideal diaphragm would have a piston-like behaviour with a variable frequency dependent radius. This is obviously not possible with an ordinary loudspeaker unit where the radius is fixed, and the diaphragm only behaves as a piston in the lower part of its frequency range. This is the reason why a typical loudspeaker has several units of different radii, in oder to cover the entire audible frequency range. Modern loudspeaker units exhibit good mechanical and acoustic behaviour, but only within a specific frequency range, which is due to the physical behaviour of the diaphragm that "breaks up" when the excitation frequency exceeds a threshold value. At the same time, while the sound radiation is uniform in all directions when the frequency is in the lower part of its range, the diaphragm has a tendency to radiate within an more narrow angle for increasing excitation frequencies. This is caused by interference phenomena that occur when the sound wave length in the air becomes equal to or larger than the circumferential distance of the diaphragm. This naturally leads to the idea of designing a diaphragm which has a frequency dependent effective radius, i.e., to perform an optimization of the diaphragm design with a view to decouple the outer parts of the diaphragm for frequencies above the threshold value.

An acoustic objective function has been developed for the optimization which is directly based on achieving a predefined form of the directivity diagram. The design variables for the problem are taken to be the masses and radial positions of a set of concentric, dead ring masses attached to the diaphragm. In order to be able to perform this optimization, a structural-acoustic uncoupled combination of the Finite Element (FE) and the Boundary Element (BE) methods has been established. The analysis of the dynamic behaviour of the diaphragm was performed with a FE discretization of the structure in vacuum and using modal analysis. The acoustic analysis was performed by a BE analysis, using the vibrational velocities obtained from the dynamic analysis of the diaphragm as input.

As mentioned in the introduction, we perform the analysis of a loudspeaker diaphragm by a combination of FE and BE which makes it possible to achieve a very flexible description of the problem. The structural analysis is based on a FE discretization of the structure and use of modal analysis, see [3]. The equation of motion is

$$[M]\{\ddot{D}\} + [C]\{\dot{D}\} + [K]\{D\} = \{F\} \tag{1}$$

where $[M]$, $[K]$, and $[C]$ denote the global mass, stiffness and damping matrices, D the global displacement vector, and dot implies differentiation with respect to time, t. $F(t)$ denotes the harmonic excitation force to which the diaphragm is subjected. As the force $F(t)$ is assumed to be harmonic, the vector D can be expressed as a linear combination of the eigenvectors of the system, and the equations of motion decouple into n independent differential equations of second order, where n denotes the degrees of freedom of the system. Each of the solutions to these n equations is the same as for a system with one degree of freedom. In this way the normal velocity of the diaphragm is found and used as the input for the acoustic analysis.

4 Acoustic analysis

The acoustic analysis is performed by using the BE method based on the Helmholtz integral in the following form, see [4] [2] and [5],

$$C(P)\,p(P) = \int_S \left(p(Q)\frac{\partial G(R)}{\partial n} + i\omega\rho_0 v(Q)G(R) \right) ds \tag{2}$$

Here, $p(P)$ is the pressure at an arbitrary point P, $v(Q)$ is the velocity at a point Q on a sound emitting surface S, and it is assumed that $p(Q)$ and $p(P)$ satisfy Helmholtz' wave equation $\nabla^2 p + k^2 p = 0$ for time harmonic waves, where k is the wave number, and ρ_0 is the density of the medium. The function $G(R)$ is the free-space Green's function and $C(P)$ is the space-angle. The procedure consists in subdividing the surface of the diaphragm into n_e elements and to make a discretization of Helmholtz' integral, that makes it possible to set up a system of equations from which it is possible to determine the pressure everywhere in the acoustic medium.

5 Optimization

As objective functions, several formulations where investigated but an objective function based directly on the directivity diagram was the most succesfull, and it showed that it was possible to obtain a uniform directivity for a flat membrane. This objective function was formulated as the sum of the differences between the actual sound pressure level at a number of points lying on a circle with a radius of 3 m from the center of the diaphragm. The design variables for the problem are taken to be the masses m_i and radial positions r_i, $i = 1,...,I$, of a set of concentric, dead ring masses attached to the diaphragm, i.e., the vector of design variables is $\{a\} = \{m_1,....,m_I,r_1,....,r_I\}^T$.

The optimization problem is formulated mathematically as

$$min[f(\{a\}) = \sum_{i=1}^{N_p} (R_i^w - R_i^o)^p] \tag{3}$$

$$\sum_{i=1}^{I} m_i \geq M$$
$$0 \leq m_i \leq m_i^u \qquad i = 1,....,I \tag{4}$$
$$0 \leq r_i \leq a \qquad i = 1,....,I$$

where R_i^w and R_i^O, respectively, are the desired and the obtained sound pressure values a a number of points i, i=1,...,N_p, and $\{a\}$ is the vector of design variables.

The first constraint specifies a total mass M of the ring masses which is a minimun allowable value. The subsequent constraints are simple side constraints on the design variables, where m_i^u are given upper values for the masses, and a denotes the outer radius of the diaphragm.

6 Example: Flat diaphragm

The diaphragm was first considered as a flat, uniform circular elastic plate, modelled with Mindlin axisymmetric elements, see [1], [6], to which a set of circular, concentric dead ring masses were attached. The radii and the magnitude of these ring masses were adopted as design variables.

Fig. 1 shows the design model where 32 ring formed dead masses are attached to a circular clamped plate exited by a central, harmonically varying point force $f(t) = Ae^{i\omega t}$ with $A = 1N$. First the design model was investigated for an excitation frequency of the
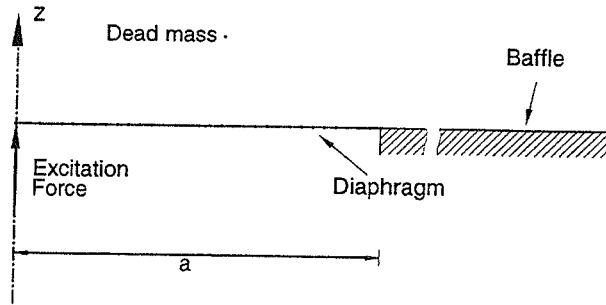
Figure 1: Design model for flat plate diaphragm

force of 10500 Hz, which results in a very directive pattern. The target level for the sound pressure level, the semi-circle of radius 3 m from the membrane, was choosen to be 85 dB.

Fig. 2A shows the directivity pattern for a flat diaphragm plate, both for an initial uniform distribution of the discrete masses, and after the optimization of the discrete masses has been performed. It is clearly seen that the optimized directivity curve is much more uniform than the initial one. The uniform directivity is obtained by placing ring masses located along the inner nodal circles, and thereby decoupling the outher parts of the membrane see Fig. 2B

It was also shown that when the optimization was carried out for the sound pressure level of 100 dB, it was possible to obtain uniform directivity in the entire audio-range from 0-20 KHz. The main difference of the optimized structure compared to the previous examples, was a significant use of very large masses.

109

A) Directivity pattern initial and after optimization at 10500 Hz

B) Modulus of velocity and mass distribution before and after optimization at 10500 Hz

Figure 2:

7 Conclusions

The directivity of a loudspeaker diaphragm has been optimized using as design variables the magnitudes and positions of a set of ring masses attached to the surface of the diaphragm. The structural vibration problem was analyzed by FE and modal analysis, while the acoustics problem was solved using a BE analysis. The objective function was formulated directly to prescribe a directivity pattern in the form of semi-circle. The optimization of a flat circular membrane showed that it was possible to obtain a uniform directivity for the hole audio frequency range (0-20 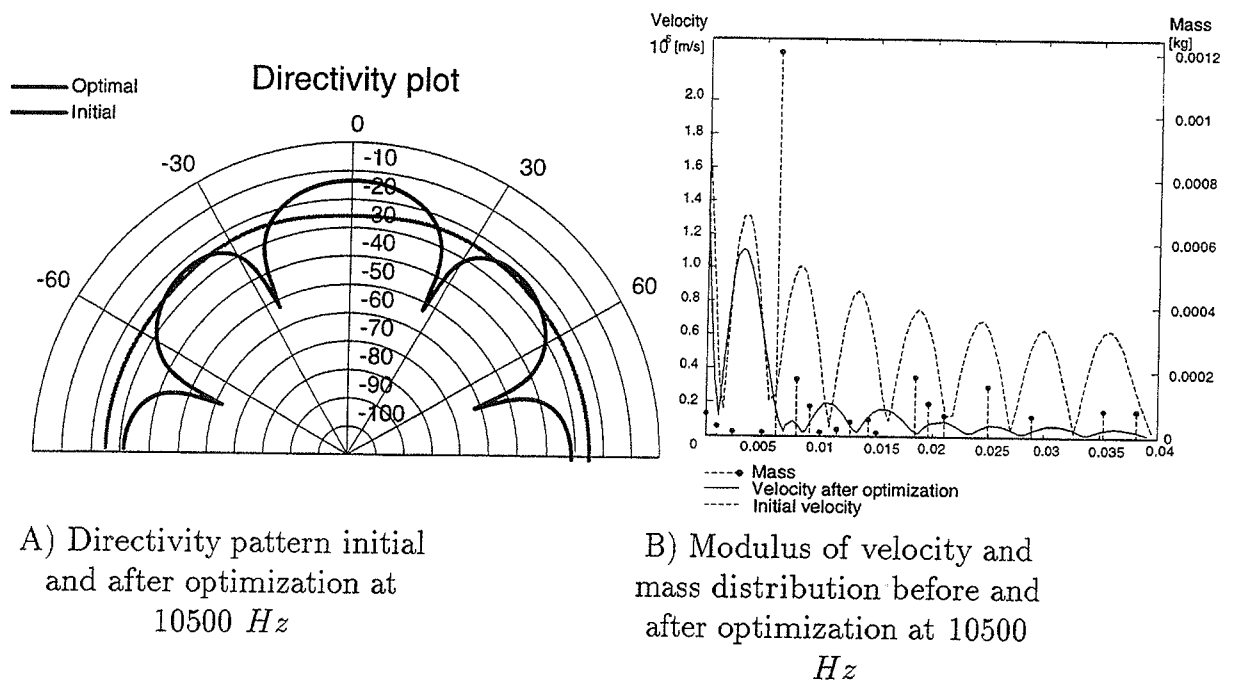KHz). By optimization the membrane was designed such as to act more or less as a point source by placing a large mass at the inner part of the membrane and decoupling the outer part of the membrane, by using only smaller masses that established a mutual cancelling effect in the vibration pattern for the outer parts.

References

[1] Robert D. Cook. *Concepts and applications of Finite Element analysis.* John Wiley & Sons, Inc., ISBN 0-471-87714-X, second edition, 1974.

[2] Moeller P. M. The boundary element method for sound field calculations. Thesis, The Acoustic Laboratory, Technical University of Denmark, 1993. Report No. 55.

[3] Singireu S. Rao. *Mechanical Vibrations.* Addison and Wesley, ISBN 0-201-52581-X, second edition, 1990.

[4] Sorokin V. S. Introduction to structural acoustics. Technical report, Institute of Mechanical Engineering Aalborg University, August 1995. Special Report No. 28.

[5] Benjamin Soenarko. A boundary element formulation for radiation of acoustic waves from axisymmetric bodies with arbitrary boundary conditions. *Journal of the Acoustical Society of America,* 93(2):631–639, 1993.

[6] Alexander Tessler. An efficient, conforming axisymmetric shell element including transverse shear and rotary inertia. *CT,* 15(5):567–574, 1982.

OPTIMAL TOPOLOGY DESIGN FOR CONTACT PROBLEMS

Joakim Petersson, Department of Mathematics, Technical University of Denmark

1 Introduction

Structural optimization is the problem of optimizing the performance of an assemblage of material which is subject to external loads. The objective function reflects what exactly is desired from the structure, and the design variables are the parameters subject to changes when extremizing this objective. In addition to constraints on these variables (design constraints), it is also necessary to introduce equilibrium conditions; since equilibrium for contact problems is governed by a variational inequality, structural optimization problems have in general, an inherent bilevel programming form, cf. [3].

Compliance topology optimization is probably the structural optimization problem which has been most frequently studied and used during the last decade, see [1] for an overview. Changes in topology usually imply drastic improvements in the structural performance, and choosing compliance as a performance measure also implies that the bilevel formulation of the problem reduces to a convex program.

The topology nature of the optimization is incorporated by allowing the thickness type design variables to take zero values.

2 Problem Statements

2.1 The Equilibrium Problem

We consider a discrete (or discretized) linear–elastic structure whose state of displacements is represented by a vector $u \in \Re^n$. Forces acting on the body are composed of forces due to contact with a rigid body and external prescribed forces $f \in \Re^n$, and therefore the *force equilibrium* equation reads:

$$f = K(h)u + C^T \lambda, \tag{1}$$

where $\lambda \in \Re^r$ is a vector of contact force magnitudes, C is an $r \times n$ kinematic transformation matrix, and $K(h)$ is the structural stiffness matrix.

We let $g \in \Re^r$ be a vector of initial distances between contact boundary nodes of the body and the rigid obstacle. We then have the frictionless Signorini contact conditions:

$$Cu \le g; \quad \lambda \ge 0; \quad \lambda^T(Cu - g) = 0, \tag{2}$$

due to requirements of *non-penetration*, *no adhesion* and *no contact action at a distance*, respectively.

2.2 The Design Optimization Problem

The considered structural optimization problem is

$$\min_{\substack{h \in \mathcal{H} \\ (1),(2)}} f^T u + g^T \lambda, \tag{3}$$

111

in which (1) and (2) constitute the *equilibrium constraints*. Here, h are the design variables, and $\mathcal{H}$ defines the *design constraints*:

$$\mathcal{H} = \left\{ h \in \Re^m \;\middle|\; \sum_{i=1}^m h_i \equiv 1^T h = V; \quad \underline{h} \leq h \leq \bar{h} \right\} \tag{4}$$

The design variables h are structural thicknesses or volumes, such as bar volumes for *trusses* or thicknesses representing the discretized (elementwise constant) thickness function for a *sheet*, and V is the available amount of material. These variables affect the structural stiffness matrix (only), and $K(h) = \sum_{i=1}^m h_i K_i$, where K_i is the global specific element stiffness matrix for the ith structural element. We let $\Pi(u,h) = 1/2u^T K(h)u - f^T u$ denote the total potential energy, and $\mathcal{U} = \{u \mid Cu \leq g\}$ the set of kinematically admissible displacements.

In case $g = 0$ we obtain the classical compliance term, but, in general (3) means a strive for small contact force magnitudes in addition to small displacements.

It is shown in [5] that (3) can be solved by finding a saddle point $(u^*, h^*) \in \mathcal{U} \times \mathcal{H}$ to Π:

$$(S\Pi) \quad \begin{cases} \text{Find } (u^*, h^*) \in \mathcal{U} \times \mathcal{H} : \\ \Pi(u^*, h) \leq \Pi(u^*, h^*) \leq \Pi(u, h^*), \quad \forall (u,h) \in \mathcal{U} \times \mathcal{H}. \end{cases}$$

If (u^*, h^*) solves $(S\Pi)$, and $\lambda^* \in \Re^r$ are Lagrange multipliers associated with the contact conditions describing the set $\mathcal{U}$, then (u^*, λ^*, h^*) solves (3).

Associated with the saddle problem $(S\Pi)$ is the dual pair of convex programs

$$(P) \quad \begin{cases} \text{Find } u^* \in \mathcal{U} : \\ \psi(u^*) \leq \psi(u), \quad \forall u \in \mathcal{U}, \end{cases}$$

where $\psi(u) \stackrel{\text{def}}{=} \sup_{h \in \mathcal{H}} \Pi(u,h)$, $u \in \mathcal{U}$, and the dual problem (D), conversely, is to maximize $\varphi(h) \stackrel{\text{def}}{=} \inf_{u \in \mathcal{U}} \Pi(u,h)$ over $\mathcal{H}$.

3 Algorithms for the Optimal Design Problem

3.1 The Subgradient Method

One succesful approach to solve (3) is to apply iterative algorithms, for convex nonsmooth programs, to (P). One such alternative is the *subgradient method*, which generates a sequence $\{u^k\}$ of feasible solutions by the formula

$$u^{k+1} = P_{\mathcal{U}}(u^k - \alpha_k \xi_\psi(u^k)), \qquad k = 1, 2, \ldots, \tag{5}$$

where $\xi_\psi(u^k) \in \partial \psi(u^k)$ is an element of the subdifferential (that is, a subgradient) of ψ at u^k, and $P_{\mathcal{U}}$ denotes the Euclidean projection map onto $\mathcal{U}$. We choose step lengths α_k according to the harmonic series formula $\alpha_k = \frac{1}{a+bk}$.

Using a well-known result on subgradients of max-functions, a subgradient of ψ is given by $\xi_\psi(u^k) = K(h^k)u^k - f$, where

$$h^k \in \mathcal{H}(u^k) \stackrel{\text{def}}{=} \arg\max_{h \in \mathcal{H}} \Pi(u^k, h). \tag{6}$$

112

The linear program (6) is a continuous knapsack problem, which means that it can be solved very effectively by so-called greedy algorithms [4].

We define an auxiliary sequence $\{h(k)\}$ by

$$h(k) = \frac{1}{k} \sum_{s=1}^{k} h^s, \qquad k = 1, 2, \ldots, \tag{7}$$

where h^k is given by (6). Clearly, $h(k) \in \mathcal{H}$ for all k. (In practice, we calculate $h(k)$ according to $h(k) = (1 - \frac{1}{k})h(k-1) + \frac{1}{k}h^k$.)

According to [6, Th. 4.3], one can guarantee convergence of the iterates u^k and $h(k)$ to solutions of (SII)!

We present a symmetric variable thickness sheet example where the thickness function is defined on a square domain. The upper design bound is constant and the lower is identically zero. The available amount of material is half the volume for the upper design bound. The optimal thickness distribution is shown in Fig. 1 where black color represent thickness values on the upper bound, and white signifies a zero volume (voids in the structure).
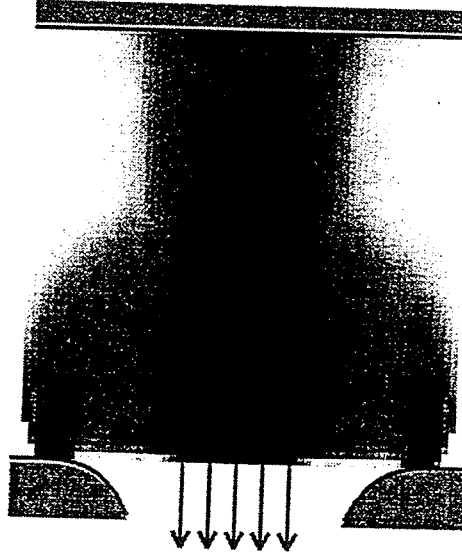
Figure 1: The optimal thickness distribution for a square sheet

3.2 Linear Programming Formulation

In case of a *truss structure* one can state a reformulation of (SII) in the special case when $\underline{h} = 0$, $\overline{h}_i = +\infty$ and $g = 0$:

$$(LP) \begin{cases} \max_{\bar{u} \in \mathfrak{R}^n} & f^T \bar{u} \\ \text{subject to} & C\bar{u} \leq 0 \\ & B\bar{u} \leq v \\ & -B\bar{u} \leq v \end{cases} \qquad (LP)_d \begin{cases} \min_{(\rho^+, \rho^-, \lambda)} & v^T(\rho^+ + \rho^-) \\ \text{subject to} & C^T\lambda + B^T(\rho^+ - \rho^-) = f \\ & \lambda \geq 0, \ \rho^+ \geq 0, \ \rho^- \geq 0 \end{cases}$$

Here we have defined $v = k(\ell_1, \ldots, \ell_m)^T$, $k = \sqrt{\frac{2}{VE}}$, and B is the $m \times n$ matrix whose ith row contains direction cosines for bar i.

113

Suppose $\bar{u} \in \Re^n$ solves (LP) and $(\rho^+, \rho^-, \lambda^*) \in \Re^m \times \Re^m \times \Re^r$ solves $(LP)_d$. Define $u^* \in \Re^n$ and $h^* \in \Re^m$ as $u^* := \mu\bar{u}$, $h^* := \mu^{-1}(\omega^+ + \omega^-)$ where $\omega^+ = \{\omega_i^+\}$, $\omega^- = \{\omega_i^-\}$ and $\omega_i^+ = \rho_i^+ \sqrt{\frac{V}{2E}} \ell_i$, $\omega_i^- = \rho_i^- \sqrt{\frac{V}{2E}} \ell_i$, $\mu := V^{-1} 1_m^T (\omega^+ + \omega^-)$. Then, provided $\mu > 0$, (u^*, λ^*, h^*) solves (3). (For details, see [2] or chapter 4.2.6 in [1]).

As a numerical example we present a plane bridge-type structure unilaterally supported from below at the two ends. Between these there are downward forces acting on the lower part. A standard LP solver was used to solve (LP) and $(LP)_d$ above, and the result is shown in Fig. 2.

$\Longrightarrow$: contact force

$\longrightarrow$: external load
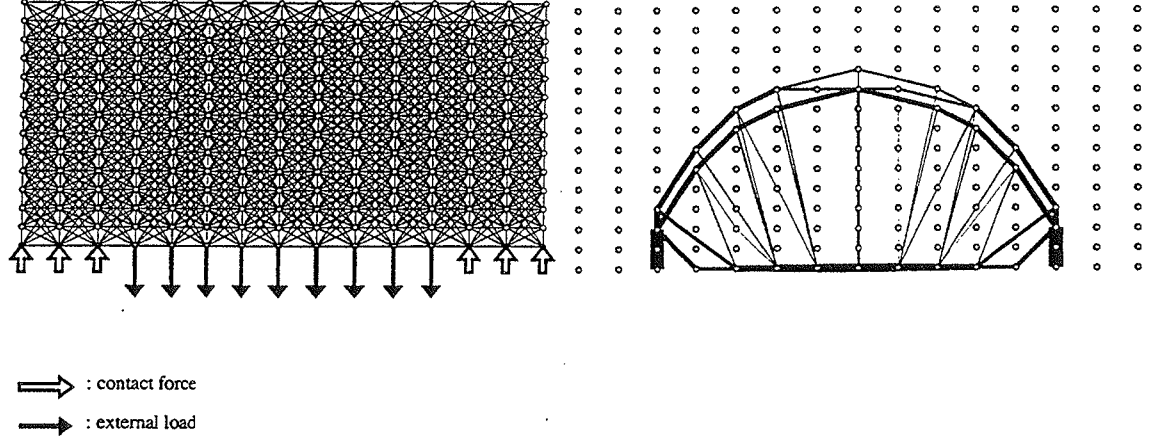
Figure 2: Subset of groundstructure and loadcase (left), and optimal design (right)

References

[1] M. P. Bendsøe, *Optimization of Structural Topology, Shape, and Material*, Springer Verlag, Berlin, Germany, 1995.

[2] A. Klarbring, J. Petersson, and M. Rönnqvist, *Truss topology optimization involving unilateral contact*, Journal of Optimization Theory and Applications, 87 (1995), pp. 1–31.

[3] Z.-Q. Luo, J.-S. Pang, and D. Ralph, *Mathematical Programs with Equilibrium Constraints*, Cambridge University Press, 1996 (forthcoming).

[4] C. H. Papadimitriou and K. Steiglitz, *Combinatorial Optimization: Algorithms and Complexity*, Prentice-Hall, Englewood Cliffs, NJ, 1982.

[5] J. Petersson and A. Klarbring, *Saddle point approach to stiffness optimization of discrete structures including unilateral contact*, Control and Cybernetics, 3 (1994), pp. 461–480.

[6] J. Petersson and M. Patriksson, *Topology optimization of sheets in contact by a subgradient method*, International Journal of Numerical Methods in Engineering, (1996) to appear.

SOME GENERAL OPTIMAL DESIGN RESULTS
USING ANISOTROPIC, NON-LINEAR MATERIALS

PAULI PEDERSEN

Department of Solid Mechanics
Technical University of Denmark, 2800 Lyngby, Denmark

Abstract — Recent results on optimal design with anisotropic materials and optimal design of the materials themselves are in most cases based on the assumption of linear elasticity.

We shall extent these results to the non-linear models classified as power-law elasticity. These models return proportionality between strain energy densities, which implies localized sensitivity analysis for the total strain energy and thus for a number of practical studies.

For two and three dimensional problems the effective strain and the effective stress are defined from an energy consistent point of view, and it is shown that a definition in analogy with von Mises stress cannot be used.

The optimization criterion of uniform energy density also holds for these non-linear materials, and several general conclusions can be based on this fact. Applications to size design of thickness and density will illustrate this.

Then the general material design problem is addressed. Based on a constraint on the Frobenius norm, the validity of recent results are extended to the non-linear materials. In this relation also the orientational design with orthotropic materials is focused on.

The result for the general material design problem in terms of a non−dimensional 3D constitutive matrix and stated in the directions of principal strain/stress is

$$[\alpha]_{\text{optimal}} = \frac{1}{\left(\epsilon_I + \epsilon_{II} + \epsilon_{III}\right)^2} \begin{bmatrix} \epsilon_I^2 & \epsilon_I \epsilon_{II} & \epsilon_I \epsilon_{II} & 0 & 0 & 0 \\ \epsilon_I \epsilon_{II} & \epsilon_{II}^2 & \epsilon_{II} \epsilon_{III} & 0 & 0 & 0 \\ \epsilon_I \epsilon_{III} & \epsilon_{II} \epsilon_{III} & \epsilon_{III}^2 & 0 & 0 & 0 \\ 0 & 0 & 0 & 0 & 0 & 0 \\ 0 & 0 & 0 & 0 & 0 & 0 \\ 0 & 0 & 0 & 0 & 0 & 0 \end{bmatrix}$$

We note that the optimal material is orthotropic, that principal directions of material, strain and stress are aligned and that there is no shear stiffness. In reality this matrix only has one non−zero eigenvalue and the material therefore has only stiffness in relation to the specified strain condition.

With respect to strength optimization, i.e. the more difficult problem with local constraints, we shall comment on the influence of the different strength criteria.

Shape optimizations by sequential linear programming are discussed in the last part of the lecture and the similarities with shape design based on linear elastic material are put forward. The biaxial problem shown below is optimized in relation to stiffness as well as strength and actual design parameters has been shape, size (thickness) and/or material orientation.
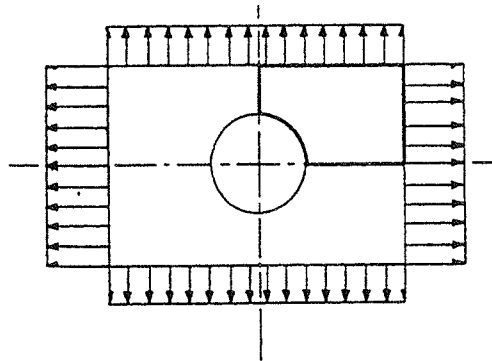
Nonlinear Continuum Mechanics with Polarity

Esben Byskov

Department of
Structural Engineering & Materials
Technical University of Denmark

Jes Christoffersen

Department of
Solid Mechanics
Technical University of Denmark

September 06, 1996

Abstract

In some situations the usual local, non-polar continuum theories are deficient in that they do not have any length scale. Therefore, they are not able to predict the width of strain localization such as kink bands in fiber reinforced epoxy in compression. Inherent in (micro)polar continuum theories is the concept of a length scale which may be determined either from the microstructure of the material or indirectly by experiments. Here, we present a nonlinear, polar continuum theory which seems to be able to handle such difficulties.

1 Introduction

Over the past decade, kink band formation in fiber reinforced epoxy in compression has received widespread attention because this type of material failure is potentially dangerous in expensive and important structures such as airplanes. Similar kink bands form in wood in compression but the severity of their existence has not been determined yet. It appears that in order to determine the kink band angle and width, introduction of a length scale is necessary if the material is treated as a continuum.

A more direct approach that considers the structure of the two-component material has been utilized by Kyriakides *et al.* (1995) under the assumption that both the fibers and the matrix are two-dimensional materials. A complete three-dimensional numerical analysis involving more than just a few fibers appears to be computaionally impracticable at the present time. Because of the extremely complicated structure of wood a full analysis of kinking of this material is even more prohibitive. In both cases, some smeared-out theory, i.e. a continuum theory involving a length scale, is therefore appealing.

2 Polarity versus Nonlocality

A nonlocal continuum theory may very well be able to handle strain localization and other similar effects as well as a micropolar continuum theory because nonlocal theories also involve a length scale. Among the reasons why we prefer a polar theory is that—to

117

us—it appears to be more intuitively clear, in particular in connection with fiber reinforc materials or other materials which are characterized by a pronounced and ordered structu For other materials such as plain concrete application of nonlocal theories have yield useful descriptions of the behavior, for example as regards the post peak characteristics the laod-displacement curve for test specimens of differents length, where the longer t specimen the steeper the drop in load, see e.g. (Schreyer and Chen 1986) and (Schrey 1990).

3   A Motivation: Kink Bands

As an example of kink bands, a deformed compression test specimen made of clear wood shown in Fig. 1. Initially, when the load is applied the fibers remain straight, but when
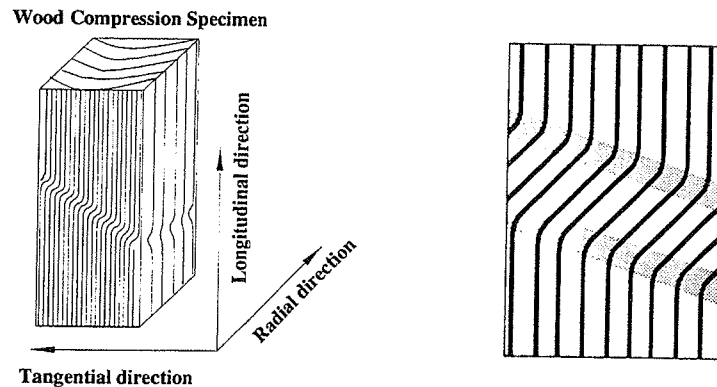
Figure 1: Kink band

reaches a certain value a kink band is formed. Both in wood and in fiber reinforced epox this band is usually at an angle of $\approx \pi/8$ with respect to the normal to the fibers. Th sketch to the right in Fig. 1 shows a schematic picture of a kink band—either in wood c in fiber reinforced epoxy. In the zones with straight fibers as shown in Fig. 2, the usu
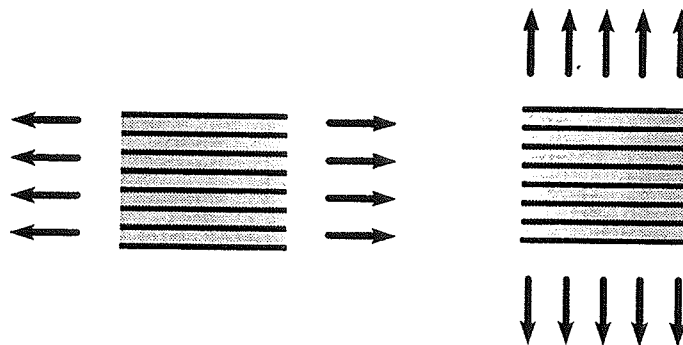
Figure 2: Non-polar material

local continuum theory may be assumed to apply, while in the shaded process zones of th figure to the right in Fig. 1, where the fibers curve, a micropolar theory must be utilized

Figure 3: Polar material

When fiber bending occurs, polarity develops because the fibers exert bending moments on the matrix material as indicated in Fig. 3. This effect has been taken into account in an *ad hoc* fashion by Fleck *et al.* (1995), who established the equations for incipient kinking. For their particular purpose the analysis seems to provide reasonable predictions, but no attempt to investigate the behavior after the first kinking was made. Also, the post peak behavior can not be handled by the method used by Fleck *et al.* (1995).

4 Basic Formulas

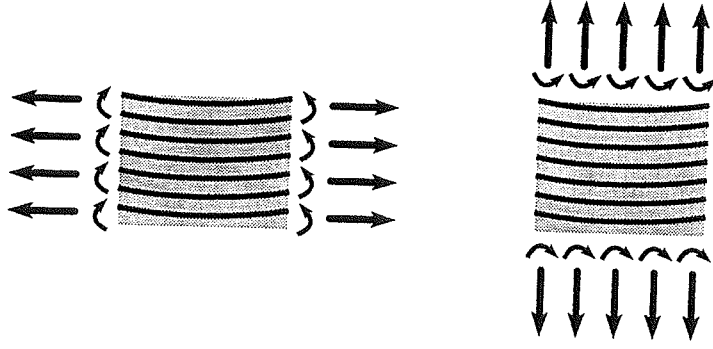It is our intention to establish a full set of (micro)polar continuum mechanics formulas that can be used to describe the kinking from its beginning till well into the post peak regime. For that purpose we utilize an incremental description that entails kinematic, static and constitutive equations. While the kinematics and the statics—at least in principle—do not present substantial difficulties, see below, the constitutive behavior involves a number of material parameters that are, in general, not known at the present time. Special care must be taken, and a number of rather severe simplifying assumptions may be necessary.

The theory presented here is in rate form which is useful because we intend to solve problems in incremental form. Some basic formulas are listed below with comments regarding our choices.

4.1 Kinematics

Let v_i denote the velocity and ω_k the spin, which is considered independent of the velocity. Then, the strain *rate* ε_{ij} is:

$$\varepsilon_{ij} = v_{i,j} - e_{ikj}\omega_k \neq \varepsilon_{ji} \tag{1}$$

and the curvature rate is κ_{ij}, where:

$$\kappa_{ij} = \omega_{i,j} \neq \kappa_{ji} \quad \text{and} \quad \omega_{ij} \neq \tfrac{1}{2}\left(v_{i,j} - v_{j,i}\right) \tag{2}$$

Thus, both the strain rate and the curvature rate are unsymmetric, and the curvature rate is *not* derived from the velocity alone. Of course, this last assumption, which is fairly common, may be enforced, if desired.

4.2 Statics

The generalized stresses are the direct stresses σ_{ij} and the couple stress (moment) μ_{ij}.

4.3 Rate Form of Statics

In the absence of body loads and body moment loads equilibrium requires:

$$\overset{\star}{\tau}_{ij,i} + e_{jkl}\kappa_{ki}\sigma_{il} = 0$$

$$\overset{\star}{\nu}_{ij,i} + e_{jkl}\left(\overset{\star}{\tau}_{kl} + \varepsilon_{ki}\sigma_{il} + \kappa_{ki}\mu_{il}\right) = 0 \qquad ($$

It is important to note that $\overset{\star}{\tau}_{ij}$ and $\overset{\star}{\nu}_{ij}$ are objective measures of stress rates given b

$$\overset{\star}{\tau}_{ij} = \dot{\sigma}_{ij} + \sigma_{ij}v_{k,k} - v_{i,k}\sigma_{kj} + \sigma_{ik}e_{klj}\omega_l$$

$$\overset{\star}{\nu}_{ij} = \dot{\mu}_{ij} + \mu_{ij}v_{k,k} - v_{i,k}\mu_{kj} + \mu_{ik}e_{klj}\omega_l \qquad ($$

where e_{klj} is the permutation symbol and $\dot{\sigma}_{ij}$ and $\dot{\mu}_{ij}$ are components of the rates of tl direct stress σ_{ij} and the couple stress μ_{ij}, respectively.

4.4 Constitutive Model

For our purpose the constitutive model may be formulated as:

$$\overset{\star}{\tau}_{ij} = A_{ijkl}\varepsilon_{lk} + B_{ijkl}\kappa_{lk}$$

$$\overset{\star}{\nu}_{ij} = B_{klij}\varepsilon_{lk} + D_{ijkl}\kappa_{lk}$$

where: A_{ijkl} are usual moduli
B_{ijkl} are polar moduli (!
D_{ijkl} are bending moduli

The crux of the matter is to determine these constitutive paramaters and their variatic with strain—a task which we have not completed at the time of writing.

References

Fleck, N., L. Deng and B. Budiansky (1995). 'Prediction of kink width in compressed fibe composites'. *Journal of Applied Mechanics* **62**, 329–337.

Kyriakides, S., E.J. Perry Arseculeratne and K.M. Liechti (1995). 'On the compressiv failure of fiber reinforced composites'. *Int. J. Solis Structures* **32**(6/7), 689–738.

Schreyer, H. (1990). 'Analytical solutions for nonlinear strain-gradient softening and loca ization'. *Journal of Applied Mechanics* **57**, 522–528.

Schreyer, H. and Z. Chen (1986). 'One-dimensional softening with localization'. *Journal (Applied Mechanics* **53**, 791–797.

NOTES ON THE CONSISTENT LINEARIZATION IN PLASTICITY FOR YIELD CRITERIA OF THE MOHR–COULOMB TYPE

by

Ragnar Larsson[*] and Kenneth Runesson[**]

[*]Department of Structural Mechanics, Chalmers University of Technology
S–412 96 Göteborg, Sweden
[**]Division of Solid Mechanics, Chalmers University of Technology
S–412 96 Göteborg, Sweden

Summary

Based on the Closest Point Projection Method for integration of the constitutive relations in plasticity, we discuss the consistently linearized tangent stiffness modulus tensor for yield criteria that are of the Mohr–Coulomb type. With the assumption of elastic and plastic isotropy, this tensor is shown to appear in the form of an additive modification of the continuum tangent stiffness tensor. The convergence properties of the consistent tangent stiffness tensor are compared with its feasible approximations. The results indicate the strong sensitivity, in terms of poor convergence properties, to careless selections.

Introduction

The incremental iterative algorithm for a FE–discretized plasticity problem must be properly designed to ensure cost–efficiency, robustness and accuracy of the solution. In particular, to ensure cost–efficiency of the algorithm, it is crucial that the computation of iterative search directions is based on the consistent linearization of the incremental constitutive relations. This will assure the quadratic convergence property that is pertinent to the Newton–Raphson scheme. As opposed to the continuum response, the algorithmic tangent stiffness (ATS) modulus tensor in plastic loading involves the "modified" elastic stiffness (AES) tensor, which requires the inversion of a weighted sum of the elastic compliance and Hessian of the flow potential, as discussed by e.g. Simo and Taylor [1]. Most investigators seem to prefer to carry out the inversion numerically, whereby the tensorial structure of the ATS–tensor is not exploited.

Based on the developments in Larsson and Runesson [2], we discuss the general format and characteristics of the Closest–Point–Projection–Method (CPPM) in principal stress space for isotropic elasticity and plasticity. Due to the inherent coaxiality between the elastic trial stress and the updated stress, the transformation to Cartesian stress components can conveniently be carried out based on the eigenbases of the trial stress. To avoid unnecessary technical complexity, we restrict to the case of perfect plasticity. The generalization to isotropic hardening (or softening) appears to be straightforward. We establish the corresponding ATS–tensor explicitly, whereby well established results from large–strain isotropic hyper–elasticity are exploited, cf. Simo and Taylor [3], for the linearization of the eigenbases.

For any temporal integration method, the *Algorithmic Tangent Stiffness* (ATS) modulus tensor E_a is defined from the consistent linearization of the incremental stress–strain relationship, i.e.

$$d\Delta\sigma = E_a : d\Delta\varepsilon \tag{1}$$

From the CPPM, we recall that the incremental relation can be written

$$(E^e)^{-1} : \Delta\sigma - \Delta\varepsilon + \Delta\lambda\, f^* = 0 \quad with \quad f^* = \sum_{i=1}^{3} f_i^*\, m_i \quad and \quad f_i^* = \frac{\partial\phi^*}{\partial\sigma_i} \tag{2}$$

where we have expanded the flow direction f^* in the *principal dyads* $m_i = g_i \otimes g_i$. Moreover, we assume an isotropic yield criterion ϕ and a flow potential ϕ^*, whereby f^* and the gradient of the yield function f are colinear, i.e. m_i are principal dyads also of f. Although, we use the generic notation E^e for the elastic stiffness modulus tensor, we also assume elastic isotropy, whereby the integrated stress σ and the elastic trial stress $\sigma^e = {}^n\sigma + E^e : \Delta\varepsilon$ are coaxial, i.e. $m_i(\sigma) = m_i(\sigma^e)$.

Upon differentiating (2), we obtain

$$(E^e)^{-1} : d\Delta\sigma - d\Delta\varepsilon + d\Delta\lambda\, f^* + \Delta\lambda\, df^* = 0 \tag{3}$$

Remark: In the literature, it is common to differentiate $f(\sigma)$ in order to formally obtain the *Algorithmic Elastic Stiffness* (AES) modulus tensor E_a^e in the relation

$$d\Delta\sigma = E_a^e : \left[d\Delta\varepsilon - d\Delta\lambda\, f^* \right] \tag{4}$$

where E_a^e is given formally, cf. Simo and Taylor [1], as

$$E_a^e = \left[(E^e)^{-1} + \Delta\lambda\, \frac{\partial^2\phi^*}{\partial\sigma \otimes \partial\sigma} \right]^{-1} \tag{5}$$

The major disadvantage is that the inversion, as indicated in (5), must be carried out numerically for a general yield criterion, whereby the tensorial structure of E_a^e is completely lost. ■

In the present paper, however, we follow a slightly different route in order to take explicit advantage of the fact that the principal components $f_i = f_i(\sigma_1, \sigma_2, \sigma_3)$ are *constant* in the case of a "linear" yield criterion (as discussed subsequently). Moreover, we use the fact that $m_i = m_i(\sigma^e)$. Upon using Serrin's theorem, we may then express m_i in closed form in terms of σ^e and δ. If all σ_i^e are distinct, then

$$m_i \equiv g_i \otimes g_i = \frac{\sigma_i^e}{d_i^e}\left(\sigma^e - \left(I_1^e - \sigma_i^e\right)\delta + I_3^e(\sigma_i^e)^{-1}(\sigma^e)^{-1} \right) \tag{6}$$

where

$$d_i^e = 2\,(\sigma_i^e)^2 - I_1^e\,\sigma_i^e + I_3^e\,(\sigma_i^e)^{-1} \quad , \quad I_1^e = \delta : \sigma^e \quad , \quad I_3^e = \det\sigma^e \tag{7}$$

We thus obtain

$$df^* = A : d\Delta\sigma + B : E^e : d\Delta\varepsilon \tag{8}$$

where we have introduced the symmetric 4:order tensors

$$A = \sum_{i=1}^{\nu} \sum_{j=1}^{\nu} \frac{\partial f_i^*}{\partial \sigma_j} \, m_i \otimes m_j \ , \qquad B = \sum_{i=1}^{3} f_i^* \, M_i \qquad (9)$$

where it is noted that $\partial f_i^*/\partial \sigma_j = \partial f_j^*/\partial \sigma_i$. Moreover, to obtain $(9)_1$, it was used that $\partial \sigma_j/\partial \sigma = m_j$. The linearized eigenbasis M_i may be expressed in close analogy with the Serrin–Simo formula, as given by Simo and Taylor [3], as follows:

$$M_i \equiv \frac{\partial m_i}{\partial \sigma^e} = \frac{\sigma_i^e}{d_i^e} \Bigg[I - \delta \otimes \delta - I_3^e(\sigma_i^e)^{-1} \left(I_{(\sigma^e)^{-1}} - (\sigma^e)^{-1} \otimes (\sigma^e)^{-1} \right) + \qquad (10)$$

$$+ \delta \otimes m_i + m_i \otimes \delta - I_3^e(\sigma_i^e)^{-2}\left(m_i \otimes (\sigma^e)^{-1} + (\sigma^e)^{-1} \otimes m_i \right) + 2\left(I_3^e(\sigma_i^e)^{-3} - 1 \right)m_i \otimes m_i \Bigg]$$

where

$$I_{(\sigma^e)^{-1}} = \frac{1}{2}\left((\sigma^e)^{-1} \,\overline{\otimes}\, (\sigma^e)^{-1} + (\sigma^e)^{-1} \,\underline{\otimes}\, (\sigma^e)^{-1} \right) \qquad (11)$$

Remark: Each M_i (and m_i) is completely defined by σ^e, whereas it is clear that f_i (and f_i^*) depends on σ in the general situation. ■

Upon introducing (8) into (3), we obtain

$$d\Delta\sigma = E_a^e : \Big[R : d\Delta\varepsilon - d\Delta\lambda \, f^* \Big] \quad \text{with} \quad R = I - \Delta\lambda \, B : E^e \qquad (12)$$

where the (reduced) AES–tensor E_a^e is now defined as

$$E_a^e = \Big[(E^e)^{-1} + \Delta\lambda \, A \Big]^{-1} \qquad (13)$$

It remains to calculate the $d\Delta\lambda$ from the consistency condition $d\phi = 0$ (in plastic loading). This gives

$$E_a^{ep} = \left(E_a^e - \frac{1}{h_a}E_a^e : f^* \otimes f : E_a^e \right) : R \quad \text{with} \quad h_a = f : E_a^e : f^* \qquad (14)$$

ATS–tensor for Linear Yield Criteria

In this section, we consider the important sub–class of yield criteria that are linear in the principal stresses, i.e. when ϕ is given as

$$\phi(\sigma_1 \, , \ \sigma_2 \, , \ \sigma_3) = a_1\sigma_1 + a_2\sigma_2 + a_3\sigma_3 - k \qquad (15)$$

for $\sigma_1 \geq \sigma_2 \geq \sigma_3$, where $a_i = f_i$ are *constant* material parameters and k is a cohesion parameter which is also assumed constant. To define physically meaningful criteria, we choose $a_1 > a_2 > a_3$. A class of useful yield criteria, which represent a generalization of the MC–criterion, is defined by the choice

$$a_1 = 1 + \frac{2 - \alpha}{2 + \alpha}\sin\Phi \ , \qquad a_2 = \frac{2\alpha}{2 + \alpha} \sin\Phi \ , \qquad a_3 = -1 + \sin\Phi \qquad (16)$$

and $k = 2c \cdot \cos\Phi$. Here, c is the cohesion, Φ is the angle of internal friction and $0 \leq \alpha \leq 1$ is a parameter. The parameter α is defined such that the classical MC and the MT criteria are obtained for $\alpha = 0$ and $\alpha = 1$, respectively. It follows that $a_1 > a_2 > a_3$ since $a_1 > 1, 0 \leq a_2 \leq 1$ and $a_3 < 0$. Moreover, $a_{vol} = 2\sin\Phi > 0$ represents dilatant behavior.

Considering the class of linear yield criteria in (15), we conclude that $A = 0$. Hence, we obtain the trivial result $E_a^e = E^e$, which implies further simplifications when it is used that E^e represents elastic isotropy defined as

$$E^e = 2G(I + \psi\, \delta \otimes \delta) \quad , \quad \psi = \frac{\nu}{1 - 2\nu} \tag{17}$$

where G and ν are the elastic constants, δ and I are the 2:order and the 4:order identity tensors, respectively. We now obtain

$$B : \delta = 0 \quad , \quad B : f = 0 \tag{18}$$

whereby it follows that

$$E^e : R = E^e - 4\Delta\lambda\, G^2\, B \quad , \quad f : E^e : R = f : E^e \tag{19}$$

From (14), we conclude that

$$E_a^{ep} = E^{ep} - 4\Delta\lambda\, G^2\, B \tag{20}$$

Here, we used the notation E^{ep} for the Continuum Tangent Stiffness (CTS) modulus tensor, defined as

$$E^{ep} = E^e - \frac{1}{h}\, E^e : f^* \otimes f : E^e \quad with \quad h = f : E^e : f^* \tag{21}$$

The ATS–tensor is thus obtained simply by subtracting the contribution $\Delta\lambda 4 G^2 B$ from the CTS-tensor.

References

1   J.C. Simo and R. L. Taylor, "Consistent material operators for rate−independent elasto−plasticity." *Comp. Meth. in Appl. Mech. and Engrg.* **48**, 101−118 (1985)

2   R. Larsson and K. Runesson, "Implicit integration and consistent linearization for yield criteria of the Mohr−Coulomb type", Int. J. Mechanics of Cohesive−Frictional Mat. (in press 1996)

3   J.C. Simo and R.L. Taylor, "Quasi−incompressible finite elasticity in principal stretches. Continuum basis and numerical algorithms." *Comp. Meth. in Appl. Mech. and Engrg.* **85**, 273−310 (1991)

Modelling of Early Age Concrete

Anders Boe Hauggaard[1] and Lars Damkilde[1]

Introduction

The scope is modelling of early age concrete which is characterised by chemical reactions between cement particles and moisture. The chemical reactions are denoted the hydration process and during hydration the properties develop, i.e. increase of strength and stiffness. A material with these characteristics is of the aging type. The important factors at early age are the development of temperature, moisture and material properties which are coupled. During hydration heat is developed and this accelerates the chemical reactions. At the same time the increased temperature influences e.g. the creep properties and gives a higher creep rate.

A creep model is set up taking into consideration some of the couplings at early age and a concept suited for numerical formulations of the couplings are discussed. The purpose of a numerical analysis is to find the development and redistribution of stresses to predict the risk of harmful cracking, [1].

The Direct Incremental Creep Model

Figure 1: Rheologic model for the direct incremental creep model.
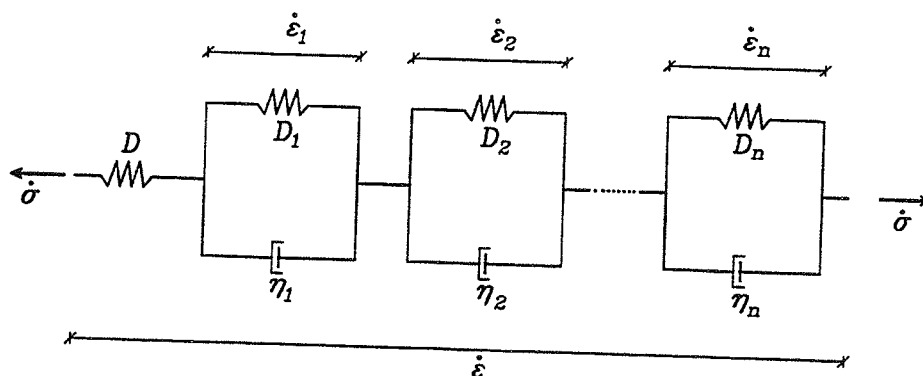
The basis for the creep model is the rheologic model shown in Fig. 1 and the elements are n Kelvin cells, each with a stiffness matrix D_n and a viscosity matrix η_n, and an initial spring of stiffness D. The properties are functions

---

[1]Department of Structural Engineering and Materials, Technical University of Denmark, DK-2800, Lyngby, Denmark.

of time and then the behavior of a Kelvin cell is given by the differential equation

$$\ddot{\varepsilon}_n + \eta_n^{-1} \left(D_n + \dot{\eta}_n \right) \dot{\varepsilon}_n = \eta_n^{-1} \dot{\sigma}$$

where ε_n are the column matrices of strain in cell number n, σ is the column matrix of stress and a superimposed dot denotes derivative with respect to time. This form of the differential equation is based on the incremental process of hydration where new layers of cement gel are deposited on the porewalls of older cement gel and adding stiffness to the concrete. Solving the differential equation we get the constitutive model

$$\dot{\sigma} = D \left(\dot{\varepsilon} - \dot{\varepsilon}_i \right)$$

where $\dot{\varepsilon}_i$ are the sum of strains in the n Kelvin cells and termed the initial strains. The model characterises the material behavior with a linearisation of the properties.

The coupling between creep and temperature is included in the model using the activation energy principle, [2]. The elastic moduli, D_n, are assumed to depend on the concrete skeleton only and then an increased temperature influences through a higher hydration rate. In excess of the skeleton the viscosities, η_n, are also assumed to depend on the state of the moisture and then a higher temperature reduces the viscosities. The adjustment of the properties has the form

$$D(T) = D_0 \, f(T) \qquad\qquad \eta(T) = \eta_0 \, g(T)$$

where T is the temperature, f, g are the scaling functions and D_0, η_0 are reference values at the temperature, T_0.
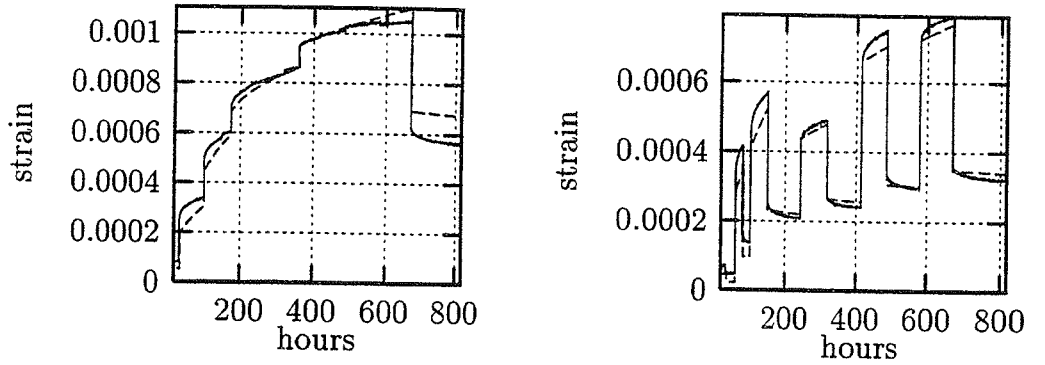

Figure 2: Creep at a variable stress history.

Examples

The proposed model has been used to fit some one-dimensional creep measurements provided by The Danish Technological Institute and the results are shown in Fig. 2. The concrete was loaded after 14 hours of hydration at 20 °C. Creep at three different constant temperature levels have also been analysed with the model and the result is shown in Fig. 3. These data are provided by Nagoya Institute of Technology, Japan. The model used to fit
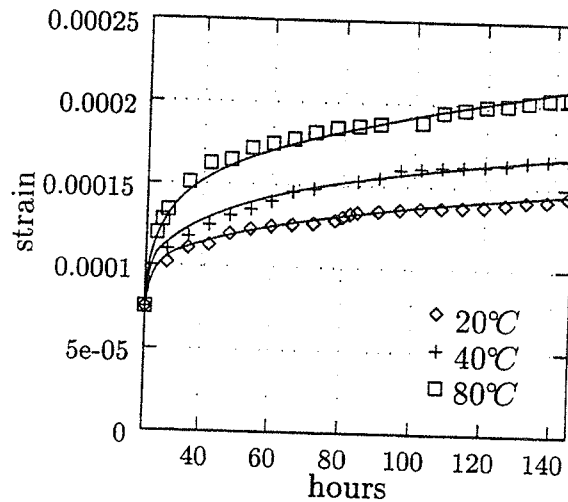

Figure 3: Creep at different constant temperature levels.

the data consists of a Kelvin cell, an initial spring and a single dashpot and the parameters have a physical analogy to the process of hydration.

Standard Modelling of Aging Materials

In standard aging creep modelling the basis is the compliance function which is expanded in exponential or potential functions. This expansion may be interpreted as a rheologic model with time dependent properties but as the properties emerge as a result of mathematics they may violate physical requirements, e.g. by decreasing in certain intervals. In the present approach the rheologic model is used directly and the properties are not allowed to decrease.

The compliance function depend on the complete history including all factors and a separation of the influence of individual factors is difficult and may lead to the same physical violations mentioned earlier. The compliance function approach implies that all memory of the process is retained in the model whereas the new approach only has memory through the material properties

and the stress in the damper. Our model can be given additional memory by introducing variables, which contain some weighted sums of previous states. In Fig. 4 an illustration of such memory variables is given. Work in this field is in progress.
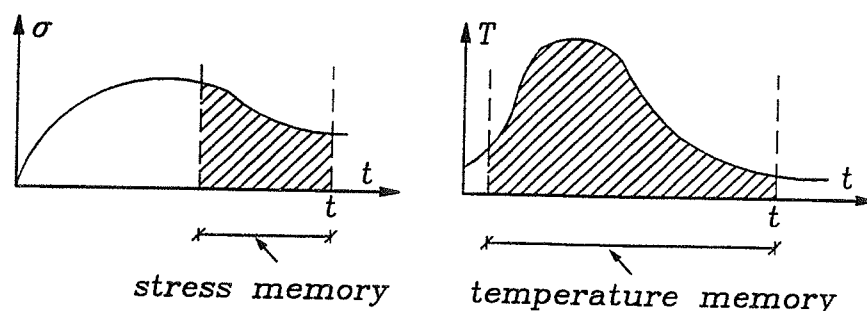
Figure 4: Memory variables.

Normally when generalising the compliance function to 3D analysis a constant Poisson ratio is assumed and this means that the deformations become proportional. With matrices for the generalisation we may have different creep rates for normal and shear strains.

Conclusion

Early age concrete is a material of the aging type where the properties develop in time as a result of the hydration process. A basis for numerical modelling is discussed where the couplings of the factors of importance are considered. A directly incremental model for creep is derived and the behavior of the model is illustrated with examples. Finally standard creep modelling is compared with the proposed model in terms of e.g. the compliance function and the memory of the material.

References

[1] Emborg, M., (1989). *Thermal stresses in concrete structures at early ages*, Doctoral Thesis, Division of Structural Engineering, Luleå University of Technology.

[2] Freiesleben Hansen, P., (1978). *Hydration Technology - 2*, (in danish), Aalborg Portland og BKF-centralen, Denmark.

Prediction of Bending Response of Wood Experiencing Compressive Strain Localization

Johannes Sand Poulsen

Department of Structural Engineering and Materials
Technical University of Denmark, Lyngby, Denmark

1 Introduction

When wood is exposed to compression parallel to the grain, strain localization will occur at some point during the load history, see e.g. (Hoffmeyer 1990). Even though timber structures usually fail by development of cracks, i.e. the ultimate failure is governed by tension and shear characteristics such as fracture toughness, strain localization in compression has a major influence on both the failure load and the type of failure because strain localization induces redistribution of the stress and strain fields.

In wood without defects the critical strength in uniaxial compression in the fiber direction can be as low as 30 % of the tensile strength. In compression microbuckling of fibers is the dominating failure mode which is governed by a shear mode that localizes into a kink band, see e.g. (Budiansky & Fleck 1993) and (Poulsen & Byskov 1996).

The stress–normalized deformation response of a typical uniaxial compression experiment is shown in Fig. 1.
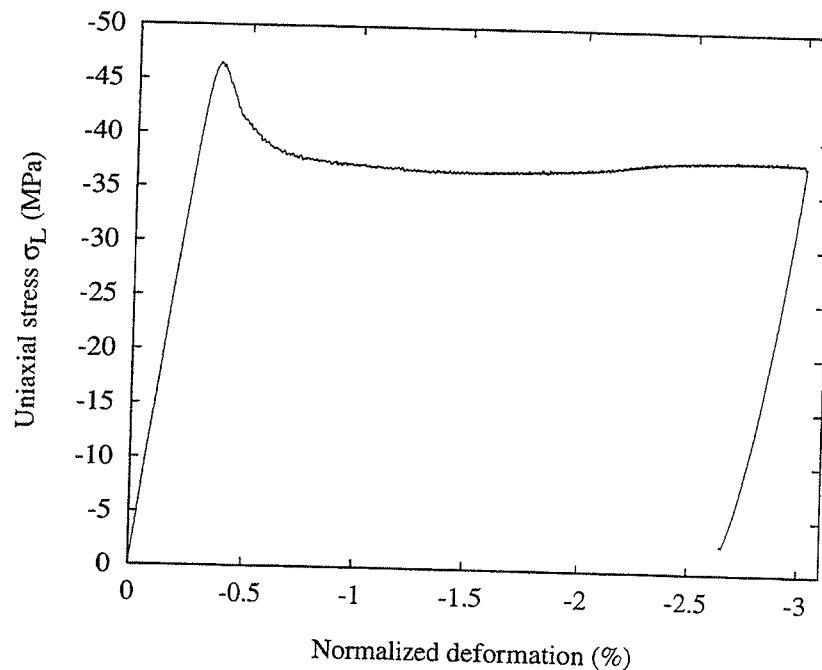

Figure 1: Typical response of uniaxial compression experiment.

When a wood beam, where tensile strength is several times higher than the compressive strength, is subjected to bending strain localization will occur in the compressive side of the beam. It is the response of such a beam that is investigated in this paper.

129

2 Modeling strain localization

A compressive constitutive response as shown in Fig. 1 together with strain localizatic can lead to numerical problems in finite element calculations. If the stress–strain curve simply implemented into the elements in the finite element code the solution found wi depend on the element mesh and the way the load is incremented, see e.g. (Pietruszcza & Mroz 1981). This is because the size of the localization zone will be determined b the element size. We solve this problem by using so-called interface elements between th finite elements. With the interface placed perpendicular to the fiber direction we can easil correlate the overall stress–strain relation to the response of the interface elements.

This approach has previously been used to investigate void nucleation between particle by interfacial decohesion, (Needleman 1987). It is, however, believed that this is the firs time this approach has been used to model compressive strain localization.

If we imagine two material points A and B on each side of the interface, initially havin the same coordinates, we can define the displacement difference across the interface a $\Delta\mathbf{u}_{AB}$. The normal and shear components of the displacement difference can be determine as

$$u_n = \mathbf{n} \cdot \Delta\mathbf{u}_{AB} \tag{1}$$

$$u_t = \mathbf{t} \cdot \Delta\mathbf{u}_{AB} \tag{2}$$

where $\mathbf{n}$ is the unit normal vector to the interface and $\mathbf{t}$ is the unit vector perpendicula to $\mathbf{n}$. Negative u_n corresponds to interfacial overlap. The normal and shear tractions, T_n and, T_t, can be expressed as

$$T_n = \mathbf{n} \cdot \mathbf{T} \tag{3}$$

$$T_t = \mathbf{t} \cdot \mathbf{T} \tag{4}$$

where $\mathbf{T}$ is the traction field. The normal and shear tractions depend on the displacemen differences, $\Delta\mathbf{u}_{AB}$, through the constitutive relations.

The constitutive relations are specified independently for the interface and the mate rial outside the interface. For the wood outside the interface the constitutive equation i taken to be orthotropic and linear elastic. The constitutive relations for the interface ar constructed so that for increasing interfacial compaction. the traction across the interfac follows the behavior determined by experiments. This means that the response of the in terface in compression is determined from the stress–strain curve in Fig. 1 after subtractio of the elastic contributions. In tension the interface will behave linear elastic until fracture In Fig. 2 a piecewise linear relation between normal traction and displacement is given.

For simplicity, the shear traction–displacement relation for the interface is taken to b linear elastic. Another relation such as linear elastic–ideal plastic could easily be specified but since the maximum shear traction is not reached in the interface this is of no interes in the present context.

Our constitutive model assumes that the normal traction response is independent o shear tractions. This approximation is in good accordance with experiments (van de Put 1993).
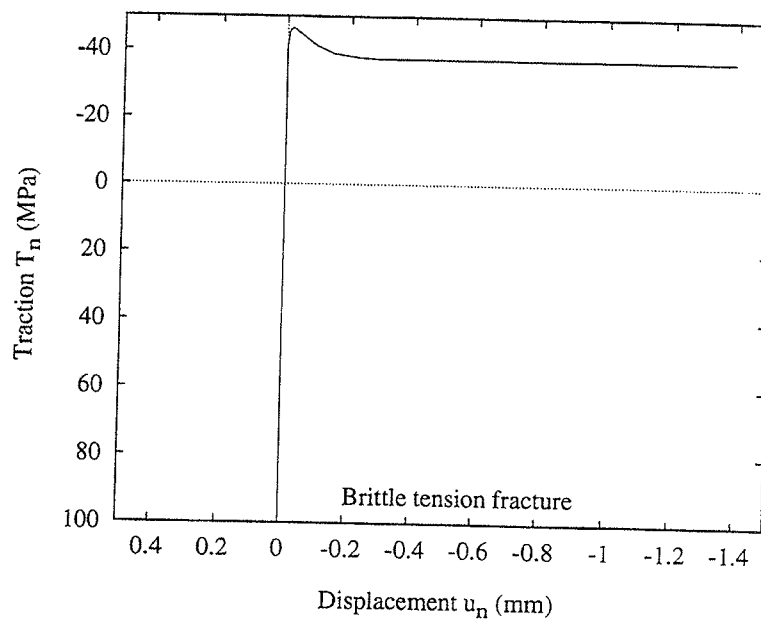
Figure 2: Constitutive relation for normal traction and displacement in interface.

The finite element code used is the commercial FEM program DIANA[1] which contains interface elements in which the above described characteristics can be adapted.

In the finite element calculations we apply the curvature of the beam as a prescribed deformation at one end. The beam must be given the possibility to compensate for the difference between the neutral axis and geometric symmetry line when strain localization takes place, otherwise axial forces will develop. This is handled by letting the supports at one end be at an angle to the fiber direction, as illustrated in Fig. 3. Thereby no axial force can arise because the beam is allowed to move in the fiber direction.
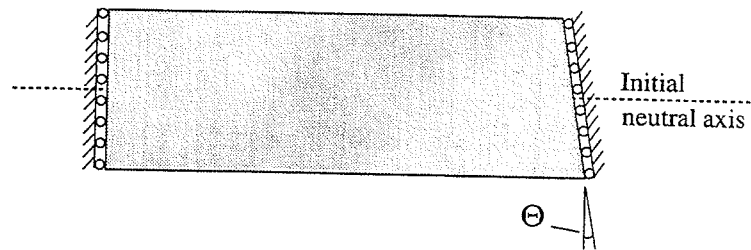
Figure 3: Prescribed deformation, Θ, and inclined support.

3 Results and Concluding Remarks

In Fig. 4 the numerical result obtained is compared with an experimental result. The figure shows very good agreement between numerical and experimental results. The strength and stiffness parameters used are mean values from compression experiments and are thus not taken from the particular experiment shown in Fig. 4.

---

[1]Trademark of TNO Building and Construction Research – Department of Computational Mechanics, The Netherlands

Our numerical calculations were terminated when the tensile stress reached 2.5 tim€ the peak compressive strength. The experiment shown in Fig. 4 had a load carryir capacity in bending of twice the elastic moment. This equals a tensile strength three tim€ the compressive strength.

It seems that implementing compressive strain localization as described in this pap€ using interface elements yields good results.
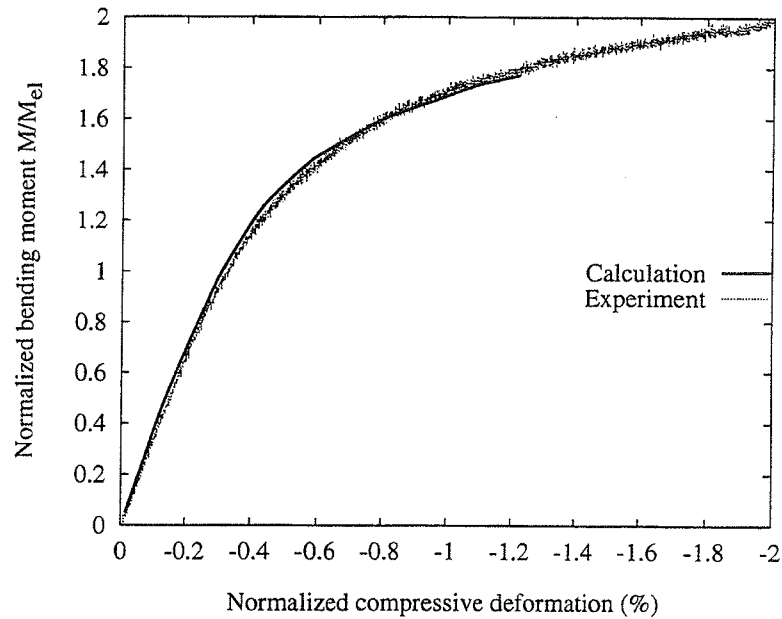
Figure 4: Result of bending calculation compared with experimental result.

References

Budiansky, B. & Fleck, N. A. (1993). Compressive failure of fibre composites, *J. Mecl Phys. Solids* **41**(1): 183–211.

Hoffmeyer, P. (1990). *Failure of Wood as Influenced by moisture and duration of Loa(* PhD thesis, State University of New York, Syracuse, New York.

Needleman, A. (1987). A continuum model for void nucleation by inclusion debonding, ⌐ *Appl. Mech.* **54**: 525–531.

Pietruszczak, S. & Mroz, Z. (1981). Finite element analysis of deformation of strain softening materials, *Int. J. num. Meth. Engng.* **17**: 327–334.

Poulsen, J. S. & Byskov, E. (1996). Micromechanical modeling of inclined localized kin band in clear wood, *Proceedings of the Fourth international Conference on Computer aided Assessment and Control*, Localised Damage '96, Fukuoka, Japan, pp. 435–442

van der Put, T. A. C. M. (1993). Explanation of the failure criterion for wood, *COST 50 Wood Mechanics Workshop on "Wood : Plasticity and Damage"*, April 1-2,, Limericl Ireland, pp. 229–250.

Numerical Simulation of Initial Defibration of Wood

Stefan Holmberg, Hans Petersson

Division of Structural Mechanics, LTH, Lund University, Lund, Sweden

Introduction

The objective in producing pulp is to separate the wood fibers and give them properties suitable for making paper. A process important in pulp manufacturing is that of refining or defibration. In manufacturing refiner pulps, wood chips are fed, randomly oriented, to the centre of two rotating refiner discs, see Figure 1. The chips are successively disintegrated, the fibers being separated while moving towards the periphery of the discs.

The huge energy consumption required in manufacturing refiner pulps is a serious drawback. The mechanisms basic to the defibration process are incompletely known. The present investigation aims at obtaining fundamental insight into the mechanics of the initial defibration, insight that can be used in efforts to optimize the process currently employed and to develop new processes and equipment in this area. The project involves both experimental and numerical work.
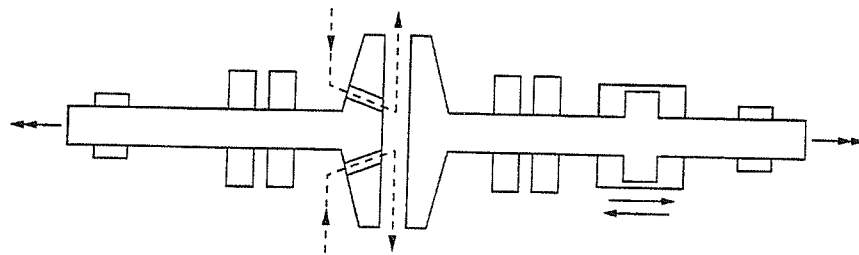
Figure 1: *Basic plan of a double-disc refiner.*

Experimental Work

The experimental investigation aimed at obtaining a better understanding of the mechanical behaviour of wood loaded perpendicular to the grain and at illustrating the complex loading conditions present in the initial defibration process. The test setup and sample dimensions were chosen in light of the geometry of typical refiner segments. The test setup is shown schematically in Figure 2. The specimen is placed between two steel plates, the test being run by moving the lower plate horizontally while the upper one remains fixed. The specimen is thus subjected to a shear

loading resembling the loading that the two rotating discs exert on the wood chips in a refiner. It should be emphasized that the tests were carried out for a very low loading rate, one of 0.02 mm/s, whereas the loading rate in a refiner can be as high as 100 m/s. Optical equipment was used to photograph the specimens during testing so as to reveal deformations and fracturing of the material.

Figure 2: *Schematic view of test setup.*

Material Modelling

From the experimental investigation it could be concluded that the following material characteristics need to be taken into account in order for proper modelling of the initial defibration process to be achieved.
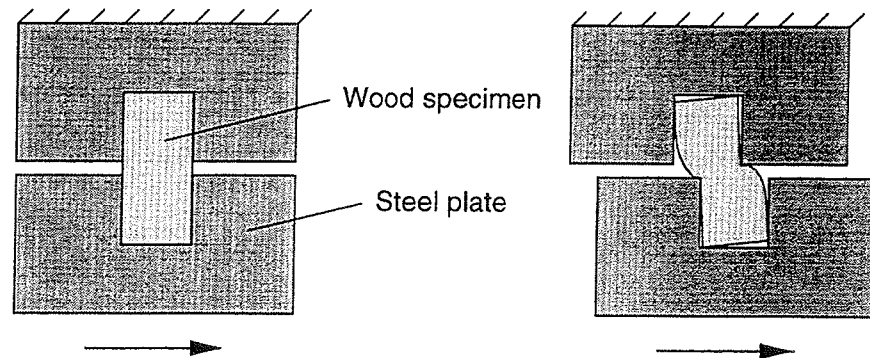
- The inhomogeneity of the material.

- The nonlinear inelastic response of earlywood when subjected to compression.

- The fracture mechanical behaviour of the material.

The material's inhomogeneity is taken into account by separating the wood into zones of earlywood and latewood, for which separate material models are employed. The earlywood zones are also subdivided in the radial direction into several layers differing slightly in their stiffness and strength properties. This is done to at least partly capture the strain localization that arises when earlywood is subjected to compression.

The response of earlywood subjected to compression perpendicular to the grain is typical for that of cellular materials. The resulting stress-strain relation is characterized by an initial linear region, followed by a plateau region with only slightly increasing stress, and finally a region of rapidly increasing stress, corresponding to the material being densified. To model this behaviour, a finite strain plasticity model was employed. That model, developed for analysis of crushable foams, is based on non-associative compressible plasticity. It uses a yield surface with an elliptical dependence of deviatoric stress on pressure stress. The evolution of the yield surface is controlled by the inelastic volume strain experienced by the material. The flow potential used gives a direction of flow identical to the stress direction for radial paths.

134

Fracture of the material is taken into account by use of a fictitious crack model (FCM). The fracturing properties are thus projected onto distinct cracking surfaces, softening stress-relative displacement relations being employed. The model is a mixed-mode expansion of bi-linear one-dimensional stress-displacement relations. This fictitious crack model is implemented in the finite element simulations by introducing special crack elements between the standard solid elements. In the present applications, the crack elements may be subjected to non-negligible rotations compared to their orientation in the initial configuration. In order to take this into account, a local rotating coordinate system is introduced. From this local system a transformation matrix is constructed for transforming the element equations.

The modelling of the material can be summarized as follows:

- Earlywood - Crushable foam plasticity combined with a fictitious crack model.

- Latewood - Linear elastic behaviour combined with a fictitious crack model.

Finite Element Analysis

The problem was analysed as a two-dimensional static one under plane strain conditions. First-order solid elements were employed: 4-noded bilinear quadrilateral elements for the latewood zones and 3-noded linear triangular elements for the earlywood. Crack elements were introduced between the solid elements at locations where large tensile and/or large shearing stresses occurred. When the strength of the material was reached, these elements captured the softening behaviour of the material. The two steel plates in the tests were modelled as rigid surfaces. A Coulomb friction model was employed, the coefficient of friction between the steel plates and the specimen being set to 0.25. The Newton Raphson method was used in solving the non-linear equations. The simulations were performed using the implicit version of ABAQUS.

Results

The major part of the deformation- and fracture processes that occurred could be predicted by the simulations. Numerical difficulties due to the large deformations, the complex material behaviour and the contact conditions arise when simulations of this sort are performed. The numerical technique that was employed did not make it possible to fully simulate the behaviour of the specimens during the complete course of events.

In comparing the results of the simulations with the experimental results, it could be concluded that the deformation- and fracture processes predicted by the simulations and the load-displacement curves obtained were in good agreement with the experimental results. This is shown for a 5 mm high specimen in Figures 3 and 4. In Figure 3, the simulated fracturing of the specimen is compared with that of a typical specimen from the corresponding test series. In figure 4, the horizontal load versus displacement relation is compared with the relations obtained in the experiments

135

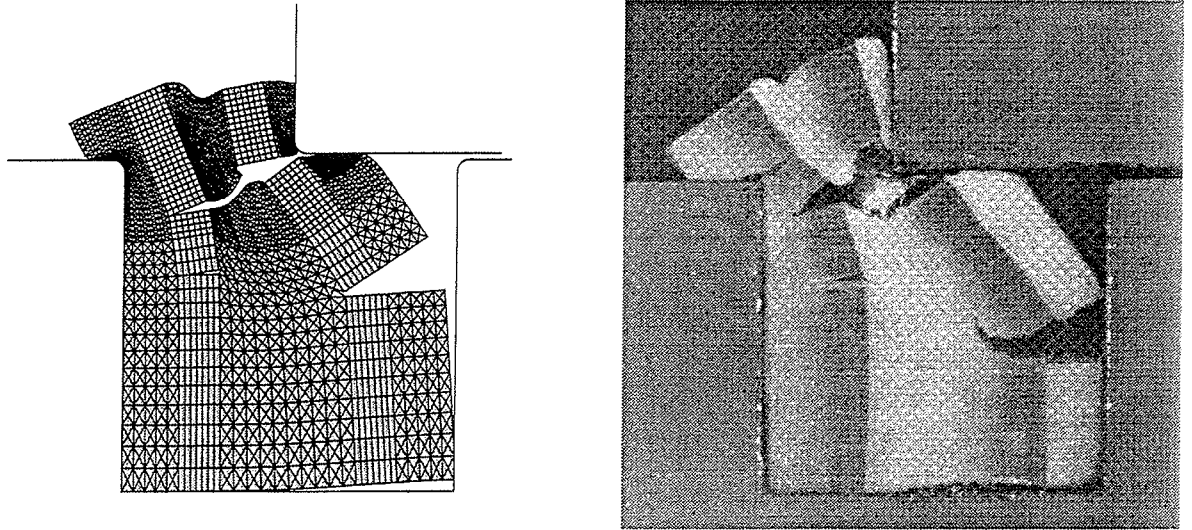Figure 3: *Comparison of numerical simulation with experimental results. Fracturing of a 5 mm high specimen.*
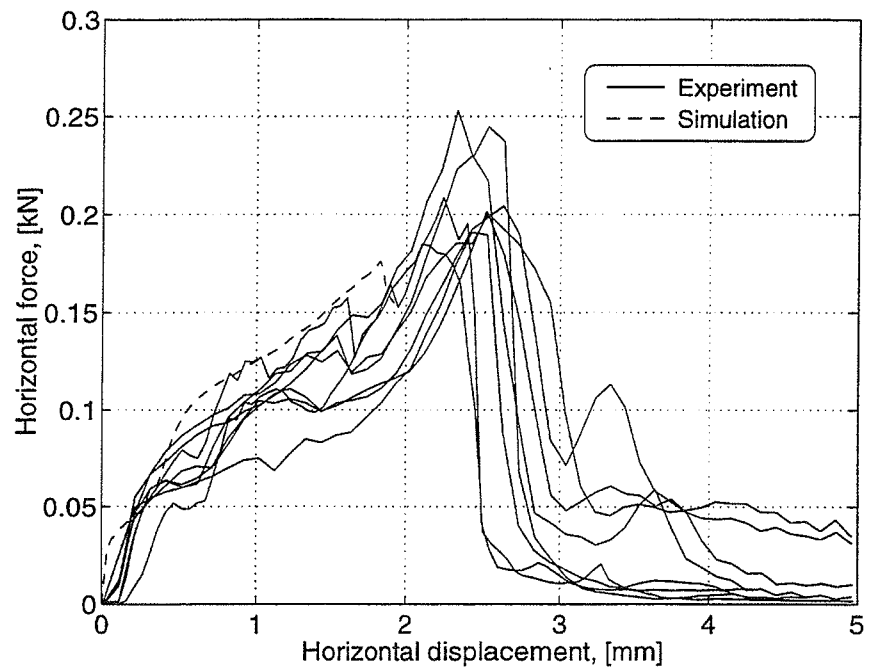

Figure 4: *Comparison of numerical simulation with experimental results. Load-displacement curves for 5 mm high specimens.*

References

Holmberg, S. *Deformation and Fracture of Wood in Initial Defibration Processes.* Report TVSM-3019, Lund Institute of Technology, Division of Structural Mechanics, Lund 1996.

Extended two-dimensional element formulation for beam analysis

O. Dahlblom   *Division of Structural Mechanics*
S. Ormarsson   *Lund Institute of Technology, Lund University*
H. Petersson   *Box 118, S-221 00 Lund, Sweden*

ABSTRACT

An extended two-dimensional finite element formulation for beam cross-section analysis is proposed. In the formulation stresses as well as deformation in the direction perpendicular to the plane analysed are considered. The formulation is applied to simulation of the deformation development of a wooden beam during change of moisture content.

INTRODUCTION

One characteristic of wood is that its behaviour is strongly orthotropic due to the internal structure of the material and very much affected by changes of moisture content. In addition, material properties such as moisture elongation coefficient and elastic modulus vary with the position. This often yields bad shape stability of wooden products. To gain knowledge about the extent to which different parameters affect the deformation development, it is of interest to perform computer simulations. Three-dimensional modelling gives valuable information about development of deformation during moisture variation, see e.g. Ormarsson (1995), Dahlblom et al. (1996a), Ormarsson et al. (1995, 1996). In some situations, when interest is focussed primarily on deformations and stresses of a cross section, and when property variations in the longitudinal direction may be neglected, a two-dimensional simulation may be sufficient. In two-dimensional modelling it is commonly assumed that either plane stress conditions or plane strain conditions are applicable. In a wooden beam during moisture change neither of these assumptions is normally fulfilled. Therefore, an extended two-dimensional formulation should be applied, where both longitudinal strains and longitudinal stresses are considered.

MATERIAL PROPERTIES

Numerical simulation of the deformation process of wood during moisture change requires a proper constitutive model. The orthotropic structure of the material, with different properties in the radial, tangential and longitudinal directions has to be considered. The present work is focussed on two-dimensional simulations and it is assumed that the fibres are perpendicular to the cross-sectional plane studied. Furthermore, it is assumed that the shear strains in the *lt*- and *lr*-planes are negligible. This means that the constitutive model only has to include four components of strain and stress. In the constitutive model, the total strain rate $\dot{\varepsilon}$ is assumed to be

$$\dot{\varepsilon} = \dot{\varepsilon}_e + \dot{\varepsilon}_w + \dot{\varepsilon}_{w\sigma} \qquad (1)$$

where the elastic strain rate $\dot{\varepsilon}_e$ is related to the stress rate by Hooke's law, i.e.

$$\dot{\varepsilon}_e = C\dot{\sigma} \qquad (2)$$

the moisture-induced strain rate $\dot{\varepsilon}_w$ is assumed to be

$$\dot{\varepsilon}_w = \alpha\dot{w} \qquad (3)$$

and the so-called mechano-sorptive strain, occurring due to moisture changes in material exposed to stress, is assumed to be given by

$$\dot{\varepsilon}_{w\sigma} = (\kappa\sigma - \frac{1}{s_{max}}\beta(\varepsilon - \varepsilon_w))\,|\dot{\varepsilon}_{w,t}| \qquad (4)$$

137

which for plane stress conditions has been proposed by Mårtensson and Svensson (1995). The matrices C, α, κ and β contain material parameters and $\dot{w}$ denotes the rate of change of moisture content. Eqs. (1) and (2) can be combined to form

$$\dot{\sigma} = D\dot{\varepsilon} - \dot{\sigma}_0 \qquad (5)$$

where

$$D = C^{-1} \qquad (6)$$

$$\dot{\sigma}_0 = D(\dot{\varepsilon}_w + \dot{\varepsilon}_{\sigma w}) \qquad (7)$$

The stress-strain relation given by Eq. (5) has been expressed in a system of coordinates with the axes in the orthotropic directions. Due to the annual ring structure of wood, these directions vary with position, and the stress-strain relation has to be transformed in order to be expressed with respect to a global system of coordinates with the axes x and y. The stress-strain relation with respect to global coordinates can be expressed as

$$\dot{\bar{\sigma}} = \bar{D}\dot{\bar{\varepsilon}} - \dot{\bar{\sigma}}_0 \qquad (8)$$

where

$$\bar{D} = G^T D G \qquad (9)$$

$$\dot{\bar{\sigma}}_0 = G^T \dot{\sigma}_0 \qquad (10)$$

in which G is a transformation matrix.

FINITE ELEMENT FORMULATION

The formulation is based on a three-dimensional eight-node solid element with 24 degrees of freedom, see Fig. 1.
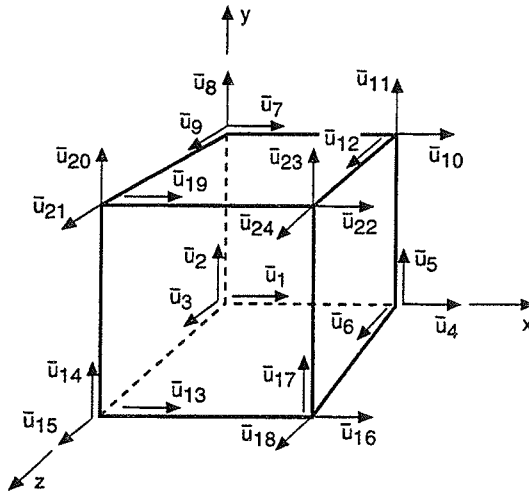

FIGURE 1. Three-dimensional eight-node solid element.

A finite element formulation for simulation of formations and stresses is given by

$$\bar{K}_e \dot{\bar{u}} = \dot{\bar{P}}_e + \dot{\bar{P}}_{e0} \qquad (1$$

where

$$\bar{u} = [\bar{u}_1 \ \bar{u}_2 \ ... \ \bar{u}_{24}]^T \qquad (1$$

$$\bar{K}_e = \int_V B^T \bar{D} B \, dV \qquad (1$$

$$\dot{\bar{P}}_e = \int_S N^T \dot{t} \, dS + \int_V N^T \dot{f} \, dV \qquad (1$$

$$\dot{\bar{P}}_{e0} = \int_V B^T \dot{\bar{\sigma}}_0 \, dV \qquad (1$$

with

$$B = \tilde{\nabla} N \qquad (1$$

$$\tilde{\nabla} = \begin{bmatrix} \frac{\partial}{\partial x} & 0 & 0 \\ 0 & \frac{\partial}{\partial y} & 0 \\ 0 & 0 & \frac{\partial}{\partial z} \\ \frac{\partial}{\partial y} & \frac{\partial}{\partial x} & 0 \end{bmatrix} \qquad (1$$

Description of shape functions for this element type can be found in e.g. Zienkiewicz and Taylor (1989). To obtain a two-dimensional formulation the shear strains in the xz- and yz-planes are assumed to be zero. The degrees of freedom may be expressed by new degrees of freedom (see Fig. 2) as

$$\begin{aligned} \bar{u}_1 &= \bar{u}_{13} = u_1, & \bar{u}_2 &= \bar{u}_{14} = u_2, \\ \bar{u}_4 &= \bar{u}_{16} = u_3, & \bar{u}_5 &= \bar{u}_{17} = u_4, \\ \bar{u}_7 &= \bar{u}_{19} = u_5, & \bar{u}_8 &= \bar{u}_{20} = u_6, \\ \bar{u}_{10} &= \bar{u}_{22} = u_7, & \bar{u}_{11} &= \bar{u}_{23} = u_8 \end{aligned} \qquad (1\text{\$}$$

The next step is to introduce restrictions for the degrees of freedom in the longitudinal direction z. It is assumed that

$$\bar{u}_3 = \bar{u}_6 = \bar{u}_9 = \bar{u}_{12} = 0 \qquad (1\text{\textsterling}$$

The remaining displacements in the z-direction $\bar{u}_{15}$, $\bar{u}_{18}$, $\bar{u}_{21}$, $\bar{u}_{24}$ are expressed as

$$\bar{u}_m = b_1 + y_m b_2 - x_m b_3 \qquad (2\text{C}$$

where $\bar{u}_m$ is the displacement, and x_m and y_m define the position of the nodal point, and b_1, b_2 and b_3 are new degrees of freedom which will be common for the whole cross section (see Fig. 2).
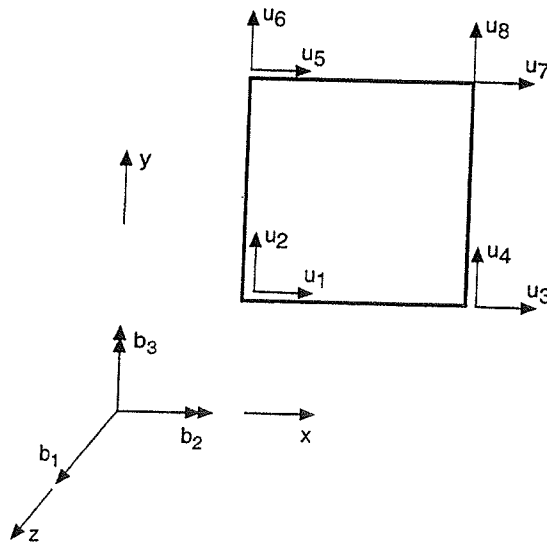
FIGURE 2. Two-dimensional element with 11 degrees of freedom.

The relations given by Eqs. (18), (19) and (20) can be expressed in matrix form as

$$\bar{u} = G_e u \tag{21}$$

where

$$u = [u_1 \; u_2 \; u_3 \; u_4 \; u_5 \; u_6 \; u_7 \; u_8 \; b_1 \; b_2 \; b_3 \;]^T \tag{22}$$

The finite element equations for the two-dimensional element with 11 degrees of freedom shown in Fig. 3 can now be expressed as

$$K_e \dot{u} = \dot{P}_e + \dot{P}_{e0} \tag{23}$$

where

$$K_e = G_e^T \bar{K}_e G_e \tag{24}$$

$$\dot{P}_e = G_e^T \dot{\bar{P}}_e \tag{25}$$

$$\dot{P}_{e0} = G_e^T \dot{\bar{P}}_{e0} \tag{26}$$

This element has 8 degrees of freedom which are handled just like a common two-dimensional element and, in addition, 3 degrees of freedom which are common for all elements in the cross section. This means that the global system of equations obtained when all elements are assembled has a displacement vector which has only three components more than when a common two-dimensional element is used.

NUMERICAL RESULTS

The theory described above has been applied to the cross section shown in Fig. 3. Displacements

in the transversal directions are prescribed to avoid rigid body motions only. The input parameters used are presented in Dahlblom et al. (1996b). The initial moisture content was assumed to be 0.27 and results from moisture simulations using the method proposed by Claesson and Arfvidsson (1996) have been used as input data to the displacement simulation. The simulation was performed for two different drying schedules; Schedule 1: $T = 60°C$, $RH = 50$ % for 192 h and Schedule 2: $T = 60°C$, $RH = 80$ % for 96 h and $RH = 50$ % for the next 96 h. The computed deformations after drying 192 h with schedule 1 are illustrated in Fig. 4. The cross section has developed a significant cup deformation.
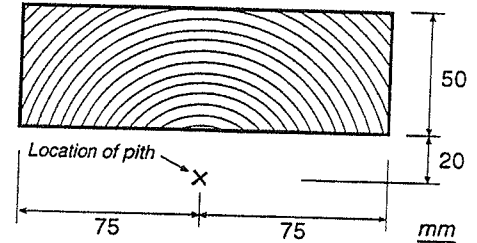
FIGURE 3. Cross section of the board studied.
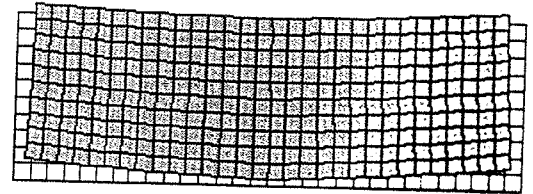
FIGURE 4. Computed deformation after drying 192 h with schedule 1.

The development of cup deformation, defined as $a_{cup} = \frac{1}{2}(a_1 + a_3) - a_2$ where a_1 and a_3 are vertical displacements of the upper-left and upper-right corners and a_2 is vertical displacement of the mid-point of the upper edge, is for the two drying schedules shown in Fig. 5. In addition to cup deformation, the formulation used yields information about bending, commonly referred to as bow and crook. The bow deformation a_{bow}, defined as midpoint transversal displacement of a beam supported at the end-points, is given by $a_{bow} = \frac{l^2}{8l_z}b_2$ where l is the beam length and l_z is the element size in the z-direction. Assuming $l = 3.0$ m, the bow development is illustrated in Fig. 6. The simulations performed consider stresses in the longitudinal direction. The distribution of longitudinal stresses after drying 192 h with schedule 1 is illustrated in Fig. 7. It can be observed that the central part of the cross section is exposed to tensile stresses, and the left and right parts are exposed to

139

compressive stresses. This is due to the higher value of the longitudinal shrinkage coefficient close to the pith.

FIGURE 5. Development of cup deformation according to schedule 1 (solid) and schedule 2 (dashed).

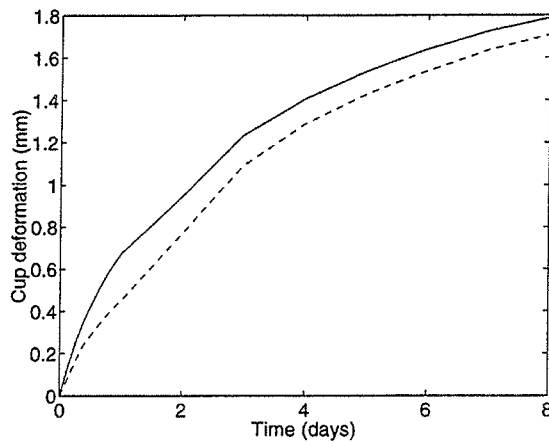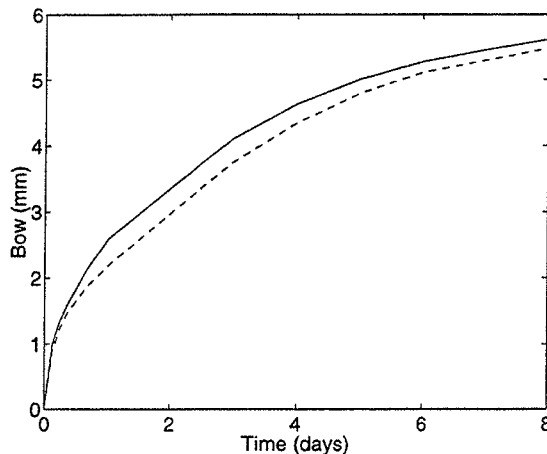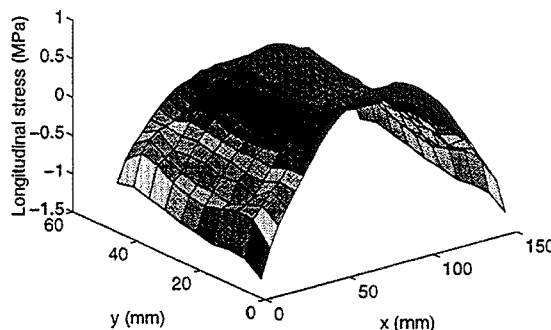FIGURE 6. Development of bow deformation according to schedule 1 (solid) and schedule 2 (dashed).

FIGURE 7. Distribution of longitudinal stresses after drying 192 h with schedule 1.

CONCLUSIONS

An extended formulation for two-dimension simulation has been presented and the capabili of the computational method to simulate defo mation development during moisture variation h; been indicated. In contrast to conventional tw dimensional formulations, assuming plane strain (plane stress, the extended formulation considers lo; gitudinal stresses, as well as longitudinal strains r sulting in bending. This is obtained with a sm; increase of the computational effort.

REFERENCES

Claesson, J.; Arfvidsson, J. 1996: The Lund woc drying model: Phenomenological analyses an comparison with experiments, In: 5th IUFR international wood drying conference, Quebec

Dahlblom, O.; Ormarsson, S.; Petersson, H. 1996; Simulation of wood deformation processes i drying and other types of environmental loac ing, Annales des Sciences Forestières, Vol. 5; No. 4. pp. 857-866.

Dahlblom, O.; Ormarsson, S.; Petersson, H. 1996l Prediction of deformations in wood during dr; ing by an extended two-dimensional formul; tion, In: 5th IUFRO international wood dryin conference, Quebec.

Mårtensson, A.; Svensson, S. 1995: Stress-strain r(lationship of drying wood, Submitted for publ cation in Journal of Materials in Civil Enginee; ing, ASCE

Ormarsson, S. 1995: A finite element study of th shape stability of sawn timber subjected t moisture variations, Report TVSM-3017, Div sion of Structural Mechanics, Lund Universit; Lund.

Ormarsson, S.; Dahlblom, O.; Petersson, H. 199; Numerical simulation of moisture induced d(formation in wood, NSCM VIII, Göteborg.

Ormarsson, S.; Dahlblom, O.; Petersson, H. 199(Influence of annual ring orientation on shap stability of sawn timber, In: 5th IUFRO inte; national wood drying conference, Quebec.

Zienkiewicz, O. C.; Taylor, R. L. 1989: The finite e; ement method, fourth editon, Vol. 1. McGraw Hill, London.

140

PLASTIC CALCULATION MODELS OF CONTINUOUS PURLINS

Markku Laine, M.Sc.
Tampere University of Technology
Box 600
SF-33101 Tampere, Finland
email:markku3@junior.ce.tut.fi

ABSTRACT

According to [1], Eurocode 3; Part 1.3, redistribution of internal forces and moments can be utilized in dimensioning of purlins at the ultimate limit state, if the dimensioning is based on experimentally derived (M,θ)-graphs. Two different behaviour types are studied: softening moment resistance and ideally plastic (M,θ)-relation. (M,θ)-relation is obtained from the support detail test and design curve for (M,θ)-relation is valitated in the full scale test. Ultimate load yielding from the softening moment resistance model is only few percents larger than the corresponding one resulting from the ideally plastic model in the example case.

INTRODUCTION

Cold-formed thin-walled members are widely used in roofing systems. Plastic dimensioning allows full exploitation of the potential of the cross-section. The paper deals with dimensioning models of gravity loaded cold-formed thin-walled multi-span purlins of C-, Z- or Zeta cross-section with continuous full lateral restraint to one flange.

According to [1] (M,θ)-graphs must be derived from tests. Rotation capacity, interaction of bending moment and shear force and softening behaviour $((M,\theta)$-relation) are studied in the internal support test [1], in which a simply supported beam is loaded with a point-load F at the mid-span. The span s is 0.4L, and it represents the portion of purlin between the points of contraflexure on each side of the internal support, L is the actual span of the purlin. Finite element analysis can be used in the simulation of the internal support tests in order to study the effect of the shear force to the bending moment capacity of the purlin and on the softening behaviour of the purlin at the internal support.

Ultimate state is reached, when mechanism appears: purlin yields in the span in addition to the yielding at the support. The relation between the bending moment M and the plastic rotation θ can be supposed to be either a softening one or ideally plastic (Fig. 1). The ideally plastic model can be used in hand calculations but for the softening model computer calculations are needed. The softening (M,θ)-relation yields safe ultimate load for the full scale test structure. The constant bending moment at the internal support M_{rest} is determined from the softening (M,θ)-relation by using the estimated maximum rotation in practice (e.g. $2°-3°$).
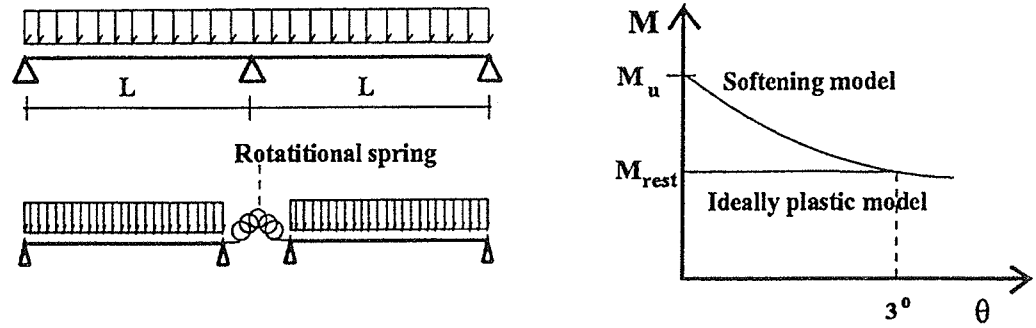
Fig. 1. Example beam, softening moment resistance model and ideally plastic one.

EXAMPLE CASE

Analytical equations (1) and (2), which are derived for the case shown in Fig. 1, are use in comparison of the plastic dimensioning models. Finite element method can be used i the computation of arbitrary multi-span continuous thin-walled beam with a softenin moment resistance. A nonlinear rotational spring element can be used to define th (M,θ)-relation of the purlin at the internal support. Suitable algorithms are presented e.g in [2].

A continuous gravity loaded two-span purlin (Z250/2.0) is used as an example. The spa L is varied. The following properties were used: maximum moment in the spa M_{span}=12.368 kNm, effective second moment of area I_{eff}=5523286 mm^4 and Young' modulus E=210000 N/mm^2.

Ultimate load q_{uip} can be calculated using ideally plastic model as follows

$$q_{uip} = \frac{2}{L^2} \cdot (M_{rest} + 2 \cdot M_{span} + 2\sqrt{M_{span} \cdot M_{rest} + M_{span}^2})$$ (1

where
M_{rest} = constant bending moment at the internal support (3.463 kNm),
M_{span} = bending moment capacity in the span and
L   = span.

Corresponding rotation θ_{ip} can be calculated from

$$\theta_{ip} = \frac{L}{E \cdot I_{eff}} \left(\frac{q_{uip} \cdot L^2}{12} - \frac{2}{3} \cdot M_{rest} \right)$$ (2

where E is Young's modulus and I_{eff} is effective second moment of area.

The softening moment resistance is taken into account by using (M,θ)-relation instead o constant M_{rest} in equations (1) and (2) (M_u=5.565 kNm). Ultimate load q_u by using th ideal plastic model is 5.55 kN/m, by using the softening model 5.69 kN/m and th corresponding test gave 7.90 kN/m, when span L is 4.5 m. Ultimate load is labelled a q_{us} and the corresponding rotation as θ_s.
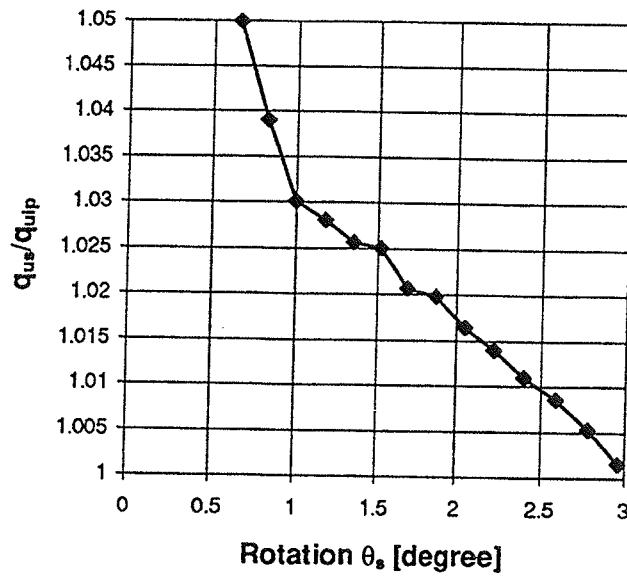
Fig. 2. $(q_{us}/q_{uip}, \theta_s)$-relation.

L (mm)	θ_s (°)
2000	0.66
2500	0.83
3000	1.00
3500	1.18
4000	1.35
4500	1.52
5000	1.69
5500	1.87
6000	2.05
6500	2.22
7000	2.40
7500	2.59
8000	2.78
8500	2.96

Fig. 3. $(\theta_s/\theta_{ip}, \theta_s)$-relation.

L (mm)	θ_s (°)
2000	0.66
2500	0.83
3000	1.00
3500	1.18
4000	1.35
4500	1.52
5000	1.69
5500	1.87
6000	2.05
6500	2.22
7000	2.40
7500	2.59
8000	2.78
8500	2.96

CONCLUSIONS

The ideally plastic model overestimates plastic rotation and underestimates ultimate load in dimensioning compared with the ones yielding from the softening moment resistance model, but the difference in design is not signifigant.

REFERENCES

[1]   ENV 1993-1-3: 1996, Supplementary rules for cold formed thin gauge members and sheeting, 1996-04-24, CEN/TC250/SC3

[2]   Thomopoulos, K.T., Mistakidis, E.S., Koltsakis, E.K., Panagiotopoulos, P.D., Softening behaviour of continuous thin-walled steel beams. Two numerical methods, J. Construct. Steel Res. Vol. 36, No 1, pp. 1-13, 1996

DIFFERENT INTERPOLATION TECHNIQUE
FOR CURVED ELEMENTS

HENRI PERTTOLA ja JUHA PAAVOLA
Laboratory of Structural Mechanics
Helsinki University of Technology
Rakentajanaukio 4A, FIN-02150 ESPOO, FINLAND

INTRODUCTION

The background of this study is in a trial to develop the analysis of curved thin-walled girders in a case where the finite element discretization is based on the theory of *Vlasov* [3] in a way suggested by the authors (*Paavola* [2]). In this formulation the displacement interpolation is spanned between certain cross-section planes, the directions of which adapt the curved geometry (Figure 1. a). In this context, we call these special cross-sections as *nodal planes*.
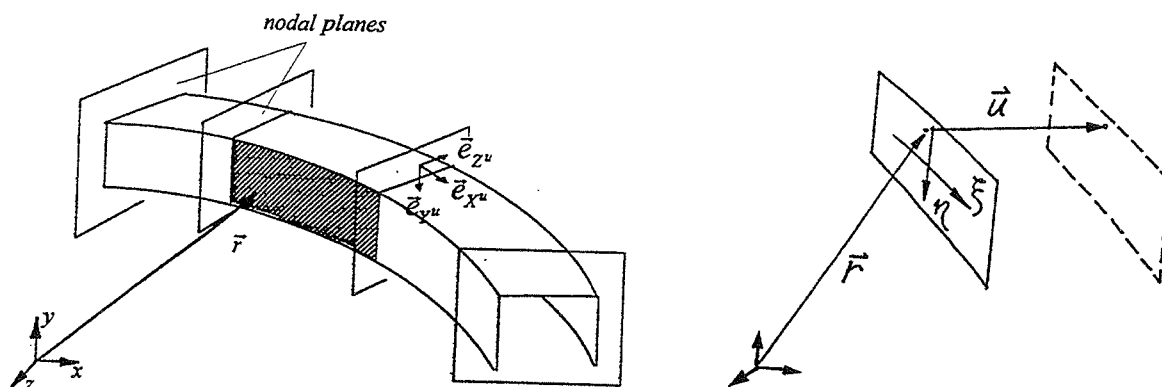
Figure 1. a) Nodal planes.   *b) ξ–η-coordinate system.*

In nodal planes the directions of the displacement components $u^o_{X^u}$, $u^o_{Y^u}$ and $u^o_{Z^u}$ are defined to coincide with the orthogonal directions of the unit vectors fixed on these planes, so that vector $\vec{e}_{X^u}$ is a normal and the other two vectors $\vec{e}_{Y^u}$ and $\vec{e}_{Z^u}$ are in these planes. Between nodal planes the corresponding directions are interpolated smoothly. Thus, the displacement vector $\vec{u}^o$ of any point on the middle surface of a wall can be written as

$$\vec{u}^o = u_{X^u}\vec{e}_{X^u} + u_{Y^u}\vec{e}_{Y^u} + u_{Z^u}\vec{e}_{Z^u}. \tag{1}$$

Now, we adopt the idea of *Vlasov* and suggest that e.g. the displacement component $u^o_{X^u}$ is presented as a series of partial products separating the dependence on the curvilinear surface coordinates ξ and η (see Figure 1 b), of which coordinate ξ corresponds the axial direction of the girder, as follows

$$u^o_{X^u}(\xi, \eta) = \sum_i \omega_i(\eta) U_i(\xi). \tag{2}$$

The other two displacement components $u^o_{Y^u}$ and $u^o_{Z^u}$ are also interpolated using the same idea of separation, which makes it possible to construct the interpolation in axial direction and in the cross-section plane separately. Hypothetically, we can describe the displacements of a cross-section as completetely as required. In this case the accuracy of the interpolation is mainly dependent on the interpolation in axial direction.

interpolated displacement components (e.g. $U(\xi)$) are defined using the local (smoothly interpolated) directions (e.g. $\vec{e}_{Xu}$) of a curved structure. This deviates from the conventional interpolation technique, where the directions of the displacement components are fixed by the global orthogonal Cartesian coordinate system in the element.

In what follows we concentrate to study the interpolation in axial direction using a simple model, where the cross-sections of the girder are supposed to be reduced to the points. Actually, only a curved girder axis is considered. To make our consideration as simple as possible we do all this in two dimensions.
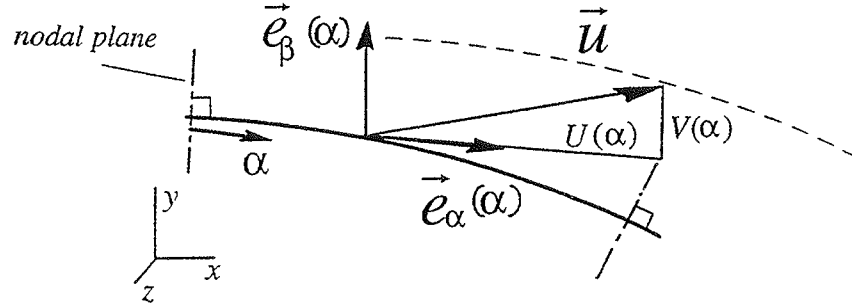

Figure 2. Girder axis as plane curve.

The curvilinear coordinate α (instead of ξ) is defined to coincide with the girder axis (Figure 2). The rectilinear normal coordinate β measures the distance from the axis. So, the coordinates α and β form an orthogonal curvilinear coordinate system. Then, let us suppose that nodal planes are normal to the axis and further, that the directions of the interpolated displacement components $U(\alpha)$ and $V(\alpha)$ are respectively $\vec{e}_\alpha$ and $\vec{e}_\beta$, which are the unit tangent vector and unit normal vector of the axis. Finally we write the displacement vector $\vec{u}$ as

$$\vec{u} = U(\alpha)\vec{e}_\alpha(\alpha) + V(\alpha)\vec{e}_\beta(\alpha). \tag{3}$$

Actually, we supposed that the displacements can be represented as a continuous vector field in the curvilinear coordinate system with the local basis $\{\vec{e}_\alpha(\alpha), \vec{e}_\beta(\alpha)\}$.

INTERPOLATION

The conventional interpolation technique

Generally, we can use finite elements to model any type of continuos tensor fields including both scalar and vector fields, which are given functions of Cartesian or of any type of curvilinear coordinates (*Oden* [1]). So, for example, we can interpolate the displacement vector $\vec{u}$ in an element as follows

$$\vec{u} = \sum_i N_i(\alpha)\vec{u}_i, \tag{4}$$

where $\vec{u}_i = \vec{u}(\alpha_i)$ are displacement vectors at nodal points (or plane) $\alpha = \alpha_i$.

In the conventional interpolation technique the directions of the interpolated displacement components are defined using a fixed Cartesian coordinate system in an element. Let us denote the corresponding base vectors with $\vec{i}$ and $\vec{j}$. The interpolation (4) can now be written in the form

$$\vec{u} = \sum_i N_i(\alpha)(u_i\vec{i} + v_i\vec{j}) = (\sum_i N_i(\alpha)u_i)\vec{i} + (\sum_i N_i(\alpha)v_i)\vec{j} = u(\alpha)\vec{i} + v(\alpha)\vec{j}, \tag{5}$$

$u(\alpha)$ and $v(\alpha)$ as

$$u(\alpha) = \sum_i N_i(\alpha)u_i \quad \text{and} \quad v(\alpha) = \sum_i N_i(\alpha)v_i. \tag{6}$$

Then, we introduce the geometry definition

$$x(\alpha) = \sum_i N_i(\alpha)x_i \quad \text{and} \quad y(\alpha) = \sum_i N_i(\alpha)y_i, \tag{7}$$

of the curved axis using the same nodes i and the same shape functions $N_i(\alpha)$ as used in (6). The shape functions N_i are assumed to be *Lagrangian* polynomials. Later we will use this same geometry definition also with other interpolation techniques. If we write the nodal displacement vectors $\vec{u}_i$ using the local basis $\{\vec{e}_{\alpha(i)}, \vec{e}_{\beta(i)}\}$ at the nodes, then (4) can be written in the form

$$\vec{u} = \sum_i N_i(\alpha)(U_i\vec{e}_{\alpha(i)} + V_i\vec{e}_{\beta(i)}) = \sum_i N_i(\alpha)U_i\vec{e}_{\alpha(i)} + \sum_i N_i(\alpha)V_i\vec{e}_{\beta(i)}. \tag{8}$$

It is notable, that in (8) vector $\vec{u}$ is referred everywhere in the element to the constant basis vectors $\vec{e}_{\alpha(i)}$ and $\vec{e}_{\beta(i)}$. Because, our aim is to find out $U(\alpha)$ and $V(\alpha)$ corresponding to $U_i(\xi)$ in equation (2), we use the transformation

$$\left\{ \begin{array}{c} \vec{i} \\ \vec{j} \end{array} \right\} = \left(\begin{array}{cc} \vec{e}_\alpha(\alpha)\cdot\vec{i} & \vec{e}_\beta(\alpha)\cdot\vec{i} \\ \vec{e}_\alpha(\alpha)\cdot\vec{j} & \vec{e}_\beta(\alpha)\cdot\vec{j} \end{array} \right) \left\{ \begin{array}{c} \vec{e}_\alpha(\alpha) \\ \vec{e}_\beta(\alpha) \end{array} \right\} = \mathbf{T}(\alpha) \left\{ \begin{array}{c} \vec{e}_\alpha(\alpha) \\ \vec{e}_\beta(\alpha) \end{array} \right\} \tag{9}$$

and its inverse $\mathbf{T}^{-1}(\alpha)$ to modify equations (8) to the form (3), in which we can see $U(\alpha)$ and $V(\alpha)$ directly. Finally

$$U(\alpha) = \sum_i N_i(\alpha)\{U_i[(\vec{e}_{\alpha(i)}\cdot\vec{i})(\vec{e}_\alpha(\alpha)\cdot\vec{i}) + (\vec{e}_{\alpha(i)}\cdot\vec{j})(\vec{e}_\alpha(\alpha)\cdot\vec{j})] +$$
$$V_i[(\vec{e}_{\beta(i)}\cdot\vec{i})(\vec{e}_\alpha(\alpha)\cdot\vec{i}) + (\vec{e}_{\beta(i)}\cdot\vec{j})(\vec{e}_\alpha(\alpha)\cdot\vec{j})]\} \tag{10 a}$$

$$V(\alpha) = \sum_i N_i(\alpha)\{U_i[(\vec{e}_{\alpha(i)}\cdot\vec{i})(\vec{e}_\beta(\alpha)\cdot\vec{i}) + (\vec{e}_{\alpha(i)}\cdot\vec{j})(\vec{e}_\beta(\alpha)\cdot\vec{j})] +$$
$$V_i[(\vec{e}_{\beta(i)}\cdot\vec{i})(\vec{e}_\beta(\alpha)\cdot\vec{i}) + (\vec{e}_{\beta(i)}\cdot\vec{j})(\vec{e}_\beta(\alpha)\cdot\vec{j})]\}, \tag{10 b}$$

where the vectors $\vec{e}_\alpha(\alpha)$ and $\vec{e}_\beta(\alpha)$ are calculated using the geometry definition (7). Both interpolations (6) and (10) reduce to (4) and thus give the same results.

The alternative interpolation technique

In view of (3), if the vector functions $\vec{e}_\alpha(\alpha)$ and $\vec{e}_\beta(\alpha)$ are assumed to be given a priori, the components $U(\alpha)$ and $V(\alpha)$ can be interpolated regarding them as a scalar fields over the element. Thus, we may introduce the approximations

$$U(\alpha) = \sum_i N_i(\alpha)U_i \quad \text{and} \quad V(\alpha) = \sum_i N_j(\alpha)V_j. \tag{11}$$

This is a more attractive choice compared with *(10)* because its simplicity. In our simple consideration we just think that the vectors $\vec{e}_\alpha(\alpha)$ and $\vec{e}_\beta(\alpha)$ defining the directions of the components $U(\alpha)$ and $V(\alpha)$ can be calculated using the geometry interpolation (7), but, in general, different approximation for these directions could be constructed as well.

Comparison

Next, we try to find out some basic differences between this alternative and the conventional interpolation techniques. Only one type of interpolation polynomials is applied. These cover both the geometry specification (7) and displacement interpolation in each formulation.

Using the interpolation (11) we can write (3) in the form

$$\vec{u} = [\sum_i N_i(\alpha)U_i]\vec{e}_\alpha(\alpha) + [\sum_i N_i(\alpha)V_i]\vec{e}_\beta(\alpha). \tag{12}$$

After substituting $\alpha = \alpha_i$ in both (8) and (11) one can see easily that the alternative and the conventional approximations coincide at the nodes. In general, they give different values elsewhere in the element, because the alternative interpolation technique (11) deviates from the approximations (10) in such a way that vector $\vec{u}$ is referred to the local basis $\{\vec{e}_\alpha(\alpha), \vec{e}_\beta(\alpha)\}$ dependent on α instead of the constant basis vectors $\vec{e}_{\alpha(i)}$ and $\vec{e}_{\beta(i)}$.

Then, we consider a linear displacement field

$$\begin{aligned} u(\alpha) &= a_0 + a_1 x(\alpha) + a_2 y(\alpha) \\ v(\alpha) &= b_0 + b_1 x(\alpha) + b_2 y(\alpha), \end{aligned} \tag{13}$$

where the coefficients are arbitrary constants. As a special case of the displacement field (13) we have the rigid body motion. We prescribe the nodal values $u(\alpha)$ and $v(\alpha)$ consistent with (13) to interpolate displacements both in the conventional (10) and alternative (11) way. The displacement state (13) is reproduced exactly in conventional interpolation technique (10) as far as condition

$$\sum_i N_i = 1 \tag{14}$$

is fulfilled.

When introducing the linear displacement state in the alternative interpolation (11) with the geometry definition (7), the condition (14) is not enough to quarantee that the displacements (13) really are reproduced exactly using consistent nodal values. Actually, it is possible to prove that the alternative procedure describes the displacement field (13) exactly only in the cases, where the girder axis is straight or the element size tends to zero. In other cases, certain discrepancies occur. The significance of these discrepancies will be estimated and analysed.

CONCLUDING REMARKS

In the conventional isoparametric type of formulation the interpolation of the displacement field and the geometry are of the same order. In the alternative interpolation technique suggested here the same technique is used, but in addition the directions of the displacements are interpolated separately.

In the continuation our purpose is to find out the restrictions for the new (or alternative) interpolation technique by deriving the relevant convergence criteria and studying various numerical examples. Developing further the intrepolation of the unit vectors defining the directions of the displacement components, on the basis of the convergence criteria is of great interest as well.

[1]   ODEN, J.T., *Finite Elements of Nonlinear Continua*, New York, 1972. *432 p.*

[2]   PAAVOLA, J., *A Study of Curved Thin-Walled Girders. Acta Polytechnica Scandinavica, Civil Engineering and Building Construction Series No. 94*, Helsinki 1990, *91 p.*

[3]   VLASOV, V.Z., *Thin-Walled Elastic Beams. Israel Program for Scientific Translations*, Israel, 1963, *493 p.*

TRACING LOCAL BUCKLING PHENOMENA (WRINKLES) IN SHEET METAL FORMING

BO HÄGGBLAD and PER NORDLUND

Department of Solid Mechanics, Royal Institute of Technology
S-10044 Stockholm, Sweden
and
ABB Corporate Research
S-721 78 Västerås, Sweden

Abstract

Numerical simulations of sheet metal forming processes are often very time-consuming and there is a need for assessing local buckling (wrinkle) tendencies at as early stages as possible of the computations. In this context, wrinkles can be characterized as short-waved out of plane deformations. Whenever the sheet is in a state of compression there is a potential risk for wrinkles. In using a quasi-dynamic approach with explicit time integration, the wrinkles usually develop gradually in the solution and can be hard to detect by visual inspection until late after the onset. An important observation is that the formation of wrinkles is characterized by the occurrence of pre-stressed areas where the deformation is dominated by strong local out of plane rotations. The onset of these local *rotations of the stress tensors* can be traced by studying the evolution of the local value of the second order increment of internal work (a scalar quantity !). Based upon these considerations, we present an algorithmic procedure for capturing the initiation of wrinkling. The procedure is primarily designed for use in connection with explicit time integration of the finite element equilibrium equations and is generally applicable to all loading situations, including cases where contact forces and large elasto-plastic deformations are involved.

power, similar to Hill's bifurcation functional, see reference 1) on the form :

$$I = \int_V \text{tr}\left\{ \overset{\circ}{\tau}\, D + \sigma(-DD^T + DW + W^T D + WW^T) \right\} dV$$

where $\overset{\circ}{\tau}$ is the Jaumann stress rate of the Kirchhoff stress tensor, $\tau = J\sigma$, given by

$$\overset{\circ}{\tau} = \dot{\sigma} + \text{tr}(D)\sigma - W\sigma - \sigma W^T$$

σ is the Cauchy stress tensor, D the rate-of-deformation tensor and W the body spin tensor. If we split I , evaluated element wise, according to

$$I = I_{01} + I_{02} + I_{03}$$

where

$$I_{01} = \int_{V_{elem}} \text{tr}\left\{ \overset{\circ}{\tau}\, D + \sigma(-DD^T) \right\} dV \quad ,$$

$$I_{02} = \int_{V_{elem}} \text{tr}\left\{ \sigma(DW + W^T D) \right\} dV$$

and

$$I_{03} = \int_{V_{elem}} \text{tr}\left\{ \sigma WW^T \right\} dV$$

we can define a "wrinkle indicator"

$$\bar{I}_{elem} = \frac{I_{01} + I_{02} + I_{03}}{|I_{01}| + |I_{02}| + |I_{03}|}$$

that satisfies strictly the relation

$$\left| \bar{I}_{elem} \right| \leq 1$$

When the incremental displacement field is dominated by body spin (rotation) we obtain

$$\bar{I}_{elem} \rightarrow \frac{I_{03}}{|I_{03}|} = \pm 1$$

where the minus sign is valid for a buckling situation (compressive membrane stresses). It is also observed that the *value* of $\bar{I}_{elem}$ can be used to measure the closeness to wrinkling. In practice, an early indication of (local) wrinkling is obtained when the indicator starts to become negative. The versatility this indicator for tracing the onset of wrinkles is demonstrated on several test problems (e.g. the Yoshida buckling test) and the connection with Bergan's *current stiffness parameter* is discussed, for more details see reference 2.

1. R. Hill, 'A general theory of uniqueness and stability in elasto-plastic solids', *J. Mech. Phys. Solids*, 6, 236-249 (1959)

2. P. Nordlund and B. Häggblad, 'Prediction of wrinkle tendencies in explicit sheet metal forming simulations', submitted to *Int. J. Num. Meth. Engn.*
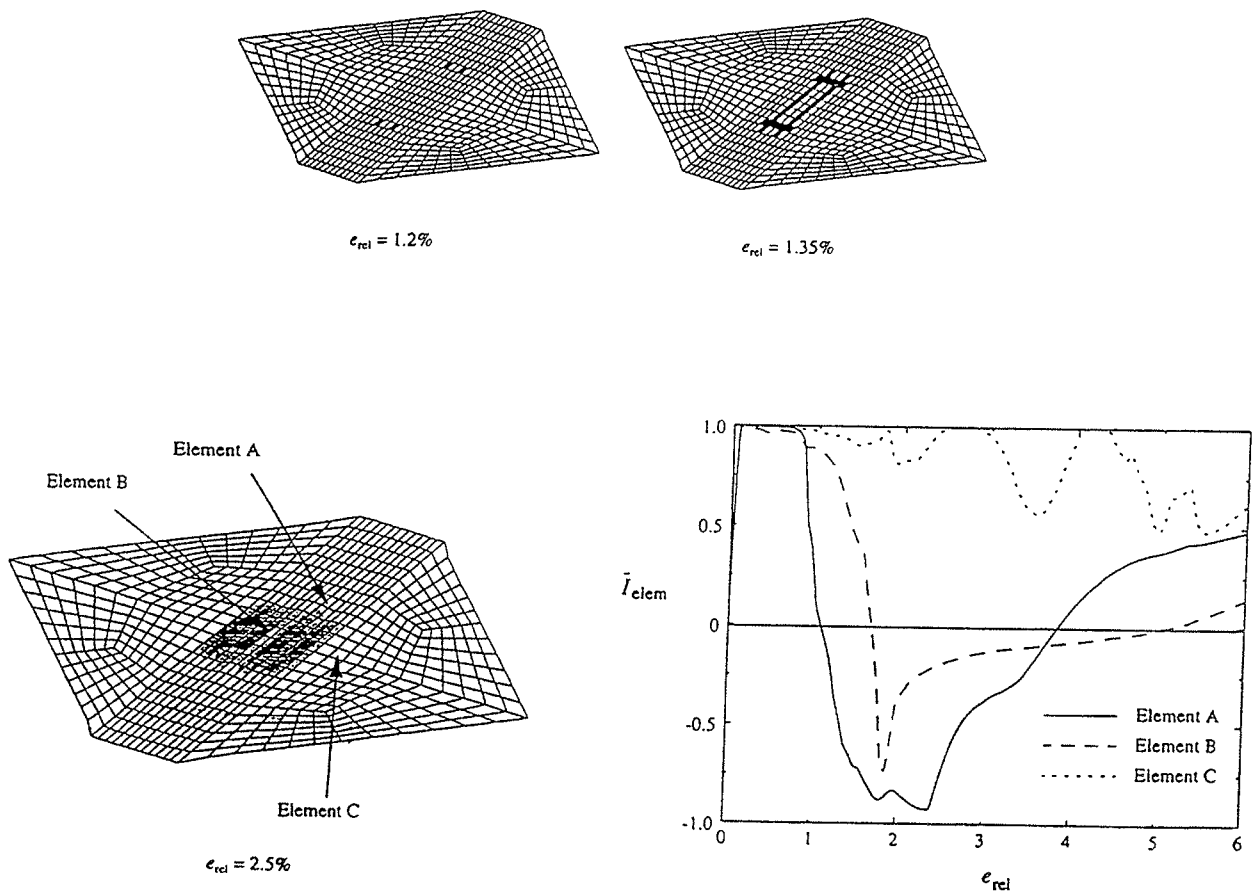
Fig. 1 The wrinkling indicator as function of the diagonal strain e_{rel} in the Yoshida buckling test.

EXPLICIT DYNAMIC FORMULATION OF LARGE STRAIN SHELL ANALYSIS FOR THE MORLEY TRIANGULAR ELEMENT

Ulrika Wendt

Dept. of Structural Mechanics, Chalmers University of Technology, S-412 96 Göteborg, Sweden

ABSTRACT

INTRODUCTION

In an explicit code the solution is basically split into two parts. One static part where the equilibrium, constitutive relations and geometric conditions are considered for the massless elements and one dynamic part where the equilibrium of nodes (point masses) is considered. No global mass- or stiffness matrices need to be established nor solved. The solution is performed node-by-node and element-by-element.

Explicit methods are very sensitive to the time step size, and the critical time step size Δt_{cr} is very small (typically microseconds) compared to time step sizes used in implicit methods. Since the explicit method does not require any factorization each time step requires very little computer time. As the time step size is so small only small displacement approximations need to be considered. The central difference time integration method is used.

The equilibrium is fulfilled at discrete time intervalls Δt apart and the variation of accelerations, velocities and displacements within each time step is assumed in some specific way.

The method is only efficient when velocity-depending damping forces are neglected and when the mass matrix can be lumped. If higher order elements are used it is rather complicated to lump the mass matrix — this is one reason to use lower order elements. Another reason is that they do not require as small critical time step, Δt_{cr}, as higher order elements do. One simple element with only one integration point and with constant strain is the Morley flat shell element [1] which is a triangular element with three displacements in each corner node and one rotational degree of freedom on each side. This element was first used by Herrmann and Campbell [2] in linear shell analysis and later by Bäcklund [3] in non-linear shell analysis. The membrane part is conforming and the bending part is the non-conforming constant curvature Morley triangle.

THE MORLEY TRIANGULAR SHELL ELEMENT

The Morley shell element is a 12 degree of freedom triangular element with three forces (displacements) in each corner node and one moment (rotation) in each mid-side node according to figure 1. The mid-side moments and rotations follow the direction of the element edges while the corner forces are defined in some coordinate system.
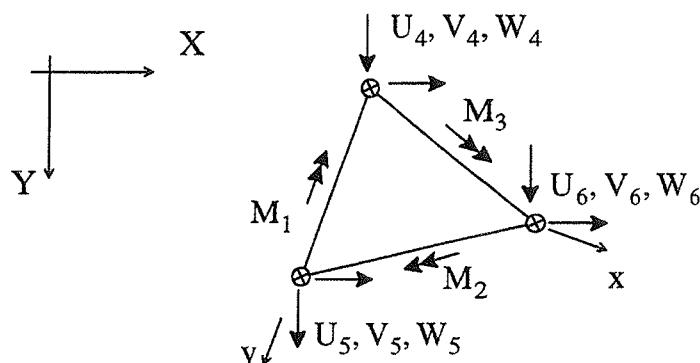
Figure 1. The Morley triangular shell element

SOLUTION SCHEME

The solution is performed node-by-node and element-by-element according figure 2 where the part including ΔF, $^{t+\Delta t}\ddot{u}$, $^{t+\frac{\Delta t}{2}}\dot{u}$ and Δu is the nodal part of the loop and the rest is the element part. It is possible to prescribe either forces or velocities.
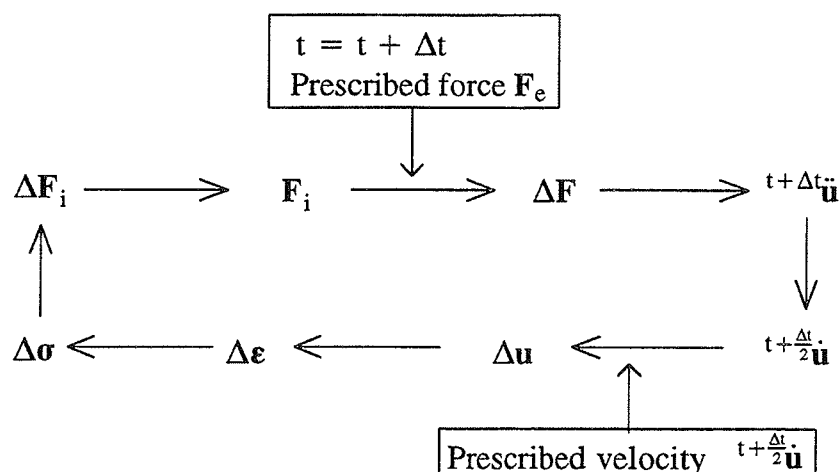
Figure 2. Solution scheme

NODAL CALCULATIONS

From the incremental nodal forces ΔF the incremental displacements Δu are calculated. Since the explicit method is only efficient when the velocity-depending damping can be neglected the dynamic equilibrium equation

$$\mathbf{M\ddot{u}}(t) + \mathbf{C\dot{u}}(t) + \mathbf{Ku}(t) = \mathbf{F}(t)$$

is reduced to

$$\mathbf{M\ddot{u}}(t) = \mathbf{F}(t) - \mathbf{Ku}(t) = \Delta\mathbf{F}$$

This equation is solved by the central difference time integration method according to

$$^{t+\frac{\Delta t}{2}}\dot{\mathbf{u}} = \frac{1}{\Delta t}(^{t+\Delta t}\mathbf{u} - {}^{t}\mathbf{u})$$

$$^{t}\ddot{\mathbf{u}} = \frac{1}{\Delta t}(^{t+\frac{\Delta t}{2}}\dot{\mathbf{u}} - {}^{t-\frac{\Delta t}{2}}\dot{\mathbf{u}})$$

$\Rightarrow$

$$^{t+\frac{\Delta t}{2}}\dot{\mathbf{u}} = {}^{t-\frac{\Delta t}{2}}\dot{\mathbf{u}} + {}^{t}\ddot{\mathbf{u}}\Delta t$$

$$^{t+\Delta t}\mathbf{u} = {}^{t}\mathbf{u} + {}^{t+\frac{\Delta t}{2}}\dot{\mathbf{u}}\Delta t$$

When the corner nodes are considered **u** are the three displacements and **M** are the nodal masses. When the mid-side nodes are considered **u** are the rotations and **M** are the moments of inertia for this node.

ELEMENT CALCULATIONS

From the incremental displacements $\Delta\mathbf{u}$ calculated in the nodal part of the loop the internal nodal forces are calculated. This is done by the use of geometry conditions to calculate the incremental strain $\Delta\boldsymbol{\varepsilon}$, constitutive conditions to calculate the incremental element stresses $\Delta\boldsymbol{\sigma}$ and finally equilibrium conditions to calculate the nodal forces $\Delta\mathbf{F}_i$

$$\Delta\mathbf{F}_i = \mathbf{B}^t\Delta\boldsymbol{\sigma} = \mathbf{B}^t\mathbf{D}\Delta\boldsymbol{\varepsilon} = \mathbf{B}^t\mathbf{D}\mathbf{B}\Delta\mathbf{u} = \mathbf{K}\Delta\mathbf{u}$$

NUMERICAL EXAMPLES

At the moment the stretching part of the code is working satisfactory while there still is some problem with the bending part of the solution. No numerical examples with bending can therefore be presented at this moment.

Cantilever shell in stretching – prescribed force

A shell according to figure 3 is analyzed and compared to the solution by LS-DYNA3D using triangular elements. The elasto-plastic material model according to von Mises has been used with $K=500$ N/mm^2 and $n=0.2$. In both codes a mesh with 162 elements and 156 nodes has been used.
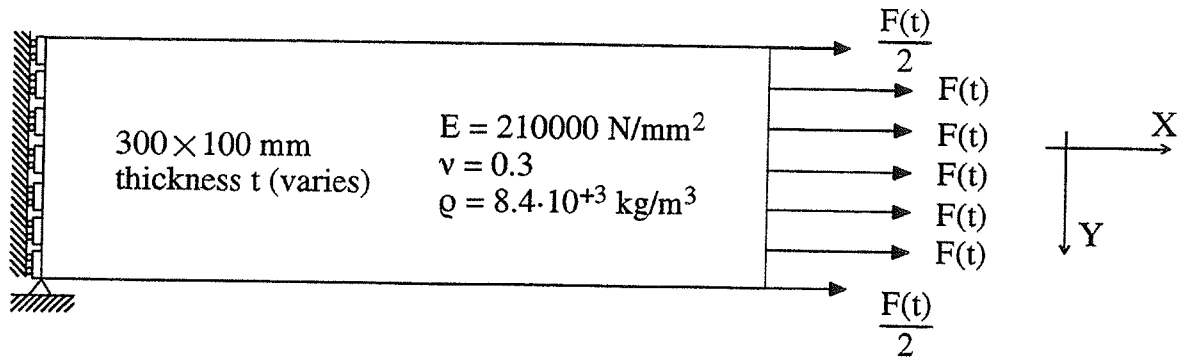

Figure 3. Cantilever plate in stretching

Along the right boundary the load according to figures 3 and 4 has been applied. The size of the load F(t) is given in the table and depends linearly on the thickness t of the shell. The left boundary is clamped even though all nodes but one are allowed to move in the Y-direction, see figure 3.
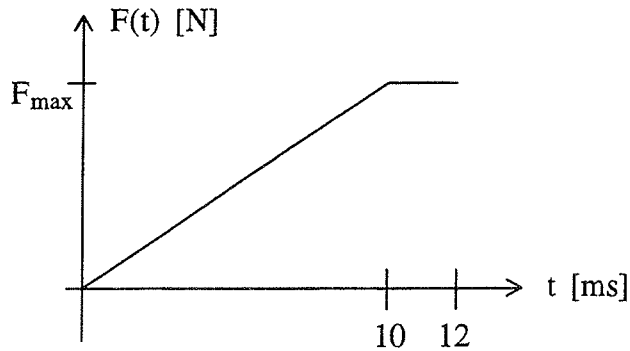
Figure 4. Time-load curve

In the table below the final displacement in the X-direction at the right corners is given by u. The maximum and minimum effective stress and effective plastic strain are also given.

case	t[mm]	F_{max}[N]	this code	LS-DYNA3D code
1	5.00	10000	u = 0.568 mm Effective stress [N/mm^2] : σ_{max} = 120 ; σ_{min} = 116 Effective plastic strain [%]: ε_{max} = 0.17 ; ε_{min} = 0.11	u = 0.577 mm Effective stress [N/mm^2] : σ_{max} = 120 ; σ_{min} = 115 Effective plastic strain [%]: ε_{max} = 0.17 ; ε_{min} = 0.12
2	2.50	5000	same result as for t = 5 mm	same result as for t = 5 mm

The solution of this code differs a little from the solution of the LS-DYNA3D code wich can be seen in the table.
As expected there is no difference between the results in cases 1 and 2.

REFERENCES

[1]   L S D Morley: The constant-moment plate-bending element, Journal of Strain Analysis, Vol 6 (1971), No 1, pp 10-24.

[2]   L R Herrmann and D M Campbell: A finite element analysis for thin shells, AIAA Journal, Vol 6 (1968), pp 1842-1847.

[3]   J Bäcklund: Finite element analysis of non-linear structures, Chalmers University of Technology, Department of Structural Mechanics (1973), No 129.

Computational Buckling Analysis of Wind Turbine Blades

Arnis Riekstiņš

Institute of Polymer Mechanics,
Aizkraukles iela 23, LV-1006 Riga, Latvia

Introduction

Cylindrical shells and panels serve as a highly optimal form of shell component in a wide range of structures, and wind turbine blades particularly. The failure of such structures is primarily caused by the loss of stability of the shell component. An overall weight reduction of the structure demands the structural instability to be investigated at various stages of the design process.

Highly non-linear theoretical solutions are able to completely reproduce the buckling behaviour of shell structures. The large-scale computer solutions have certainly increased the capacity to analyse complex systems, but a straightforward incorporation of these sophisticated solutions appears to be doubtful for an engineering design. It is not yet clear how they could be of assistance at the initial, as opposed to the final checking stage of the design process [1,2].

In the design process of a wind turbine blade, there are numerical modelling methods used which allow to meet adequate predictions of the overall structural response under service or ultimate loading conditions. For example, moments and shearing forces are calculated for various cross sections taking into consideration the section shape and material properties. However, unless the shell elements are used, these methods do not encounter for a possible blade skin buckling. The purpose of this paper is to show how the buckling of the structural elements of wind turbine blades could be effectively modelled by means of the finite element method.

Modelling of a Blade Section

Let us consider a typical case of stability loss of a wind turbine blade subjected to static loading during a blade test. If buckling occurs, it takes place in the compressive part of the blade skin, and the buckling mode can have several waves along the blade. Therefore, when the buckling has to be analysed, it is worth to concentrate the attention solely on the 'risky' parts of the blade and use more refined methods of modelling there.
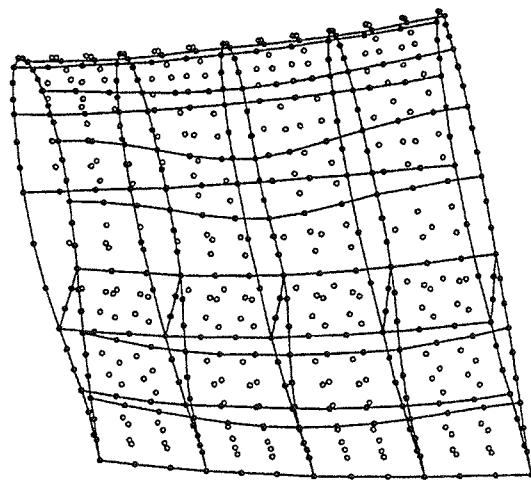
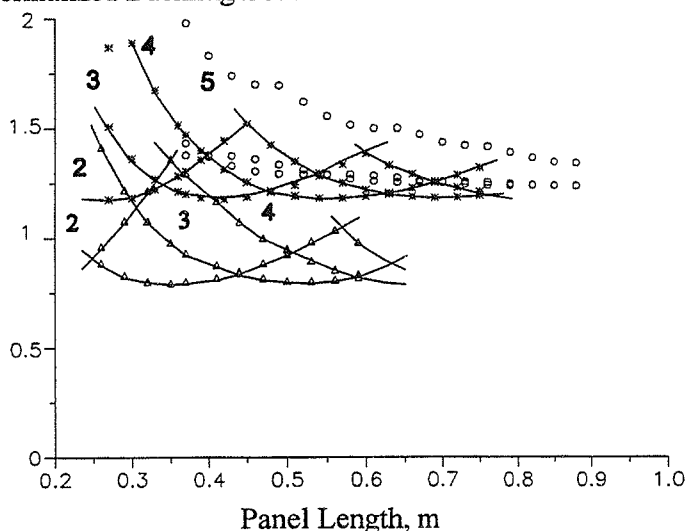**Figure 1**   Deformed shape of the blade section

As an example, the model of a section of the whole blade is considered. In this case, both the inner structure - the web - and the faces are modelled by means of the sixteen-node shell elements. A rigid in-plane supporting is assumed for each end of the blade section. Bending moments are applied at the section ends. Geometrically nonlinear formulation is used, and the equilibrium equations are solved by means of the well known predictor-corrector procedure [3]. When the limit point is reached, the deformed shape of wingblade section has one buckle in the compressed part of the blade section (Fig. 1).

Apparently, it would be advisable to perform the buckling analysis of just the compressed part of the blade. The blade panel has to be modelled using appropriate boundary conditions.

Buckling Models of Axially Compressed Blade Panels

In the present work, effect of various types of boundary conditions on the panel behaviour has been studied regarding the critical buckling load and the buckling mode. A proper choice of the panel dimensions has been considered regarding the reliability and efficiency of buckling calculations. Influence of various boundary conditions has been investigated regarding the lowest buckling load of the wingblade panels of different lengths. Eight-node shell elements were used to model the panels in question.

Figure 2 Buckling loads of cylindrical panels of various length and supporting conditions

In all cases, the buckling mode had one halfwave crosswise and several ones lengthwise. The wave length was depending on the type of boundary conditions at the straight

edges. The main results of the buckling analysis are summarized in Fig. 2, where the buckling loads are given versus the panel length for three types of panel supporting: all edges clamped (o), straight edges clamped (*), and all edges hinged (Δ).

As expected, the effect of clamped ends decreases for longer panels having all edges clamped (o). In this case, the value of the critical buckling load tends to be that of a clamped panel having hinges at both ends (*). Models with clamped straight edges give the buckling load of a cylindrical panel rigidly supported by two webs along the straight edges.

The model with hinged straight edges (Δ) appears to give an 'underestimated' buckling load of the panel being situated between two webs or one web and the front edge of the wingblade. Thus, the boundary conditions of type (*) should be used to have better predictions of the buckling behaviour. Length of the panel should be taken equal to the length of at least one wave of the buckling pattern.

Modelling of the Buckling Behaviour of Sandwich Panels

Sandwich panels of a typical section of the wind turbine blade have been analysed using 3D solid elements for the core part, whereas the faces were modelled by layered composite shell elements. The same approximation order was used for both types of elements. Three displacement degrees of freedom were used for the nodes of the 3D element. Two rotational d.o.f. have been added for the joint nodes of the 3D solid and the shell elements. The nodal points of the upper and lower surfaces were joined together by rigid links at all four edges of the panel. Thus, a possible delamination has been avoided at the panel edges.
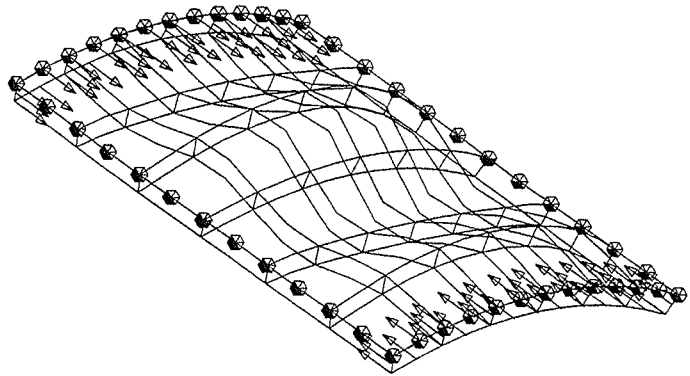
Figure 3 Buckling mode of a curved cylindrical panel under compressive loading.

Comparison of the Results with Blade Tests

Results of the numerical analysis has been compared with the static test data of a 21m blade. During the blade test only one buckle inwards the blade has been observed at 0.45% compressive strain level. For the FE modelling, example of an axially compressed cylindrical panel has been used with 3.67m radius, 0.49m width,

159

0.7m length, and 0.016m thickness. The elastic properties of the multilayered composite were: E_1=25GPa, E_2=5GPa, G_{12}=2.6GPa and v_{12}=0.3.

Edge Shortening, %
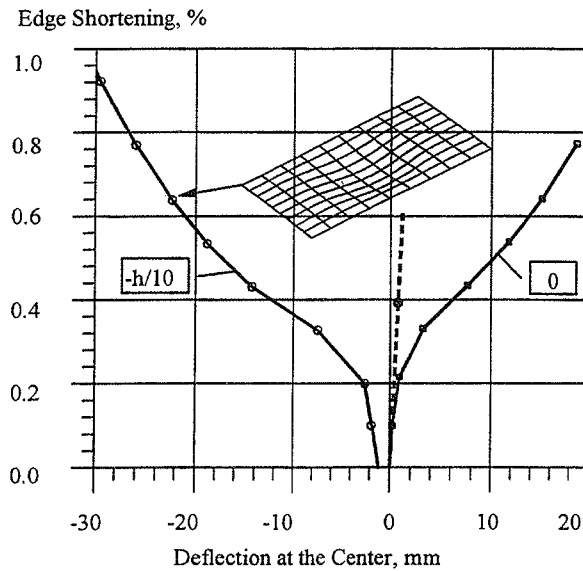
Both the linear buckling analysis and geometrically nonlinear calculations were performed. The results obtained are depicted in Fig. 4. The dashed line corresponds to the linear analysis (buckling strain level 0.4%). The solid line (0) shows the nonlinear behaviour of the perfect structure. Small initial imperfections (-h/10) were added to the perfect geometry to force an inward deflection of the panel. It can be seen that the results of nonlinear analysis differ considerably from the linear prediction and are underestimating the behaviour experimentally observed.

Figure 4

Acknowledgment

References

1. J.G.A. Croll. Incorporating the mechanics of shell post buckling into design. 11th ACMSM University of Auckland 1988.
2. Z.P. Baz'ant and L. Cedolin. Stability of Structures. Oxford University Press, New York 1991.
3. E. Riks. The application of Newton's method to the problem of elastic stability. *J. Appl. Mech.*, **39** (1972) 1060-6.

of
Repetitive Vertical Human Loading

Jeppe Jönsson, ES-Consult A/S, Staktoften 20, 2950 Vedbæk

Analytical expressions for the spectral distribution of repetitive vertical human loading, mainly jumping, are validated through the use of simulated discrete time series of the load. The simulation is performed on the basis of halfsine impulse shapes and experimentally determined mean values and standard deviations of the pulse period, the pulse starting time and the contact duration. The simulations shows that the developed analytical expressions for the spectral load distribution are adequate. However the use of halfsine impulses has to be modified in order to include the influence of heel impact in the high frequency domain of the load spectrum.

Introduction

The loads produced by humans vary a great deal and new motion patterns on for example sports stadiums or in keep fit gymnastics may develop. Knowledge of the loads are needed in order to perform structural analysis in the ultimate limit state and in order to fulfil the requirements in the serviceability state. A literature survey is given by Per-Erik Eriksson in his work on *Vibration of Low-Frequency Floors* from 1994, [1]. The Swiss researchers Bachmann and Ammann give many valuable references and a thorough treatment of man induced vibrations in [2]. Stochastic load models giving the spectral density distribution of loads have been proposed, see for example Rebelo and Schere [3] and specially the work by Per-Erik Eriksson [1]. An investigation of the mechanics of repetitive human motion has recently been performed by Jönsson and Pilegaard Hansen in [4], this work resulted in different analytical expressions for approximate spectral load distributions. These analytical spectra are validate by simulations, some of which are presented in this paper. An experimental investigation has also been performed by Jönsson and Pilegaard Hansen in [5]. It involves one person performing 5 different repetitive vertical motions on a very stiff loading platform with eigenfrequencies above 60 Hz.
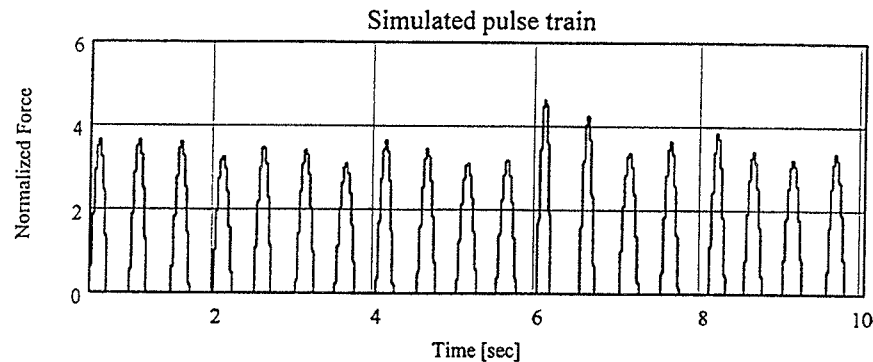
Figure 1. Simulated repetitive vertical human load.

Simulated repetitive vertical human load

A halfsine impulse shape function is introduced and the load amplitude is determined by the periodic load impulse of the contact force $I=MgT_p$. Using the unit function $u(t)$ a single load pulse is given by

$$f(t, t_p, T_p) = \frac{\pi}{2} \frac{MgT_p}{t_p} \sin(\frac{\pi t}{t_p}) \, u(t) \, u(t_p - t) \qquad (1)$$

A pulse train is defined as a series of n impulses using the load impulse function defined above however we will include an additional impulse starting time t_s within each period as follows

$$h(t, t_s, t_p, T_p, n) = \sum_{j=0}^{n-1} f\left(t - t_{sj} - \sum_{k=1}^{j} T_{pk}, t_{pk}, T_{pk}\right)$$

The pulse periods T_{pk}, the contact durations t_{pk} and the pulse starting times t_{sk} are random data whi follow a normal probability distribution. Note that the mean impulse starting time is zero, $\bar{t}_s = 0$. T simulated load shown in figure 1 and in the following figures corresponds to jumping at a frequency 2Hz with a contact duration ratio of 0.45 and standard deviations of 0.02sec for the impulse starting ti or the pulse period and the contact duration.

Discrete force amplitude spectra

The pulse train is used to simulate about 10 seconds of experimentally measured data by discr evaluation at a sampling frequency of $f_s = 600$Hz. The m simulated measured loads h_r are Four transformed using a discrete complex fast Fourier transform. The transformed load data are then used find the single sided force amplitude spectrum A_r shown in figure 2 as follows

$$h_r = \sum_{j=0}^{n-1} f\left(t_r - t_{sj} - \sum_{k=1}^{j} T_{pk}, t_{pk}, T_{pk}\right), \qquad H_r = \frac{1}{m}\sum_{k=0}^{m-1} h_k e^{-i\frac{2\pi r}{m}k}, \qquad A_r = 2\sqrt{H_r H_r^*}$$

Before Fourier transforming the data it is treated as if it were real measured data as in [5].

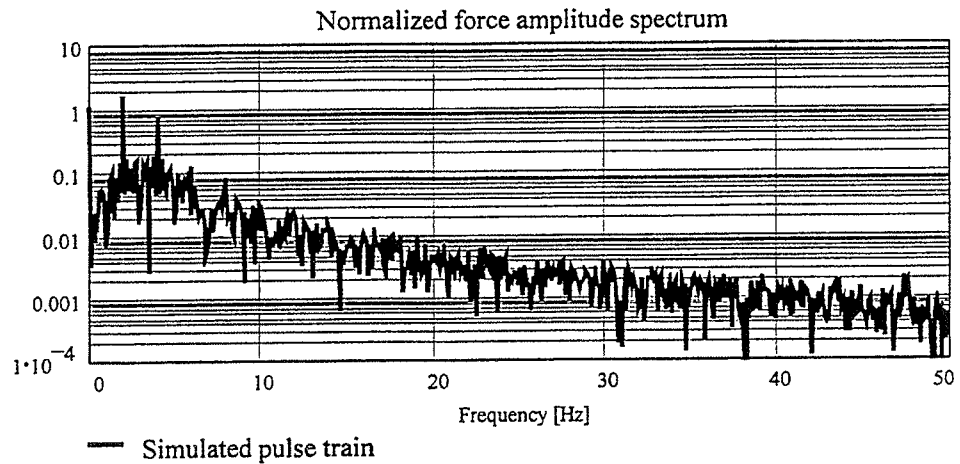Normalized force amplitude spectrum

— Simulated pulse train

Figure 2. Normalized force amplitude spectrum of simulated human loading.

Analytical force amplitude spectra

The following four load models are analyzed and the corresponding normalized load spectra are sho in figures 3 and 4.

   I.   A deterministic model using mean values $T_{pk} = \bar{T}_p$, $t_{pk} = \bar{t}_p$ and $t_{sk} = \bar{t}_s = 0$.

   II.   A model where the impulse starting time t_{sk} is stochastic and the remaining variables deterministic, ie $T_{pk} = \bar{T}_p$ and $t_{pk} = \bar{t}_p$.

   III.   A model with a deterministic impulse $I = Mg\bar{T}_p$, but where the pulse period T_{pk} is stochas the contact duration as well as the impulse starting time are deterministic, ie $t_{pk} = \bar{t}_p$ and t_{sk}

   IV.   A model where the impulse starting time t_{sk} and the contact duration t_{pk} are stochastic and the pulse period is deterministic, $T_{pk} = \bar{T}_p$.

In the following we will state the analytical results found in Jönsson and Pilegaard Hansen [4] for es of the above given models, however before doing so we need to introduce a few functions. The Four transform of a pulse train normalized by the time period $n\bar{T}_p$ is approximated by assuming that impulses are determined by the mean pulse period as $I = Mg\bar{T}_p$. The approximate Fourier transform is

$$H(\omega, t_s, t_p, T_p, n) \approx \frac{1}{n\bar{T}_p}\int_{-\infty}^{\infty} \sum_{j=0}^{n-1} f\left(t - t_{sj} - \sum_{k=1}^{j} T_{pk}, t_{pk}, \bar{T}_p\right) e^{-i\omega t} dt$$

$$F(\omega, t_p) = \frac{1}{T_p} \int_{-\infty}^{\infty} f(t, t_p, T_p) e^{-i\omega t} dt = -\frac{1}{2} Mg \frac{\pi^2}{\omega^2 t_p^2 - \pi^2} (1 + e^{-i\omega t_p}) \qquad (5)$$

The "length" of the fourier transform of the impulse function is

$$|F(\omega, t_p)| = \sqrt{FF^*} = \frac{1}{2} Mg \frac{\sqrt{2}\pi^2}{|\omega^2 t_p^2 - \pi^2|} \sqrt{1 + \cos(\omega t_p)} \qquad (6)$$

Further more we need the normal probability distribution $p(x)$, its Fourier transform $P_x(\omega)$ and its length $|P_x(\omega)|$ for the variable x with a mean value μ_x and a standard deviation of σ_x as follows

$$p(x) = \frac{1}{\sigma_x \sqrt{2\pi}} e^{-\frac{(x-\mu_x)^2}{2\sigma_x^2}}, \qquad P_x(\omega) = e^{-\frac{1}{2}\omega^2 \sigma_x^2} e^{-i\omega\mu_x}, \qquad |P_x(\omega)| = \sqrt{P_x P_x^*} = e^{-\frac{1}{2}\omega^2 \sigma_x^2} \qquad (7)$$

In the following we also use a spectral factor $N(\omega, n)$ and its length defined as

$$N(\omega, n) = \frac{1}{n} \sum_{j=0}^{n-1} e^{-i\omega j T_p} = \frac{1}{n} \frac{1 - e^{-i\omega n T_p}}{1 - e^{-i\omega T_p}}, \qquad |N(\omega, n)| = \frac{1}{n} \sqrt{\frac{1 - \cos(\omega n T_p)}{1 - \cos(\omega T_p)}} \qquad (8)$$

The force amplitude spectra of a pulse train of n pulses is found by use of the mean power spectrum as

$$\tilde{A}(f, n) = 2\sqrt{HH^*} \qquad (9)$$

The force amplitude spectra of the four load models can be written as follows, see [4],

$$A_I(f, n) = 2 \; |N(2\pi f, n)| \; |F(2\pi f)|$$

$$A_{II}(f, n) = 2 \sqrt{|P_{t_s}(2\pi f)|^2 |N(2\pi f, n)|^2 + \frac{1}{n} - \frac{1}{n} |P_{t_s}(2\pi f)|^2} \; |F(2\pi f)|$$

$$A_{III}(f, n) = 2 \sqrt{\frac{1}{n} + 2Re\left(P_{T_p}(2\pi f) \frac{n(1 - P_{T_p}(2\pi f)) - (1 - P_{T_p}^n(2\pi f))}{n^2 (1 - P_{T_p}(2\pi f))^2}\right)} \; |F(2\pi f)| \qquad (10)$$

$$A_{IV}(f, n) = 2 \sqrt{|P_{t_s}(2\pi f)|^2 |N(2\pi f, n)|^2 + \frac{1}{n} - \frac{1}{n} |P_{t_s}(2\pi f)|^2} \; \sqrt{FF^*}$$

For model IV it is necessary to evaluate the mean power spectrum for a single pulse numerically since an analytical result has not been found.

$$\overline{FF^*} = \int_{-\infty}^{\infty} F(\omega, t_{pj}) F^*(\omega, t_{pj}) p(t_{pj}) \; dt_{pj} \qquad (11)$$

Thus the evaluation is eased by using the Fourier transform of the halfsine load pulse.

Concluding remarks

The quality of the stochastic load models reflect their simplicity, model II is the simplest, then comes model III and finally model IV. A remaining topic is how to include the influence of a heel impact. It is proposed that the individual impulse is decomposed into a 95% halfsine impulse with the measured contact duration t_p and a 5% heel halfsine impact with a short contact duration of $0.2t_p$. The impulse of the heel impact can be estimated using the level of the force amplitude at high frequencies.

163
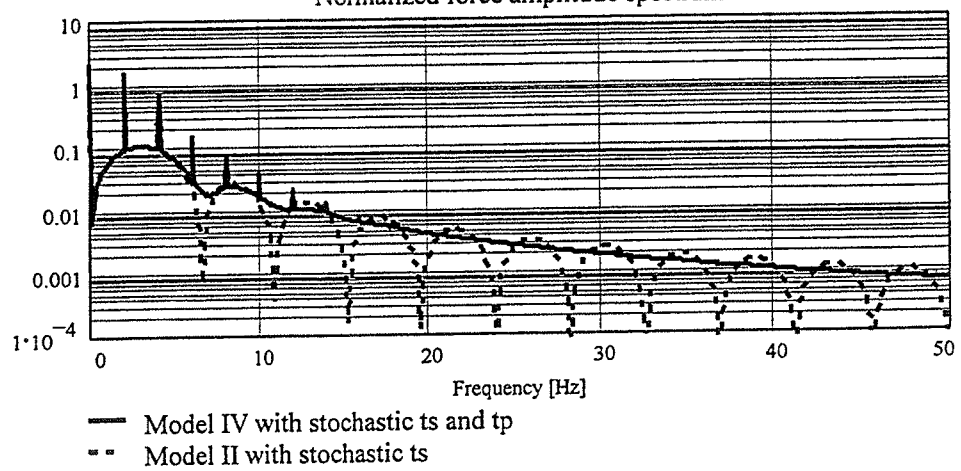
Figure 3. Analytical normalized force amplitude spectra for model II and IV.

Normalized force amplitude spectrum
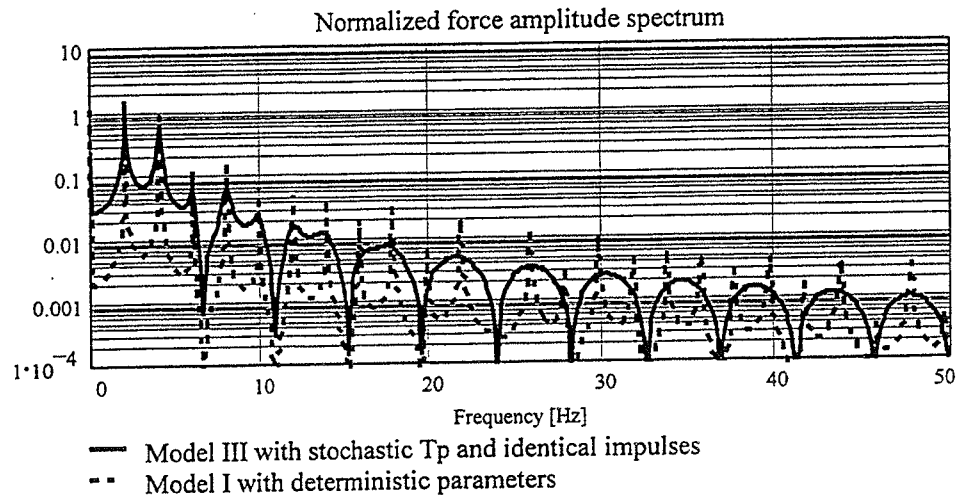
Figure 4. Analytical normalized force amplitude spectra for model IV and I.

Acknowledgement

References

[1] P.-E. Eriksson. Vibration of Low-Frequency Floors - Dynamic Forces and Response Prediction Ph.D. dissertation, Chalmers University of Technology, Unit for Dynamics in Design, Göteborg Sweden, Publication D94:3, 1994.

[2] H. Bachmann and W. Ammann. *Vibrations in Structures- Induced by Man and machines*. Structural engineering Documents. IABSE, ETH-Hönggerberg, CH-8093 Zurich, Switzerland, 1987.

[3] C. Rebelo and R. J. Scherer. A stochastic model for human induced rhythmic loads. *Structural Safety & Reliability*, Schuëller, Shinozuka & Yao (eds), Balkema, Rotterdam, 1994.

[4] J. Jönsson & L. Pilegaard Hansen, *Repetitive vertical human loading, Part I - Theoretical investigation*, to be published at Dept. of Building Technology and Structural Engineering, Aalborg University, Denmark, 1996.

[5] J. Jönsson & L. Pilegaard Hansen, *Repetitive vertical human loading, Part II - Experimental investigation*, to be published at Dept. of Building Technology and Structural Engineering, Aalborg University, Denmark, 1996.

164

A preliminary study of Error Estimation in Ultimate Load Analysis of Structural Components

Ivar TILLER, Kjell Magne MATHISEN, Odd Sture HOPPERSTAD, and Knut Morten OKSTAD

Department of Structural Engineering
Norwegian University of Science and Technology
N-7034 Trondheim, Norway

1. INTRODUCTION

The development of general purpose finite element computer programs has made it possible to perform reliable analysis of structures and structural components taking into account material and geometric non-linearities. In typical structural engineering problems, such as inelastic local buckling of beams and plastic collapse of plates, a shell formulation based on finite displacements and finite rotations but small strains gives a sufficiently accurate representation of the kinematics, whereas the material is often well described by an elastic-plastic constitutive model. In order to ensure reliable results for a given class of structural problems it is necessary to check the finite element solution against experimental results, and thus obtain a verified model for the problem at hand. However, in application of this 'calibrated model' to various problems within the given class, error estimation and adaptive solution strategies plays an important role. In prior studies, geometrically non-linear problems involving linear elastic materials have been investigated [1, 2]; but in ultimate load analysis the inelastic material behavior has to be taken into account, and therefore error estimates and adaptive strategies for elastic-plastic materials are required.

The main difference in trying out adaptive mesh refinement in nonlinear analysis compared to linear analysis, is that the state variables have to be mapped from one finite element model to another, in order for the solution variables to be transformed from one step to the next. For elasticity problems involving two-and three-dimensional continuum elements, this transfer may be carried out straight forward, as only displacements are involved. However, for shell-type problems, mapping of state variables may be a crucial step, as explained in detail in [1, 2]. In the case of plasticity, the situation is even more complex, and so far no mathematically proved estimators exist, even for small strain theory of plasticity. Only Johnson et al [3] have developed an adaptive strategy for small strain elasto-plasticity using the Henchy model. However, due to restrictions in the Henchy model, this method is generally not applicable to standard elastic-plastic and elastic-viscoplastic history dependent problems.

This paper presents a study of projection-type error estimators for elastoplastic materials. In this study the improved C^0-continuous solution is obtained by the superconvergent patch recovery (SPR) method [4], which has proved to be an efficient tool for this purpose in both two-dimensional elasticity and plate bending applications [2]. Theoretical proofs concerning the convergence of this method is established in the elastic range only, and are thus not necessarily valid for elasto-plastic problems. The approach is therefore based on the assumption that the improved solution is closer to the exact one than the finite element solution. In our preliminary study several error estimators are evaluated: L_2-norms of total stress, total strain, incremental total strain and equivalent total strain error, energy rate, error based on plastic dissipation and error based on incremental plastic work, respectively. In order to judge the quality of these estimators, the numerical results are compared to results obtained experimentally.

The paper presents numerical results comparing the local and global effects of the different error estimators desribed above on a perforated strip. Other industrial examples on ultimate load analysis of structural components for which numerical results are compared to results obtained

2. ERROR ESTIMATORS

In the displacement formulated finite element method the displacements are the primary variables, while the stresses and strains are derived from the displacements. This causes the stresses and strains to be discontinuous across the element boundaries. A better approximation of these quantities could be obtained by some smoothing process of the finite element quantities. Several smoothing approaches have been proposed during the last decade, of which the SPR [4] has become the most popular method. This method exploits the fact that the derived quantities are of better quality at certain points within the element, the superconvergent points. An even better approximation may be obtained by including boundary conditions and interior equilibrium as constraints on the recovery process. A thorough description of these methods may be found in [5]. In the current work only the plain SPR-method is employed for smoothing.

The error is approximated by the difference between the quantities obtained by the finite element solution and the corresponding smoothed quantities. For the stresses this reads

$$e = \sigma^* - \sigma^{\mathrm{h}} \tag{1}$$

where σ^* is the smoothed stresses and σ^{h} is the stresses obtained directly from the finite element solution. Based on (1), several error estimates have been proposed by different authors, see, e.g. [6]. Herein, we use the following error estimates which also apply to elastic-plastic analyses:

1. L_2-norm of stress error

$$e = \left(\int_\Omega \left(\sigma^* - \sigma^{\mathrm{h}} \right)^{\mathrm{T}} \left(\sigma^* - \sigma^{\mathrm{h}} \right) \mathrm{d}\Omega \right)^{\frac{1}{2}} \tag{2}$$

2. L_2-norm of total strain error

$$e = \left(\int_\Omega \left(\varepsilon^* - \varepsilon^{\mathrm{h}} \right)^{\mathrm{T}} \left(\varepsilon^* - \varepsilon^{\mathrm{h}} \right) \mathrm{d}\Omega \right)^{\frac{1}{2}} \tag{3}$$

3. L_2-norm of incremental total strain error

$$e = \left(\int_\Omega \left(\dot{\varepsilon}^* - \dot{\varepsilon}^{\mathrm{h}} \right)^{\mathrm{T}} \left(\dot{\varepsilon}^* - \dot{\varepsilon}^{\mathrm{h}} \right) \mathrm{d}\Omega \right)^{\frac{1}{2}} \tag{4}$$

4. L_2-norm of total equivalent strain error

$$e = \left(\int_\Omega \left(\varepsilon^*_{\mathrm{eqv}} - \varepsilon^h_{\mathrm{eqv}} \right)^2 \mathrm{d}\Omega \right)^{\frac{1}{2}} \tag{5}$$

5. Energy rate error norm

$$e = \left(\int_\Omega \left(\sigma^* - \sigma^{\mathrm{h}} \right)^{\mathrm{T}} \left(\dot{\varepsilon}^* - \dot{\varepsilon}^{\mathrm{h}} \right) \mathrm{d}\Omega \right)^{\frac{1}{2}} \tag{6}$$

In the above, ε is the total strain tensor $\dot{\varepsilon}$ is the total strain rate tensor and $\varepsilon_{\mathrm{eqv}}$ is the equivalent total strain. The latter is given by

$$\varepsilon_{\mathrm{eqv}} = \frac{1}{\sqrt{2}} \left[(\varepsilon_{xx} - \varepsilon_{yy})^2 + (\varepsilon_{yy} - \varepsilon_{zz})^2 + (\varepsilon_{zz} - \varepsilon_{xx})^2 + \frac{2}{3}(\varepsilon_{xy}^2 + \varepsilon_{yz}^2 + \varepsilon_{zx}^2) \right]^{\frac{1}{2}} \tag{7}$$

of plastic work:

6. Error estimator based on the plastic dissipation

$$e = \int_{\Omega} \left(\left(\sigma^* - \sigma^h \right)^T \left(\Delta \varepsilon^* - \Delta \varepsilon^h \right) + \left(\bar{\sigma}^* - \bar{\sigma}^h \right) \left(\Delta \bar{\varepsilon}_p^* - \Delta \bar{\varepsilon}_p^h \right) \right) d\Omega \qquad (8)$$

7. Error estimator based on incremental plastic work

$$e = \int_{\Omega} \left(\sigma^* - \sigma^h \right)^T \left(\dot{\varepsilon}_p^* - \dot{\varepsilon}_p^h \right) d\Omega \qquad (9)$$

Here, Δ denote incremental quantities, $\bar{\sigma}$ is the radius of the yield surface and $\bar{\varepsilon}_p$ is the equivalent plastic strain.

The key task now is to assess the accuracy of the different error estimators. In elasticity the estimates might be assessed by employing them on problems where the analytical solution is known. This is not the case in elastic-plastic problems. One solution might in such cases be to perform several analyses with increasingly number of degrees of freedom to obtain convergence rates. It is then possible to calculate the "exact" global energy and then the error in global energy for a certain mesh. An other possibility is to compare the finite element analysis with experimental data obtained from laboratory test.

3. NUMERICAL EXAMPLE

A plate of length $L = 36$ mm and width $W = 10$ mm with a hole of radius $R = 5$ mm at its center, is considered. The material of the plate is elastic-plastic with Young's modulus $E = 7000$ N/mm^2 and Poisson's constant $\nu = 0.2$, yield stress $\sigma_y = 243$ N/mm^2 and tangent modulus $E_t = 4220$ N/mm^2. The plate is subjected to a uni-axial tension of $P = 150$ N/mm^2. Half the plate is modeled with 48 elements using symmetry conditions, and the load is applied in 10 equal increments. The analysis is performed using a four node Geometrically Exact Shell element (GES) [2]. The element uses a stress resultant formulation of the material using the Ilyushin yield criterion which is a good approximation to the von Mises criterion. The material model is implemented with a consistent tangent modulus which is crucial for preserving a quadratic rate of convergence of the Newton-Raphson method employed. Convergence is established with an energy norm criteria with convergence tolerance equal to 1.0^{-6}. Error estimation is performed at the end of each increment.

The results presented herein are compared to those obtained by Tetambe et al. [6]. They used in their investigation an eight-noded elastic-plastic element, while in the current study a four-noded element is used. This causes the results to be somewhat different when it concerns magnitudes, but the trends should be the same.

The global percentage error is plotted against the load level for the various error estimators and is shown in Figure 1. The figure shows that the estimators are nearly constant up to a load level equal to 5, which corresponds to a tension equal to 75 N/mm^2. This is because the model is still elastic up to this point. From load level 5 and upward the stress and strain error exhibit a monotonic increasing behavior, even though the stresses are increasing very little. This is in accordance with the results obtained in [6]. The incremental total strain error is, however, increasing in a smoother fashion than in [6]. The energy rate norm shows a jump in error initially after plasticity occurs, but flattens out later in the load history.

When it comes to the error estimators based on plastic dissipation and incremental plastic work they shows equal behavior. In the elastic region, up to increment number 6, they are identical, which also may be seen directly from their expresssions. The difference between these two estimators is respresented by the second part of the expression for the plastic dissipation which takes into account the yield-stress $\bar{\sigma}$ and the equivalent plastic strain $\bar{\varepsilon}^p$. The yield stress is equal to its initial value in the whole model apart from a small area in the bottom of the hole where
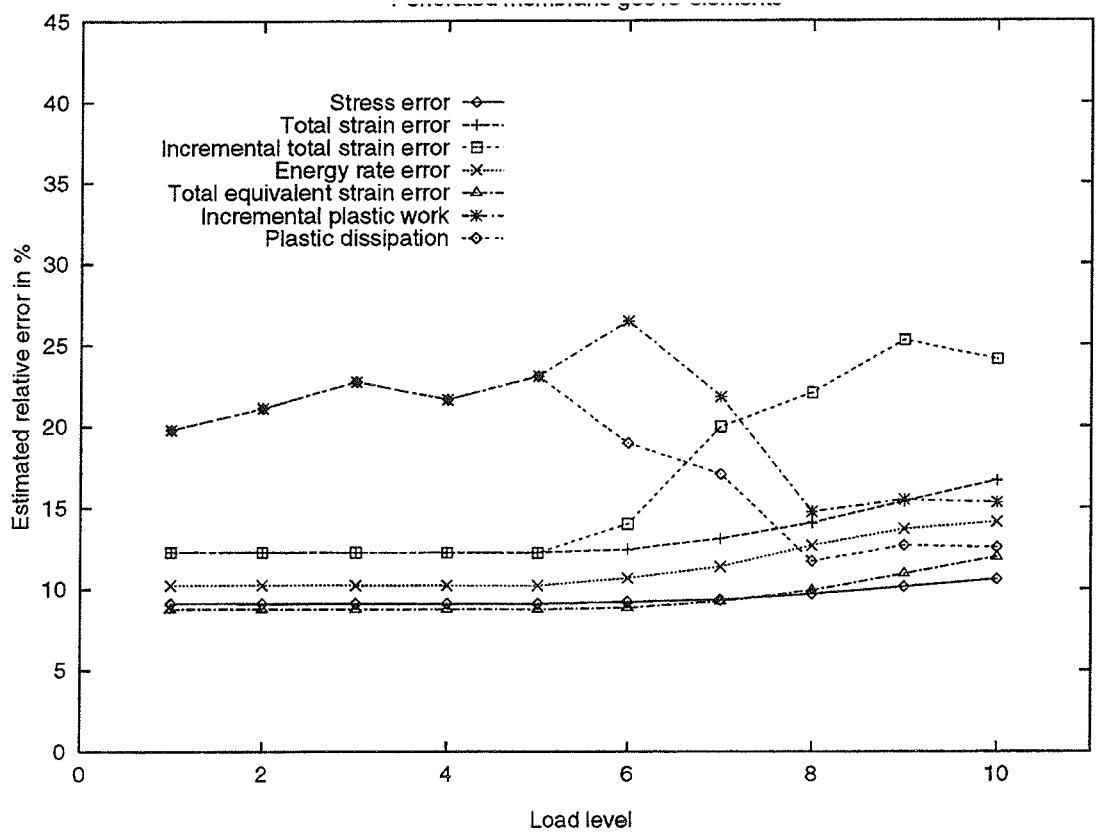
Figure 1: Estimated global errors for the perforated strip.

yielding is initiated. The equivalent plastic strain is zero apart from this area. An explanation of the magnitude of these error estimators in the "elastic" region is that the magnitude of the plastic strain is very small in the area mention above and since this area is small, the percentage error becomes fairly large.

4. REFERENCES

[1] K. M. Okstad and K. M. Mathisen. Towards automatic adaptive geometrically nonlinear shell analysis. Part I: Implementation of an h–adaptive mesh refinement procedure. *International Journal for Numerical Methods in Engineering*, 37:2657–2678, 1994.

[2] K. M. Okstad. *Adaptive Methods for Nonlinear Finite Element Analysis of Shell Structures*. Dr. Ing. dissertation, Department of Structural Engineering, The Norwegian Institute of Technology, Trondheim, Norway, 1994.

[3] C. Johnson and P. Hansbo. Adaptive finite element methods in computational mechanics. *Computer Methods in Applied Mechanics and Engineering*, 101:143–181, 1992

[4] O. C. Zienkiewicz and J. Z. Zhu. The superconvergent patch recovery and a *posteriori* error estimates. Part 1: The recovery technique. *International Journal for Numerical Methods in Engineering*, 33:1331–1364, 1992.

[5] N.-E. Wiberg, F. Abdulwahab, and S. Ziukas. Enhanced superconvergent patch recovery incorporating equilibrium and boundary conditions. *International Journal for Numerical Methods in Engineering*, 37:3417–3440, 1994.

[6] R. P. Tetambe, S. M. Yunus, C. Rajakumar, and S. Saigal. Examination of Flux Projection-Type Error Estimators in Nonlinear Finite Element Analysis. *Computers and Structures*, 54:641–653, 1995.

[7] D. Perić, J. Yu, and D. R. J. Owen. On error estimates and adaptivity in elastoplastic solids: Applications to the numerical simulation of strain localization in classical and Cosserat continua. *International Journal for Numerical Methods in Engineering*, 37:1351–1379, 1994.

Analysis of contact-impact problems using parallel computers

Per Persson and Larsgunnar Nilsson
Division of Solid Mechanics
Linköping Institute of Technology

Abstract

This paper concerns the numerical solution of contact-impact problems using parallel computers. The theoretical problem is stated, followed by a semi-discretisation in time and space. An explicit finite element method is used to form the solution. The contact search used is based on the Hierarchical Territory Algorithm, HITA, and the contact forces are calculated using the Defence Node Algorithm, DENA. The parallel implementation and numerical results are presented, and the parallel version of HITA-DENA performs well on all test examples compared to 'standard' LS-DYNA3D algorithms.

Introduction

The evolution of High Performance Computers (HPC), has led computer manufacturers to develop computers based on multiple CPU:s using a message passing paradigm for the inter-processor exchange of data. To efficiently exploit these so called MIMD computers, both algorithms and implementation strategies must be revised.

In Finite Element (FE) analyses the use of MIMD computers may be very efficient, since large parts of the problem can be solved in parallel. By using a domain decomposition of a FE mesh and distributing the different parts to different processors, only a very small fraction of all computations needs to be done in serial. This is especially true for explicit calculations, which does not need the forming of a large stiffness matrix.

However, the parallel solution of FE problems requires new algorithms. Particularly contact-impact algorithms need to be rewritten to deal with parts of a FE mesh that reside in different domains (processors). This article describes a re-implementation of the contact-impact algorithm HITA-DENA, Nilsson et al. [3], for use in a parallel computing environment.

Problem formulation

To form the dynamical contact problem we need to state

1. the equations of motion,

2. the constitutive equations,

3. the boundary conditions,

4. the contact conditions,

5. the initial conditions.

Discretisation

A semi-discretisation is made, i.e. a FE discretisation in space, and a central difference discretisation in time, and standard explicit FE procedures are used. The contact conditions require a contact search and contact force evaluation.

Contact search

The contact search is based on the Hierarchical Territory Algorithm, HITA, where a hierarchical concept is adopted. Thediscretised contact system is described by five primitives: contact body, contact surface, contact segment, contact edge and contact node. For the parallel algorithm the concept sub-body is introduced. A sub-body is the part of a physical body that is contained within the same sub-domain. Thus a physical body may be split into several sub-bodies, each residing in different sub-domains.

For the searching algorithm this means that information of all sub-bodies must be distributed to all processors involved in the calculation. If common territories are encountered, further calculations will be needed to evaluate if contact between the two hierarchies occurs.

Contact force

Contact forces are evaluated using the Defence Node Algorithm (DENA) with Lagrange multipliers for the contact constraints. The Lagrange multiplier method requires the solution of a system of coupled equations, but with a decoupling of the equations the need for implicit calculations is released. Since DENA reducesthe contact to be a node to node contact, this decoupling makes the algorithm very efficient and simple to parallelise.

Implementation

The algorithm is implemented into the LS-DYNA3D program, Hallquist et al. [1]., using MPI, (Message Passing Interface) by Message Passing Interface Forum [2], as the message passing library. Flow charts of the implementation are shown, and a discussion regarding some of the problems found in programming for parallel computers is held.

Numerical results

The results are found to be good on all tested examples. Total calculation time for the HITA-DENA algorithm is smaller than for 'standard' LS-DYNA3D algorithms in the case of a smaller number of processors. In Figure 1, HITA-DENA can be compared to 'standard' LS-DYNA3D. Further tuning of the implementation is needed to be able to compete with other contact-impact algorithms for cases with a larger number of processors.

All timings have been performed on a 64 node (128 processors) Parsytec Gigacube Power Plus, which has also served as the development platform.
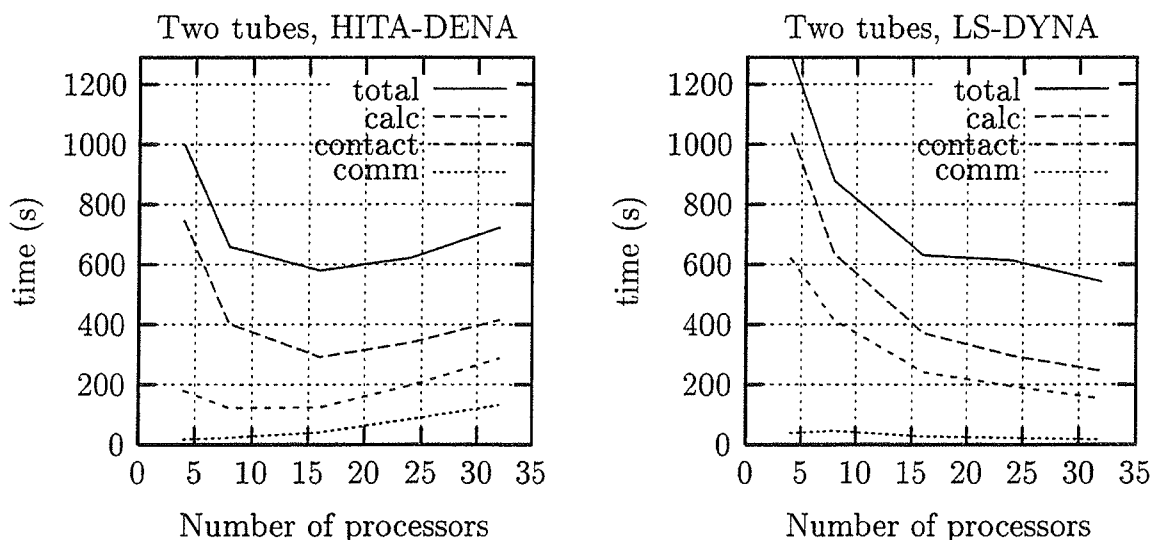
Acknowledgement

Figure 1: Timing results for the two tubes example

References

[1] J. O. Hallquist. *LS–DYNA3D Theoretical Manual*. Livermore Software Technology Corporation, Livermore, 1991. LSTC Report 1018.

[2] Message Passing Interface Forum, University of Tennessee, Knoxville, Tennessee. *MPI: A Message-Passing Interface Standard*, 1993.

[3] L. Nilsson, Z. H. Zhong, and M. Oldenburg. Analysis of shell structures subjected to contact-impacts. In A. K. Noor, T. Belytchko, and J. C. Simo, editors, *Analytical and Computational Models for Shells*, San Francisco, California, Winter annual meeting 1989. ASME.

Dynamic Response of Multibody Systems with Joint Clearance

Peter Ravn
Department of Solid Mechanics
Technical University of Denmark
Building 404, DK-2800 Lyngby
Email: pr@fam.dtu.dk

1. Introduction

Clearance from manufacturing tolerances or wear is likely to degrade the dynamic performance of connected machine parts. When joint clearance is introduced, the mechanism behaviour changes because kinematically undetermined degrees of freedom are introduced - possibly leading to chaos[1]. The dynamic response of the mechanical system is substantial changed, seen as high acceleration and force peaks and dissipation of energy.

As for contact models, the simpler ones, such as Kelvin-Voigt or the Hertz model, are characterized by a set of parameters. These include material parameters, coefficient of restitution, e, and possibly the ratio, μ, of tangential to normal impulses[2]. The models can be divided into two groups - continuous and discontinuous[3] - related to whether integration is carried out through the period of contact, or stopped and restarted with new initial conditions obtained from solving a set impulse related equations.

Based on the equations of motion for a system of rigid bodies, simple models for contact forces are used to model joint clearance in a multibody system. The dynamic response of a mechanism is investigated, looking at the levels of acceleration, force and energy dissipation.

2. Continuous Contact Models

The continuous analysis approach of two impacting bodies is performed simply by including the contact force in the system equations of motion during the period of contact. The most simple, known as the Kelvin-Voigt visco-elastic model, assume linear relation between penetration depth and the impact force. Energy loss is simply accounted for by multiplying the rebound force (impact force in the separation phase) by the coefficient of restitution.

A more superior model, known as the Hertz force-displacement law, assumes a nonlinear relation between penetration and impact force. The normal force to the

plane of contact between two colliding spheres is written as[3]

$$f = K\delta^n + D\dot{\delta} \tag{1}$$

where δ is the relative penetration depth and $n = 1.5$. The parameter K depend on material and radii of the spheres

$$K = \frac{4}{3\pi(h_i + h_j)} \left[\frac{R_i R_j}{R_i + R_j}\right]^{\frac{1}{2}} \tag{2}$$

$$h_k = \frac{1 - \nu_k^2}{\pi E_k} \quad ; \quad k = i, j \tag{3}$$

Because of dissipation in the form of heat or permanent deformation, the relative rebound velocity is reduced. Assuming the energy loss can be modeled as internal damping - valid only for low impact velocities - damping can be included in the form of a damping coefficient, D, proportional to the penetration velocity $\dot{\delta}$. The damping factor is estimated by means of the impulse-momentum equations[3] and the coefficient of restitution as

$$D = \delta^n \left[\frac{3K(1 - e^2)}{4\dot{\delta}^-}\right] \tag{4}$$

where $\dot{\delta}^-$ is the initial penetration velocity. The effect of this form for damping is seen in Figure 1A, which shows the hysteresis of multiple impact of a heavy sphere on a rigid barrier. Also the Hertz' contact force for the first impact, is plotted in Figure 1B
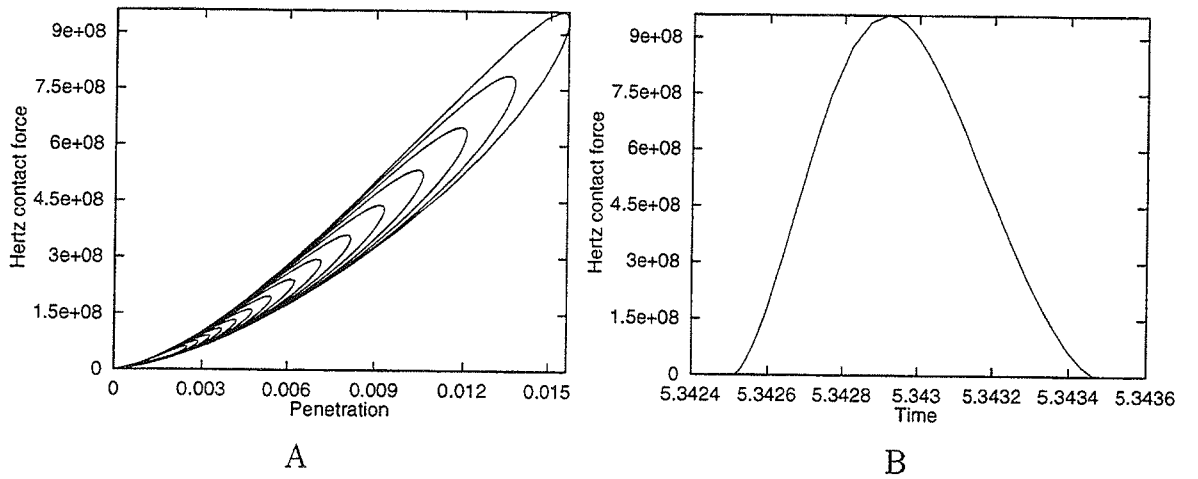

| A | B |

Figure 1.   A) Hysteresis of a ball with multiple impact on a rigid barrier. e=0.8. B) Hertz contact force of the balls first impact.

174

3. Discontinuous Contact Model

The discontinuous model assumes that the period of contact is short and thereby instantaneous changes in velocity occur. Since this leads to infinite accelerations of the bodies in contact, the overall mechanical system is subject to a energy dis-continuity, requiring the numerical integration to be restarted with new initial conditions.

A central impact of two colliding bodies, i and j, where also tangential impact velocities are present, are written in terms of impact-momentum equations as

$$m_i v_{in}^+ + m_j v_{jn}^+ = m_i v_{in}^- + m_j v_{jn}^- \tag{5}$$

$$m_i v_{it}^+ + m_j v_{jt}^+ = m_i v_{it}^- + m_j v_{jt}^- \tag{6}$$

where subscript n and t refer to normal and tangential direction, respectively and superscript $-$ and $+$ denote before and after the impact, respectively.

If the initial velocities are known, two more equations are needed to solve for the four unknown velocities after the impact

$$v_{jn}^+ - v_{in}^+ = -e(v_{jn}^- - v_{in}^-) \tag{7}$$

$$m_i v_{it}^+ - \mu m_j v_{jn}^+ = m_i v_{it}^- - \mu m_j v_{jn}^- \tag{8}$$

where Eq. 7 use the coefficient of restitution to provide energy loss in the normal direction, and Eq. 8 accounts for the tangential impulse or friction by means of the ratio μ.
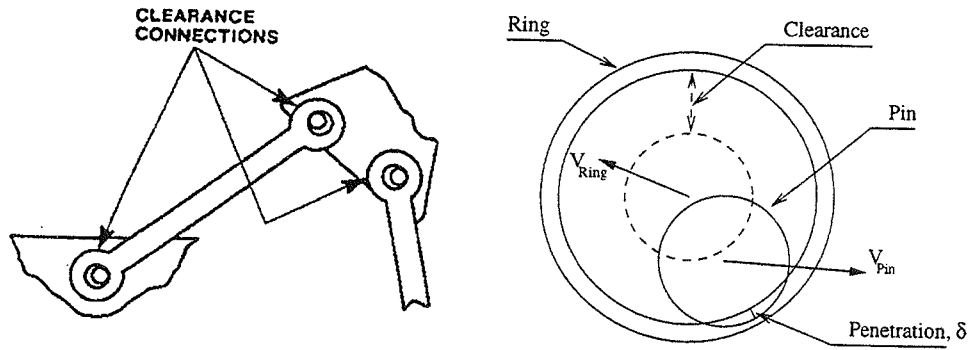
4. Dynamic Response

Figure 2. Revolute joint with clearance.

Based on the equations of motion for a constrained multibody system

$$\begin{bmatrix} \mathbf{M} & \mathbf{\Phi}^T \\ \mathbf{\Phi} & \mathbf{0} \end{bmatrix} \left\{ \begin{array}{c} \ddot{\mathbf{q}} \\ \lambda \end{array} \right\} = \left\{ \begin{array}{c} \mathbf{F} \\ \gamma \end{array} \right\} \tag{9}$$

a mechanism simulation is performed by integrating forward in time. Eq. 9 both include kinematic constraints from joints and independent degrees of freedom. To

175

demonstrate the effect of joint-clearance, a revolute joint, as seen in Figure 2, is modeled with clearance, and thereby controlled by contact forces instead of kinematic constraints.

In a Slider Crank mechanism a revolute joint with clearance, connecting the connecting-rod with the slider, is introduced. The mechanism simulation results with and without clearance are compared. Figure 3A shows the horizontal slider velocity and Figure 3B shows the according acceleration.
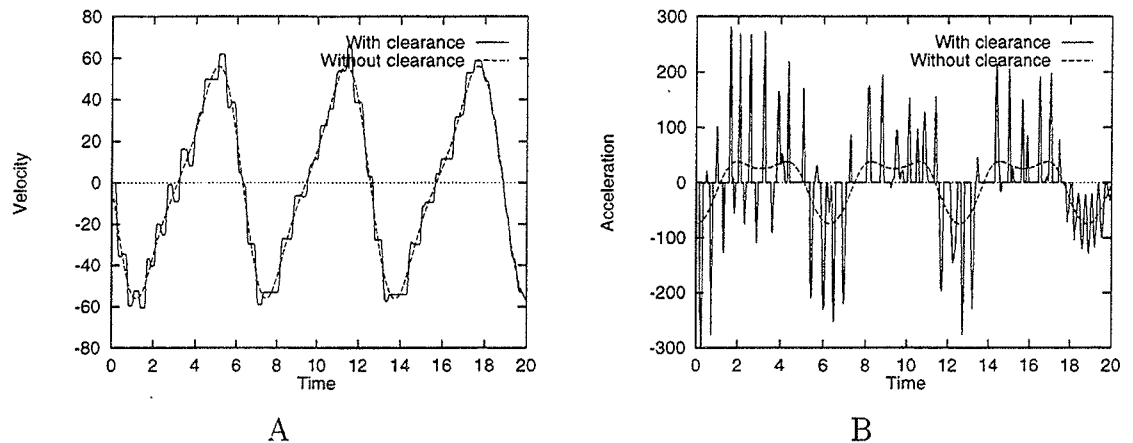

Figure 3. Horizontal velocity and acceleration response of the slider in a Slider Crank mechanism simulated with and without clearance in the rod-slider revolute joint.

From the velocity plot, it is clearly seen that de-acceleration is smoother since the impacts naturally dissipate some of the kinetic energy possessed by the slider. From the acceleration plot, it is seen how the acceleration peaks are increased almost by a decade.

References

1. Farahanchi, F., Shaw, S. W. (1994) Chaotic and Periodic Dynamics of a Slider-Crank Mechanism with Slider Clearance. *Journal of Sound and Vibration*, **Vol. 177**, pp. 307-324.
2. Brach, R. M. (1989) Rigid Body Collisions. *Journal of Applied Mechanics.*, **Vol. 56**, pp. 133-138.
3. Lankarani, H. M., Nikravesh, P. E. (1994) Continuous Contact Force Models for Impact Analysis in Multibody Systems. *Nonlinear Dynamics*, **Vol. 5**, pp. 193-207.
4. Dubowsky, S., Norris, M., Aloni, E., Tamir, A. (1984) An Analytical and Experimental Study of the Prediction of Impacts in Planar Mechanical Systems With Clearances. *Transactions of the ASME*, **Vol. 106**, pp. 444-451.
5. Wang, Y., Mason, M. T. (1992) Two-Dimensional Rigid-Body Collisions With Friction. *Journal of Applied Mechanics*, **Vol. 59**, pp. 635-642.

Single Hardening Plasticity Model for Frictional Materials

by

Poul V. Lade
Department of Civil Engineering
The Johns Hopkins University
Baltimore, Maryland 21218, U.S.A.

The constitutive model for frictional materials presented here has been developed on the basis of thorough review and evaluation of data from experiments on frictional materials, such as soil, concrete and rock (Kim and Lade 1988; Lade and Kim 1988a, 1988b). The framework for the evaluation and subsequent development consisted of concepts contained in elasticity and work-hardening plasticity theories.

The total strain increments observed in a material when loaded are divided into elastic and plastic components so that

$$d\varepsilon_{ij} = d\varepsilon_{ij}^e + d\varepsilon_{ij}^p \tag{1}$$

Both the elastic and the plastic strain increments are expressed in terms of effective stresses, and all functions for the elastic behavior, failure criterion, flow rule, yield criterion, and work-hardening/softening law are expressed in terms of the stress invariants I_1, I_2, and I_3 and the stress deviator invariant J_2.

Elastic Behavior.- The elastic strain increments are calculated from Hooke's law using a recently developed model for nonlinear variation of Young's modulus with stress state (Lade and Nelson 1987) The value of Poisson's ratio, ν, limited between zero and one-half for most materials, is assumed to be constant. The expression for young' modulus was derived from theoretical considerations based on the principle of conservation of energy. According to this derivation, Young's modulus E can be expressed in terms of a power law involving nondimensioal material constants and stress functions as follows:

$$E = M \cdot p_a \cdot \left[\left(\frac{I_1}{p_a} \right)^2 + R \cdot \frac{J_2}{p_a^2} \right]^\lambda \tag{2}$$

in which

$$R = 6 \cdot \frac{1+\nu}{1-2\nu} \tag{3}$$

and p_a is atmospheric pressure expressed in the same units as E, I_1, and $\sqrt{J_2}$, and the modulus number M and the exponent λ are constant dimensionless numbers.

Eq. 2 and Fig. 1 indicate that Young's modulus is constant along rotationally symmetric ellipsoidal surfaces whose long axis coincide with the hydrostatic axis and whose center is located at the origin of the principal stress space. The magnitude of Poisson's ratio determines the shape of the ellipsoidal surface. For $\nu=0$, R=6, and the surface becomes spherical, whereas for $\nu=0.5$, R=∞, and the surface degenerates into a line coinciding with the hydrostatic axis.
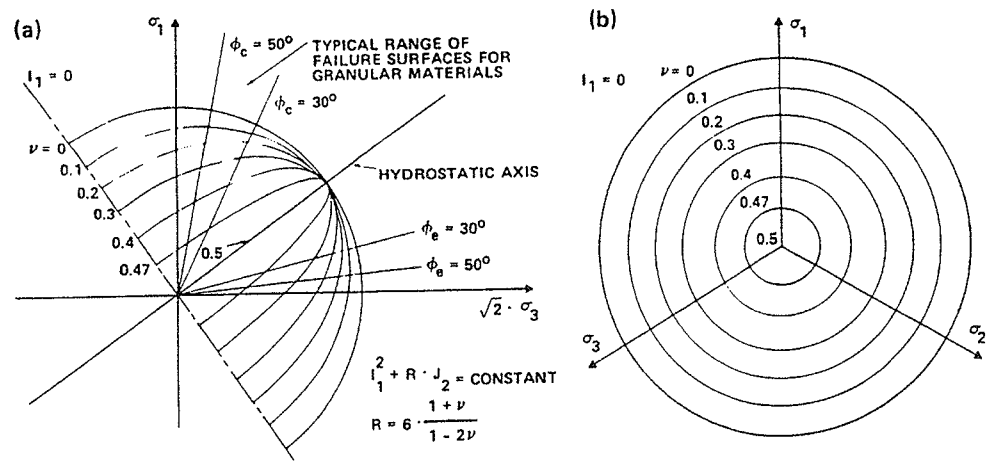
FIG. 1. Contours of Constant Young's Modulus Shown in (a) Triaxial Plane; and (b) Octahedral Plane

Failure Criterion.- A general three-dimensional failure criterion has been developed for soils, concrete and rock (Lade 1977, 1982, 1993). This criterion is expressed as follows:

$$\left(\frac{I_1^3}{I_3} - 27\right)\left(\frac{I_1}{p_a}\right)^m = \eta_1 \tag{4}$$

in which η_1 and m are constant dimensionless numbers. In principal stress space, the failure surface is shaped like an asymmetric bullet with the pointed apex at the origin of the stress axes, a shown in Fig. 2. The apex angle increases with the value of η_1. The failure surface is always concave towards the hydrostatic axis, and its curvature increases with the value of m. For m=0 the failure surface is straight, and if m>1.979 the failure surface becomes convex towards the hydrostatic axis. Analysis of numerous sets of data for concrete and rock indicates that m values rarely exceed 1.5. For constant value of m and increasing η_1 values, the cross-sectional shape in the octahedral plane changes from circular to triangular with smoothly rounded edges in a fashion that conforms to experimental evidence. The shape of these cross sections does not change with the value of I_1 when m=0. For m>0, the cross-sectional shape of the failure surface changes from triangular to become more circular with increasing value of I_1. Similar changes in cross-sectional shape are observed from experimental studies on soil, concrete, and rock.
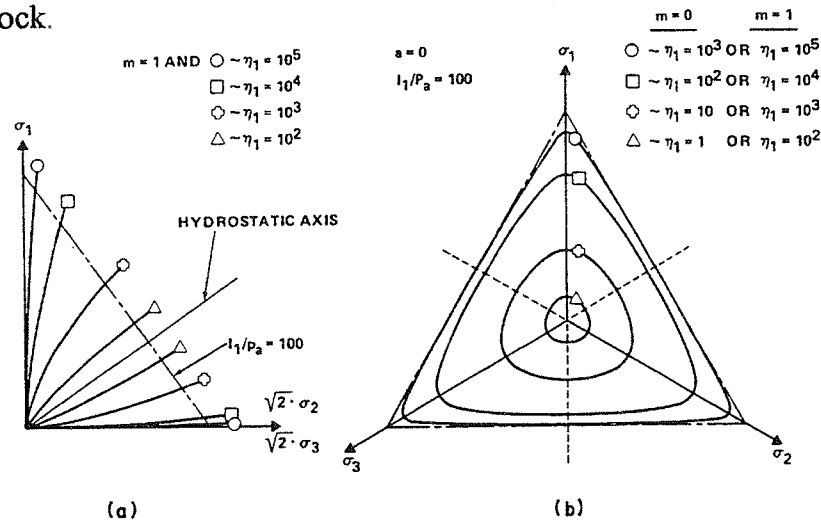

FIG. 2. Characteristics of Failure Surfaces Shown in Principal Stress Space: Traces of Failure Surfaces Shown in (a) Triaxial Plane; and (b) Octahedral Plane

178

<u>Flow Rule.-</u> The plastic strain increments are calculated from the flow rule:

$$de_{ij}^{p} = d\lambda_p \cdot \frac{\partial g_p}{\partial \sigma_{ij}}$$

(5)

in which g_p is a plastic potential function, and $d\lambda_p$ is a scalar factor of proportionality. For frictional materials the plastic potential function must be different from the yield function and nonassociated flow is consequently obtained. A suitable plastic potential function has the following form:

$$g_p = \left(\Psi_1 \cdot \frac{I_1^3}{I_3} - \frac{I_1^2}{I_2} + \Psi_2 \right) \cdot \left(\frac{I_1}{p_a} \right)^{\mu}$$

(6)

in which Ψ_1, Ψ_2, and μ are dimensionless constants. The parameter Ψ_1 acts as a weighting factor between the triangular shape (from the I_3 term) and the circular shape (from the I_2 term). The parameter Ψ_2 controls the intersection with the hydrostatic axis, and μ determines the curvature in the meridians. The corresponding plastic potential surfaces are shown in Fig. 3. They are shaped as asymmetric cigars with smoothly rounded triangular cross sections similar to, but more rounded than those for the failure surfaces shown in Fig. 2.
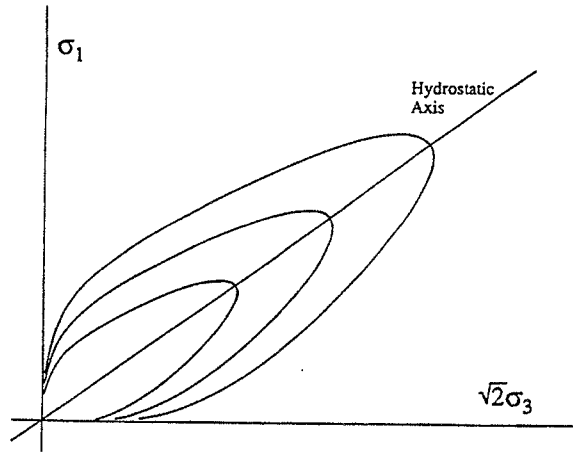

FIG. 3.   Plastic Potential Surfaces Shown In Triaxial Plane

<u>Yield Criterion and Work-Hardening/Softening Relation.-</u> The single isotropic yield surface is expressed as a contour of constant plastic work:

$$f_p = f_p'(\sigma) - f_p''(W_p) = 0$$

(7)

in which

$$f_p' = \left(\Psi_1 \cdot \frac{I_1^3}{I_3} - \frac{I_1^2}{I_2} \right) \cdot \left(\frac{I_1}{p_a} \right)^h \cdot e^q$$

(8)

in which h is constant, and q varies from zero at the hydrostatic axis to unity at the failure surface. The parameter Ψ_1 acts as a weighting factor as in the expression for the plastic potential.

The yield surfaces are shaped as asymmetric teardrops with smoothly rounded triangular cross-sections and with traces in the triangular plane as shown in Fig. 4. The relation between the yield criterion and the plastic work (Eq. 7) is described by a
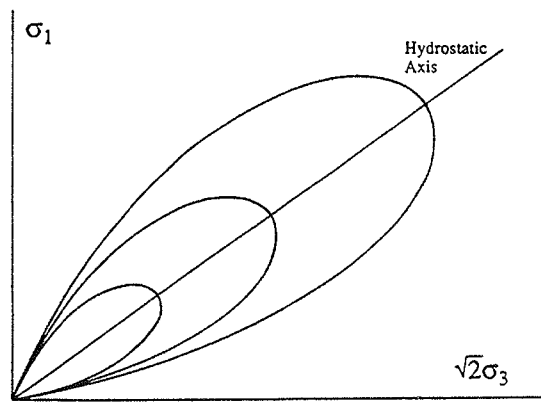
179

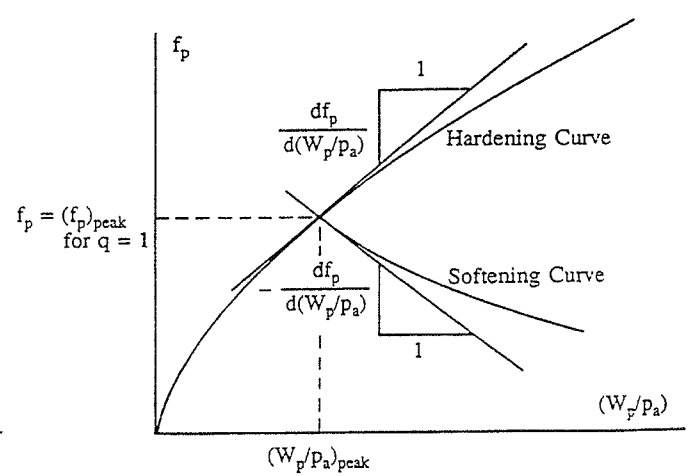FIG. 4. Yield Surfaces Shown in Triaxial Plane

FIG. 5. Modeling of Work Hardening and Softening

monotonically increasing function whose slope decreases with increasing plastic work, as shown in Fig. 5. As the plastic work increases, the isotropic yield surface inflates like a balloon until the current stress point reaches the failure surface. Beyond failure the yield surface contracts isotropically, like a deflating balloon, with increasing amount of plastic work, as also shown in Fig. 5.

Capabilities.- The single hardening model has been shown to capture the behavior characteristics observed in frictional materials. This is because the behavior of materials such as soils, concrete, and rock allows for a unified approach in describing their failure surfaces as well as their stress-strain relations. The constitutive model described here combines all the governing functions studied individually in a mathematically consistent entity. All required parameter values can be determined from simple laboratory tests, such as isotropic compression and conventional triaxial compression tests

The model has been shown to predict the stress-strain and strength behavior of soils of different types for drained and undrained conditions and for various two- and three-dimensional stress paths. Calculations for materials with effective cohesion and tensile strength such as concrete have also shown overall acceptable and accurate predictions.

References.-

Kim, M.K., and Lade, P.V. (1988) "Single hardening constitutive model for frictional materials, I. Plastic potential function," Computers and Geotechnics, 5(4), 307-324.

Lade, P.V., and Kim, M.K. (1988a) "Single hardening constitutive model for frictional materials, II. Yield criterion and plastic work contours," Computers and Geotechnics, 6(1), 13-29.

Lade, P.V., and Kim, M.K. (1988b) "Single hardening constitutive model for frictional materials, II. Comparison with experimental data," Computers and Geotechnics, 6(1), 30-47.

Lade, P.V., and Nelson, R.B. (1987) "Modelling the elastic behaviour of granular materials," Int. J. Numer. Anal. Methods Geomech., 11, 521-542.

Lade, P.V. (1977) "Elasto-plastic stress-strain theory for cohesionless soil with curved yield surfaces," Int. J. Solids Struct., 13, 1019-1035.

Lade, P.V. (1982) "Three-parameter failure criterion for concrete, J. Engrg. Mech. Div., ASCE, 108(5), 850-863.

Lade, P.V. (1993) "Rock strength criteria: The theories and the evidence," in Comprehensive Rock Engineering, Principles, Practice & Projects, Editor-in-Chief: J.A. Hudson, Chapter 11 in Vol. 1: Fundamentals edited by E.T. Brown, Pergamon Press, Oxford, England, 255-284.

180

Calibration of ABAQUS cap model to Copenhagen Limestone

Ole Hededal

COWI - Consulting Engineers and Planners AS
Transportation Division
Parallelvej 15, DK-2800 Lyngby
Denmark

Introduction

The ABAQUS cap model is applied to Copenhagen Limestone. The elasto-plastic material model is used for failure analyses of the pylon and pier foundations of the Øresund Bridge.

Copenhagen Limestone

The Øresund High Bridge pylons are founded on Copenhagen Limestone. Test series on limestone formations comparable to the is-situ conditions have been carried out by the Danish and Swedish Geotechnical Institutes, SGI/DGI(1994). The limestone on which the bridge is founded is characterized as slightly indurated and with a horizontal layering. The material is thus relatively soft and orthotropic by nature. As most available material models still apply to isotropic materials, an isotropic prototype material for elasto-plastic modelling has been suggested by DGI/SGI(1994), cf. Fig. 1.

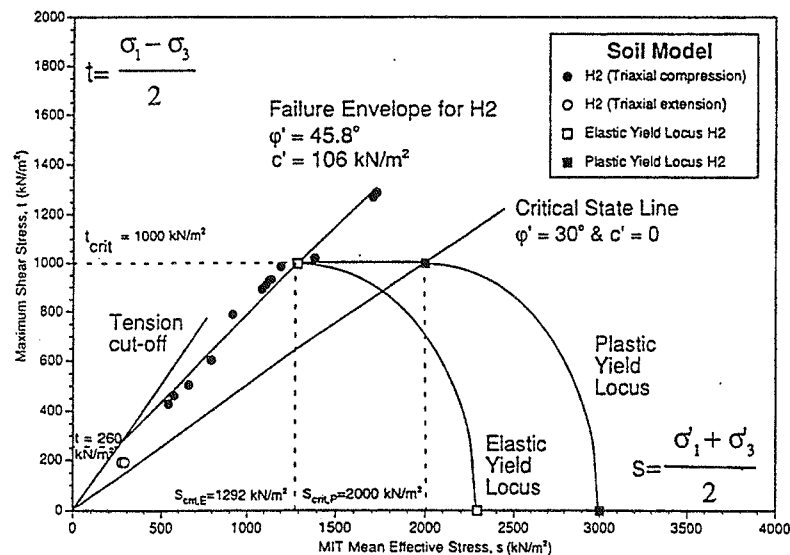Figure 1: Elasto-plastic prototype model for Copenhagen Limestone

The material model is a combination of a Critical State Line model and a cap model. It includes a Drucker-Prager type friction surface, a cap to limit the maximum deviatoric stress and control the isotropic compaction. For stress states on the Critical State Line the material is allowed move to stress states outside the failure locus.

Model calibration

The prototype model has been used to calibrate the ABAQUS cap model to Copenhagen Limestone, cf. Fig. 2. The choice of the cap model instead of e.g. a CSL model is motivated by the fact that the dominating failure mode of the pylon foundations will be combined sliding and shear, thus mainly governed by the friction parameters. The cap is mainly introduced to limit the maximum shear stress.
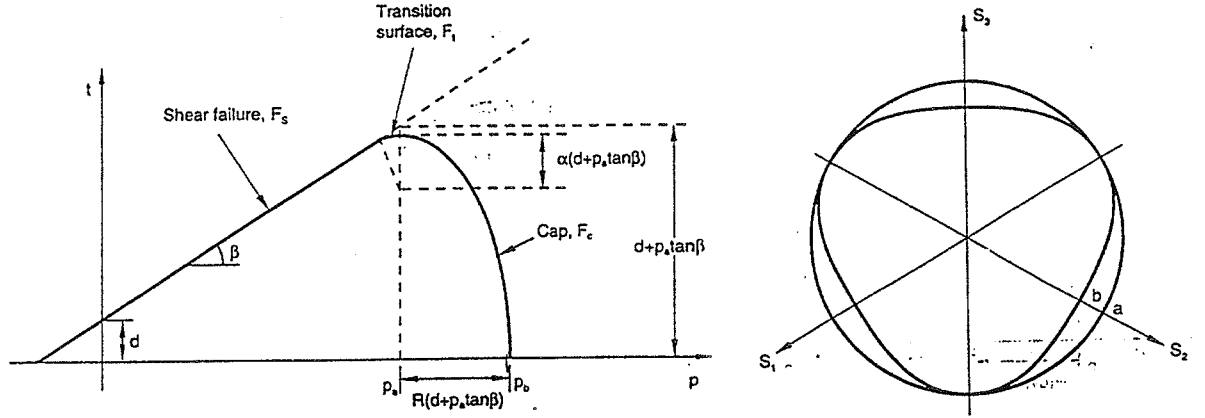

Figure 2: ABAQUS cap model

The ABAQUS cap model yield surface consists of a linear Drucker-Prager surface and an elliptic cap. It is defined in terms of the stress invariants (p,q) and the material parameters $(d, \tan\beta, p_a, R)$, cf. Fig. 2.

$$f = \begin{cases} t - p \tan\beta - d & \text{for } p \leq p_a \\[2mm] \sqrt{(p - p_a)^2 + (Rt)^2} - R(p \tan\beta + d) & \text{for } p > p_a \end{cases}$$

where

$p = -\sigma_{ii}/3$ is the hydrostatic pressure

$t = q\, F(K)/2$ is the deviatoric stress radius

$q = \sqrt{\frac{3}{2} s_{ij} s_{ij}}$ is the von Mises stress

$F(K)$; $K \in [0.8; 1]$ is a function of the ratio $K = \sigma_t/\sigma_c$, where σ_t and σ_c are the uniaxial tensile and compressive strength, respectively.

If $F(K) < 1$ then the deviatoric contour becomes more triangular, thus modelling a difference between the triaxial compressive and tensile strength. The lower bound $K > 0.8$ is imposed to ensure that the deviatoric contour remains convex. However, the numerical integration of the consistutive equations have shown to fail for $K \neq 1.0$ and therefore it has been necessary to use to circular deviator contour, even though triaxial tests on the limestone show that $K \approx 0.8$ for the limestone. Therefore, it has been necessary to choose which type of failure mode is governing and then calibrate accordingly.
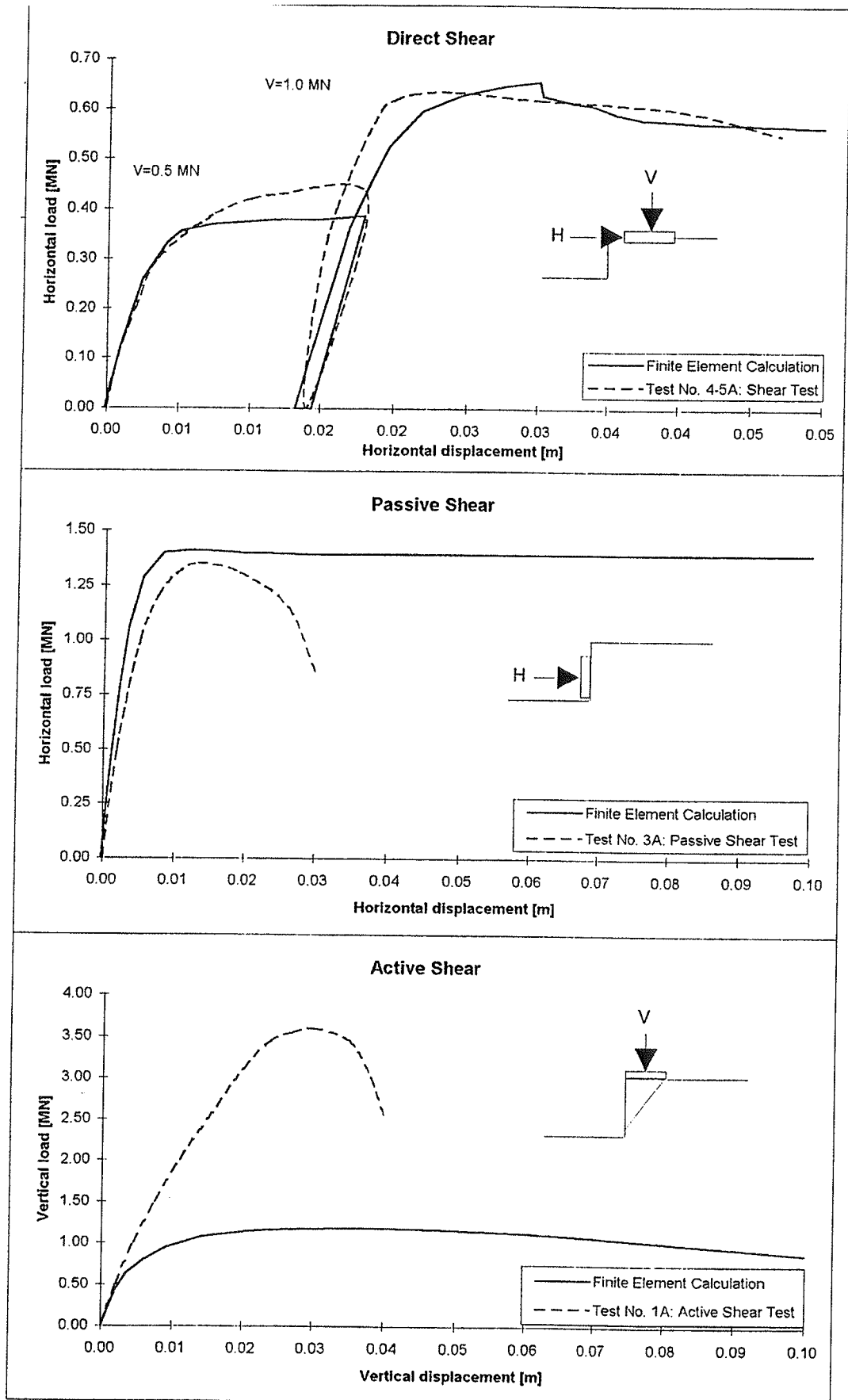
Figure 3: Model predictions

3 types of tests have been modelled in the calibration process

1. Sliding/shear

2. Passive failure

3. Active failure

It is assumed that the sliding/shear will dominate the failure of the pylon foundation and therefore the model is calibrated to this type of test. The same material parameters are then applied to the other 2 tests. The set-ups and results are shown in Fig. 3.

It is seen that the sliding/shear and the passive failure modes are well described. The failure load of the active failure test is, however, extremely underestimated by the model. This result is due to the application of the isotropic model to a orthotropic material. Weak horizontal layers are embedded in the limestone formations and they govern the strength in horizontal loading. For vertical loading, as in the active failure test, the failure line crosses both strong and weak layers, thus for vertical loading the strength is dominated by the stronger layers. In order to get conservative predictions on the failure loads the stronger layers are neglected.

Conclusions

The non-associated ABAQUS cap model has been applied to Copenhagen Limestone. A single set of material parameters has been used to predict the failure loads of the 3 in-situ tests. Sliding/shear and passive failure loads are close to the measured values, whereas the active failure load is underestimated. The deformation properties are not modelled equally well by a non-associated elliptic potential surface. The main problem is here the lack of an explicit tension cut-off, which for low hydrostatic pressures leads to effective dilation angles of $\psi \approx 60°$.

References

ABAQUS (1995): *ABAQUS Vers. 5.5 - manuals*, Hibbitt, Karlson & Sorensen, Inc.

SGI/DGI (1994): *Digest Report on Strength and Deformation Properties of Copenhagen Limestone*, Swedish Geotechnical Institute and Danish Geotechnical Institute.

A Characteristic State Model for Friction Materials

STEEN KRENK

Division of Mechanics, Lund University
Box 118, S-211 00 Lund, Sweden

Introduction

The classical critical state concept for soil is based on a self-similar family of yield surfaces with an isotropic hardening rule controlled by the so-called critical state. The critical state theory was developed in a two-dimensional setting using mean stress p and max stress difference q, and assuming associated plastic flow. In the original model, Schofield & Wroth (1968), the yield surface was derived from an intuitive model of plastic straining in a friction material, while this yield surface was replaced by an ellipse in the 'modified' theory of Roscoe & Burland (1968).

In this paper the concepts of critical state theory are generalized by introducing nonassociated plasticity, use of a general invariant surface format that reflects the influence of all three principal stresses, and introduction of a generalized hardening rule that permits the development of dilation prior to material failure. An associated formulation was presented by Krenk (1996b).

The surface format

A friction material without cohesion can not support tension, and therefore all three principal stresses are compressive. Figure 1a shows a typical yield surface in principal stress space with compression reckoned positive. The surface is generated by the curves in the octahedral and meridian planes shown in Fig. 1b.
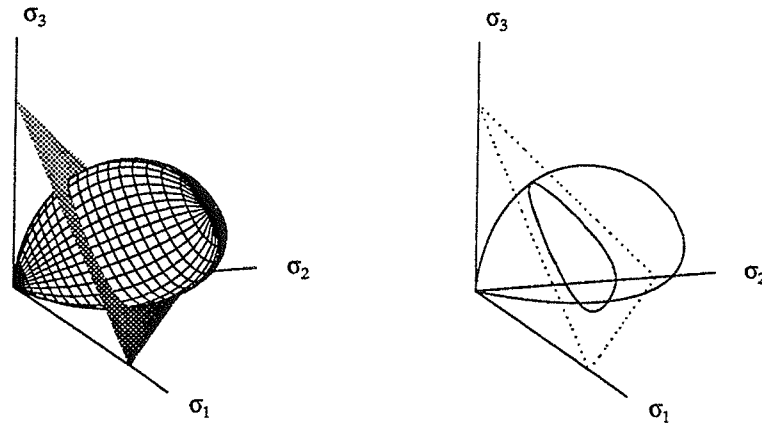

FIG. 1: a) Yield surface in principal stress space, b) Generating curves in octahedral and meridian planes.

The model is formulated in terms of the mean stress $p = \frac{1}{3}\sigma_{ii}$ and the deviatoric stress $s_{ij} = \sigma_{ij} - p\delta_{ij}$. The simplest form of an octahedral contour that satisfies symmetry with respect to the three principal deviator stress components is the cubic polynomial

$$(s_1 + d)(s_2 + d)(s_3 + d) = \eta d^3$$

The size of the circumscribing triangle is determined by the stress parameter d and the shape by the non-dimensional parameter and η, Krenk(1996). For a friction material $d \propto p$ and for $d = p$ the intersection of

185

the octahedral plane and the coordinate planes $\sigma_j = 0$ constitutes the circumscribing triangle. With th assumption the equation of the surface takes the form

$$f(\sigma) = -J_3 + p J_2 - (1 - \eta(p)) p^3 = 0$$

in terms of the deviatoric stress invariants

$$J_2 = \tfrac{1}{2} s_{ij} s_{ij} = -(s_2 s_3 + s_3 s_1 + s_1 s_2) \quad, \quad J_3 = \tfrac{1}{3} s_{ij} s_{jk} s_{ki} = s_1 s_2 s_3$$

Alternatively the surface can be expressed in terms of the total stress invariant $I_3 = \det(\sigma_{ij}) = \sigma_1 \sigma_2 \sigma_3$

$$f(\sigma) = -I_3 + \eta(p) p^3 = 0$$

This format was used by Lade & Duncan (1975) with constant η to generate a triangular cone, and by Lac & Kim for a curved triangular failure surface. The general format also contains the surface of Matsuoa & Nakai (1984), giving a smooth interpolation of the Coulomb criterion.
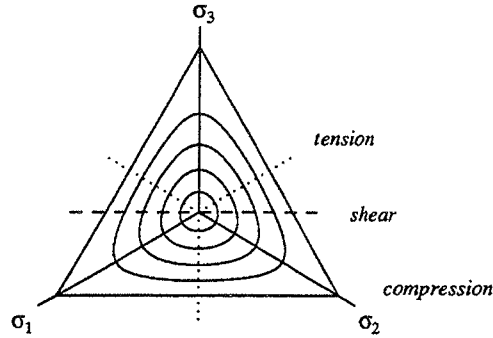

FIG. 2: Octahedral stress contours, $\eta = 0, 0.2 \cdots, 1$.

The family of octahedral contours are shown in Fig. 2. The yield function $f(\sigma)$ and the plastic potenti $g(\sigma)$ are obtained by selecting suitable functions $\eta_f(p)$ and $\eta_g(p)$, respectively.

The meridian curve takes a particularly simple form in the state of triaxial stress, $\sigma_2 = \tfrac{1}{2}(\sigma_1 + \sigma_3)$, show in Fig. 2. In this state of stress $J_3 = 0$, and thus the equation of this octahedral contour reduces t quadratic form,

$$J_2 = (1 - \eta(p)) p^2$$

It is now convenient to introduce the function $\gamma(p)$, defined by $\gamma^2 = 1 - \eta$. The shape of the triaxial shea meridian contour is then directly defined by

$$\gamma(p) = \sqrt{1 - \eta(p)} = \sqrt{J_2}/p$$

Thus γ is the secant inclination in a $p, \sqrt{J_2}$ plot.

Yield surface

The yield surface is assumed to have the coordnate planes σ_j as tangent planes at $p \simeq 0$, and thus for closed surface the function $\eta_f(p)$ must vary between 0 and 1, when the mean stress p varies between 0 an the current maximum value p_f. A simple function representing the typical shape of a yield function is

$$\eta_f(p) = (p/p_f)^m$$

where the exponent m is a model parameter. A typical yield function is shwn in Fig. 1.

Plastic potential

The plastic potential is constructed from constitutive considerations regarding the plastic work increment

$$p\,d\varepsilon_v^p + q\,d\varepsilon_q^p = dW^p$$

For generalized strain increments dp, dq along the plastic potential $dq/dp = -d\varepsilon_v^p/d\varepsilon_q^p$, and for triaxial shear the relation $\gamma = q/2p$ leads to

$$\frac{q}{p} - \frac{dq}{dp} = -2p\frac{d\gamma_g}{dp} = \frac{dW}{p\,d\varepsilon_q^p}$$

In the original Cam Clay model the plastic work was introduced via the classical Taylor hypothesis as $dW^p = M\,p\,d\varepsilon_q^p$. However, this hypothesis violates the no-tension condition, and leads to potential surfaces that intersect the coordinate planes σ_j. A simple 'consistent' alternative is obtained by assuming the plastic work increment to be related to the miimum principal stress, i.e. assuming a relation of the form $dW = 2n\sigma_{min}d\varepsilon_q^p$, where n is a model parameter. With this representation the plastic work relation can be integrated to give

$$\gamma_g(p) = 1 - (p/p_g)^n$$

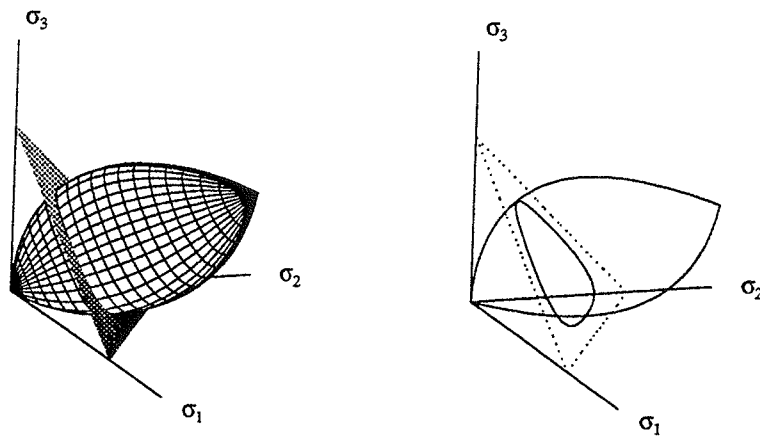A typical plastic potetial surface is shown in Fig. 3.

FIG. 3: a) Plastic potential surface in principal stress space, b) Generating curves in octahedral and meridian planes.

Stiffness and Hardening

The hardening rule should permit passage of the charcteristic state, i.e. the state of no (plastic) dilation, into the dilatant part of stress space. This is obtained by the weighted linear work hardening rule

$$dp_f = \frac{v}{\lambda - \kappa}\left(p\,d\varepsilon_v^p + w\,s_{ij}\,de_{ij}^p\right)$$

where w is a non-dimensional weight parameter that determines the dilation in the ultimate state. This hardening rule leads to ideal plastic behaviour at the ultimate state defined by $dp_f = 0$.

Examples

A typical example for a triaxial compression test on loose sand using experimental results from Borup & Hedegaard (1995) is shown in Fig. 4. The model containing only three stiffness parameters, the two shape parameters m, n, and the weight parameter w for dilation appears to capture the general behaviour well. Figure 5 shows simulated results for triaxial constant volume (undrained) tests with loose and dense sand.
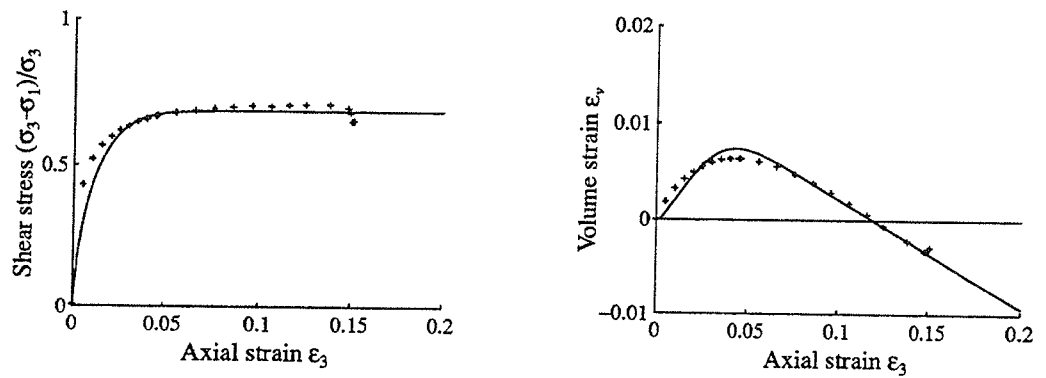
187

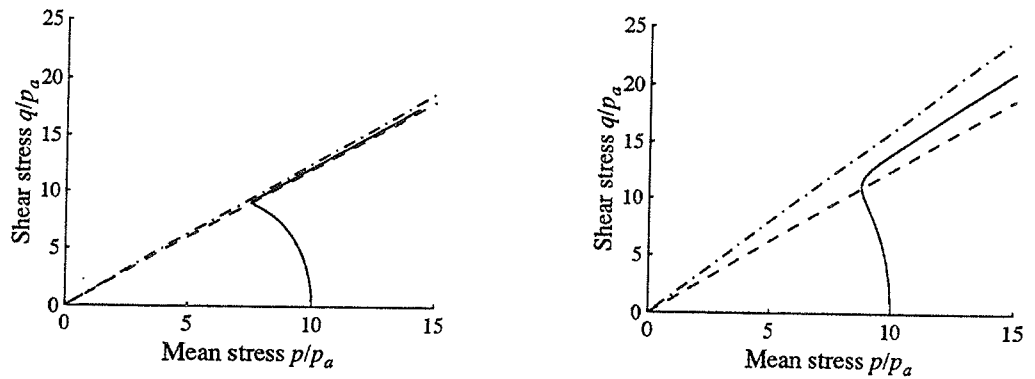FIG. 4: Stress and strain curves for loose Baskarp sand, $p_0 = 160$ kPa.

FIG. 5: Stress paths for loose and dense Baskarp sand.

References

Borup, M. and Hedegaard, J. (1995). *Characteristic State Modelling of Friction Materials*. M.Sc. Thesi Aalborg University, Aalborg, Denmark.

Krenk, S. (1996a). A family of invariant stress surfaces. *Journal of Engineering Mechanics*, **122**, pp. 20 208.

Krenk, S. (1996b). A charactristic state plasticity model for granular materials. *IUTAM Symposium (Mechanics of Granular and Porous Materials*, N. Fleck (Ed.), Kluwer, Doordrecht.

Lade, P.V. and Duncan (1975). Elasto-plastic stress-strain theory for cohesionless soil. *Journal of tl Geotechnical Engineering Division, ASCE*, **101**, pp. 1037-1053.

Lade, P.V. and Kim M.K. (1995). Single hardening constitutive model for soil, rock and concrete. *Inte national Journal of Solids and Structures*, **32**, pp. 1963-1978.

Matsuoka, H. and Nakai, T. (1985). Relationship among Tresca, Mohr-Coulomb and Matsuoka-Nak; failure criteria. *Soils and Foundations*, **25**, pp. 123-128.

Roscoe, K.H. and Burland, J.B. (1968). On the generalized stress-strain behaviour of 'wet' clay, in *Eng neering Plasticity*, J. Heyman and F.A. Leckie, (Eds.). Cambridge University Press, pp. 535-609.

Schofield, A.N. and Wroth, C.P. (1968). *Critical State Soil Mechanics*. McGraw-Hill, New York.

MODELLING OF GRANULAR
FLOW IN A SILO

Jørgen Flemming Olsen and Leif Otto Nielsen

Department of Structural Engineering and Materials

Technical University of Denmark

Introduction

Many granular materials such as sand, gravel and grain are stored in silos. Designing a silo one has to assess the loads on the silowalls arising from the silo medium during filling, storage and discharge and it is important to avoid geometries which are likely to promote e.g. dead zones (Fig. 1a) or arching (Fig. 1b).

(a)   (b)
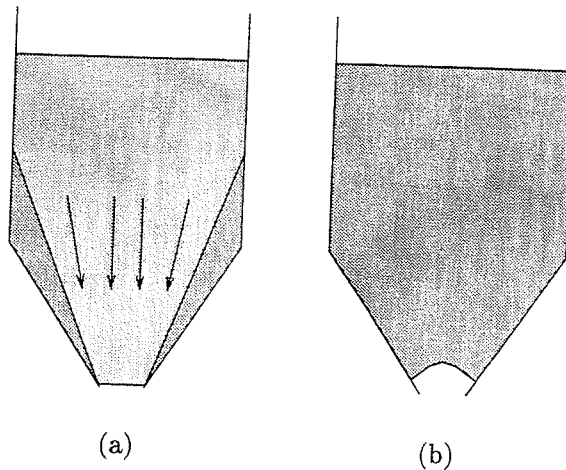
Fig. 1.

The classic solutions to silo-problems assume simple geometries and simple constitutive laws like the ideal Coulomb law. These solutions, see e.g. (Nedderman 1992), form together with empirically derived correction factors the basis of existing codes. In recent years much work has been done as to the numerical analysis of silo-problems and a number of different constitutive laws and computational methods have been applied. The pioneering work on this subject was carried out mainly by german researchers, see e.g. (Eibl & Häussler 1984), (Eibl & Rombach 1988).

Formulation

The equilibrium equations are given as

$$\sigma_{ij,j} + \varrho\, b_i = \varrho\, \ddot{u}_i \tag{1}$$

where σ_{ij} is the Cauchy stress tensor, b_i the body force vector, $\ddot{u}_i$ the acceleration vector and ϱ the density of the material.

The granular material is regarded as a solid body exposed to large strains. For that reason a Lagrangian formulation is chosen meaning that all static and kinematic variables are referred to a reference configuration. The material is modelled with an elastic-plastic constitutive law which is expressed as

$$\overset{\circ}{\sigma}_{ij(Ja)} = C_{ijkl}\, D_{kl}$$
$$D_{kl} = \tfrac{1}{2}\left(v_{k,l} + v_{l,k}\right) \tag{2}$$

where $\overset{\circ}{\sigma}_{ij(Ja)}$ is the Jaumann stress rate, C_{ijkl} the material stiffness tensor, D_{ij} the rate-of-deformation tensor and v_i the velocity vector.

The material is assumed to be isotropic and the chosen yield surface belongs to a family of invariant stress surfaces (Krenk 1996) in which the deviatoric contours (Fig. 2) are defined by a size parameter and a shape parameter.
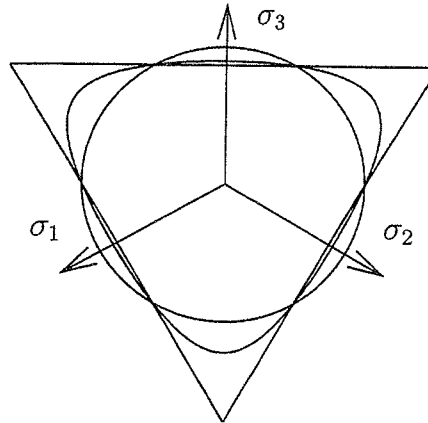

Fig. 2. Deviatoric contours

Further assumptions besides isotropy have been made. All yield surfaces are identical in shape and the size of a yield surface is a function of the

190

density of the material and thus obtainable from an isotropic compression test. The assumption regarding the size of a yield surface determines at the same time a simple hardening and softening rule. The size and the shape of the deviatoric contours are functions of the average principal stress solely. A yield surface is shown in Fig. 3.
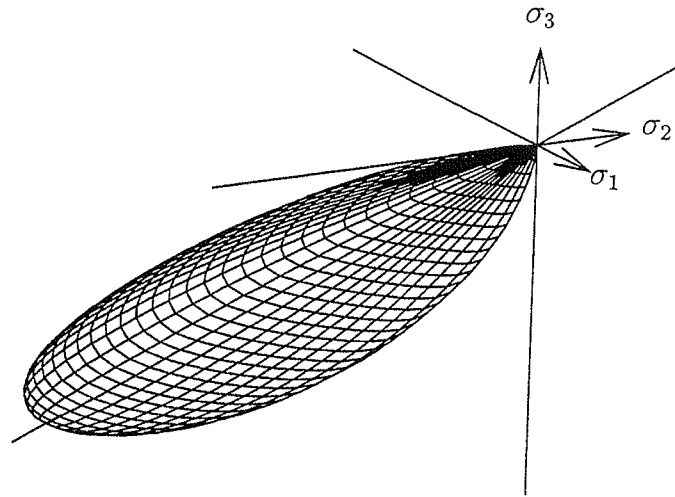
Fig. 3. Yield surface

At present the associated flowrule is used implying that plastic strains are perpendicular to the yield surface. A non-associated flowrule as well as a rate dependent stress term will be added later.

References

Eibl, J. & Häussler, U. (1984). Numerical investigations on discharging silos, *Journal of Engineering Mechanics* **110**(6): 957–971.

Eibl, J. & Rombach, G. (1988). Consistent modelling of filling and discharging processes in silos, *Silos - Forschung und Praxis Tagung '88*, Universität Karlsruhe.

Krenk, S. (1996). Family of invariant stress surfaces, *Journal of Engineering Mechanics* **122**(3): 201–208.

Nedderman, R. M. (1992). *Statics and Kinematics of Granular Materials*, Cambridge University Press.

Error Estimation of Reissner–Mindlin Elements using Statically Admissible Stress Resultants

Knut Morten OKSTAD, Trond KVAMSDAL* and Kjell Magne MATHISEN

Department of Structural Engineering
Norwegian University of Science and Technology
N–7034 Trondheim, Norway

1. INTRODUCTION

Error estimation in structural finite element (FE) analysis by the well-known Zienkiewicz–Zhu approach involves the recovery of an improved C^0-continuous stress field as a basic component. The superconvergent patch recovery (SPR) method [1], has proved to be an efficient tool for this purpose in both two-dimensional elasticity and plate bending applications. In the SPR-method, the recovered stress field is expressed as a polynomial over a small patch of elements, typically the group of elements that have one node in common. The coefficients of the polynomial are the determined from a least squares fit of the polynomial to the FE stress values at the superconvergent points (also known as Barlow points) of the elements in the patch.

The stress field obtained in this manner normally violates the governing equilibrium equations of the problem. Therefore, in order to increase the quality of the recovered field, the method is often enhanced by constraining the field to also satisfy interior equilibrium as well as natural boundary conditions in a least square manner over the patch, see e.g. [2]. The square of the residual of the equilibrium equations is then added to the SPR-functional. Instead of doing this, the interior equilibrium can be accounted for more directly by selecting a polynomial basis for the recovered field that *a priori* satisfies equilibrium. This approach is presented for two-dimensional elasticity problems in [3] and is herein applied on plate problems with transverse shear deformation.

2. RECOVERY OF STATICALLY ADMISSIBLE STRESS RESULTANTS

Given an open bounded domain $\Omega \in \mathbb{R}^2$, with boundary $\partial\Omega = \partial\Omega_u \cup \partial\Omega_t$. The governing equations of the Reissner–Mindlin plate theory then reads

$$[\mathbb{D}_b^T \ \mathbb{D}_s^T] \begin{Bmatrix} \mathbf{m} \\ \mathbf{q} \end{Bmatrix} + \mathbf{f} \ = \ 0 \qquad \text{in } \Omega \tag{1}$$

$$\mathbf{u} \ = \ \bar{\mathbf{u}} \qquad \text{on } \partial\Omega_u \tag{2}$$

$$\mathbf{Q} \begin{Bmatrix} \mathbf{m} \\ \mathbf{q} \end{Bmatrix} \ = \ \bar{\mathbf{t}} \qquad \text{on } \partial\Omega_t \tag{3}$$

Here, $\mathbf{f} = \{p_z, 0, 0\}$ represents the distributed load, $\mathbf{u} = \{w, \theta_x, \theta_y\}^T$ is the unknown displacement field, and $\bar{\mathbf{u}}$ and $\bar{\mathbf{t}} = \{\bar{V}_z, \bar{M}_x, \bar{M}_y\}^T$ are the prescribed displacements and tractions along $\partial\Omega_u$ and $\partial\Omega_t$, respectively. The bending moments $\mathbf{m} = \{m_{xx}, m_{yy}, m_{xy}\}^T$ and transverse shear forces $\mathbf{q} = \{q_x, q_y\}^T$ are coupled to the displacement field through $\mathbf{m} = \mathbf{C}_b \mathbb{D}_b \mathbf{u}$ and $\mathbf{q} = \mathbf{C}_s \mathbb{D}_s \mathbf{u}$, respectively, where $\mathbf{C}_b$ and $\mathbf{C}_s$ are the plate constitutive matrices. The strain-giving differential operators $\mathbb{D}_b$ and $\mathbb{D}_s$ and the 'stress resultant-to-boundary traction' transformation matrix $\mathbf{Q}$ are

---

*Currently at SINTEF Applied Mathematics, N–7034 Trondheim, Norway

given by, respectively

$$
\mathbb{D}_b = \begin{bmatrix} 0 & \frac{\partial}{\partial x} & 0 \\ 0 & 0 & \frac{\partial}{\partial y} \\ 0 & \frac{\partial}{\partial y} & \frac{\partial}{\partial x} \end{bmatrix}, \quad \mathbb{D}_s = \begin{bmatrix} \frac{\partial}{\partial x} & -1 & 0 \\ \frac{\partial}{\partial y} & 0 & -1 \end{bmatrix} \quad \text{and} \quad \mathbf{Q} = \begin{bmatrix} 0 & 0 & 0 & n_x & n_y \\ 0 & -n_y & -n_x & 0 & 0 \\ n_x & 0 & n_y & 0 & 0 \end{bmatrix} \tag{4}
$$

where n_x and n_y are direction cosines of the outward unit normal vector of the boundary $\partial\Omega$.

Following the approach presented in [3], we want to construct a statically admissible stress resultant field, $(\mathbf{m}^*, \mathbf{q}^*)$, that satisfies the equilibrium equation (1), on the form

$$
\left\{ \begin{array}{c} \mathbf{m}^*(x, y) \\ \mathbf{q}^*(x, y) \end{array} \right\} = \mathbf{P}_h(x, y)\, \mathbf{a}_h + \mathbf{P}_p(x, y)\, \mathbf{a}_p \tag{5}
$$

where $\mathbf{P}_h$ and $\mathbf{P}_p$ are matrices of monomials in x and y, and $\mathbf{a}_h$ and $\mathbf{a}_p$ are corresponding vectors of coefficients giving the magnitude of each monomial. The subscript $_h$ and $_p$ here denote the homogeneous and particular solution, respectively. Assuming the distributed load can be expressed as a polynomial $\mathbf{f}(x, y) = \mathbf{P}_f(x, y)\, \mathbf{a}_f$ with $\mathbf{P}_f$ being another matrix of monomials and $\mathbf{a}_f$ a vector of known coefficients, the following constraints may be deduced from (1)

$$
\begin{bmatrix} \mathbb{D}_b^T & \mathbb{D}_s^T \end{bmatrix} \mathbf{P}_h = 0 \tag{6}
$$

$$
\begin{bmatrix} \mathbb{D}_b^T & \mathbb{D}_s^T \end{bmatrix} \mathbf{P}_p + \mathbf{P}_f = 0 \tag{7}
$$

in addition to $\mathbf{a}_p = \mathbf{a}_f$. Obviously, the constraints (6) and (7) do not define a unique choice for $\mathbf{P}_h$ and $\mathbf{P}_p$. To find explicit expressions for these matrices we start by assuming a complete polynomial up to a certain order for each component of $\mathbf{m}^*$ and $\mathbf{q}^*$. Insertion into (1) and collecting coefficients of each monomial in $\{x, y\}$, then yield a linear system of equations through which some of the coefficients are eliminated. The resulting polynomial is then reordered into the form (5).

Starting with a complete bi-quadratic polynomial for each of the five stress resultant components, i.e. a total of $5 \times 9 = 45$ unknown coefficients, the above procedure reduces the number of unknowns to 21 ending up with a 5×21 $\mathbf{P}_h$-matrix. From this matrix we herein pick the following 17 columns as a basis for the statically admissible field

$$
\mathbf{P}_{h17} = \begin{bmatrix}
1 & 0 & 0 & x & 0 & 0 & 0 & y & 0 & xy & 0 & x^2 & 0 & 0 & 0 & y^2 & 0 \\
0 & 1 & 0 & 0 & y & 0 & 0 & 0 & x & 0 & xy & 0 & y^2 & 0 & 0 & 0 & x^2 \\
0 & 0 & 1 & 0 & 0 & y & x & 0 & 0 & 0 & 0 & -xy & -xy & x^2 & y^2 & 0 & 0 \\
0 & 0 & 0 & 1 & 0 & 1 & 0 & 0 & 0 & y & 0 & x & -x & 0 & 2y & 0 & 0 \\
0 & 0 & 0 & 0 & 1 & 0 & 1 & 0 & 0 & 0 & x & -y & y & 2x & 0 & 0 & 0
\end{bmatrix} \tag{8}
$$

It is now easily verified that (8) satisfies the constraint (6). Depending on the polynomial order of the load function, $\mathbf{f}(x, y)$, we will also have a $\mathbf{P}_p$-matrix. For a constant load p_z, for instance, we obtain $\mathbf{a}_p = \{p_z\}$ and the 5×1-matrix $\mathbf{P}_{p1} = \{0, 0, -\frac{1}{2}xy, -\frac{1}{2}x, -\frac{1}{2}y\}^T$. More details on the construction of the statically admissible polynomials are given in [4].

In the original SPR-approach [1], an improved stress field is determined over a small patch of elements by a least squares fit of a bi-linear (or higher for higher-order elements) polynomial to the FE values at the superconvergent points of the elements in the patch. Instead of a bi-linear basis we now use the polynomials defined by (5) and (8). Accordingly, we have the following SPR-functional to minimize with respect to the coefficients $\mathbf{a}_h$

$$
\mathcal{F}(\mathbf{a}_h) = \sum_{i=1}^{n_{bp}} \left(\mathbf{s}_i^h - \mathbf{P}_h(x_i)\, \mathbf{a}_h - \mathbf{P}_p(x_i)\, \mathbf{a}_p\right)^T \mathbf{W} \left(\mathbf{s}_i^h - \mathbf{P}_h(x_i)\, \mathbf{a}_h - \mathbf{P}_p(x_i)\, \mathbf{a}_p\right) \tag{9}
$$

Here, $x_i = \{x_i, y_i\}^T$ denotes the Cartesian coordinates of Barlow point i, $\mathbf{s}_i^h = \{m_{xx}^h, \ldots, q_y^h\}_i^T$ represents the FE stress resultants computed at that point, and n_{bp} denotes the total number of Barlow points in the patch. Since the matrix (8) introduces coupling between the bending moments and the transverse shear forces which have different dimensions, a matrix of weighting factors, $\mathbf{W}$, is introduced in the functional to enforce the same dimension on all terms. A natural choice for

this weighting matrix is the inverse of the constitutive matrix (or a diagonalized version of it, as used in [4]) such that (9) turns into an energy functional.

The minimization of (9) yield a linear system of equations to solve for the unknowns a_h and the recovered stress resultant values are in turn obtained by evaluating (5) at the integration points. For patches containing five (or more) elements we use the whole matrix $\mathbf{P}_{p17}$ given above (i.e. 17 unknowns). For four-element patches, however, we drop the two last columns containing the x^2- and y^2-terms, as these two terms tend to give poorly conditioned equation systems for regular shaped patches. For patches consisting of only three elements we use only the 13 first columns of $\mathbf{P}_{p17}$.

3. NUMERICAL EXAMPLE

Figure 1 shows a semi-infinite rectangular plate bounded by two parallel edges $y = \pm\frac{a}{2}$ and the edge $x = 0$. The deflection w and the bending moments m_{yy} are prescribed equal to zero along the edges $y = \pm\frac{a}{2}$ whereas the free edge $x = 0$ is subjected to a constant transverse shear load, q_0. An analytical solution to this problem based on Reissner plate theory is given in [5].

A finite portion of the plate corresponding to the rectangle $(x, y) \in [0, b] \times [0, \frac{a}{2}]$ is analyzed as indicated by the shaded area in Figure 1. Along the line $y = 0$ symmetry boundary conditions are applied (i.e., $\theta_x = m_{xy} = q_y = 0$). Neither the twisting moments m_{xy} nor the rotations θ_y are equal to zero along the edges $y = \pm\frac{a}{2}$. The actual variation of m_{xy} along these edges, according to the analytical solution, is depicted in Figure 1. These tractions are applied as external loads along the boundary $y = \frac{a}{2}$ in the FE analysis whereas the rotation θ_y is free. Similarly, tractions according to the analytical solution are applied as external loads also along the line $x = b$.

The problem is analyzed adaptively using a Reissner–Mindlin based four-noded quadrilateral element [6], and a relative error tolerance of $\eta_a = 2\%$. In addition, we use a sequence of five uniform meshes ranging from 8×2 elements up to 128×32 elements. For each mesh we compute the effectivity index Θ, i.e. the ratio between the estimated global error and the corresponding exact error based on the analytical solution. In addition, we compute the 'root-mean-square' of the estimated local errors, defined through

$$\|e^*\|_{\text{R.M.S.}} = \frac{\sqrt{\frac{1}{n_{\text{el}}} \sum_{e=1}^{n_{\text{el}}} \left(\|e_e^*\|_E - \|e^*\|_{\text{avg}}\right)^2}}{\|e^*\|_{\text{avg}}} \quad ; \quad \|e^*\|_{\text{avg}} = \frac{1}{n_{\text{el}}} \sum_{e=1}^{n_{\text{el}}} \|e_e^*\|_E \qquad (10)$$

where $\|e_e^*\|_E$ denotes the usual energy norm of the estimated local error in element e, see [4]. The quantity (10) provides a global measure on the distribution of the estimated error over the mesh and should ideally approach zero when the mesh is refined adaptively. The results of the analyses are presented in Figure 2. The current recovery approach (denoted SPR+S) is here compared with the original SPR-procedure [1] and SPR with equilibrium enhancement (SPR+E) according to [2]. The adapted mesh sequence based on SPR+S recovery is shown in Figure 3 and demonstrates clearly the boundary layer effect along the edge $x = 0$.

4. REFERENCES

[1] O. C. Zienkiewicz and J. Z. Zhu. The Superconvergent Patch Recovery and a posteriori Error Estimates. Part 1: The Recovery Technique. Int. J. Num. Meth. Eng., 33, 1331–1364 (1992).

[2] N.-E. Wiberg, F. Abdulwahab, and S. Ziukas. Enhanced Superconvergent Patch Recovery Incorporating Equilibrium and Boundary Conditions. Int. J. Num. Meth. Eng., 37, 3417–3440 (1994).

[3] T. Kvamsdal and K. M. Okstad. Error Estimation Based on Superconvergent Patch Recovery Using Statically Admissible Stress Fields. Technical Report R-7-96, Department of Structural Engineering, Norwegian University of Science and Technology, Trondheim, Norway, 1996. Submitted to Int. J. Num. Meth. Eng..

[4] K. M. Okstad, T. Kvamsdal, and K. M. Mathisen. Superconvergent Patch Recovery for Plate Problems Using Statically Admissible Stress Resultant Fields. Technical Report R-19-96, Department of Structural Engineering, Norwegian University of Science and Technology, Trondheim, Norway, 1996. Submitted to Int. J. Num. Meth. Eng..

[5] S. P. Timoshenko and S. Woinowksy-Krieger. Theory of Plates and Shells. McGraw–Hill, New York, NY, 1970.

[6] K.-J. Bathe and E. N. Dvorkin. A Four-noded Plate Bending Element based on Mindlin/Reissner Plate Theory and a Mixed Interpolation. Int. J. Num. Meth. Eng., 21, 367–383 (1985).
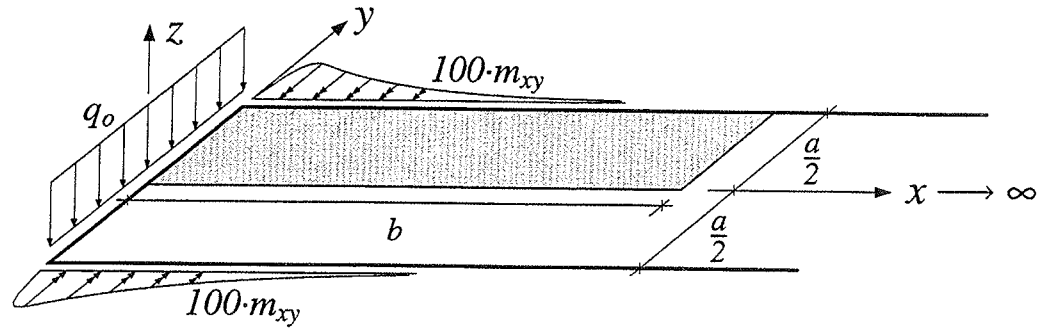
Width	:	a	=	2.0	Elasticity :	E	=	$25.8 \cdot 10^6$
Length	:	b	=	4.0		ν	=	0.2
Thickness	:	t	=	0.2	Load :	q_0	=	1.0

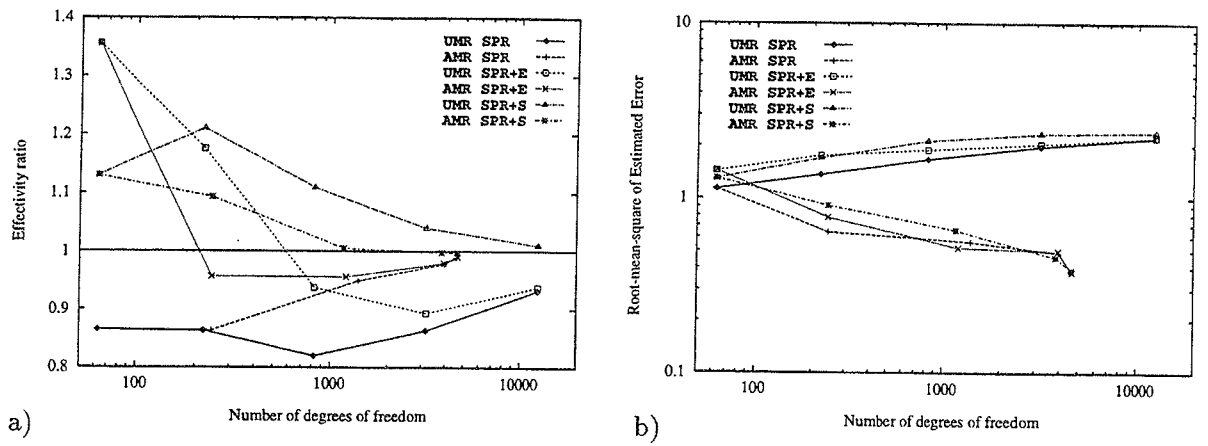Figure 1: The semi-infinite plate problem: Geometry and properties.

Figure 2:   Results for the semi-infinite plate problem: a) Global effectivity indices (Θ). b) Root-mean-square of estimated local errors ($\|e^*\|_{\text{R.M.S.}}$).

Mesh 0 : 16 elements
Error   : 25.84%

Mesh 1 : 71 elements
Error   : 10.86%

Mesh 2 : 366 elements
Error   : 4.13%

Mesh 3 : 1223 elements
Error   : 2.12%

Mesh 4 : 1478 elements
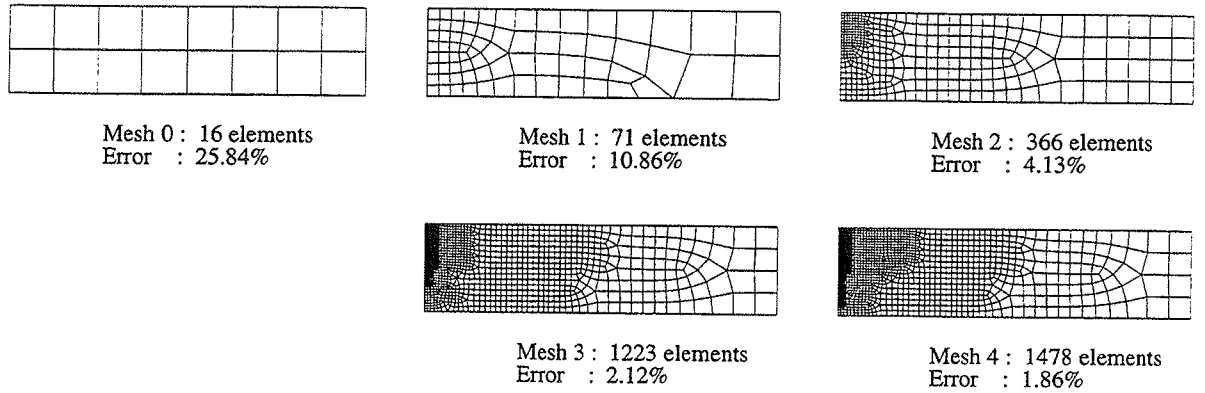Error   : 1.86%

Figure 3: Sequence of adaptively refined meshes obtained with SPR+S.

ADAPTIVE FINITE ELEMENT METHOD WITH RECOVERY BASED ESTIMATOR FOR PARABOLIC PROBLEMS

S. Ziukas[†] *and N.-E. Wiberg*

Department of Structural Mechanics
Chalmers University of Technology
S-412 96 Göteborg, Sweden

1. Abstract

Performance of Zienkiewicz-Zhu error estimator is considered for linear parabolic equations. Estimate of the local elliptic discretization error in energy norm is obtained by constructing a recovered gradient field of a higher order of accuracy at each time step using superconvergent properties of the solution.

2. Motivation

The method of lines (MOL) is a very popular method to solve initial-boundary value problems in engineering. In this approach a problem is first discretized in space using, for example, Galerkin method, and then the resulting system of ordinary differential equations (ODE) is solved in time with the finite difference method (FDM). As the smoothness of a solution may vary considerably in space and time, discretizations with variable mesh sizes in both space and time are needed. Thus, a problem of selection effective and reliable error estimator becomes the main concern in the adaptive analysis.

Error estimates developed for elliptic equations can be used to estimate space discretization errors for parabolic problems. One of such estimators based on the recovered solutions was developed by Zienkiewicz and Zhu, see [1].

3. Model problem and objectives

Let us consider a parabolic initial-boundary value problem for the heat equation (groundwater flow)

$$\frac{\partial u}{\partial t} - \nabla \cdot [A(x)\nabla u] = f(x,t) \quad in \ (x,t) \in \Omega \times I, \ I = (0,T]$$
$$u(x,t) = 0 \quad on \ \partial\Omega \times I; \qquad u(x,0) = u_0(x) \quad in \ \Omega \qquad (3.1)$$

Formulating the *standard Galerkin method* in $H = L_2(\Omega)$ with $V = H_0^1(\Omega)$ leads to the approximate semidiscrete problem: find $u_h(t) \in S_h(\Omega)$ such that

$$\left(u_{h,t}, \chi\right) + a\left(u_h, \chi\right) = (f, \chi), \quad \forall \chi \in S_h(\Omega) \ t \in (0,T],$$
$$u(0) = u_0 \qquad (3.2)$$

which can be integrated in time using *the backward difference approximation*

$$(U^n, \chi) + k_n a(U^n, \chi) = \left(U^{n-1} + k_n f(t_n), \chi\right), \quad \forall \chi \in S_h, \ n > 0 \qquad (3.3)$$

Our goal is to discuss an *estimate of the space discretization error* in the 'energy' norm $\|\cdot\|_{E,\Omega} = \sqrt{a(\cdot,\cdot)}$ using Zienkiewicz-Zhu error estimator

---

†. e-mail: *saulius@sm.chalmers.se*

$$\eta_\tau(t) := \left[\int_\tau (Gu_h - A\nabla u_h)^t A^{-1}(Gu_h - A\nabla u_h) \right]^{\frac{1}{2}} ; \quad E(t) := \left[\sum_{\tau \in T_h} \eta_\tau^2 \right]^{\frac{1}{2}} \tag{3}$$

G denotes some recovery operator which acts on the finite element solution u_h to give an appro̱ mation to the gradient $A\nabla u$.

4. Error analysis

Solving parabolic problems with the finite element method of lines it is reasonable to study total discretization error in two steps – to analyze separately the finite element method error the **error incurred in solving the system of ODE**

$$u(x,t) - U(x,t) = u(x,t) - u_h(x,t) + u_h(x,t) - U(x,t) = e(h,x,t) + e(k,x,t) \tag{4}$$

Let us first separate the error arising from the finite element discretization and consider meth of estimating it only. Replacing u by $u_h + e$, the discretization error satisfies Galerkin formu tion: find $e \in H_0^1(\Omega)$ such that

$$(v, e_t) + a(v, e) = (v, f) - a(v, u_h) - (v, u_{h,t}) , \quad \forall v \in H_0^1 , \ \forall t > 0 \tag{4}$$

$$a(v, e) = a(v, u_0 - u_h) , \quad \forall v \in H_0^1 , \ t = 0 \tag{4}$$

Error estimates can be established by solving or approximating equations (4.2) and (4.3) find a magnitude of the error.

By introducing the so called elliptic (Ritz) projection $R_h : H_0^1 \rightarrow S_h$ as the orthogonal project with respect to the bilinear form $a(.,.)$ and using the following decomposition

$$u - u_h = \left(u - R_h u \right) + \left(R_h u - u_h \right) = \rho + \Theta \tag{4}$$

we see that the gradient of Θ is of order $O(h^r)$, whereas the gradient of the total error is o $O(h^{r-1})$. This implies that that estimator for the local elliptic projection $\|\rho\|$ is also an asympto cally exact one for $\|e\|$, i.e. $\|e\| \sim \|\rho\|$ up to higher order terms. Further, aiming to reduce comple ity of the error estimator, we neglect the time rate of change of the error, and thereby, seek approximate solution to the local elliptic problem: find a magnitude of $e \in H_0^1(\Omega)$ in $\|\cdot\|_{E(\Omega)}$ su that

$$a(v, e) = (v, f) - a(v, u_h) - (v, u_{h,t}) , \quad \forall v \in H_0^1 , \ \forall t > 0 \tag{4}$$

interpreting $u_{h,t}$ as given data.

In order to find an approximation to the bilinear form we shall use Zienkiewicz-Zhu error estim tor. The SPR is used to obtain the gradient of higher accuracy and ensure narrow bounds of effectivity index [2]. The procedure represents a problem of finding $Gu_h \in [S_h]^d$ such that

$$\| Gu_h - A\nabla u_h \|_{L^2(\omega)} = \inf \| Gu_h - A\nabla u_h \|_{L^2(\omega)} \tag{4}$$

Local time integration error of the Euler method can be estimated by constructing a new high order approximation to the solution or by evaluation of the second derivative of the solution w respect to the time in the *a–priori* estimate. The second order correction η^n is used as the estim of the local truncation error

$$(B + k_n A)\eta^n = \frac{k_n}{2} \left\{ A\left(U^n - U^{n-1} \right) - \left(\tilde{f}(t_n) - \tilde{f}(t_{n-1}) \right) \right\} \tag{4}$$
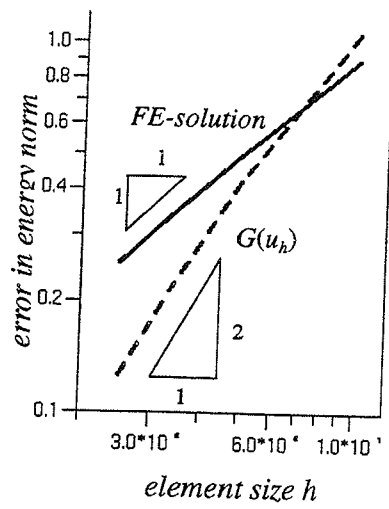
Figure 1. Rate of convergence of FE-solution and recovered gradient $G(u_h)$ in energy norm. Uniform triangulation.
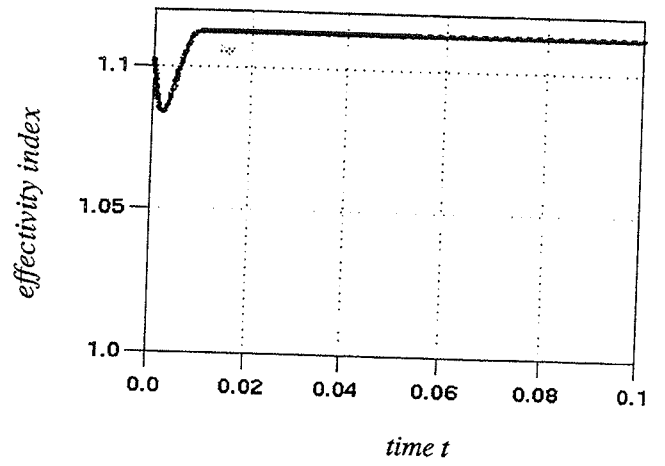

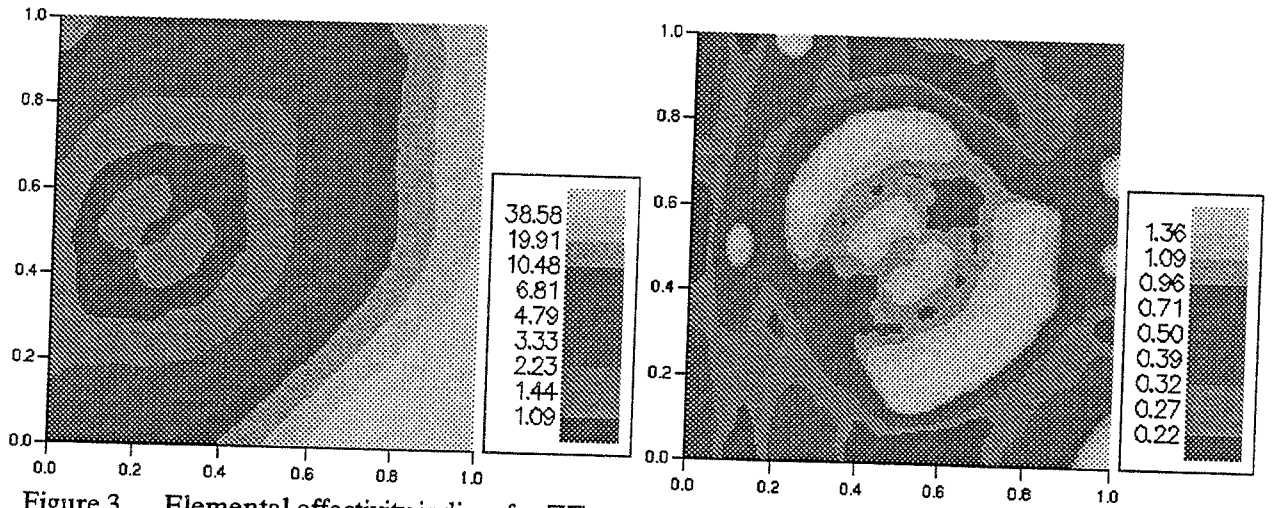Figure 2. Global effectivity index vs time in the adaptive analysis

Figure 3. Elemental effectivity indices for ZZ error estimator in energy norm at $t = 0$ and $t = 0.1$. Uniform triangulation 20x20 with linear elements.
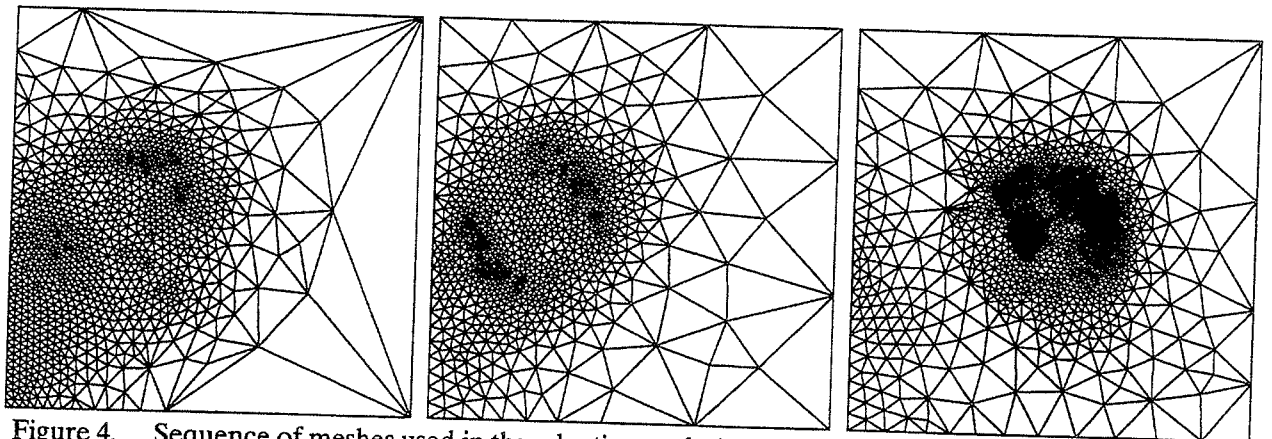

Figure 4. Sequence of meshes used in the adaptive analysis aiming 12% accuracy global error in energy norm

5. Results and discussion

The test example is a problem in which the source function $f(x, t)$ and Dirichlet boundary conditions are chosen such that the exact solution is given by

$$u(x, y, t) = \exp\left[- 80\left((x - r(t))^2 + (y - 0.5)^2\right)\right] \qquad (5.1)$$

199

where $r(t) = 0.5 - 0.25 \exp(-1000t)$. This represents a cone which is centered at (0.5, 0. at $t = 0$ and moves with a continuously decreasing speed towards the center of the domain

In order to investigate efficiency and applicability of the estimator, the problem was solved us a sequence of uniform triangular meshes using 10, 20, 30, and 40 linear finite elements per si The convergence of the global error in energy norm of the finite element solution $\|u - u_h\|_l$ and the recovered gradient field $\|A\nabla u - G(u_h)\|_{L^2(\Omega)}$ by original SPR procedure at $t = 0$. shown in Figure 1. Distribution of elemental effectivity indices for the initial projection and final state is presented in Figure 3. We notice some overestimation of the discretization error the initial projection. Elemental effectivity indices become worse as time passes in regions n to the boundaries, i.e. where the exact solution and its gradient are small, however, in regions w a high solution gradient elemental effectivity indices are near unity for all time steps. That plains the fact that the global effectivity index remains almost unchanged with even small tend cy for overestimation of the error and it is very close to unity, see Figure 3.

The performance of Zienkiewicz-Zhu estimator was tested also in the context of adaptive ana sis. The problem was solved using a variable time step aiming $TolS=12\%$ accuracy relative er in energy norm in space and $TolT=2\%$ accuracy of local temporal error. Starting from triangu 20x20 grid, three additional grids were used, see Figure 4.

6. Conclusions

- It is shown that such *error estimator is asymptotically exact* for sufficiently regular solutions that is confirmed by a numerical example. The original Superconvergent Patch Recovery procedure gives a recovered gradient field which is more accurate and have a higher convergence rate $O(h^2)$ than the finite element solution $O(h^1)$ in energy norm.

- The *global effectivity index does not differ much from unity* for uniform meshes as well as for those used in the adaptive analysis. The error estimator does not yield an upper bound of the error in general, however, it can be noticed that the estimator tends slightly to overestimate the discretization error for triangular meshes.

- The error estimator requires only a *small fraction of the computational cost* used for the finite element analysis.

- Performance of the estimator can be improved by *forcing the recovered gradient field to satisfy the local equilibrium equation* as in the elliptic case, (see [3]).

7. References

[1] O.C.Zienkiewicz and J.Z.Zhu, 'A simple error estimator and adaptive procedure for pra tical engineering analysis', *Int. j. numer. methods eng.*, **24**, 337–357 (1987).

[2] O.C.Zienkiewicz, J.Z.Zhu, 'The superconvergent patch recovery and *a posteriori* er estimates. Part 1: The recovery technique', *Int. j. numer. methods eng.*, **33**, 1331–13 (1992); Part 2: Error estimates and adaptivity', *Int. j. numer. methods eng.*, **33**, 1365–13 (1992).

[3] N.-E. Wiberg and F. Abdulwahab, 'Patch recovery based on superconvergent derivativ and equilibrium', *Int. j. numer. methods eng.*, **36**, 2703–2724 (1993).

Distortion measures for general quadrilateral plane finite elements with straight and curved boundaries.

Nina Lautersztajn-S. and Alf Samuelsson

Department of Structural Mechanics, Chalmers University of Technology, S-412 96 Göteborg, Sweden

INTRODUCTION

The sensitivity of general isoparametric quadrilateral low order finite elements due to their distorted geometry has been analyzed since 1973. Then, an isoparametric non-conforming element was developed by Wilson et al.[1] and Wilson's incompatible shape functions have entered to the history of the finite element method. After more then twenty years that have passed, the full comprehension on the influence of the shape of quadrilaterals on the finite element solutions is still missing. A broad class of new mixed elements based on assumed stress or strains has been developed, References [1]-[8]. The element of Pian-Sumihara[3], 1984, appeared to be less sensitive to distorted meshes and new approaches have slightly improved this result, since then.

The use of differential geometry by Yuan[6,7] et al. allowed to define the distortion parameters for a general quadrilateral, an isoparametric four-node finite element. Further attempts in this field, [7], and by utilizing systematically differential geometry, [9], led to the extension of the description of distortion measures even for quadrilaterals with curved boundaries, eight-node finite elements.

The normal (geodesic) coordinates $(\bar{\xi}, \bar{\eta})$ are used as a local coordinate system for each quadrilateral element. In the case of plane geometry on the Euclidean space $\mathbb{R}^2$, these normal coordinates are skew Cartesian and they are linearly related to the Cartesian coordinates (x, y). Both systems are developed at the origin of the natural coordinates (ξ, η).

The concept of normal coordinates induces the intrinsic properties of a geometric object, an isoparametric finite element. Given Riemannian metric defines the connection and thus existence of the geodesic equations. Any straight line on $\mathbb{R}^2$ is a geodesic. The setting of the problem in differential geometry regime is of a general character and it is independent of the choice of coordinate system.

The inverse maps between natural and normal coordinates are found by using the Taylor expansion and the theory of geodesic curves. Integral curves, solutions of equations of geodesics, are expressed by series which terms depend on variables $\bar{\xi}, \bar{\eta}$ and the distortion measures. The rate of convergence is similar when analyzing four- and eight-node elements.

An attempt to find the geometrical meaning of the distortion measures is made in [9]. There, it appeared that these parameters define the orientation of a manifold, a topological Hausdorff space. Here, any quadrilateral defined by smooth isoparametric maps from the closed biunit domain, including the origin, onto closed subsets in $\mathbb{R}^2$. Pure mathematical analysis of this problem is in the developing phase.

FOUR- AND EIGHT-NODE ISOPARAMETRIC FINITE ELEMENTS - LOCAL REPRESENTATIONS

Cartesian coordinate system

The usual representation of the isoparametric map

$$\mathbf{x} : [-1, 1] \times [-1, 1] \to M \subset \mathbb{R}^2$$

of a biunit on $\mathbb{R} \times \mathbb{R}$ onto a quadrilateral is defined for a **four-node element** by

$$\mathbf{x}_1 = \begin{Bmatrix} x \\ y \end{Bmatrix} = \sum_{i=1}^{4} N_i(\xi, \eta) \begin{Bmatrix} x_i \\ y_i \end{Bmatrix} = \left\{ \begin{array}{l} a_0 + a_1\xi + a_2\xi\eta + a_3\eta \\ b_0 + b_1\xi + b_2\xi\eta + b_3\eta \end{array} \right\} ,$$

with shape functions

$$N_i = \tfrac{1}{4}(1 + \xi_i\xi)(1 + \eta_i\eta)$$

for each corner node, where x_i, y_i are nodal coordinates of an element.

The isoparametric map for an **eight-node element** is defined by

$$x_2 = \begin{Bmatrix} x \\ y \end{Bmatrix} = \sum_{i=1}^{8} N_i(\xi, \eta) \begin{Bmatrix} x_i \\ y_i \end{Bmatrix} =$$

$$= \begin{Bmatrix} a_0 + a_1\xi + a_2\eta + a_3\xi\eta + a_4\xi^2 + a_5\eta^2 + a_6\xi^2\eta + a_7\xi\eta^2 \\ b_0 + b_1\xi + b_2\eta + b_3\xi\eta + b_4\xi^2 + b_5\eta^2 + b_6\xi^2\eta + b_7\xi\eta^2 \end{Bmatrix},$$

with shape functions for each node

$$N_i = \tfrac{1}{4}(1 + \xi_i\xi)(1 + \eta_i\eta)(\xi_i\xi + \eta_i\eta - 1) \qquad \text{for} \quad i = 1 - 4, \quad \textit{corner nodes}$$

$$= \tfrac{1}{2}(1 - \xi^2)(1 + \eta_i\eta) \qquad\qquad\qquad i = 5,7 \qquad \textit{boundary nodes}$$

$$= \tfrac{1}{2}(1 + \xi_i\xi)(1 - \eta^2) \qquad\qquad\qquad i = 6,8 \qquad \textit{boundary nodes}$$

Normal (geodesic) coordinate system

The normal coordinate system for any quadrilateral is based on the theory of geodesic curves.

The following settings are common for quadrilaterals with straight and curved boundaries, 4-8-node elements, respectively. The geometric properties of 8-node elements are inherited from t. basic chord quadrilaterals spanned on corner nodes.

Let

$$\bar{x} : [-1,1] \times [-1,1] \to M \subset \mathbb{R}^2$$

be an isoparametric map such that the compositions $x_1 \circ \bar{x}^{-1}$ and $x_2 \circ \bar{x}^{-1}$ are the isomorphisms. 1 map defines the normal coordinate system, Fig. 1.1.
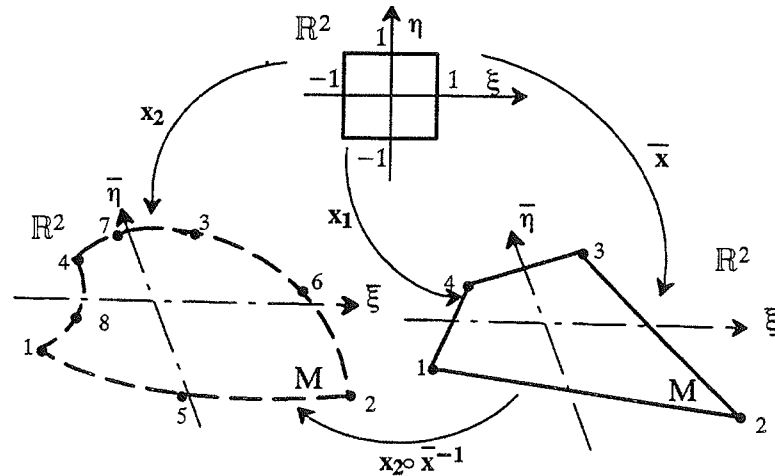

Figure 1.1.   *Local normal coordinate systems for 4-node and 8-node finite elements*

An isoparametric map $x_1(\xi, \eta)$, represents a four-node basic general quadrilateral. A geodesic ξ^i through the origin, is the integral curve of the set of second order differential equations,

$$\frac{d^2\xi^i}{ds^2} + \Gamma^i_{jk}\frac{d\xi^j}{ds}\frac{d\xi^k}{ds} = 0, \qquad i,j,k = 1,2$$

where $\xi^1 = \xi$, $\xi^2 = \eta$ and a parameter s is the arc length of the geodesic curve. Γ^i_{jk} are the Christo] symbols, [9].

The tangent vectors at $p \in M$, where M is a manifold, to any curve passing through 0 are defined by

$$\left(\frac{d\xi^i}{ds}\right)_p = \left(\frac{\partial \xi^i}{\partial x}\frac{dx}{ds} + \frac{\partial \xi^i}{\partial y}\frac{dy}{ds}\right)_p .$$

If the above equation is determined at the origin and multiplied by s and noting that the direction vector components through the origin are $\frac{dx}{ds} = \frac{x}{s}$ and $\frac{dy}{ds} = \frac{y}{s}$, the normal coordinates are denoted as follows,

$$\bar\xi = \left(\frac{d\xi}{ds}\right)_0 s = \left(\frac{\partial \xi}{\partial x}\frac{x}{s} + \frac{\partial \xi}{\partial y}\frac{y}{s}\right)_0 s = \left(\frac{\partial \xi}{\partial x}x + \frac{\partial \xi}{\partial y}y\right)_0$$

$$\bar\eta = \left(\frac{d\xi}{ds}\right)_0 s = \left(\frac{\partial \eta}{\partial x}\frac{x}{s} + \frac{\partial \eta}{\partial y}\frac{y}{s}\right)_0 s = \left(\frac{\partial \eta}{\partial x}x + \frac{\partial \eta}{\partial y}y\right)_0 .$$

or in matrix form,

$$\bar{X} = \left\{\begin{matrix}\bar\xi \\ \bar\eta\end{matrix}\right\} = (J^{-1})_0^T \left\{\begin{matrix}x \\ y\end{matrix}\right\} = \frac{1}{J_0}\begin{bmatrix} b_3 & -a_3 \\ -b_1 & a_1 \end{bmatrix}\left\{\begin{matrix}x \\ y\end{matrix}\right\},$$

where the Jacobian J is,

$$J = \begin{bmatrix} a_1 + a_2\eta & b_1 + b_2\eta \\ a_3 + a_2\xi & b_3 + b_2\xi \end{bmatrix} .$$

The determinant

$$J = J_0(1 + \alpha\xi + \gamma\eta)$$

of the Jacobian J is a function of two parameters

$$\alpha = (a_1b_2 - a_2b_1)/J_0$$
$$\gamma = (a_2b_3 - a_3b_1)/J_0$$

which are called the **distortion measures**. The determinant evaluated at the origin is,

$$J_0 = a_1b_3 - a_3b_1 .$$

By simple manipulations the set of normal coordinates becomes

$$\bar{X} = \left\{\begin{matrix}\bar\xi \\ \bar\eta\end{matrix}\right\} = \begin{bmatrix} \xi + \gamma\xi\eta \\ \eta + \alpha\xi\eta \end{bmatrix}$$

a function of the distortion measures.

DISTORTION MEASURES

Let

$$e_1 = \left\{\begin{matrix}a_1 \\ b_1\end{matrix}\right\}, \qquad e_2 = \left\{\begin{matrix}a_2 \\ b_2\end{matrix}\right\}, \qquad e_3 = \left\{\begin{matrix}a_3 \\ b_3\end{matrix}\right\}$$

be the basis vectors of the normal coordinate system for a given quadrilateral, Fig. 1.2, such that

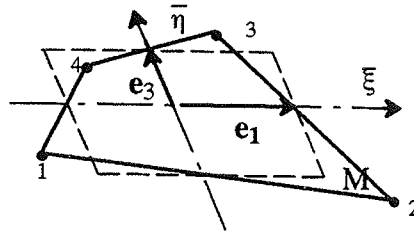$$x_1 = \xi e_1 + \xi\eta e_2 + \eta e_3$$

Figure 1.2.   *The basic vectors for a normal (geodesic) coordinate system*

The distortion parameters α, γ and the determinant J_0 can be equivalently represented by the tr scalar product

$$J_0 = \left(e_1 \times e_3\right) \cdot k$$

$$\alpha = \left(e_1 \times e_2\right) \cdot k/J_0$$

$$\gamma = \left(e_2 \times e_3\right) \cdot k/J_0$$

where the unit vector k is in the direction of the z-axis, perpendicular to x-y plane.

α, γ are the real numbers, multiples of the basic volume J_0. This fact, in differential geometry, def an orientation of a manifold M, in our case a plane quadrilateral, [9]. The sign of the distortion par eters gives information about shape of a quadrilateral.

CONCLUSIONS

The result of this analysis is the significant reduction of the number of the distortion parameters general quadrilaterals with curved boundaries compared with the work of Yuan[7] et al. due to pro utilizing of differential geometry. The consequences of it can lead to better understanding of sensi ity on distorted shapes of incompatible and enhanced mixed classes of finite elements when expres in terms of distortion measures.

The obtained result is the appropriate basis for the pure mathematical analysis on the behavior of s ple geometrical objects, approximating physical bodies, in the field of computational mechanics.

REFERENCES

[1]   E.L. WILSON, R.L. TAYLOR, W.P. DOHERTY and J. GHABOUSSI, 'Incompatible displacement moc in Num. and Comput. Meths. in Struct. Mech. (Ed. S J. Fenves, et al), Academic Press, New York, 1973

[2]   R.L. TAYLOR, P.J. BERESFORD and E.L. WILSON, 'A non-conforming element for stress analysis', Ii Num. Meth. Eng., 10, 1211-1219, 1976.

[3]   T.H.H. PIAN and K. SUMIHARA, 'Rational approach for assumed stress finite element', Int. J. Num. M Eng., 20, 1685-1695, 1984.

[4]   J.C. SIMO and M.S. RIFAI, 'A class of assumed strain methods and the method of incompatible modes' Ii Num. Meth. Eng., 29, 1595-1638, 1990.

[5]   J.C. SIMO and F. ARMERO, 'Geometrically nonlinear enhanced mixed methods and the method of inc patible modes', Int. J. Num. Meth. Eng., 1413-1449, 1992.

[6]   K.Y. YUAN and T.H.H. PIAN, 'The reference coordinates and distortion measures for quadrilateral hy stress membrane element', Comp. Mechanics, 14, 311-322, 1994.

[7]   K.Y. YUAN, Y.S. HUANG and T.H.H. PIAN, 'Inverse mapping and distortion measures for quadrilate with curved boundaries', Int. J. Num. Meth. Eng., 37, 861-875, 1994.

[8]   J. KORELEC and P. WRIGGERS, 'Efficient enhanced strain element formulation for 2D and 3D problei Advances in finite element technology (Ed.N.-E. Wiberg), CIMNE, Barcelona, 1995.

[9]   N. LAUTERSZTAJN-S and A. SAMUELSSON, 'Distortion measures and inverse mapping for isoparar ric 8-node plane finite elements with curved boundaries', to be submitted in Int. J. Num. Meth. Eng.

Reduction of
Under-Determined Linear Systems
by a Sparse Block Matrix Technique

Niels Jacob Tarp-Johansen*   Peter Noe Poulsen[†]
Lars Damkilde[‡]

Dept. of Structural Mechanics and Materials
Technical University of Denmark, Build. 118, 2800 Lyngby, DK

Introduction

Under-determined linear equation systems occur in different engineering applications. In structural engineering they typically appear when applying the force method. As an example one could mention limit load analysis based on The Lower Bound Theorem. In this application is a set of under-determined equilibrium equations restrictions in an LP-problem. A significant reduction of computer time spent on solving the LP-problem is achieved if the equilibrium equations are reduced before going into the optimization procedure, [1]. Experience has shown that for some structures one must apply full pivoting to ensure numerical stability of the aforementioned reduction. Moreover is the coefficient matrix for the equilibrium equations typically very sparse.

The objective of the work presented here is to deal efficiently with the full pivoting reduction of sparse rectangular matrices using a dynamic storage scheme based on the block matrix concept. The problem of reducing sparse rectangular matrices has already been discussed by Kaneko [2] and treated by Pellegrino & Heerden [3], Kaveh [4] and others. They all present methods based on static storage. Pellegrino suggests a method of partial pivoting on banded matrices. The advantage of this method is due to the fact that partial pivoting will only cause fill-in inside the band, a property which is lost if full pivoting is applied and consequently other algorithms are required. To be thorough it should be noted that iterative methods are inapplicable, though very popular in connection with sparse matrices.

*e-mail: njtj@bkm.dtu.dk
[†]e-mail: pnp@bkm.dtu.dk
[‡]e-mail: ld@abk.dtu.dk

1 Mathematical Problem

The linear system restricting the LP-problem is given by:

$$H\beta = R \tag{1}$$

Assume for simplicity that H has full rank – i.e. rank is equal to the number of rows. Since Eq. (1) is an under-determined system H may be separated into two parts, H_0 and H_1, where H_0 has full rank:

$$\begin{bmatrix} H_0 & H_1 \end{bmatrix} \begin{bmatrix} \beta_0 \\ \beta_1 \end{bmatrix} = R \tag{2}$$

Under the assumptions above there is clearly more than one candidate for H_0. However, from a numerical point of view, all these candidates are not equally suitable. The best choice is the one which is chosen by means of Gauss-elimination including full pivoting.

The LP-optimization requires that β_0 is expressed as a function of β_1:

$$\beta_0 = H_0^{-1} R - H_0^{-1} H_1 \beta_1 \tag{3}$$

As reduction of the coefficient matrix in Eq. (2) yields

$$H = \begin{bmatrix} LDU & LD\tilde{H}_1 \end{bmatrix} \tag{4}$$

it is seen that $H_0^{-1} R = (LDU)^{-1} R$ and $H_0^{-1} H_1 = U^{-1}\tilde{H}_1$ which are computed using forward and backward substitution.

The dual LP-problem corresponding to the LP-problem involving the restrictions (1) requires the computation of $(H_0^T)^{-1} v$ where v is a vector. As $H_0 = LDU$ the LDU-factorization of H_0^T is $U^T DL^T$ rendering the backward substitution procedure for $(H_0^T)^{-1} v$ similar to the backward substitution procedure for $(H_0)^{-1} u$, u being a vector. Therefore, the algorithm presented here furthermore provides a cornerstone for the solution of the dual LP-problem which also is of importance.

2 Storage Scheme and Reduction Algorithm

Dynamic storage schemes for sparse matrices are traditionally based on linked lists of elements – one list for each row. The problem of such strategies is the time spent on searching for elements. If the elements are in stead grouped together in blocks the addressing will be faster. This grouping is only advantageous if there will not be too many zeros in each block as the sparseness will otherwise be destroyed. Equilibrium equations of structures possess the block feature and thus invite for the use of a block strategy. Figure 1 shows how the submatrices (in the following denoted h) are linked together. To speed up addressing even more the blocks are also cross-linked.
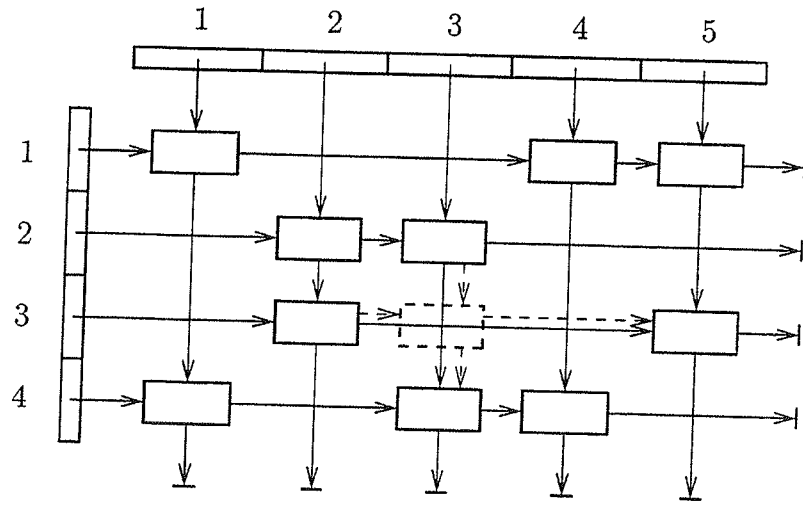
Figure 1: *Block matrix storage scheme.*

Figure 1 also shows how additional storage is required during factorization motivating the use of dynamic storage allocation. The solid boxes illustrate the submatrices at some point of factorization. The dashed box illustrates a submatrix which will be allocated if for instance the next pivot element is in block $h_{2,2}$ – say element $(h_{2,2})_{3,5}$. In that case subrow 3 of blockrow 2 is subtracted from the subrows of blockrow 3 in general causing the elements of block $h_{3,3}$ to become non-zero and hence $h_{3,3}$ must be allocated. However, if the elements in subcolumn 5 of $h_{2,3}$ are all zero (in practice numerically zero) no subtractions are required and consequently the allocation of $h_{3,3}$ is unnecessary. To reduce such unnecessary fill-in a zero-subcolumn-check is incorporated in the code.

As mentioned in earlier the reduction algorithm is Gauss-elimination applying full pivoting. The LDU-notation used in Eq. (4) is not strictly correct as, due to pivoting, rows and columns are in principle permuted as factorization proceeds. However, the storage scheme does not allow swapping of rows and columns as that would cause a lot of blocks with only one non-zero subrow or subcolumn in contradiction with the advantage of the block concept. In stead logical arrays are introduced to keep track of the pivot elements.

Logical arrays are also introduced to minimize the pivot search time. Subrows eliminated during a factorization step are flagged. At the end of the factorization step each of the flagged rows are searched for their numerically largest element which is stored in an array having an entry for each subrow in H. At the beginning of the next step this array is traversed and its numerically largest element chosen as the next pivot element.

Besides reducing overhead the block concept provides a pleasant side effect, namely that input is given in blocks allowing a simple input structur with no need for additional topological information.

207

3 Example

The following example is taken from [5]. The objective is to illustrate how storage develops during factorization. The total size is approximately 700 × 850. The sparsity, defined as the ratio between the size of actually allocated storage and the size of the fully allocated matrix storage, is depicted in Figure 2. Naturally, as a consequence of allocating blocks in stead of single elements, some zero-elements are stored though this is not strictly necessary. The dashed curve gives the amount of non-zero elements while the solid line gives the amount blocks as functions of step number in the factorization. Clearly further storage may be saved but compared to the 32% storage consumed by the bandwidth method, [3], the method presented here is competitive.
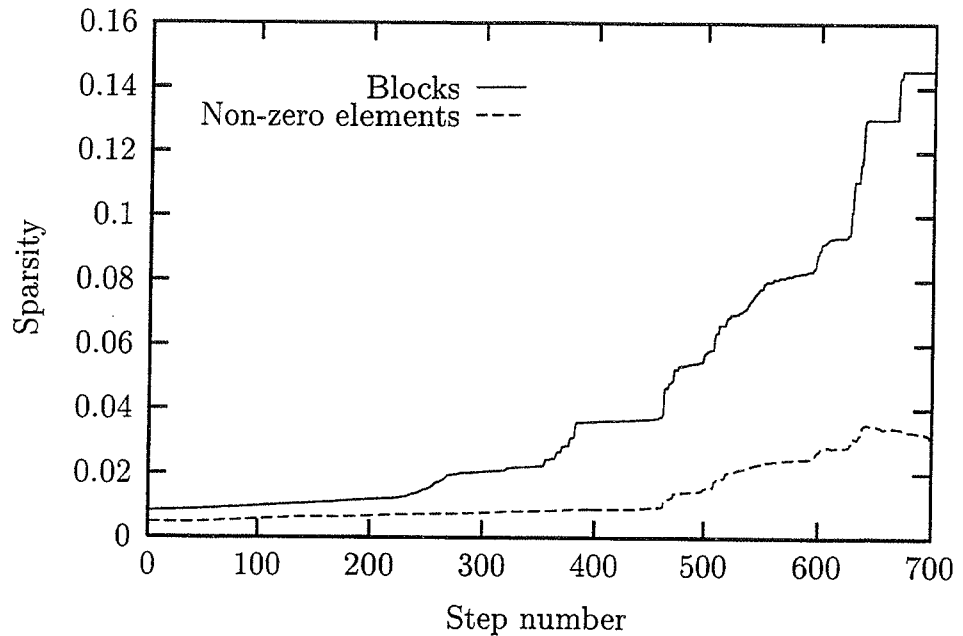

Figure 2: *Development of sparsity (allocated storage relative to fully allocated matrix storage) during factorization.*

Sparsity is almost lost if the above mentioned zero-subcolumn-check is not included in the code. In addition to almost destroying sparsity, lack of the zero-subcolumn-check makes the storage consumption increase quite rapidly in the beginning and then stagnate, contrary to what appears in Figure 2. The result is superfluous time consuming manipulations on zeros already at an early state of factorization, rendering the factorization rather time costly.

Conclusion

A method for full pivoting reduction of rectangular sparse matrices has been presented. Since full pivoting causes unsystematically spreading of fill-in all over the matrix a dynamic storage scheme especially suitable for matrices

naturally thought of as block matrices has been implemented. The method proves to be competitive to a well-known bandwidth technique [3] only providing partial pivoting.

References

[1] L. Damkilde and O. Høyer. An Efficient Implementation of Limit State Calculations Based on Lower-bound Solutions. *Computers & Structures*, 49(6):953–962, 1993.

[2] I. Kaneko. On Computational Procedures for the Force Method. *International Journal for Numerical Methods in Engineering*, 18:1469–1495, 1982.

[3] S. Pellegrino and T. Van Heerden. Solution of Equilibrium Equations in the Force Method: A Compact Band Scheme for Underdetermined Linear Systems. *Computers & Structures*, 37(6):743–751, 1990.

[4] A. Kaveh. Bandwidth Reduction of Rectangular Matrices. *Commucations in Numerical Methods in Engineering*, 9:259–267, 1993.

[5] P. N. Poulsen and L. Damkilde. Limit State Analysis of Reinforced Concrete Plates subjected to in-plane Loads. In *Eight Nordic Seminar on Computational Mechanics*, 1995. p. 4.

SEMI-ANALYTICAL FINITE ELEMENTS FOR THE THIN-WALLED STRUCTURES

Rimantas Kačianauskas
Department Strength of Materials, Vilnius Gediminas Technical University,
Saulėtekio 11, LT-2022 Vilnius, Lithuania

1. Introduction

Many of structures being used in various fields of engineering are composed of different thin-walled structural members. Analysis and design of these structures are based on the statements and relations of classical beam, plate and/or shell theories. It is necessary to remark that classical theories may be applied for the structural members the shape and geometric relations of which lie within the certain boundaries. Validity of the above statements may be examined by development of non-classical higher-order theories.

Despite a great difference in the existing models of thin-walled structures all of them provide analytical or semi-analytical approximation of a three-dimensional body into cross-sectional direction with the following reduction of the dimension of problem. As an alternative to the existing classical models the finite element approximation of cross-sectional distribution is introduced and presented in this paper. Such an approximation contains the essential features of semi-analytical discretisation [1]. The above approach has already been used for the development of particular equations of beams [2-4]. On this base the semi-analytical finite elements (SFE) are introduced in-order to develop the governing equations of linear elastostatic problems. Here, SFE approach is generalised and extended to more complex thin-walled structures.

2. Concepts of the semi-analytical elements and basic relations

The main issue in the development of any beam, plate or shell theory is the separation of longitudinal (surface) and cross-sectional (thickness) distribution. For this purpose, we define the approximation of three-dimensional displacement field by expressions

$$u(x, y, z) = f(y, z)U(x),$$

(1a)

$$u(x, y, z) = f(z)U(x, y)$$

(1b)

for beams (1a) and plates or shells (1b), respectively. Here, f is the displacement approximation matrix while U is the semi-discrete vector of generalised displacements.

The similar approximations may be developed for the strains. The three-dimensional strain field $\varepsilon(x, y, z)$ may now be described as follows:

$$\varepsilon(x,y,z) = F(y,z)\Theta(x)$$

(2a)

and

$$\varepsilon(x, y, z) = F(z)\Theta(x, y),$$

(2b)

The above expressions (2) present conventional approximations used in the displacement approach, where the vector Θ expresses generalised strains and F is the strain approximation matrix. The stress field may be approximated independently in the same manner as displacements (1). For beams

$$\sigma(x, y, z) = \Phi(y, z)S(x),$$

(3a)

and for plates or shells

$$\sigma(x, y, z) = \Phi(z)S(x, y),$$

(3b)

where S is the vector of nodal stresses and Φ - the stress approximation matrix.

The approximations (1-3) provide the basis for the derivation of the governing equations of beams, plates or shells. Actually, this derivation is partial discretisation problem, which reduces the three-dimensional solid body by retaining the variables depending on longitudinal or surface co-ordinates. We introduce to use the partial approximations (1-3) where approximation matrices are formed by the finite element method. Finite elements describing the cross-sectional distribution are defined as the semi-analytical finite elements. The explicit evaluation of the expression (1-3) depends on choosing of the appropriate shape functions. Once these are obtained the derivation of the governing equations follows a standard well-defined path.

The final set of the governing equations of thin-walled structures is formulated in the same way as that in three-dimensional elastostatics. It consists of the compatibility, equilibrium and constitutive relations and boundary conditions expressed in terms of semi-discrete variables such as displacements $U(x)$, strains $\Theta(x)$ and stresses $S(x)$. Here and in the future the co-ordinate vector x is defined as $x \equiv \{x\}^t$ for beams and as $x \equiv \{x, y\}^t$ for plates and shells.

The compatibility equations relating the generalised strains and displacements are found by simple comparison of the displacement and strain approximations (1) and (2). The remainder relations are derived as Euler equations associated with the modified Hellinger-Reissner functional written for a three-dimensional solid body and containing two independent displacement and stress fields u and σ.

For the further investigations we introduce the transformation

$$Q(x) = C(x)S(x)$$

(4)

relating stresses S with their resultants - generalised stresses Q. Here, the transformation matrix C is defined as

$$C(x) = \int_{A(x)} F^t \Phi \, dA,$$

(5)

where A is a cross-sectional area.

Depending on relative approximation order of both functions u and σ, this matrix may have different properties and to lead to different final relations resulting in different types of semi-analytical elements: isoparametric, subparametric or superparametric. The main difficulties occur, when the rank of transformation matrix C differs from the number of components of both vectors S and Q. In spite of appropriate differences, it is always possible to modify the forward relationship (4) expressing them in terms of modified model variables S_M and Q_M and uniquely establish the corresponding backward transformation.

After integration over cross-section and performing of some matrix manipulations, finally, the set of elasticity equations may be presented as follows

compatibility equations

$$A_c^t(x)U_M(x) \; - \; \Theta_M(x) \; = \; O \; ;$$

(6a)

equilibrium equations

$$A_e(x)Q_M(x) \; = \; p(x) \, ;$$

(6b)

constitutive equations

$$K(x)\Theta_M(x) \; - \; Q_M(x) \; = \; O \, .$$

(6c)

Here, A_c^t, A_e and K presents the new mixed differential-algebraic equation operators, p is vector of the semi-discrete external loads while subscript M denotes modified variables. The solution of the set of governing equations (6) provides the fields of modified generalised variables. In some of the cases, this solution is insufficient for complete recovering of the three-dimensional stress-strain fields in the shell because some of the initial generalised variables are lost by the modification. This situation is well-known in classical structural mechanics and described in terms of statically (kinematically) underteminated systems where redundant variables have to be found from additional equations.

The basic relations (6) proposed have no preliminary limitation due to geometry of structure or due to approximation laws. The semi-analytical finite element approach is the formal possibility to develop the non-classical higher-order theories with the desired degree of accuracy.

3. Illustrative examples

The versatility of SFE is demonstrated in practical applications involving well-known solutions. The classical Euler-Bernoulli and Timoshenko theories are derived using a single one-dimensional element. The beams with a thin-walled cross-section are described as an assemblage of semi-analytical elements. Cross-section with three SFE correspond to thin-walled beam theory with bimoment while cross-section with large number of SFE has no classical analogues. On the basis of non-classical equations the

conventional finite elements of new type are derived. Possible extensions of SFE to dynamics are also briefly discussed.

As a rule, for description of shells and development of their equations is performed in the curvilinear co-ordinate system. For this purpose the tensor notations are most convenient and tensor calculus especially covariant differentiation rules are applied. The classical shell theories may be derived by a single one-dimensional semi-analytical element. In order to illustrate the use of semi-analytical finite elements in the shell theory, a circular cylindrical shell is considered in details.

4. Concluding remarks

The SFE method as a formal technique is put forward to develop non-traditional of thin-walled structures. The state variables are referred not to the central axis or the middle surface as in classical theories but to the appropriate generatrix axes or surfaces. The higher-order terms may be simply taken into account by refining the finite element mesh or by increasing the order of approximation polynomials.

The SFE method proposed has some principle advantages with classical shell theories:

    a) The semi-discrete displacements of shell are compatible with the displacements of three-dimensional body;

    b) The governing equations contain only the first-order derivatives;

    c) Method provides extended possibilities for introducing more wide type of loading and supports;

    d) Method is independent on geometry of the structure and different types of curved or thick structures may be considered in the same standard manner;

    e) The symbolic manipulations and computer algebra may be applied for the derivation of standard operators.

It is clear, however, that comprehensive analysis and future research are needed to develop and extend the SFE method to more wide class of structures.

REFERENCES

1. *O.C.Zienkiewicz.* The Finite Element Method, Third edition. London, McGraw-Hill, 1977.
2. *R.Kačianauskas.* Finite Element Approximations in the Development of Non-Classical Beam Theory. Sixth Nordic Seminar on Computational Mechanics, Sweden, October 18-19, 1993. University of Linköping, 1993, p. 168-171.
3. *J.Argyris, R.Kačianauskas.* Semi-Analytical Finite Elements in the Three-Dimensional Theory of Beams. University of Stuttgart, ICA-Report No. 47, 1994.
4. *R.Kačianauskas.* Multi-Level Modelling of Beam-Type Structures by Finite Element Method. An International Conference of Mechanical Engineering, MECHANICS 94, Proceedings, Mechanical Section. Vilnius, Technika, 1994, p. 215-220.

Collapse Analysis of Offshore Jackets with Co-Rotating Nonlinear Beam Elements

S. Krenk[1], C. Vissing-Jørgensen[2], S. Fredsgaard[2] and J. Wægter[2]

[1]Division of Mechanics, Lund University, S-22100 Lund, Sweden

[2]RAMBØLL, Frodesgade 125A, DK-6700 Esbjerg, Denmark

Collapse of framed offhore structures can be formulated in terms of elastic beam elments connected at nodes, where plastic hinges can develop. In order to obtain accurate results with large elements it is desirable to incorporate the nonlinear effect of the normal force in the beam elements, while additional geometric stiffness is accounted for via the co-rotation of the beam element reference frame. In this paper we present the general format of beam stiffness for large diplacements and rotations, specialise to beam-column elements in closed form for moderate local deformation, and derive the general global geometric stiffness matrix. Plastic hinges at one or both ends of the beam elements are introduced via a block matrix format, and hardning and local imperfections are discussed. A couple of examples are presented.

Finite Rotations in Beam Theory

Any general beam theory is based on the equilibrium equations

$$\frac{d\mathbf{N}}{ds_0} + \mathbf{p} = 0 \quad , \quad \frac{d\mathbf{M}}{ds_0} + \frac{d\mathbf{x}}{ds_0} \times \mathbf{N} + \mathbf{m} = 0$$

where $\mathbf{N}, \mathbf{M}$ are the section force and moment vector, respectively. The equilibrium equations refer to the deformed geometry, where $\mathbf{x}$ is the current position vector and s_0 the arc length in the initial undeformed state.

In order to develop a finte element formulation the equilibrium equations are reformulated in the form of a statement of virtual work. For finite rotation theories the crux is that the virtual infinitesimal rotation $\delta\overline{\varphi}$ is expressed in terms of the *rotation parameter vector* φ as - see e.g. Krenk (1996),

$$\delta\overline{\varphi} = \delta\varphi - \tfrac{1}{2}\delta\varphi \times \varphi + O(\varphi^2)$$

from the state $\varphi = 0$. This implies that the first variation $\delta\overline{\varphi}$ can be expressed directly by its parametric counterpart, while the *increment og the variation* $d(\delta\overline{\varphi})$, needed in the tangent stiffness relation, takes a non-trivial quadratic form,

$$\delta\overline{\varphi} = \delta\varphi \quad , \quad d(\delta\overline{\varphi}) = -\tfrac{1}{2}\delta\overline{\varphi} \times d\overline{\varphi}$$

The internal forces in the current configuration are expressed via the internal virtual work

$$\delta V_{int} = \int_0^l \left(\delta\varepsilon_j \, N_j + \delta\kappa_j \, M_j \right) ds_0$$

where ε_j, κ_j are the local components of strain and curvature, respectively.

The element tangent stiffness follows from the increment of the current iternal forces, i.e. from the increment of the internal virtual work,

$$d(\delta V_{int}) = \int_0^l \left(\delta\varepsilon_j \, dN_j + \delta\kappa_j \, dM_j + d(\delta\varepsilon_j) \, N_j + d(\delta\kappa_j) \, M_j \right) ds_0$$

The two first terms are the material stiffness expressed via the constitutive equations, while the last two terms express the geometric stiffness, arising from the change in geometry.

By a straightforward calculation the geomtric stiffness terms can be expressed as - see e.g. Krenk (1996)

$$d(\delta\varepsilon_j)\,N_j \;+\; d(\delta\kappa_j)\,M_j \;=\; [\,\delta\mathbf{u}'\ \delta\overline{\varphi}'\ \delta\overline{\varphi}\,]\begin{bmatrix} 0 & 0 & (\mathbf{N}\times\mathbf{I})^T \\ 0 & 0 & \tfrac{1}{2}(\mathbf{M}\times\mathbf{I})^T \\ (\mathbf{N}\times\mathbf{I}) & \tfrac{1}{2}(\mathbf{M}\times\mathbf{I}) & \begin{array}{c}\tfrac{1}{2}(\mathbf{N}\,\mathbf{x}'+\mathbf{x}'\,\mathbf{N}) \\ -(\mathbf{N}\cdot\mathbf{x}')\,\mathbf{I}\end{array} \end{bmatrix}\begin{bmatrix} d\mathbf{u}' \\ d\overline{\varphi}' \\ d\overline{\varphi} \end{bmatrix}$$

This general formula can then be specialized to specific beam theories via the assumed representations of $d\mathbf{u}(s_0)$ and $d\overline{\varphi}(s_0)$.

Nonlinear Co-Rotating Beam Element

In the co-rotating formulation a coordiante system is located through the beam element end points, an the displacements consist of two parts: extension and end point rotations, see Fig. 1a, plus a rotatio without deformation generated by the diplacement of the local coordinate system.
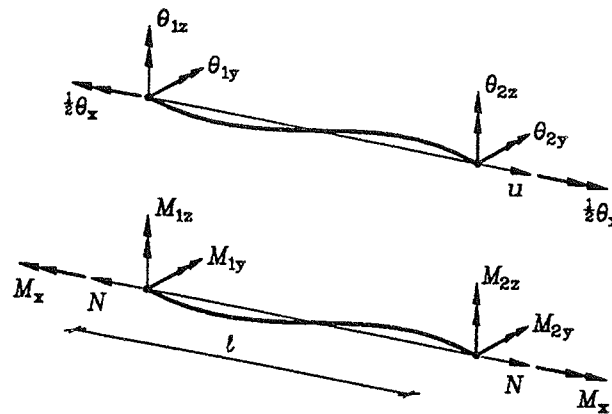

FIG. 1: Beam element with natural deformation parameters.

The effect of the normal force N can be built into a co-rotating beam-column element, Krenk (1995). Th *total* section forces and displacements shown in Fig. 1 are related by the nonlinear relations

$$N = EA\varepsilon \quad , \quad \mathbf{M} = \mathbf{A}(\varepsilon)\,\boldsymbol{\theta}$$

In this formulation the bending stiffness is a function of the normal force, and thereby of the axial strain ε The appropriate nonlinear axial strain definition is given by the derivative of the bending stiffness matri $\mathbf{A}(\varepsilon)$ as - Krenk (1995) -

$$\varepsilon = \frac{1}{l}\left(u + \tfrac{1}{2}\boldsymbol{\theta}^T\mathbf{B}\boldsymbol{\theta}\right) \quad , \quad \mathbf{B} = \frac{1}{EA}\frac{d\mathbf{A}}{d\varepsilon}$$

These relations determine the current section forces from the displacements. The corresponding incremer tal stiffness relation follows by differentiation,

$$\begin{bmatrix} dN \\ d\mathbf{M} \end{bmatrix} = \left(\begin{bmatrix} 0 & \mathbf{0}^T \\ \mathbf{0} & \mathbf{A} \end{bmatrix} + \frac{EA}{L}\begin{bmatrix} 1 \\ \mathbf{B}\boldsymbol{\theta} \end{bmatrix}[\,1, \boldsymbol{\theta}^T\mathbf{B}\,]\right)\begin{bmatrix} du \\ d\boldsymbol{\theta} \end{bmatrix}$$

where the effective length $L = l - \tfrac{1}{2}\boldsymbol{\theta}^T\,d\mathbf{B}/d\varepsilon\,\boldsymbol{\theta}$ accounts for the change in normal force for constan end point separation u.

Rotation stiffness

In addition to the nonlinear effects already included in the beam-column element stiffenss additional terms arise from the rotation of the local coordinate system. Several different forms of these terms are given in the literature.. A unique and consistent geometric stiffness matrix follows from the general form of the increment of the virtual work given above. When the usual polynomial shape functions are substituted and the geometric stiffness terms already included via the nonlinearity of the beam-column element are subtracted, the resulting rotation stiffness matrix $\mathbf{K}_r$ has the following block matrix format,

$$
\mathbf{K}_r = \begin{bmatrix} \mathbf{K}_A & \mathbf{K}_B & -\mathbf{K}_A & \mathbf{K}_C \\ \mathbf{K}_B^T & \mathbf{K}_D & -\mathbf{K}_B^T & \mathbf{K}_F \\ -\mathbf{K}_A & -\mathbf{K}_B & \mathbf{K}_A & -\mathbf{K}_C \\ \mathbf{K}_C^T & \mathbf{K}_F^T & -\mathbf{K}_C^T & \mathbf{K}_E \end{bmatrix}
$$

with the block matrices

$$
\mathbf{K}_A = \frac{1}{a} \begin{bmatrix} 0 & -Q_y & -Q_z \\ -Q_y & N & 0 \\ -Q_z & 0 & N \end{bmatrix} \qquad \mathbf{K}_B = \frac{1}{a} \begin{bmatrix} 0 & 0 & 0 \\ M_{1y} & M_x & 0 \\ M_{1z} & 0 & M_x \end{bmatrix}
$$

$$
\mathbf{K}_C = \frac{1}{a} \begin{bmatrix} 0 & 0 & 0 \\ M_{2y} & -M_x & 0 \\ M_{2z} & 0 & -M_x \end{bmatrix} \qquad \mathbf{K}_F = \frac{1}{6} \begin{bmatrix} 0 & aQ_y & aQ_z \\ aQ_y & 0 & 3M_x \\ aQ_z & -3M_x & 0 \end{bmatrix}
$$

$$
\mathbf{K}_D = \frac{1}{6} \begin{bmatrix} 0 & -(2M_{1z} - M_{2z}) & (2M_{1y} - M_{2y}) \\ -(2M_{1z} - M_{2z}) & 0 & 0 \\ (2M_{1y} - M_{2y}) & 0 & 0 \end{bmatrix}
$$

$$
\mathbf{K}_E = \frac{1}{6} \begin{bmatrix} 0 & -(2M_{2z} - M_{1z}) & (2M_{2y} - M_{1y}) \\ -(2M_{2z} - M_{1z}) & 0 & 0 \\ (2M_{2y} - M_{1y}) & 0 & 0 \end{bmatrix}
$$

where the shear forces are $Q_y = -Q_{1y} = Q_{2y} = -\frac{1}{a}(M_{1z} + M_{2z})$ and $Q_z = -Q_{1z} = Q_{2z} = \frac{1}{a}(M_{1y} + M_{2y})$. a is the current distance between the two end points, and the notation $M_x = -M_{1x} = M_{2x}$ is used. Note, that in a rigid body rotation this geometric stiffness matrix gives the theoretically correct, but somewhat counterintuitive result, that end forces turn by the full angle and end moments by half the angle.

Plastic Hinges

The generalized forces of the plastic hinges $s_j = (N, Q_x, Q_y, M, M_y, M_z)$ at the beam element ends are combined into the vector $s^T = [s_1, s_2]^T$. The generalized plastic strains are the corresponding displacement discontiuities $\mathbf{u}^{pT} = [\mathbf{u}_1^p, \mathbf{u}_2^p]^T$. In terms of the plastic potentials $g_j(s_j)$ the flow relation takes the matrix form

$$
d\mathbf{u}^p = \begin{bmatrix} \mathbf{u}_1^p \\ \mathbf{u}_2^p \end{bmatrix} = \begin{bmatrix} \partial g_1/\partial s_1 & 0 \\ 0 & \partial g_2/\partial s_2 \end{bmatrix} \begin{bmatrix} d\lambda_1 \\ d\lambda_2 \end{bmatrix} = \mathbf{G}\, d\lambda
$$

In terms of the total element tangent stiffnes matrix $\mathbf{K}$ the generalized force increment is determined by

$$
d\mathbf{s} = \mathbf{K}\, d\mathbf{u}^e = \mathbf{K}\, d\mathbf{u} - \mathbf{K}\,\mathbf{G}\, d\lambda
$$

When the gradients of the yield surfaces are contained in the matrix $\mathbf{F}$ the condition for remaining on the yield surface(s) is

$$
\mathbf{F}^T\, d\mathbf{s} - \mathbf{H}\, d\lambda = 0
$$

where $\mathbf{H} = \lceil H_1, H_2 \rfloor$ is the diagonal matrix containing the hardening moduli. The corresponding elast plastic incremental stiffness follows by elimination of $d\lambda$ as

$$d\mathbf{s} = \left(\mathbf{K} - \mathbf{KG} \left(\mathbf{F}^T \mathbf{KG} \right)^{-1} \mathbf{F}^T \mathbf{K} \right) d\mathbf{u}$$

When only one of the plastic hinges is active the block matrix format degenerates into a sigle set of acti blocks.

Kinematic hardening of tubular sections is introduced following Fujikubo et al. (1991). When h is the m terial hardening modulus, the hardening of the generalized strains at a section is determined by $f_j = f_j(s_j$ $\alpha_j)$ and $d\alpha_j = \mathbf{H}_j de_j^p$, with the diagonal section hardenig matrix $\mathbf{H}_j = \lceil hA_x, \frac{1}{3}hA_y, \frac{1}{3}hA_z, \frac{1}{3}hJ, hI_y, hI_z$ The accumulated effect in the beam elemet depends on the length ℓ_j of the yield hinge, estimated frc the moment distribution in the beam. The hardenig modulus of he plastic hinge is

$$H_j = \frac{1}{\ell_j} \frac{\partial f_j}{\partial s_j} \mathbf{H}_j \frac{\partial g_j}{\partial s_j}$$

leading to gradual hardening of the beam element.

Examples

The theory has been implemented into a computer programme, also including the effect of shear flexibili and initial imperfections in the beamcolumn elements, and special yield conditions for dented membe The programme is computationlly very efficient, because all element matices are given in closed form.
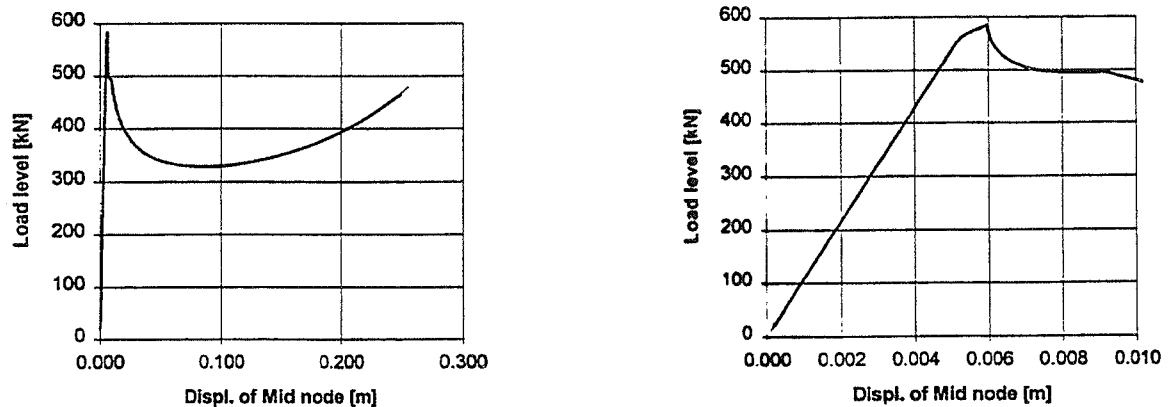

FIG. 2: K-brace under vertical force.

Figure 2 shows results from an analysis of a K-brace. The secondary maximum is followed by furth unloading to 330 kN before an increase caused by a transfer of load to tension in the upper members. T secondary maximum and the local minima consitiute a severe test on the nonlinear solution algorithi Both the equilirium correction method and the orthogonal residual method performed well.

References

M. Fujikubo, Y. Bai & Y. Ueda: Dynamic elastic-plastic analysis of offshore framed structures by plast node method considering strain hardening effects, Proc. 1st ISOPE Conference, Edinburgh, August 19C

S. Krenk: Stiffness of co-rotating elastic beam elements, in *Advances in Finite Element Technology*, N.-Wiberg (Ed.), CIMNE, Barcelona, 1995.

S. Krenk: Finite Rotation Beam Analysis, Lecture Notes. Division of Mechanics, Lund University, Janua 1996.

Mode Interaction in Thin-Walled Structures

Peter Noe Poulsen and Lars Damkilde
Department of Structural Engineering and Materials,
Technical University of Denmark

Introduction

The design of thin-walled structures often leads to two or more nearly simultaneous buckling modes. This could e.g. be a global buckling mode and a local buckling of a plate in some part of the structure. These buckling modes can each have a stable postbuckling behaviour not indicating any imperfection sensitivity. However the interaction of stable buckling modes can produce unstable postbuckling behaviour. In order to find the most critical imperfection leading to mode interaction and failure of the structure many different imperfections have to be analysed. These computations can be very costly. The size of the problem can be reduced by making an expansion of the displacements in a pertubation series using the nearly simultaneous buckling modes, see e.g. (Byskov & Hutchinson 1977). The solution has been formulated in a general finite element concept (Olsen & Poulsen 1994). This finite element concept is implemented for a flat triangular shell element DKTL (Poulsen & Damkilde 1996).

Formulation

Assuming the prebuckling state is linear and that there are M nearly simultaneous buckling modes u_i the displacements can be expanded in a pertubation series

$$u = \lambda\, u_0 + \xi_i\, u_i + \xi_i\, \xi_j\, u_{ij} + \ldots \qquad \text{where} \qquad i,j \in [1, M] \qquad (1)$$

The expansion reduces the number of degrees of freedom N for the structure to M where $N \gg M$ is typical. The imperfections are taken as a combination of the buckling modes $\bar{u} = \bar{\xi}_i\, u_i$.

This expansion of the displacements leads to a solution giving M non-linear equations.

$$\xi_I\left(1 - \frac{\lambda}{\lambda_I}\right) + \xi_i\,\xi_j\, a_{ijI} + \xi_i\,\xi_j\,\xi_k\, b_{ijkI} = \bar{\xi}_I\, \frac{\lambda}{\lambda_I} \qquad \text{where} \qquad I \in [1, M] \qquad (2)$$

The load path of the imperfect structure is determined by solving these M non-linear equations which can be done using standard methods.

The unknown terms in (1) and (2) are calculated from the behaviour of the perfect structure and they are formulated (Olsen & Poulsen 1994) in a general finite element concept e.g.

$$a_{ijI} = \frac{\sum_{el=1}^{nel}(V_I^T S_l V_j I_l^T D B V_i + \frac{1}{2} V_j^T S_l V_i I_l^T D B V_I)}{\sum_{el=1}^{nel} V_I^T B^T B V_I} \quad (3)$$

where $D B V$ is the linear stress terms and $V^T S_l V I_l^T$ is a summation over the non-linear strain terms.

When determining the load path for different imperfections it is necessary to have a measurement of the level of imperfections in order to compare these. This measurement is based on the total amount of energy E_t necessary to give the perfect structure the imperfections $\bar{u} = \bar{\xi}_i u_i$

$$E_t = \frac{1}{2} \sigma(\bar{u}) \cdot \varepsilon(\bar{u}) = E \sum_{i=1}^{M} \bar{\xi}_i^2 \quad (4)$$

where each buckling mode is scaled so that the amount of energy is E.

This measurement leads to a plane in the variables $\bar{\xi}_i^2$ as shown in Fig. 1(a). When determining the most critical imperfection at a certain level the points shown in Fig. 1(a) can be used remembering that each point $\bar{\xi}_i^2$ gives two points $\pm\bar{\xi}_i$.

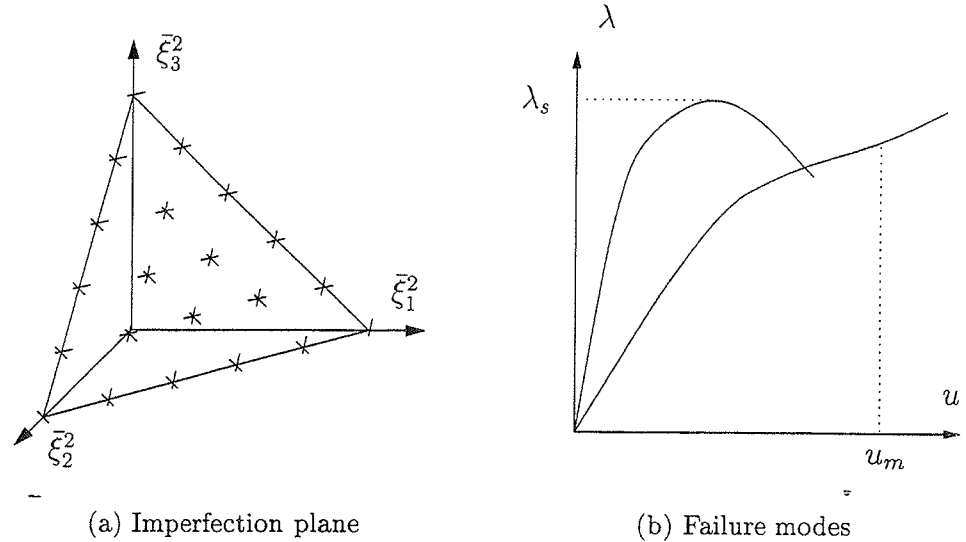(a) Imperfection plane   (b) Failure modes

Fig. 1.

When assessing the structure it seams reasonable to regard both a snap through at λ_s and the displacements exceeding a certain limit u_m as a failure, see Fig 1(b).

220

Computational effort

The computational scheme for a mode interaction analysis is

1. The prebuckling displacements are found solving a linear problem

2. The N buckling modes $\boldsymbol{u}_i$ are found solving an eigenvalue problem

3. The displacement fields $\boldsymbol{u}_{ij}$ are found solving a linear problem with different load vectors

4. The terms a_{ijI} and b_{ijkI} are computed by an element loop calculating expressions like (3)

5. The N non-linear equations are solved for each point in the $\bar{\xi}_i^2$ plane

The first 4 steps are calculated using the N degrees of freedom in the total structure but the computational effort is relatively small and independent of the imperfections. Step 5 involves solution of a non-linear problem but for the reduced M degrees of freedom. The total computational effort in a mode interaction analysis is therefore small compared to a full non-linear computation.

Conclusion

A mode interaction analysis formulated in a general finite element concept is implemented using a flat shell element DKTL. The method allows a structural optimization at a reduced computational cost and the optimized structure can be analysed using a full non-linear analysis.

References

Byskov, E. & Hutchinson, J. W. (1977). Mode interaction in axially stiffened cylindrical shells, *AIAA Journal* 15(7): 941–948.

Olsen, J. F. & Poulsen, P. N. (1994). *Stability and Postbuckling of Plate structures*, M.Sc. Thesis, Department of Structural Engineering, Technical University of Denmark. (in Danish).

Poulsen, P. N. & Damkilde, L. (1996). A flat triangular shell element with loof nodes, *International Journal for Numerical Methods in Engineering*. in press.

Integration in Numerical Phase Change Analysis

Anders Boe Hauggaard[1], Lars Damkilde[1] and Steen Krenk[2]

Introduction

Numerical analysis of non-linear phase change problems is of interest in relation to arctic engineering and settlement of frozen ground. Coupled problems in concrete also involves non-linear phase change analysis e.g. in relation to fire. The problems that need to be considered are illustrated in Fig. 1 and they are a sharp step in conductivity and the latent heat. Several numerical
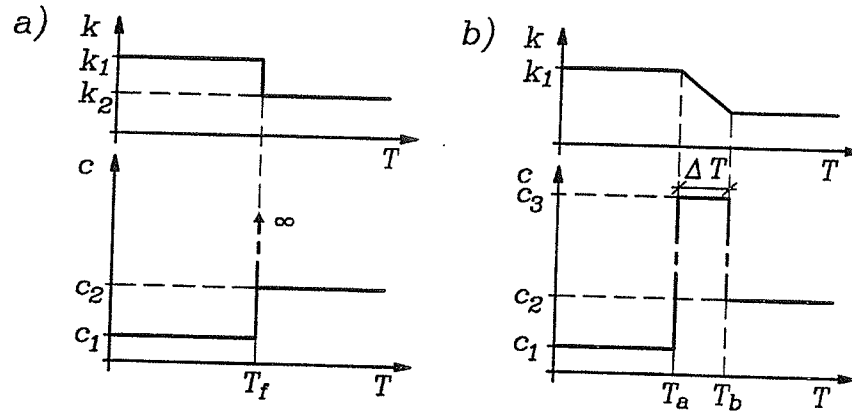

Figure 1: Modelling of phase change.

strategies exist e.g. extending the phase change zone over a finite interval as indicated in Fig. 1. The purpose of the present work is to identify some modelling problems and propose solutions. Focus is on integration of the conductivity matrix and it is shown that the standard procedure of nodal averaging leads to a systematic overestimation of the conductivity. A finite element is proposed which explicitly accounts for the step in conductivity, thus removing the overestimation.

[1]Department of Structural Engineering and Materials, Technical University of Denmark, DK-2800, Lyngby, Denmark.

[2]Division of Mechanics, Lund Institute of Technology, Lund University, S-22100, Lund, Sweden.

Overshoot in Temperature

The one-dimensional problem shown in Fig. 2 has been analysed with linear triangular elements and nodal averaging of the conductivities. The material is water which has a step in conductivity corresponding to a factor 4. Initially the temperature is 10 °C and suddenly the free end is brought to -20 °C. The variation of temperature at the points indicated in Fig. 3 is shown and
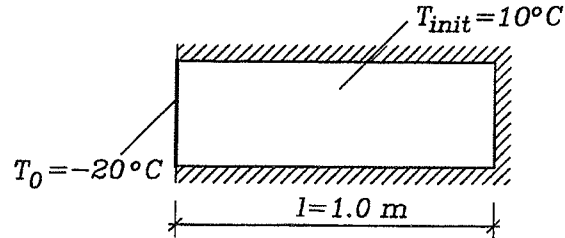

Figure 2: One-dimensional bar problem.

two problems are apparent

- overshoot in temperature

- non-symmetric temperature distribution
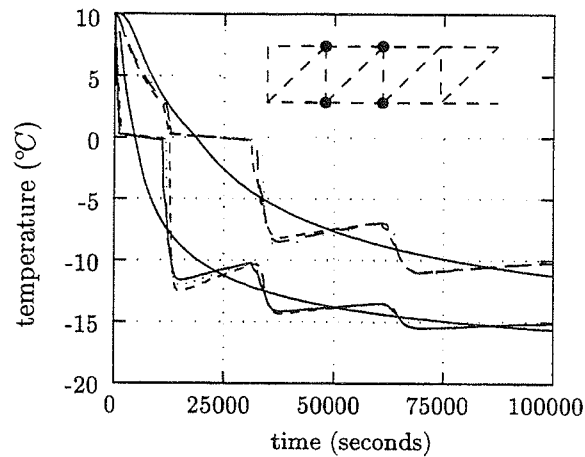
Figure 3: Temperature evolution.

The reason for this overshoot may be related to either positive off-diagonal elements in the conductivity/capacity matrix and/or an overestimation of the conductivity. In [1] it is shown that positive off-diagonal elements appear for linear triangles when one of the angles exceed 90°. For higher order elements

224

it may be shown that the problem is worse as there will always be positive off-diagonal elements. The problem and the matrix implications are discussed in [2] and it is shown that positive off-diagonal elements represents physical unrealistic couplings.
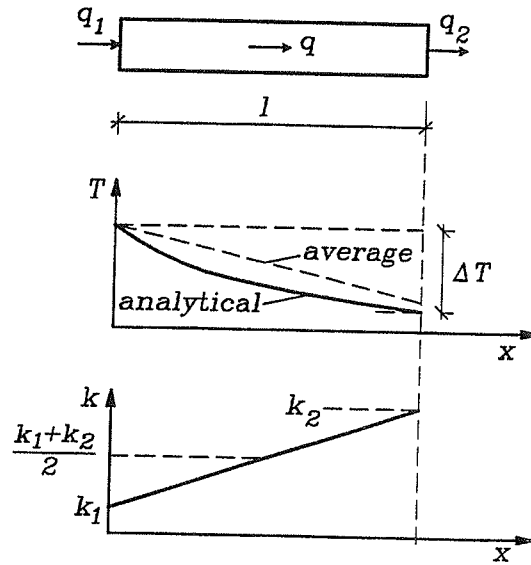

Figure 4: Overestimation of conductivity.

To illustrate the problem of overestimation of the conductivity the one-dimensional element shown in Fig. 4 is considered. The conductivity varies linearly along the element and the nodal values are k_1 and k_2 respectively, and the temperatures T_1 and T_2. At equilibrium there is no heat storage which means that the heat flux, $q = -k\,dT/dx = $ const., and then the temperature increment over an element can be found by direct integration

$$\Delta T = -q \int_l \frac{1}{k}\,dx = -ql\,\frac{1}{k^*} = -ql\,\frac{\ln(k_2/k_1)}{k_2 - k_1} \tag{1}$$

where k^* is the effective conductivity. It may be shown that k^* is less than the average conductivity, $\bar{k} = (k_1 + k_2)/2$, meaning that nodal averaging gives a systematic overestimation.

Proposed integration scheme

A finite element applicable for phase change analysis is proposed based on the assumption of constant flux along the sides. This results in a temperature interpolation where two linear parts meet at the phase front, thus accounting for the different conductivities in the two phases. Using the proposed element

the same problem as above has been analysed and the result is shown in Fig. 5 where the overshoot and non-symmetric temperature distribution have been removed. The element has been implemented in two dimensions and used.
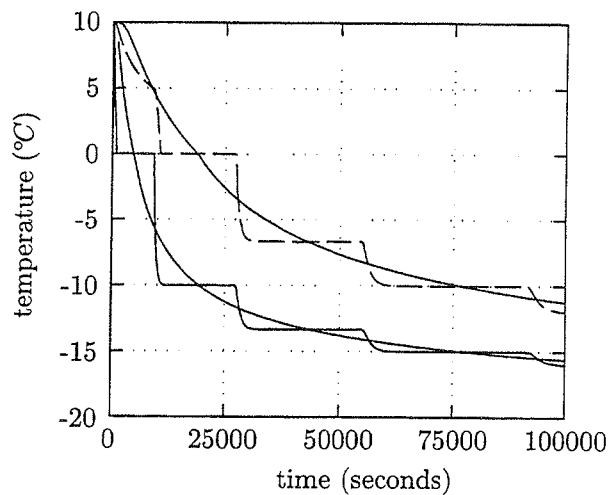

Figure 5: Temperature evolution using the proposed element.

for examples of more practical interest.

Conclusion

The problem of overshoot in temperature in relation to numerical phase change analysis has been discussed and it is shown that overshoot is related to the integration procedure chosen. A bi-linear finite element has been proposed that explicitly take into account the step in conductivity. Examples demonstrate that the proposed procedure removes the disturbances introduced upon passage of the phase change front.

References

[1] Hauggaard, A.B., Damkilde, L. and Krenk, S., (1996). *An Energy Based Numerical Approach to Phase Change Problems*, DCAMM report no. 528, Technical University of Denmark.

[2] Segerlind, L.J., (1984). *Applied Finite Element Analysis*, Wiley and Sons.

FINITE ELEMENT MODELLING OF FREEZING OF FINE GRAINED IRON ORE

by

Arild Tørlen and Geir Horrigmoe
NORUT Teknologi AS, N-8501 NARVIK, NORWAY

INTRODUCTION

During railway transportation of fine grained iron ore from Kiruna, Sweden to Narvik, Norway, the Swedish mining company LKAB experiences freeezing of iron ore every winter. The temperature may be as low as -30 degrees centigrade causing the iron ore to freeze in the train cars. This makes unloading the iron ore a time consuming process.

Laboratory tests on scale models have been carried out to investigate the effects of changes in initial temperature of the iron ore and ambient temperature, see ref. 1. In the present study the aim was to verify the laboratory results and to map the effects of changes in several other parameters by numerical simulations. Non-linearities during freezing processes were of particular interest.

HEAT TRANSFER

The governing equation of heat conduction in solids assuming isotropic and constant thermal conductivity (k) is given by

$$\frac{\partial^2 T}{\partial x^2} + \frac{\partial^2 T}{\partial y^2} + \frac{\partial^2 T}{\partial z^2} + \frac{q'''}{k} = \frac{1}{\alpha} \cdot \frac{\partial T}{\partial t} \tag{1}$$

where T is temperature, t is time, q''' is internal heat generation and α thermal diffusivity of the material. Heat transfer is discussed in ref. 2.

On the boundaries of the solid, heat is tranferred from the body to the surrounding air due to convection. The rate of heat transfer, which depends on the temperatures of the solid on the surface and the ambient air temperature, is given by Newton's law of convection,

$$q'' = h \cdot (T_s - T_\infty) \tag{2}$$

here, T_s is surface temperature of the body and T_∞ is the ambient temperature. The convection coefficient, h, is depending on properties of the air flow at the surface.

Radiation effects were also added in the finite element analyses. The rate of radiation heat transfer to the surroundings is given by

$$q''_{rad} = \varepsilon\sigma \cdot \left(T_s^4 - T_\infty^4 \right) \tag{3}$$

where ε is the emissivity of the surface and σ is the Stefan-Boltzmann constant.

MODEL PARAMETERS

Fine grained iron ore is a porous medium consisting of iron oxides (in the Kiruna mines mainly magnetite), moisture, voids and several other constituents. Thermal properties of the iron ore were calculated on the basis of properties of the constituents due to a continuum approach. These properties were temperature dependent, so non-linear behaviour occurred also outside the freezing region.

The initial conditions were uniform temperature (T > 0) in the iron ore, and constant ambient temperature (T < 0).

On the surface of the solid, heat were transferred out of the solid by convection and radiation according to eqs. 2 and 3. The convection coefficients were calculated according to theory of fluid flow over flat plates. At distance x from the leading edge of the plate the convection coefficient is given by

$$h_x = \frac{Nu_x \cdot k_f}{x} \tag{4}$$

where Nu_x is the Nusselt number which is dependent on fluid flow characteristics and k_f is the thermal conductivity of the fluid. The convection coefficients are somewhat temperature dependent due to variations in fluid properties.

A two dimensional finite element model representing a cross section of a model of the train car (Fig. 1) were implemented using four node quadrilateral elements with one temperature DOF at each node.
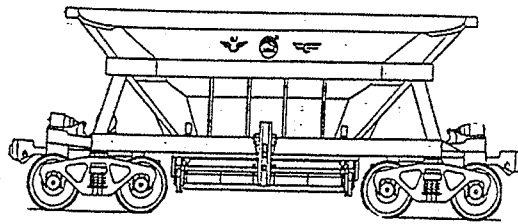

Figure 1. *The iron ore train car.*

Material properties were implemented in the finite element software as stepwise linear functions of temperature as indicated by Fig. 2. Phase change is assumed to take place at a temperature interval rather than at a discrete point to avoid convergence problems. Latent heat is modelled by the enthalpy method. Numerical modelling of heat transfer is discussed in detail in refs. 3 and 4.
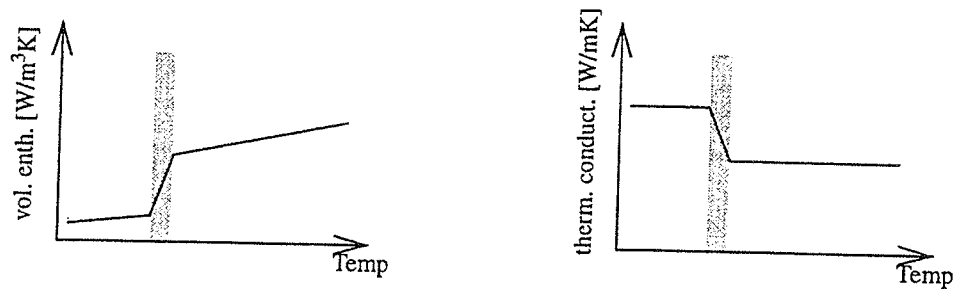
Figure 2. *Material properties. Phase change is assumed to take place in shaded area.*

Boundary conditions consist of specified convection and radiation heat transfer at the surface of the body. Emissivity was considered constant which implies that heat transfer by radiation is proportional to T_s^4 as the surrounding temperature remains constant. Convection coefficients were implemented as a stepwise linear function of film temperature $((T_s + T_\infty)/2)$.

The model was extended to three dimensions to investigate effects of heat transfer in three directions at the corners of the model.

A one-dimensional model was also implemented, and it performed quite well compared to the two- and three-dimensional models. The simple one-dimensional model was used in a sensitivity study where multiple runs were executed in order to map the effects of changes in different

model parameters. The results from this study were mapped for easy determination of effects from changes in any property inspected.

NUMERICAL RESULTS

During the laboratory experiments, temperatures were logged at locations as described in ref. 1. Several numerical analyses were carried out on the laboratory model using different initial conditions. Results from the finite element analyses were compared to laboratory test results. The numerical results compared very well with the experimental data. There were some deviation in temperature distribution and frost propagation, probably due to inaccurate material properties and boundary conditions.

The sensitivity study showed that modelling the steel casing containing the iron ore and icluding radiation heat transfer had very little effect on the results. Changes in thermal diffusivity of the iron ore and changes in the convection coefficients resulted in significant changes in frost propagation.

CONCLUDING REMARKS

Numerical models of freezing processes will be a very useful tool when the problem of freezing of fine grained iron ore is to be resolved. Different solutions can be evaluated without having to build expensive prototypes. When designing new iron ore train cars, the effects of different designs can be evaluated at an early stage of the design process.

The approach outlined in this paper will also be applicable in similar problems concerning heat transfer in porous media. Effects of mass transfer could also be included in a revised model.

REFERENCES

[1]   Sveen, S.E. and Rindal, D.B.: Freezing of KBF Fines, NORUT Teknologi AS, Report no. NTAS A94045, Narvik, 1994 (in Norwegian).

[2]   Welty, J.R., Wicks, C.E. and Wilson, R.L.: Fundamentals of Heat and Mass Transfer 2, John Wiley & Sons, New York, 1982.

[3]   Wrobel, L.C., Brebbia, C.A. and Nowak, A.J.: Advanced Computational Methods in Heat Transfer, Vol. 1-3, Computational Mechanics Publications, Springer Verlag, Southampton, 1990.

[4]   Lewis, R.W., Morgan, K. and Zienkiewicz, O.C.: Numerical Methods in Heat Transfer, Department of Civil Engineering, University of Wales, John Wiley & Sons, Swansea, 1981.

Convection- diffusion problems with significant first-order reversible reactions

Björn Johannesson

Division of Building Materials, Lund Institute of Technology
Box 118, S-221 00 LUND, Sweden
E-mail: Bjorn.Johannesson@byggtek.lth.se

Abstract- Corrosion of steel in concrete occurs whenever the external influences change the composition of the pore solution, present in the concrete, to an aggressive condition. For example, chloride ions present in the pore solution and carbonation of the concrete may destroy the passivity which results in corrosion of the reinforcement. For this reason, one is interested in predicting the magnitude of mass transfer of deleterious substances, e.g. $NaCl$, from external sources into concrete. External influences such as capillary suction of water will also contribute to flows of deleterious substances carried by the water phase (convection). In this paper, however, a general discussion of a numerical method (*Petrov-Galerkin* method) capable of solving convection-diffusion problems with good accuracy will be presented. Only averaged phenomena at the macroscopic level will be dealt with concerning the description of mass balance and the constitutive behaviors. Three constituents are considered in the model, that is, $NaCl$ (pollutant γ), the pore water phase (α phase) and the solid matrix (s, i.e. the solid parts of the concrete) which is restricted to be non-deformable.

1 Convection- diffusion problems; mass balance

The mass balance for a solute γ (*e.g. NaCl*) in the α phase (*e.g.* pore water) is given by [1], as

$$\frac{\partial \theta_\alpha \overline{c}_\alpha}{\partial t} = -div\left[\overline{c}_\alpha \mathbf{q}_\alpha + \theta_\alpha \overline{c_\alpha V_\alpha} + \theta_\alpha \overline{J(c_\alpha / \rho_\alpha)}\right] - f \tag{1.1}$$

where $\overline{c}_\alpha$ is the (averaged) mass of the pollutant γ per unit volume of α phase. θ_α is the volumetric fraction of α in the porous material. To obtain the *macroscopic* balance equation (1.1), the equation describing the *microscopic* balance [2] must be averaged. The averaging process performed to reach equation (1.1) results in two additional terms, compared with the microscopic balance equation [1]; first, $\theta_\alpha \overline{c_\alpha V_\alpha}$, which is the term describing the macroscopic *dispersive* flux of γ carried by the fluctuating velocity. The phenomenon at the macroscopic scale represents the loss of information by the passage from one scale of description to another, larger, one [1]. The second additional term, due to averaging, is the f term which describes the transfer of γ across the boundaries of the α phase, e.g., *adsorption* or *desorption* of the pollutant γ. The first term in the bracket of (1.1) is the *convective* part of the flux, where the *specific discharge* $\mathbf{q}_\alpha = \theta_\alpha \overline{\mathbf{u}}_\alpha$ and $\overline{\mathbf{u}}_\alpha$ is the *mean velocity of the mixture* (in this case the mean velocity of α). The third term in the bracket of (1.1) describes the flux of molecular diffusion of γ in the α phase.

The mass balance equation for the α phase, without source or sink terms, becomes

$$\frac{\partial \theta_\alpha \overline{\rho}_\alpha}{\partial t} + div\left(\theta_\alpha \overline{\rho}_\alpha \mathbf{u}_\alpha\right) = 0 \tag{1.2}$$

where $\overline{\rho}_\alpha$ is the averaged mass density of the α phase. If the α phase is assumed to be incompressible (i.e. $div\overline{\mathbf{u}}_\alpha = 0$) and assuming also small changes in $\overline{\rho}_\alpha$ due to the dissolved pollutant γ present in the α phase, i.e. $\overline{\rho}_\alpha = const.$, (1.2) becomes

$$\frac{\partial \theta_\alpha}{\partial t} + div(\theta_\alpha \overline{\mathbf{u}}_\alpha) = 0 . \tag{1.3}$$

The problem now reduces to an *ideal tracer problem*, or alternatively a *forced convection problem*, i.e. the mean velocity field $\overline{\mathbf{u}}_\alpha$ is known (from equation (1.3)) before (1.1) is solved.

When considering a porous medium which is deformable, the porosity will not be constant, i.e. θ_α will be affected; furthermore the specific discharge vector $\mathbf{q}_\alpha$ is defined with respect to the (possibly moving) solid parts of the porous medium. However, in this paper it is assumed that the mean velocity of the solid phase is zero ($\overline{\mathbf{u}}_s = 0$) i.e. no *consolidation* or *deformation* in the solid phase is dealt with.

2 Constitutive equations

The macroscopic flux, $\overline{J(c_\alpha / \rho_\alpha)}$, due to molecular diffusion of γ in the α phase, is expressed by *Fick's law* as

$$\overline{J(c_\alpha / \rho_\alpha)} = -\mathbf{D}_{\gamma diff} \cdot grad\, \overline{c}_\alpha \tag{2.1}$$

where $\mathbf{D}_{\gamma diff}$ is the *second rank constitutive matrix*, which in many applications is assumed to be a function of $\overline{c}_\alpha$. Of course, the molecular diffusion takes place even if the bulk mean velocity is zero, *i.e.* if $\overline{\mathbf{u}}_\alpha = 0$. The dispersive flux (not to be confused with the convective flux) induced by the spreading of γ in the α phase due to velocity variations at the microscopic level is, however, dependent on the bulk flow, molecular diffusion and the porous matrix geometry. In [1] it has been proposed to use a Fickian type of law to describe the dispersive flux, such as

$$\overline{c_\alpha V_\alpha} = -\mathbf{D}_{\gamma disp} \cdot grad\, \overline{c}_\alpha \tag{2.2}$$

and to let the constitutive matrix $\mathbf{D}_{\gamma disp}$ be a function of the bulk mean velocity $\mathbf{u}_\alpha$ and the *Peclet number* ($Pe = l \overline{\mathbf{u}}_\alpha / D_{\gamma diff}$), where l is some characteristic length of the pores. For more details concerning the constitutive relation (2.2), compare [1].

The macroscopic flux, $\theta_\alpha \overline{\mathbf{u}}_\alpha$, due to *capillary suction* of the α phase is expressed as

$$\theta_\alpha \overline{\mathbf{u}}_\alpha = -\mathbf{D}_\alpha \cdot grad\, \theta_\alpha \tag{2.3}$$

where $\mathbf{D}_\alpha$ is a function of θ_α.

The adsorption and desorption of the tracer γ across the α phase boundaries is constituted with a *non-equilibrium isotherm* which describes a *reversible system*, e.g. [3], as

$$\overline{f} \equiv \frac{\partial \overline{F}}{\partial t} = k(C - mF); \qquad \overline{f}_s = -\overline{f} \tag{2.4a-b}$$

where $C = \overline{c}_\alpha / \overline{\rho}_\alpha =$ mass of γ per unit mass of α phase, and k and m are constants. $F = \overline{c}_s / \overline{\rho}_s$ is the mass of γ per unit mass of solid. The right-hand side of (2.4a) expresses the rate of transfer, f_s, of γ from the liquid phase α onto the solid phase s.

Introducing the constitutive relations (2.1-2.2, 2.4) into (1.1), and assuming that the mass change of the solid phase s due to adsorption and desorption of the tracer γ is small, i.e. $\overline{\rho}_s = const.$, $\theta_s = const.$, one will obtain

$$\overline{\rho}_\alpha \frac{\partial \theta_\alpha C}{\partial t} + \overline{\rho}_s \theta_s k(C - mF) = -div\left[\overline{\rho}_\alpha C \mathbf{q}_\alpha - \overline{\rho}_\alpha \theta_\alpha \mathbf{D}_h \cdot grad\, C\right] \tag{2.5}$$

where $\mathbf{D}_h = \mathbf{D}_{\gamma diff} + \mathbf{D}_{\gamma disp}$ is the matrix describing *hydrodynamic dispersion*.

By combining (2.5) and (1.3) and using the identity $div(C\mathbf{q}_\alpha) = Cdiv\mathbf{q}_\alpha + \mathbf{q}_\alpha \cdot grad\, C$, (2.5) may be written as

$$\theta_\alpha \frac{\partial C}{\partial t} + \tilde{k}(C - mF) = div\left[\theta_\alpha \mathbf{D}_h \cdot grad\, C\right] - \mathbf{q}_\alpha \cdot grad\, C \tag{2.6}$$

which is the convective-diffusion equation with an additional term describing a non-equilibrium reversible reaction.

The equation for the α phase is given by (1.3) and (2.3), as

$$\frac{\partial \theta_\alpha}{\partial t} - div\left[\mathbf{D}_\alpha \cdot grad\, \theta_\alpha\right] = 0, \qquad and \qquad \mathbf{q}_\alpha = -\mathbf{D}_\alpha \cdot grad\, \theta_\alpha. \tag{2.7a-b}$$

The model contains three state variables: θ_α given by (2.7a), C given by (2.6) and F given by (2.4a). The specific discharge, $\mathbf{q}_\alpha = \theta_\alpha \overline{\mathbf{u}}_\alpha$, for the α phase is calculated with (2.7a-b); the result is used to express $\mathbf{q}_\alpha$ in equation (2.6).

3 Finite element formulation

A finite element formulation for the convective- diffusion equation (2.6) is given by

$$\mathbf{C}\dot{\mathbf{a}} + \left(\mathbf{K}_d + \mathbf{K}_c\right)\mathbf{a} + \mathbf{f} = 0, \qquad where \qquad \dot{\mathbf{a}} = \frac{d}{dt}\mathbf{a} \tag{3.1a-b}$$

and where $\mathbf{C}$ is the *consistent damping matrix* $\mathbf{K}_d$ is the *diffusion stiffness matrix*, $\mathbf{K}_c$ is the *convection stiffness matrix*, and the vector $\mathbf{f}$ carries information about both the source/sink terms (*i.e.* adsorption and desorption) and the boundary conditions. The finite element formulation of equation (2.7) is in fact the same, i.e. with $\mathbf{K}_c = 0$, and will therefore not be discussed further.

The discretization, in the time domain, of the nodal parameter $\mathbf{a}$ in (3.1) is performed using a *single time-step algorithm* [4], as

$$\frac{\mathbf{C}(\mathbf{a}_{n+1} - \mathbf{a}_n)}{\Delta t} + \left(\mathbf{K}_d + \mathbf{K}_c\right)\left[(\mathbf{a}_n + \Theta(\mathbf{a}_{n+1} - \mathbf{a}_n)\right] + \mathbf{f}_n + \Theta\left(\mathbf{f}_{n+1} - \mathbf{f}_n\right) = 0 \tag{3.2}$$

where $\mathbf{a}_n$ is the known values at time t_n, and (3.2) is solved for $\mathbf{a}_{n+1}$ at time $t_n + \Delta t$. The *weighting parameter* Θ (in the time domain) could be chosen with values between 0 and 1. $\Theta = 0$ corresponds to an *explicit* (or *Euler*) scheme, $\Theta = 1$ is a *backward difference scheme* and the value $\Theta = 0.5$ is the well-known *Crank-Nicolson scheme*. Values of Θ greater or equal to 0.5 are shown to be *unconditionally stable* for equation systems which are symmetric and positive definite. However, when dealing with the convective-diffusion equation (3.2), more elaborate procedures for assessment of stability and performance are needed since the problem is not symmetric. One process is to determin the so-called *amplitude* and *relative celerity* ratios, e.g. [4].

The discretization of nodal parameter $\mathbf{a}$ in the spatial domain is performed using the shape function $\mathbf{N}$; compare equation (3.3a). Using the *standard Galerkin weighting* means that

the weight function (in the spatial domain) is also described with the shape function $\mathbf{N}$, equation (3.3b) where $\mathbf{c}$ is arbitrary.

$$C = \mathbf{Na}; \qquad\qquad v = \mathbf{c}^T\mathbf{N}^T \qquad\qquad (3.3a\text{-}b)$$

However, the standard Galerkin weighting is an unfavorable approximation when dealing with the diffusion-convection equation, which could be shown by writing down the one-dimensional steady-state version of equation (3.1), without source/sink terms, for a typical internal node i [5]; compare equation (3.4a) where the standard Galerkin weighting has been used, i.e. (3.3a) and (3.3b). If, for example, $\tilde{a}_{i-1} = 0$ and $\tilde{a}_{i+1} = 100$, equation (3.4a) gives $\tilde{a}_i = 50(1\text{-}Pe)$, which yields a negative value if $Pe > 1$, which is a physically unrealistic result! However, using the *exponential method* which matches the analytical solution of the steady-state version of (3.1) (again, without source/sink terms), equation (3.4b) is obtained for a typical internal node i; compare [5]

$$(-Pe^e - 1)\tilde{a}_{i-1} + 2\tilde{a}_i + (Pe^e - 1)\tilde{a}_{i+1} = 0 \qquad\qquad (3.4a)$$

$$-e^{2Pe^e}\tilde{a}_{i-1} + (1 + e^{2Pe^e})\tilde{a}_i - \tilde{a}_{i+1} = 0 \qquad\qquad (3.4b)$$

where the *element Peclet number* is $Pe^e = \overline{u}h / 2k_d$, $\overline{u}$ is the mean velocity of the mixture (in this example, i.e. in equations (3.4a) and (3.4b), is the the mean velocity of the mixture $\overline{u}$ assumed to be greater or equall to zero), h is the nodal spacing and k_d is the diffusion constant. Note that for $Pe^e = 0$ the relation in (3.4b) reduces to the Galerkin method, i.e. (3.4a), corresponding to the diffusive term only (because the convective term is zero) [5]. The scheme shown in (3.4b) gives exact values of C at the nodes, since it is based on the analytical solution. Further, it should be noted that both the Galerkin method and the exponential method yield non-symmetric equation systems.

An identical solution as that obtained with the nodal equation (3.4b), i.e. the exponential method (but now generalize the result to consider any value of $\overline{u}$), could be secured using the finite element method (here given in two dimensions) by setting

$$C = \mathbf{Na}, \qquad v = \mathbf{c}^T\left(\mathbf{N}^T + \alpha_{opt}\frac{h_{ch}}{2}\frac{q_{ox}(\partial\mathbf{N}^T/\partial x) + q_{oy}(\partial\mathbf{N}^T/\partial y)}{|\mathbf{q}_\alpha|}\right) \qquad (3.5a\text{-}b)$$

$$\alpha_{opt} = \coth Pe^e - \frac{1}{Pe^e}. \qquad\qquad (3.5c)$$

By using $\alpha = 0$ the standard Galerkin approximation is recovered, and with $\alpha = 1$ the so-called *full-upwind approximation* is obtained; e.g. compare [4],[5]. However, by using α_{opt} according to (3.5c), the *optimal Petrov-Galerkin approximation* is achieved which gives exact values of the nodal parameter at the nodes in the one-dimensional case; compare [6]. Using the definition of the *Peclet number* as $Pe^e = |\mathbf{q}_\alpha|h_{ch} / 2k_d$ where h_{ch} is the *characteristic length* of the element in the *streamline direction* of $\mathbf{q}_\alpha$, [4], accurate solutions for two or three-dimensional cases could also be achieved (assuming that the diffusion part of the flux is isotropic). This is accomplished because the convective flow is active only in the direction of the mean velocity of the mixture.

Now using rectangular *bi-linear* elements, i.e. $\nabla^2\mathbf{N} = \nabla\mathbf{B} = 0$, $\mathbf{C}$, $\mathbf{K}_d$, $\mathbf{K}_c$ and $\mathbf{f} = \mathbf{f}_l + \mathbf{f}_b$, could be explicitly expressed as (where the Petrov-Galekin weighting is used on all terms in the convective-diffusion equation)

$$C = \int_A \left(\mathbf{N}^T + \alpha_{opt} \frac{h_{ch}}{2} \frac{q_{\alpha x}(\partial \mathbf{N}^T / \partial x) + q_{\alpha y}(\partial \mathbf{N}^T / \partial y)}{|\mathbf{q}_\alpha|} \right) \theta_\alpha \mathbf{N} \, dA \tag{3.6}$$

$$\mathbf{K}_d = \int_A \mathbf{B}^T \mathbf{D}_h \mathbf{B} \, dA \tag{3.7}$$

$$\mathbf{K}_c = \int_A \left(\mathbf{N}^T + \alpha_{opt} \frac{h_{ch}}{2} \frac{q_{\alpha x}(\partial \mathbf{N}^T / \partial x) + q_{\alpha y}(\partial \mathbf{N}^T / \partial y)}{|\mathbf{q}_\alpha|} \right) \mathbf{q}_\alpha^T \mathbf{B} \, dA \tag{3.8}$$

$$\mathbf{f}_b = \int_s \left(\mathbf{N}^T + \alpha_{opt} \frac{h_{ch}}{2} \frac{q_{\alpha x}(\partial \mathbf{N}^T / \partial x) + q_{\alpha y}(\partial \mathbf{N}^T / \partial y)}{|\mathbf{q}_\alpha|} \right) q_{\alpha n} \, dS \tag{3.9}$$

$$\mathbf{f}_l = \int_A \left(\mathbf{N}^T + \alpha_{opt} \frac{h_{ch}}{2} \frac{q_{\alpha x}(\partial \mathbf{N}^T / \partial x) + q_{\alpha y}(\partial \mathbf{N}^T / \partial y)}{|\mathbf{q}_\alpha|} \right) f \, dA \tag{3.10}$$

where it should be noted that the source/sink term f is also affected by the Petrov-Galerkin weighting. To solve equation (3.2) numerical integration is used, since the weighting function v, in (3.5b), is discontinuous, i.e. the discontinuity of v is considered within the element rather than at the nodes when using numerical integration [4].

4 Examples of the streamline optimal Petrov-Galerkin method in two-dimensional problems

Numerical integration and equally sized bi-linear elements with 3x3 integrating points are used to solve the diffusion-convection equation (3.2). Only pure convection with and without adsorption of mass is considered, as it represents the essence of the problems related to numerical solutions of the diffusion-convection equation. An unconditional stable integration scheme in the time domain, which minimizes the error in the whole domain [4] ($\Theta = 0.878$), has been used since Pe^e tends to infinity. Due to a high *element Peclet number*, realistic *critical time-steps* cannot be reached within the family of explicit schemes. Furthermore, the mean velocity field is assumed to be constant in direction and magnitude throughout the whole considered (space-time) domain, and the characteristic length in the direction of the mean velocity is assumed to be $h_{ch} = \sqrt{2}\,h$, where h is the length of the sides of the elements.

The first example, figures 4.1 and 4.2, illustrates pure convection. The maximum value of the initial concentration field is decreased by approximately 2% after 3.5 seconds when 120 time-steps are used; this is a measure of the error since the shape of the initial concentration field should be the same throughout the process.
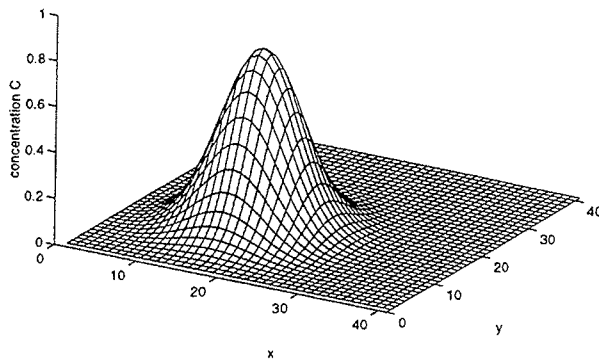
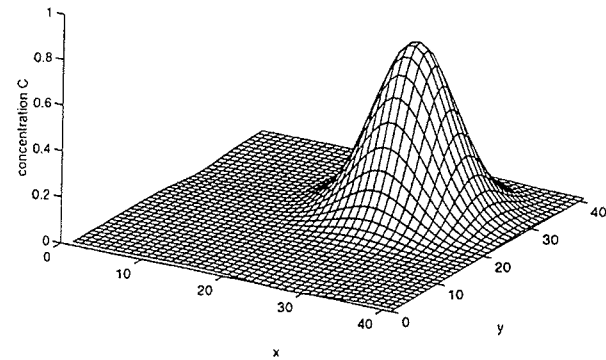Figure 4.1. Initial concentration field of C at time t = 0.

Figure 4.2. Concentration field, C, after 3. seconds. The initial concentration field (figure 4.1 is convected throughout the domain.

The second example, figures 4.1, 4.3 and 4.4 illustrates pure convection with adsorption o mass. 120 time-steps were used. The transient sink term f is integrated in the time domaii using the value Θ = 0.878.
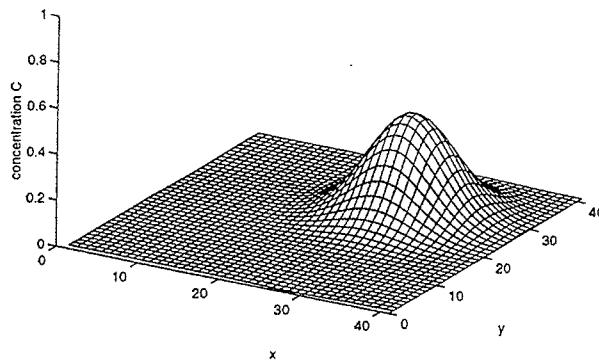

Figure 4.3. Concentration field, C, after 3.5 seconds. The initial concentration field (figure 4.1) is convected throughout the domain; simultaneously mass is adsorbed onto the solid parts of the porous medium; compare figure 4.4.
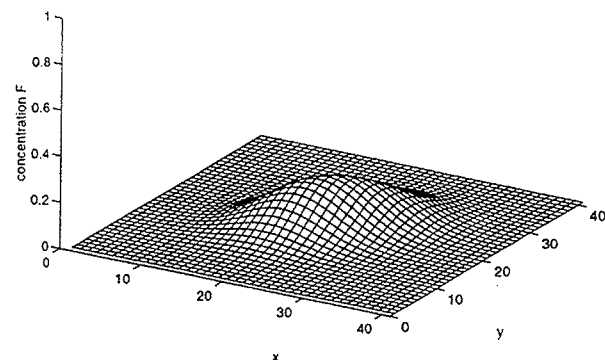
Figure 4.4. Concentration field, F, of motionles: adsorbed mass after 3.5 seconds.

References

[1]   Bear, J. (1979) Hydraulics of Groundwater, McGraw-Hill Series in Water Resources and Environmenta Engineering, New York.

[2]   Truesdell, C. and Toupin, R.A. (1960). Classical field theories, in Handbuch der Physic, Vol. III-1 Springer, Berlin.

[3]   Hougan, O.A. and Marshall, W.R. (1947). Adsorption from fluid stream flowing through a stationar; granular bed, Chem. Eng. Prog., 43(4).

[4]   Zienkiewicz, O.C. and Taylor, R.L. (1989). The Finite Element Method, Fourth Edition, Vol. 2. McGraw Hill, London.

[5]   Bathe, K.J. (1996). The Finite Element Procedures, Prentice Hall, Englewood Cliffs, New Jersey.

[6]   Christie, I. et al. (1976). The Finite Element Methods for second order differential equations with significant first derivatives, Int. J. Num. Meth. Eng., 10.

ON THE CORE CONGRUENTIAL TOTAL LAGRANGE FORMULATION FOR FINITE DEFORMATION ANALYSIS OF BAR STRUCTURES

Mats Ander and Alf Samuelsson

Dept. of Structural Mechanics, Chalmers University of Technology, S–412 96 Göteborg, Sweden

ABSTRACT

INTRODUCTION

During the recent years, there has been a newborn interest in Total Lagrange formulations for geometrically nonlinear problems. We can find articles by Felippa et al. -94 [2] describing the Core Congruential formulation. Zang and Peil -96 [3] has presented a modified bar element and Oñate -95 [4] has examined the possibilities of using the secant stiffness matrix. This presentation concerns analysis of geometrically nonlinear bar structures. The Core Congruential Total Lagrange Formulation (CCTLF) has been implemented for solving 3-D truss problems. The CCTLF will be described and numerical results for some well known examples will be shown and compared with analytical as well as numerical solutions by others.

CORE CONGRUENTIAL TOTAL LAGRANGE FORMULATION

The origin to this total Lagrange formulation was described by Rajasekaran and Murray [1]. The formulation was later generalized by Felippa and Crivelli and by Felippa, Crivelli and Haugen [2]· In this method the incremental form finite element equations, on element level, is developed in two steps. The first concerns derivation of 'core' stiffness equations for an individual particle in the continuum, expressed in terms of displacement gradients g for the particle. Then, at the second step, the core stiffness equations are transformed to physical-DOF stiffness equations for the nodal variables q through 'congruential' type transformations.

Let us consider a conservatively loaded body that undergoes finite displacements u. These displacements are measured from a reference configuration C_0 at time t=0 to a current configuration C at time t=t as $u_i = x_i - X_i$. Here $x_i(X_i)$ is the current position of a particle in the continuum originally situated at X_i in the reference configuration.

The material of the body is assumed to be linear elastic obeying the constitutive relation $S_i = S_i^0 + C_{ij}E_j$ or $S = S^0 + CE$. Here E is a vector containing the Green-Lagrange strain components E_j and S is a vector of corresponding conjugate Piola-Kirchhoff stresses S_i. Initial stresses S_i^0 are collected in the array S^0 and the elastic constants C_{ij} are elements of the symmetric matrix C. Now we aim to establish the Core-tangent stiffness matrix. The starting point is the Core analogue to the potential energy: The potential energy density. This energy is differentiated twice w.r.to the displacement gradients.

The development is exemplified for a 2 -node 3D bar element. This element is referred to a local Cartesian system $\{\overline{X}, \overline{Y}, \overline{Z}\}$ with $\overline{X}$ located along with the initial location the bar axis. The motion of a particle initially at $\overline{X}$ is described by the displacement components $\overline{u}_x(\overline{X}), \overline{u}_y(\overline{X})$ and $\overline{u}_z(\overline{X})$. As "Core-DOF" for the particle the three displacement gradients g_1, g_2 and g_3 are chosen, defined by

$$g = \begin{bmatrix} g_1 \\ g_2 \\ g_3 \end{bmatrix} = \begin{bmatrix} \partial\overline{u}_x/\partial\overline{X} \\ \partial\overline{u}_y/\partial\overline{X} \\ \partial\overline{u}_z/\partial\overline{X} \end{bmatrix}$$

As uniaxial strain measure we adopt the Green−Lagrange axial strain defined as

$$E \equiv E_1 = \frac{\partial\overline{u}_x}{\partial\overline{X}} + \frac{1}{2}\left[(\frac{\partial\overline{u}_x}{\partial\overline{X}})^2 + (\frac{\partial\overline{u}_y}{\partial\overline{X}})^2 + (\frac{\partial\overline{u}_z}{\partial\overline{X}})^2 \right] = g_1 + \frac{1}{2}(g_1^2 + g_2^2 + g_3^2)$$

This can also be written

$$E = \begin{bmatrix} 1 \\ 0 \\ 0 \end{bmatrix}^T \begin{bmatrix} g_1 \\ g_2 \\ g_3 \end{bmatrix} + \frac{1}{2}\begin{bmatrix} g_1 \\ g_2 \\ g_3 \end{bmatrix}^T \begin{bmatrix} 1 & 0 & 0 \\ 0 & 1 & 0 \\ 0 & 0 & 1 \end{bmatrix}\begin{bmatrix} g_1 \\ g_2 \\ g_3 \end{bmatrix} = h^T g + \frac{1}{2}g^T H g$$

Following Felippa et. al.[2] we calculate the vector b to be used in the core tangent stiffness.

$$b = \frac{\partial E}{\partial g} = h + \cdot Hg = \begin{bmatrix} 1 + g_1 \\ g_2 \\ g_3 \end{bmatrix}$$

Finally, we get the core tangent stiffness matrix as

$$\hat{K} = Cbb^T + SH = E\begin{bmatrix} (1 + g_1) & g_2(1 + g_1) & g_3(1 + g_1) \\ & g_2^2 & g_2 g_3 \\ symm & & g_3^2 \end{bmatrix} + S\begin{bmatrix} 1 & 0 & 0 \\ 0 & 1 & 0 \\ 0 & 0 & 1 \end{bmatrix}$$

Here S is the second Piola-Kirchhoff (PK2) axial stress and E is Young's modulus.

So far, in establishing the core tangent stiffness, no approximations are made. The finite element approximations are implemented in the next step transforming the core tangent stiffness to element tangent stiffness according to

238

$$K = \int_{V_0} G^T \hat{K} \, G \, dV \,, \qquad g = G \, q,$$

(6)

Here G is a "core" to physical degree of freedom transformation matrix that is independent of q. G is expressed as a chain of transformations

$$G = T\bar{G} \,, \quad \bar{G} = DN$$

(7)

where matrix $\bar{G}$ transforms g to local node displacements, and T transforms local to global node displacements. The D matrix is a differential operator matrix and N contains the element shape functions.

NUMERICAL EXAMPLES

The snap-through behaviour of the following test examples has been traced using the CCTLF together with a displacement incremental algorithm. The displacement components are given as linear approximations along each bar.
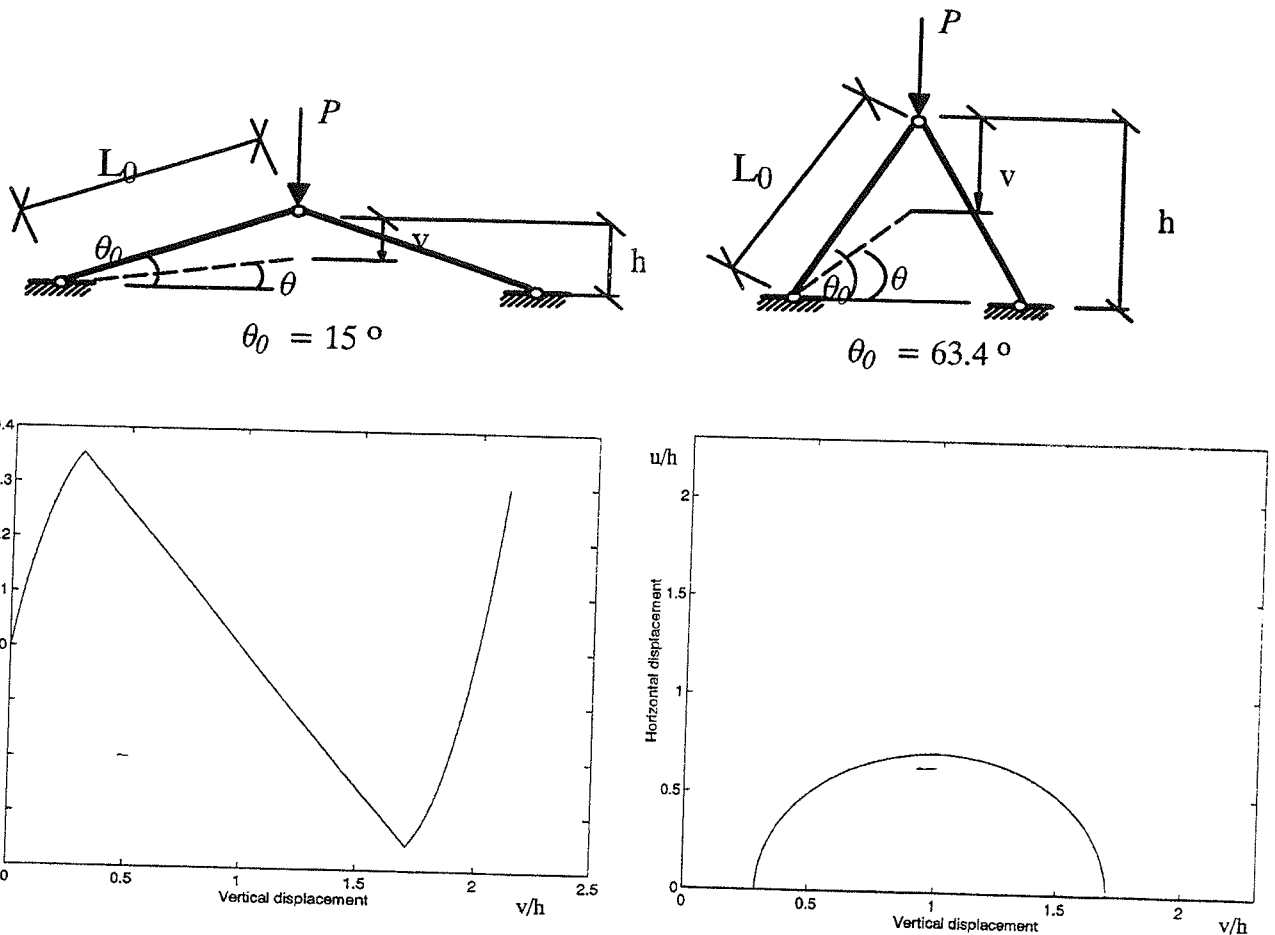
Fig. 1.a, b. Equilibrium path for the deep Von Mises truss with a small horizontal initial imperfection at the top node. Obs that shallow truss does not exhibit any bifurcation.

239
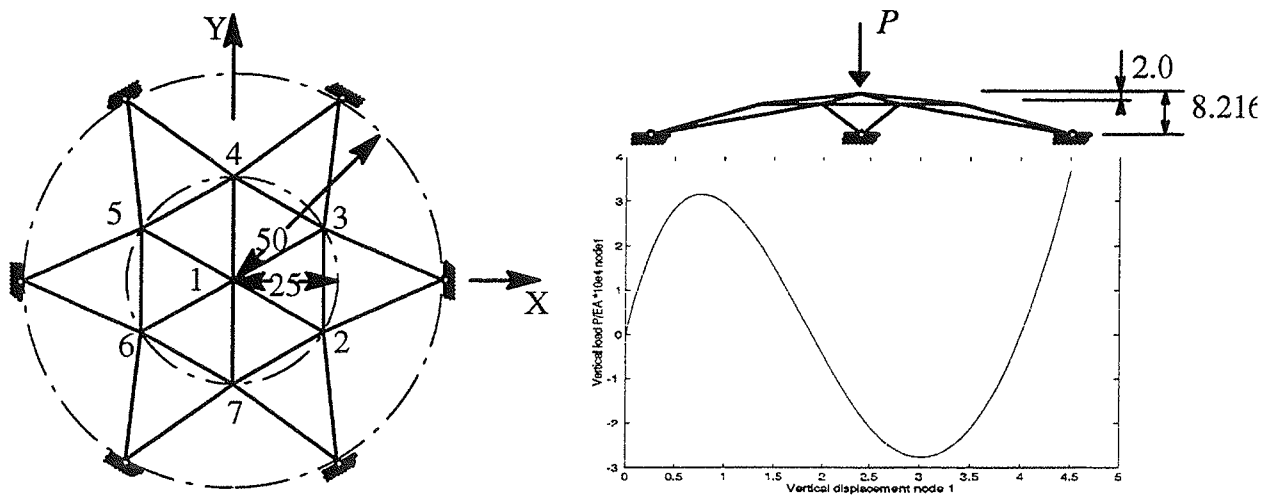
Fig. 2. Equilibrium path for the top node of a 24—bar truss dome.

CONCLUSIONS

The CCTLF has been implemented and reexamined for large deformation of bar structures. Especially for problems with translational DOFs only, the formulation is clear: First expressing everything in terms of displacement gradients without any approximations, then the FEM approximation is incorporated into the transformation of the core equations to the global DOFs equations. For treatment of problems with rotational DOFs the formulation still applies, but becomes slightly more complicated. We refer to Felippa et al.[2] and the 'Generalized CCTL Formulation'. The results for the Von Mises truss problems coincide with the analytical solution by Pecknold et al.[5]. The solution for the 24-bar truss dome correspond well to the numerical results by Paradiso et al.[6].

REFERENCES

[1] S. Rajasekaran and D.W. Murray : "Incremental Finite Element Matrices ", *J.Str. Div. ASCE*, **99** , pp 2423—2438, 1973

[2] C.A.Felippa, I.A. Crivelli and B. Haugen: "A Survey of the Core-Congruential Formulations for Geometrically Nonlinear TL Finite Elements", *Archives of Computational Methods in Engineering* **1**, pp 1—48, 1994

[3] Q.—L.Zhang and U.Peil: "A Modified Non-linear Member Element allowing Large Loading and Displacement Increments" *Comm. Num. Meth. Engng.* **12**, pp 235—242, 1996

[4] E.Oñate: "On the Derivation and Possibilities of the Secant Stiffness Matrix for Non Linear Finite Element Analysis", *Comp. Mech.* **15**, pp 572—593, 1995

[5] D.A.Pecknold, J. Ghaboussi and T.J.Healey:"Snap-Through and Bifurcation in a Simple Structure" *J. Eng. Mech. ASCE*, 111(7), pp 909—922, 1985

[6] M.Paradiso, E.Reale, G.Tempesta: "Non Linear Post-Buckling Analysis of Reticulated Dome Structures." World Congress on Shell and Spatial Structures, Vol 1 pp 1.67—1.80, Madrid 1979

FLEXIBLE MULTIBODY SYSTEMS WITH CONSTANT MASS MATRIX

NIELS L. PEDERSEN
Department of Solid Mechanics
Technical University of Denmark, Lyngby, Denmark

1. Introduction

By describing the flexible multibody only by the position of the nodes in the inertial frame, we have the ability to use isoparametric shape functions which results in a constant mass matrix. The constant mass matrix makes it possible to invert the mass matrix in a preprocessing stage. The already inverted mass matrix can then be used in the numerical integration of the mechanical system, instead of making the inversion in every time step. This helps reducing the computer time for the numerical simulation of mechanical systems with flexible members, which may otherwise be considerable. By this formulation where we only use as many variables to describe the flexible body, as there are degrees of freedom, we do not need to introduce reference conditions, as is needed in most other formulations for flexible multibody systems.

2. Formulation of the equations of motion

By using the principle of virtual work (variation in elastic energy equals variation in external work) we can find the equations of motion of the flexible body. The derivations follow the same principles as in Pedersen and Pedersen [2] and are intended to give a clear and direct derivation

Variation of work of inertial forces

The variation in the work done by the inertial forces is given below. It can be seen that the mass matrix is the standard mass matrix from FE-analysis, which in the case of isoparametric shape functions is a constant.

$$\delta W_{inertial} = -\{\delta q\}^T \rho \int_V [\Psi]^T [\Psi] dV \{\ddot{q}\} \Rightarrow [M] = \rho \int_V [\Psi]^T [\Psi] dV \qquad (1)$$

$[\Psi]$ is a matrix constituted by the shape functions
$\{q\}$ is the nodal coordinates in the inertial frame.

Variation in elastic energy

We are still focusing on the case of small strains. The traditional small strain measure can be used if we can find a way to express $\{q_{dis}\}$ where we have removed /minimized the rigid body movements. This can be done as illustrated in figure 1. The dashed rectangle in figure 1 is the original shape of the element, which has been rotated and moved in such a way that three of the eight displacements of the element are zero

when given in the element coordinate system, which in this case has been attached to node (q_1, q_2) and aligned so that the node (q_5, q_6) lies on one of the coordinate axes. In the blown-up circle the displacement of one of the four nodes is indicated.
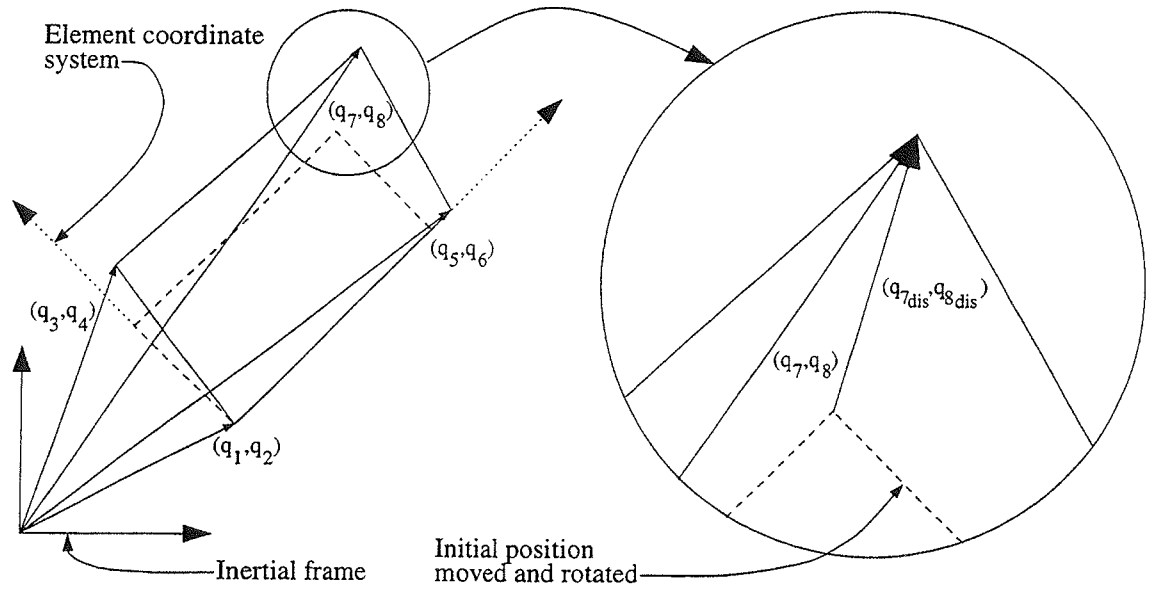
Figure 1 Displacement of an element in the inertial frame

The displacement in the element coordinate system can be written as

$$\{u''\} = [\Psi]\{q_{dis}''\} = [\Psi]([T]^T(\{q\} - \{q_t\}) - \{q_0''\})$$ (2)

where

$$[T] = \begin{bmatrix} [A] & [0] & [0] & [0] \\ [0] & [A] & [0] & [0] \\ [0] & [0] & [A] & [0] \\ [0] & [0] & [0] & [A] \end{bmatrix}, \quad [A] = \frac{1}{\sqrt{(q_5 - q_1)^2 + (q_6 - q_2)^2}} \begin{bmatrix} q_5 - q_1 & -(q_6 - q_2) \\ q_6 - q_2 & q_5 - q_1 \end{bmatrix}$$

$$\{q_t\} = \{q_1, q_2, q_1, q_2, q_1, q_2, q_1, q_2\}^T$$

$\{q_0''\}$ = Initial position of nodes in element coordinate system.

Double prime ('') indicates that the vector is given with respect to the element coordinate system. Some of the above derivations were specially related to the 4-node element but the extension to other elements should be clear. Since the elastic energy is not affected by translation we can rewrite the displacement used to calculate the variation in elastic energy as

$$\{q_{dis}''\} = ([T]^T\{q\} - \{q_0''\})$$ (3)

The variation in elastic energy can now be found. We first write the strain as

$$\{\varepsilon\} = [D]\{u\} \Leftrightarrow \{\varepsilon''\} = [D]\{u''\} \tag{4}$$

where $[D]$ is the standard differential operator and $\{u\}$ is the displacement of the nodes. We can now write the variation in elastic energy

$$\delta U = \int_V \{\delta\varepsilon''\}^T \{\sigma''\} dV = \int_V \{\delta u''\}^T [D]^T [C][D]\{u''\} dV =$$

$$\{\delta q\}^T \int_V \left[\frac{d\{\delta u''\}}{d\{q\}}\right]^T [D]^T [C][D]\{u''\} dV =$$

$$\{\delta q\}^T \left[\frac{d([T]^T\{q\})}{d\{q\}}\right]^T \int_V [\Psi]^T [D]^T [C][D][\Psi] dV \{q_{dis}''\} \Rightarrow$$

$$\delta U = \{\delta q\}^T ([T] + [G])[K]\{q_{dis}''\} \tag{5}$$

where

$$[G] = \frac{d(\{q\}^T[T])}{d\{q\}} \tag{6}$$

The bar over the node position in (6) is to indicate that in this differentiation only the transformation matrix $[T]$ is treated as a function of $\{q\}$, while the premultiplied $\{q\}^T$ is treated as a constant.

Equations of motion for a mechanical system

In the general case of a mechanical system with both flexible and rigid elements, it is still possible to get a constant "mass matrix" for the complete system. If we express the rotational degrees of freedom for the rigid bodies in the body coordinate system, the mass matrix of the individual rigid body is also constant. We may then connect rigid and flexible bodies in the same way as we connect rigid bodies to each other by applying constraints, for reference see Nikravesh [1]. In this way the size of the matrix to be inverted in every time step is reduced to the number of constraints as given in (7). This formulation does not rule out the effect that finer mesh in the FE-model of the flexible body introduces higher frequencies which slow down the integration of the system. This effect must still be avoided by use of modalsuperposition and/or the introducing of damping.

$$\{\lambda\} = \left([\Phi_x][M_{system}]^{-1}[\Phi_x]^T\right)^{-1}\left([\Phi_x][M_{system}]^{-1}\{f\} - \{\gamma\}\right)$$

$$\{\ddot{x}\} = [M_{system}]^{-1}\left(\{f\} - [\Phi_x]^T\{\lambda\}\right) \tag{7}$$

3. Kane's driver

The well known Kane's driver or Spin-Up maneuver, as it is called in Simo and Vu-Quoc [3], is used as an example. The data for the beam are given below and are taken from [3]

$$\Theta(t) = \begin{cases} \frac{6}{15}\left[\frac{t^2}{2} + \left(\frac{15}{2\pi}\right)^2\left(cos\frac{2\pi t}{15} - 1\right)\right]rad & 0 \le t \le 15\,s \\ (6t - 45)rad & t > 15\,s \end{cases}$$

$$r = \sqrt{\frac{1}{500}}m \cong 0.0447m, \quad E = \frac{500 \cdot 2.8 \cdot 10^7}{\pi} Pa \cong 4.46 \cdot 10^9 \, Pa, \quad \rho = \frac{1.2 \cdot 500}{\pi} \, ^{kg}/_{m^3} \cong 1.91 \cdot 10^2 \, ^{kg}/_{m^3},$$

$$v = 0.4, \quad L = 10m$$

The element used in this example is an 8 node rectangular element, and the result corresponds to the ones found in literature and illustrates the ability of the formulation. In this case 20 elements (206 degrees of freedom) were used. The high number of degrees of freedom was necessary since the element is not the best suited for a long slim beam. The CPU-time for this calculation was 1½ days, or 15 minutes with modal superposition. The standard element used in this simulation is the beam element, normal simulation time is 10 hours, but the number of degrees of freedom used is lees e.g. 18.
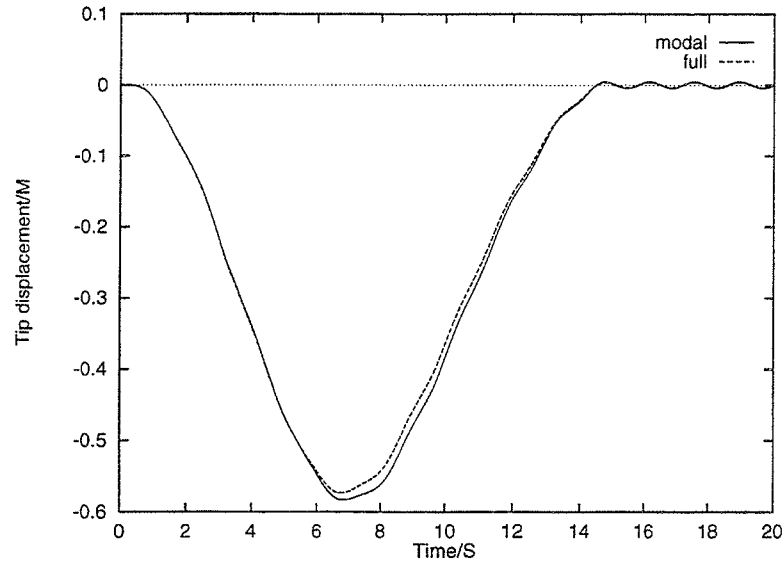
Figure 2. Transverse tip displacement of beam.

References

1.   Nikravesh,. E., (1988) *Computer-aided analysis of mechanical systems*, Prentice-Hall International, Inc., 370.
2.   Pedersen, N. L. and Pedersen, M. L. (1996) A direct derivation of the equations of motion for 3D-flexible mechanical systems, (submitted).
3.   Simo, J. C. and Vu-Quoc, L. (1986) On the Dynamics of Flexible Beams Under Large Overall Motions - The Plane Case Part I and II, *Journal of Applied Mechanics*, **53**, 849-863.

Patrik Hager[*], Romualdas Bausys[**] and Nils-Erik Wiberg[*]

[*]Department of Structural Mechanics, Chalmers University of Technology
S−41296 Göteborg, Sweden

[**]Department of Computer Assisted Engineering, Vilnius Technical Univerity
LT−2054 Vilnius, Lithuania

Summary

The computation of natural frequencies and modes in dynamics must be able to meet a demanded level of accuracy. The paper presents a method to control the error from the discretization of an engineering structure in the sense of the finite element method. This technique can be used as an error estimator and an error indicator in an adaptive analysis. The error estimator and error indicator are based on post-processed eigenmodes. The post-processing technique consists of two parts, local and global updating. The local updating is a variant of the Super convergent Patch Recovery technique (SPR). The global updating is performed by a preconditioned conjugate gradient technique.

1. Introduction

It is common in dynamics to compute natural frequencies and modes of vibration. This task is preferably accomplished by the finite element method. Applying the finite element method results in a discretization error which must be controlled for the solution to be acceptable. Generally only the lower eigenfrequencies of the discretized structure gives reasonable approximation to the corresponding exact eigenfrequencies of the real engineering structure. The most important ingredient of the error estimation is the construction of the new solution of a higher quality since the exact solution for complex engineering problems is generally unknown. Typically, this new improved solution is obtained by *a posteriori* procedure which utilize the original finite element solution itself.

The SPR technique for displacements (SPRD) has been applied to free vibration problems giving improved eigenmodes and by the Rayleigh quotient improved eigenfrequencies, Ref. [1]. A separate patch recovery must be made for each eigenpair. The SPRD approach is a local updating method, why a global system of equations never has to be solved. The method shows good results for the lower eigenfrequencies but for the higher eigenfrequencies the improvement is not enough to provide a reliable error estimation. In order to improve the higher eigenfrequencies we employ a preconditioned conjugate gradient method to optimize successive deflated Rayleigh quotients.

A brief description of our way to obtain reliable error estimators for all the eigenfrequencies of interest: Improve the Finite Element (FE) solution of order p by the SPRD method and use this improvent as starting trial eigenvector in the preconditioned conjugate gradient scheme, this yields a solution similar to the FE solution of order $p + 1$. Apply again SPRD on this improved solution to get an improved solution of order $p + 2$. A short survey of the literature on the SPR technique and the preconditioned conjugate gradient method is supplied in Ref. [2]. The techniques are also described there at a detailed level.

The traditional finite element approach to free vibration analysis of linear elastic continuum leads to the linear eigenvalue problem

$$(K - \lambda^h M)u^h = 0 \quad , \quad \lambda^h = (\omega^h)^2 \tag{1}$$

where K is the stiffness matrix and M is the consistent mass matrix of the structure. ω_i^h are the eigenfrequencies and u_i^h is a displacement field representing the corresponding eigenmode. If we know an eigenvector then we can compute the corresponding eigenvalue by the Rayleigh quotient

$$R(u_i^h) = \lambda_i^h = \frac{u_i^h K u_i^h}{u_i^h M u_i^h} \tag{2}$$

3. Post-processed Eigenfrequencies by Local Updating

The postprocessed eigenfrequencies will be calculated using Rayleigh quotient without solving the generalized eigenvalue problem. A new improved eigenfrequency will be of the form

$$(\omega_i^*)^2 = \left[\sum_{elem} \int_{\Omega_{elem}} (\tilde{\nabla} u_i^*)^T D \tilde{\nabla} u_i^* \, dx \right] \bigg/ \left[\sum_{elem} \int_{\Omega_{elem}} (u_i^*)^T \varrho u_i^* \, dx \right] \tag{3}$$

where u_i^* is a displacement field over the elements which has a higher order of accuracy.. The recovered displacement field of the eigenmode u_i^* will be determined by the SPRD technique, described below.

It has been known that the nodal points of the finite element approximation are points at which the prime variables have higher order accuracy than the order of accuracy in global sense. This knowledge is used to construct a dispacement field of order $p + 1$ for each element where this displacement field benefit from the higher accuracy in the nodal values. The field is constructed as: an element subject to SPRD, the master element, defines a patch including some surrounding elements, Figure 1. The nodal values in the patch are assumed fixed and the recovered displacement field are obtained by a least squares fit of a local polynomial to these nodal values.
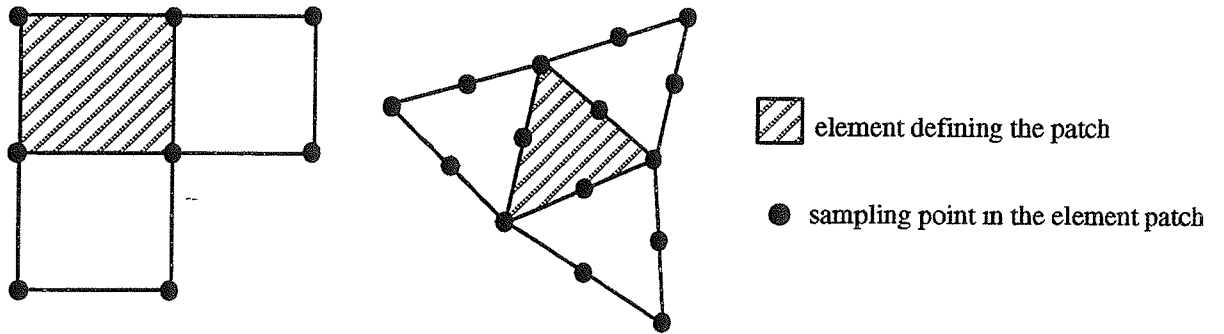

◻ element defining the patch

● sampling point in the element patch

Figure 1. Patches used for triangular and quadrilateral elements.

This method has a good convergence for the lower eigenfrequencies, but for the higher eigenfrequencies the improvement of the eigenpairs is still not enough due to the fact that the proposed approach is local and strongly depends on the original finite element solution and in this case on a too coarse

4. Improved Eigenfrequencies by Global–Local Updating

The eigenvectors can be characterized by

$$R(u_j) = \min_{y \perp_M V_{j-1}} R(y) \tag{4}$$

where $V_{j-1} \equiv \text{span}\{u_i,\ i = 1, ..., j - 1\}$. The basic idea underlying the employment of the conjugate gradient method is to minimize the Rayleigh quotient over the vector space that is the M–orthogonal complement to V_{j-1}. We anticipate that by chosing the SPRD solution of order $p + 1$ as starting vector in the conjugate gradient scheme we will have a rapid convergence. After the global updating we apply SPRD of order $p + 2$ to obtain the final improvement used in the error estimator in the adaptive algorithm.

The error in eigenfrequencies of the original finite element solution $\Delta\omega_i^h$ of the post–processed solution $\Delta\omega_i^*$ and the estimated error of the finite element solution $\Delta\bar{\omega}_i^h$, are defined as

$$\Delta\omega_i^h = \omega_i^h - \omega_i\ , \quad \Delta\omega_i^* = \omega_i^* - \omega_i\ , \quad \Delta\bar{\omega}_i^h = \omega_i^h - \omega_i^* \tag{5}$$

5. Numerical example

We consider vibrational problems of elastic two–dimensional structures which, in the equilibrium position, lie in a plane. We will be concerned with transverse vibration of thin membranes of uniform thickness. A square thin membrane of uniform thickness has been used, Figure 2a, as the analytical eigenfrequencies are available, and the quality of improved eigenfrequencies can be studied. The problem has been solved with consistent mass matrix. For simplicity, the wave propagation velocity $c = \sqrt{T/\varrho}$ is assumed to be $1.0\frac{m}{s}$, where T is the uniform tension in the membrane. In the finite element calculation, a sequence of four regular meshes with 4x4, 8x8, 10x10 and 15x15 elements are used to study the rate of convergence and the accuracy of the results for most commonly used linear quadrilateral elements.

One can observe that the rate of convergence towards each separate eigenfrequency is not uniform and sufficient accuracy is achieved after a few global updating iterations. In order to keep computational efficiency of the proposed global updating procedure the number of the iterations is therefore set to be 3 for all numerical experiments. This is done due to the reason that our goal is not to calculate the convergent eigenfrequencies for $p + 1$ finite element formulation, but to perform a sufficient number of global updating iterations to calculate improved eigenpairs in order to provide sufficient quality and reliability of the eigenfrequency error estimator. With the results of the numerical experiments at hand, Figures 2b and 2c, we can make the following observations:

(i) The eigenfrequencies of the original finite element solution exhibit $O(h^{2p})$ as predicted by *a priori* error estimation.

(ii) The recovered eigenfrequencies ω_i^*, obtained by SPRD technique and by global updating, (GL) demonstrate approximately $O(h^{2(p+1)})$ for quadrilateral and triangular elements.

We can also observe that the SPRD technique enables us to provide good error estimates of the eigenfrequencies only for sufficiently small size of the elements. The global updating enables us to overcome this shortcoming of the SPRD technique.

The proposed local updating (SPRD) technique provides an effective and reliable mean for eigenfrequency improvement for free vibration problems. By this approach, the recovered stresses or strains, used in strain energy calculation, are extracted from the recovered displacement field without any user tuned coefficients.

For all studied cases of the numerical experiments, the improved eigenfrequencies exhibit superconvergence, that is the rate of the convergence of the improved values is usually two orders higher compared to the finite element solution. The SPRD improved solution gives good initial trial eigenvector for the modified conjugate gradient scheme, which immediately put us on the asymptotic phase of the convergence profile resulting in a global-local updating technique.

References

[1] N.-E. Wiberg and R. Bausys. Error estimation for eigenfrequencies and eigenmodes in dynamics, In Pahl&Werner editors, *Proc. of the sixth Int. Conf. on Computing in Civil and Building Engrg.*, *Berlin, Germany, 12–15 July 1995*, pp 611–616. A.A. Balkema, Rotterdam, 1995.

[2] N-E. Wiberg, R. Bausys and P. Hager, *Adaptive h-version eigenfrequency analysis*, Pub. 96:11, Department of Structural Mechanics, Chalmers University of Technology, Göteborg, (1996).
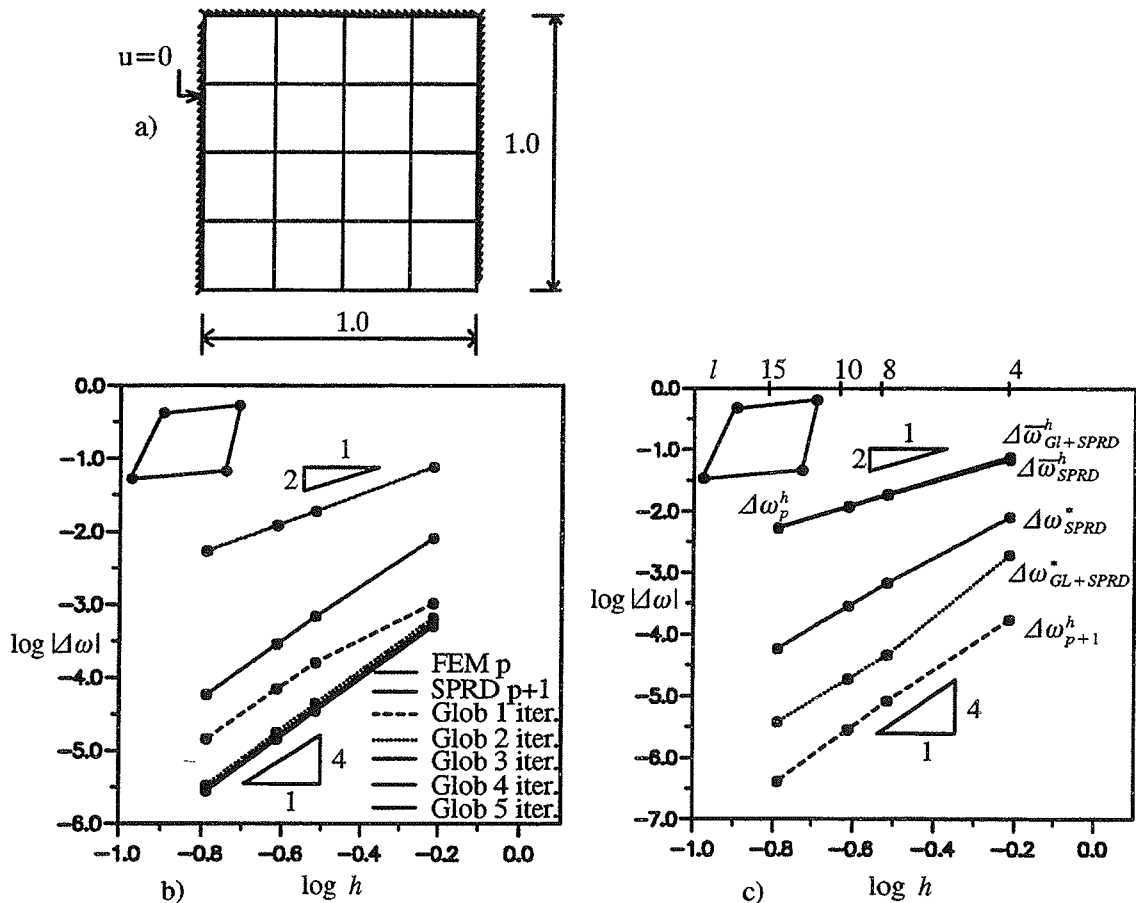
Figure 2. a) A finite element model of a square membrane

      b) Convergence rates of the 1:st eigenfrequency in iterations of global updating procedure

      c) Estimated rate of convergence of the 1:st eigenfrequency and rate of convergence of global updating with only 3 iterations + SPRD using quadrilateral elements.

Index